Final Report

A FUNDAMENTAL STUDY OF NUCLEATE POOL BOILING UNDER MICROGRAVITY

by

Jamie S. Ervin
Herman Merte, Jr.

NASA Grant NAG3-663
Report No. UM-MEAM-91-08

Conducted under:

National Aeronautics and Space Administration
Lewis Research Center
Cleveland, Ohio

Grant NAG3-663

August 1991

ABSTRACT

A FUNDAMENTAL STUDY OF NUCLEATE POOL BOILING UNDER MICROGRAVITY

by

Jamie Ervin

Herman Merte, Jr.

An experimental study of incipient boiling in short-term microgravity and with a/g = ± 1 for pool boiling was performed. Calibrated thin gold films sputtered on a smoothly polished quartz surface were used simultaneously for thermal-resistance measurements and heating of the boiling surface. The gold films were used for both transient and quasi-steady heating surface temperature measurements. Two test vessels were constructed for precise measurement and control of fluid temperature and pressure: a laboratory pool boiling vessel for the a/g = ± 1 experiments and a pool boiling vessel designed for the 131 m free-fall in the NASA Lewis Research Center Microgravity Research Facility for the microgravity tests. Measurements included the heater surface temperature, the pressure near the heating surface, the bulk liquid temperatures. High speed photography (up to 1,000 frames per second) was used in the experiments.

With high quality microgravity and the measured initial temperature of the quiescent test fluid, R113, the temperature distribution in the liquid at the moment of boiling inception resulting from an imposed step in heat flux is known with a certainty not possible previously. The types of boiling propagation across the large flat heating surface, some observed here for the first time, are categorized; the conditions necessary for their occurrence are described. Explosive boiling propagation with a striking pattern of small scale protuberances over the entire vapor mass periphery not observed previously at low heat flux levels (on the order of 5 W/cm^2) is described.

For the heater surface with a/g = -1, a step in the heater surface temperature of short duration was imposed. The resulting liquid temperature distribution at the moment of boiling inception was different from that obtained with a step in heat flux.

This report constitutes a major part of a dissertation submitted by the first author in partial fulfillment of the requirements for the degree of Doctor of Philosophy in the University of Michigan, 1991.

TABLE OF CONTENTS

LIST OF FIGURES

LIST OF TABLES

LIST OF APPENDICES

Appendix

NOMENCLATURE

A	Pre-exponential multiplier for equilibrium size distribution;		
	Area		m^2
a	Acceleration		m^2/s
B	Empirical constant, equation 2.18		
b	Bubble height		m
c_p	Specific heat		J/kg °C
c	Empirical constant, equation 2.25		
c_1	Empirical constant, equations 2.30 and 2.31		
F	Heterogeneous nucleation factor		
G	Gibbs free energy		
Gr	Grashof number	$\beta g L^3 \Delta T/\nu^2$	
g	Standard earth gravitational acceleration		m^2/s
h	Planck constant;		Js
	Enthalpy;		kJ/kg
	Convective heat transfer coefficient		W/m^2 °C
J	Nucleation rate		$1/cm^3$ s
k	Thermal conductivity;		W/m°C
	Boltzmann constant		J/°K
L	Characteristic dimension		m
n	Molecular concentration		
N	Number of spherical embryos of radius r		
Nu	Nusselt number	hL/k	
P	Pressure		kPa
q"	Heat flux		W/cm^2
R	Distance defined in figure 2.1;		m
	Resistance;		Ohms
	Bubble surface radius		m
r	Distance defined in figure 2.1		m
Ra	Raleigh number	$\beta g L^3 \Delta T/\nu^2\alpha$	
Re	Reynolds number	uL/ν	
Ri	Richardson number	Gr/Re^2	
ΔT_i	T_w-T_i		°C
ΔT_{ws}	T_w-T_s		°C
T	Temperature		°C
t	Time		s
u	Mean velocity		m/s

V	Volume	m^3
x	Distance from heater surface	m
Z	Distance defined in Figure 2.1	m

Superscripts

*	Boiling inception

Subscripts

b	Distance from heating surface to top of bubble nucleus
c	Cavity; Critical point property
crit	Critical
fg	Liquid-to-vapor phase change
het	Heterogeneous nucleation
hom	Homogeneous nucleation
i	Initial
l	Liquid
max	Maximum
min	Minimum
n	Nucleus
nc	Natural convection
o	Incipient boiling
qtz	Quartz
s	Saturation; Solid
sh	Shunt
sup	Superheated
spr	Boiling propagation
T	Total
v	Vapor
w	Heater surface

Greek

α	Thermal diffusivity	$k/\rho c_p$	m^2/s
δ	Thermal boundary layer thickness		m
δ^*	Superheated thermal boundary layer thickness		m
θ	Temperature difference		°C
ρ	Density		kg/m^3
σ	Surface tension		N/m
Ψ	Defined in Equation 2.8		
ν	Kinematic viscosity	μ/ρ	m^2/s
β	Coefficient of volume expansion		1/°C

CHAPTER 1

INTRODUCTION

The design of power generation systems and the extra-terrestrial storage of cryogenic fuels in microgravity for the U.S. space program require a knowledge of boiling and nucleation of the vapor phase. Boiling in microgravity is fundamentally different from boiling in earth gravity: the buoyancy force which induces liquid and vapor motion in boiling with earth gravity is effectively eliminated in microgravity. The study of boiling in microgravity can give some basic insight into the boiling process in the earth and space environment.

Because of the sometimes imprecise use of terms in connection with boiling research, it is desirable to clearly define a number of terms to be used here. The following discussion is for a pure substance, one that has a homogeneous and invariable chemical composition throughout.

Nucleation, pertinent to any discussion of boiling, is the formation of an interface between an initial parent phase and a second phase. Nucleation is classified as either homogeneous or heterogeneous. Homogeneous nucleation refers to nucleation taking place within a pure liquid bulk in the absence of any foreign particles or pre-existing phases at a uniform temperature as a result of local random density fluctuations. These density fluctuations can result in agglomerations of a sufficient number of molecules to form a nucleus of critical size such that subsequent growth can occur. (The thermodynamic requirements for this critical size will be given in Chapter Two.) Heterogeneous nucleation occurs at the interface between the

fluid and other materials, usually solid. The conditions necessary for heterogeneous nucleation to occur are not well understood, and may be quite different for disparate interfaces, such as smooth rigid surfaces (glasses for example), liquid-liquid interfaces, and non-smooth solid surfaces (crystalline metallic surfaces for example).

The terms incipient boiling, initiation of boiling, and onset of boiling all refer to the appearance of the first observable vapor bubble. Incipient boiling can result from either homogeneous or heterogeneous nucleation. The first observable bubble may be the consequence of growth from either a pre-existing nucleus or a newly formed nucleus.

Nucleation and boiling of liquids generally takes place by heating the liquid at a solid boundary, so that the liquid does not have a uniform superheat as under the circumstances of a pressure decrease. The heating of a liquid to a critical superheated state from a solid boundary until the onset of boiling occurs may be performed in a transient or a quasi-steady manner. Transient heating is inherently unsteady, while quasi-steady heating to the onset of boiling results from the application of a series of incremental steps in heat flux to a system where a steady temperature distribution is obtained following each of these steps until nucleation occurs. For example, a heated flat surface facing upward in a liquid pool in standard gravity results in natural convection, which permits a series of steady-state increments in heat flux before boiling first occurs. A quasi-steady heating process is not possible in the true absence of gravity, and may or may not be possible in microgravity, depending on the imposed heat flux level.

This is a study of incipient boiling in which body forces of $a/g = \pm 1$ and microgravity are used as a means of varying the temperature distribution in the liquid at the time of nucleation with all other parameters held constant. The liquid temperature distribution in microgravity, since buoyancy induced liquid motion is drastically reduced, is well defined relative to the liquid temperature distribution in a/g

$= \pm 1$. The conditions in microgravity existing at the moment of boiling inception will be compared with those at standard earth gravity. This study is limited to short term microgravity conditions, because of the practical limitations of achieving long term microgravity at the present time.

Incipient pool boiling was investigated in an attempt to assess the influence of liquid velocity under circumstances where buoyancy is anticipated to play a role. Short duration microgravity was available only for the pool boiling experiments. An imposed constant heat flux, constant surface temperature, and quasi-steady heating constitute the three different boundary disturbances used in the pool boiling experiments.

The principal objectives of this work are:

(1) To determine if known temperature distributions at the onset of boiling can be used to characterize the incipient boiling process.

(2) To examine how the onset of boiling is influenced by the method of heating using an imposed heat flux, an imposed surface temperature, and a quasi-steady heating procedure.

(3) To explore the features of observed phase change dynamics, and to characterize the parameters which produce particular types of vapor motion.

CHAPTER 2

LITERATURE SURVEY

Homogeneous nucleation in a pure liquid phase is unlikely in normal engineering applications because heterogeneous nucleation usually takes place before the large superheats necessary for homogeneous nucleation are attained. A metallic heating surface, for example, has numerous pits which not only serve as reservoirs for trapped gases, but also expose more grain boundary area (grain boundaries are regions of higher energy) to the liquid than would otherwise be available if there were no pits present.

For nucleation of a heated liquid to be homogeneous, the probability for the agglomeration of sufficiently energetic molecules to form a nucleus of critical size in the interior of the liquid must be greater than the probability for agglomeration of energetic molecules at its surface. A necessary condition for this to occur is that the heated liquid not be in contact with any vapor phase. According to Blander and Katz (1975), another condition which is sufficient but not necessary for homogeneous nucleation is that the liquid wet any other phase with which it is in contact. Jarvis et al (1975) have shown that if a liquid has a zero contact angle with any body that it contacts, then a bubble in the interior of the liquid is more stable than a similar size bubble at the interface. Hence, homogeneous nucleation is more likely to take place than heterogeneous nucleation. These conditions are met when the liquid is completely enclosed by a smooth surface. Examples are glass or another liquid which is non-volatile, as discussed in Blander and Katz (1975).

Homogeneous nucleation theory and its extension to heterogeneous nucleation is basic to any understanding of incipient boiling. A brief review of homogeneous nucleation theory will be presented first, followed by a discussion of heterogeneous nucleation.

2.1 Homogeneous Nucleation

Homogeneous nucleation may be considered from two perspectives. The first is the classical theory, attributed to Gibbs (1928), Volmer (1945), and Becker and Doring (1935), and refined by Frenkel (1955), and Zeldovich (1942). The second is the statistical mechanical point of view, associated with Reiss (1952a) (1952b), Mayer and Harrison (1938), Lothe and Pound (1966), and Abraham (1974), and others. The motivation behind the development of the latter perspective is that the assumption of the applicability of macroscopic thermodynamic properties to a small vapor bubble (which may be on the order of 25 molecules) was not deemed appropriate. However, it is difficult to obtain numerical results with the statistical approach and to relate these to experimentally measurable variables. As a way to circumvent these problems, some workers have combined concepts from both macroscopic and microscopic thermodynamics, bringing statistical thermodynamics into the classical expressions in the form of a correction factor, as in Lothe and Pound (1962). However, disagreement exists over the validity of this type of correction factor, as discussed in Reiss (1952), Lothe and Pound (1966), Reiss (1970), Reiss and Katz (1967), and Lothe and Pound (1968). The classical theory has been used successfully in predicting homogeneous nucleation temperatures for many fluids, as in Skripov (1974), Springer (1978), and Kotake and Glass (1981). Only the classical theory will be presented in the present work, as it provides insight into the basic physics of homogeneous nucleation.

Homogeneous nucleation of the vapor phase in the absence of solid surfaces, impurities, or ionizing radiation occurs within the bulk of the liquid as a result of molecular fluctuations in an isothermal system. These fluctuations give rise to a population of vapor embryos or agglomerations of molecules which may be described by a Boltzmann-like distribution of sizes, as discussed in Frenkel (1955):

$$N(r) = A \exp\left[\frac{-\Delta G(r)}{kT}\right] \tag{2.1}$$

N is the number of spherical embryos of radius r. ΔG is the change in the Gibbs free energy of an isolated isothermal system associated with the formation of a spherical vapor nucleus in the metastable superheated liquid. For the assumption of a spherical vapor nucleus in a liquid of uniform temperature, the Laplace equation provides the equilibrium pressure difference across a curved interface arising from the effect of surface tension:

$$P_v - P_l = \frac{2\sigma}{r} \tag{2.2}$$

With equation 2.2, an expression for ΔG can be derived:

$$\Delta G = r^{*2} 4\pi\sigma\left[\left(\frac{r}{r^*}\right)^2 - \frac{2}{3}\left(\frac{r}{r^*}\right)^3\right] \tag{2.3}$$

The first term on the RHS of equation 2.3 represents the surface energy contribution related to the formation of a spherical vapor liquid interface. The second term on the RHS of equation 2.3 is associated with the formation of a volume of the vapor phase. r^* is the critical size of the embryo, above which spontaneous growth of the

agglomeration occurs. Below r*, however, the embryo collapses. The surface tension is assumed to be a function of T only, which may be valid for agglomerations of sufficient size, as explained in Springer (1978). For phase transitions, the Gibbs free energy of the system is a minimum for stable equilibrium, while it is a maximum for metastable equilibrium since the Gibbs free energy of the system decreases for either an increase or a decrease in the size of an embryo of critical size, as discussed in Kottowski (1973). The second derivative of equation 2.3 evaluated at r* is negative, demonstrating that a superheated liquid is in a metastable state. An embryo of critical size corresponds to a maximum ΔG, or ΔG^* below. Hence, with $r = r^*$ in equation 2.3:

$$\Delta G^* = 4/3\ \pi\sigma r^{*2} \tag{2.4}$$

with equation 2.2:

$$\Delta G^* = \frac{16\pi\sigma^3}{3(P_v - P_l)^2} \tag{2.5}$$

The nucleation rate, or the rate of formation of embryos of critical size is given by Fisher (1948) as:

$$J = \frac{nkT}{h}\left[\exp\left[\frac{-\Delta G^*}{kT}\right]\right] \tag{2.6}$$

This expression for the nucleation rate neglects the term for the free energy of activation of the motion of an individual molecule of liquid past its neighbors into or away from the liquid-vapor interface. ΔG^* may be considered as a thermodynamic energy barrier for the liquid-to-vapor transition. In classical homogeneous nucleation

theory, vapor embryos are assumed to have the macroscopic properties of the liquid bulk phase. Hence, the surface tension in the above equations is the macroscopic flat-film surface tension. This assumption is often referred to as the capillary approximation. Different versions analogous to equation 2.6 exist but provide similar calculated results, as discussed by Skripov (1974). For simplicity, equation 2.6 will be used in the present work to represent J. The pre-exponential factor, $\frac{nkT}{h}$, is a large number, on the order of the number of molecules in the volume of liquid considered. T in equation 2.6 may be defined as the homogeneous nucleation temperature, denoted by T_{hom}, for a critical range of J, as discussed in Skripov (1974) and Nghiem (1980). T_{hom} actually covers a very narrow range of T and varies little even for a large change in the critical value of J. The maximum practical attainable superheat of a liquid is limited by T_{hom}, as discussed in Blander and Katz (1975) and Sinha (1980). It is noted from equations 2.5 and 2.6 that the exponential term of equation 2.6 is temperature dependent. As the temperature of a pure liquid is raised above its boiling point, the surface tension decreases and the vapor pressure increases. Each of these two factors leads to a decrease in the activation energy barrier, resulting in an increase in the likelihood of vapor nucleation.

Experimental studies of homogeneous nucleation abound and the following are selected as a representative sampling:

Simpson and Walls (1965-1966) used a pulsed wire technique to investigate nucleation. Their homogeneous nucleation temperature measurements were within $\pm$ 2 % of the theoretical homogeneous nucleation temperature of various organic fluids. The experimental apparatus consisted of a thin platinum wire immersed in different test fluids, including benzene, acetone, n-hexane, ethyl ether, and demineralized water at atmospheric pressure. The wire was subjected to an intense current pulse of short duration, so that nucleation would occur in the superheated thermal boundary layer of

the liquid near the wire surface. The transient heat flux from the wire was interpreted to be convection-free conduction to the liquid.

Skripov (1974) studied homogeneous nucleation in saturated hydrocarbons and fluorohydrocarbons by superheating floating droplets of saturated hydrocarbons and fluorohydrocarbons in sulfuric acid in a temperature gradient on the order of 0.1-0.5 ^{o}C/mm. Since the hydrocarbons were immiscible in the sulfuric acid, the nucleation taking place approached homogeneous nucleation. The homogeneous nucleation temperatures calculated by classical homogeneous nucleation theory agreed with measurements (differences were typically less than 1-2 ^{o}C).

Skripov (1974) also studied homogeneous nucleation in an expanding liquid achieved by means of a rapid pressure drop in a bubble chamber. He observed mean homogeneous nucleation temperatures which were within a few degrees Celcius of those predicted by classical homogeneous nucleation theory for n-pentane, n-hexane, diethyl ether, benzene, and hexafluorobenzene for various saturation pressures.

Derewnicki (1985) performed boiling tests using pulsed platinum wires (0.025 mm diameter by 10 mm length) immersed in degassed, distilled water. He claimed to find, by photographic means, homogeneous nucleation in the thermal boundary layer near the wire surface which became highly superheated as a result of the fast temperature rise.

Sinha (1980) measured the homogeneous nucleation temperature for Helium I using a transient bismuth magnetoresistive thermometer. Homogeneous nucleation temperatures for liquid nitrogen for reduced pressures, P/P_c, ranging from 0.03 to 0.91 were obtained by pulse heating a platinum wire (7 cm length by 0.102 mm diameter). The experimental temperature measurements were in good agreement with the classical nucleation theory. A corresponding state analysis for the case of homogeneous nucleation in liquid noble gases, both classical and quantum, was developed.

2.2 Heterogeneous Nucleation and Incipient Boiling

Heterogeneous nucleation, which is more probable in most engineering applications of boiling than homogeneous nucleation, is influenced by the geometrical, chemical, and physical properties of the boiling surface. Heterogeneous nucleation in boiling is extremely difficult to formulate mathematically as it is different for any given liquid-surface combination and depends on fluid contact angles, surface cold working (for metallic surfaces), grain boundary area (for metallic surfaces), and surface chemadsorption. In addition, minute cavities which might not be entirely wetted by a liquid may trap air or other gas molecules as potential centers for nucleation.

Several models for heterogeneous nucleation which utilize the macroscopic point of view based on the concept of surface tension have been proposed: Fisher (1948), Hirth and Pound (1963), Sigsbee (1969), Boucher (1969), Cole (1974), Zimmels (1976), Blander and Katz (1975), and Kotake and Glass (1981). The discussion in Blander and Katz (1975) will now be summarized, presenting the basic concepts of the macroscopic heterogeneous nucleation.

A bubble nucleating on a smooth liquid-solid interface is shown in Figure 2.1. The minimum work to form a bubble of critical radius in chemical and mechanical equilibrium is given by:

$$\Delta G^* = \sigma_{lv} A_{lv} + \left[\sigma_{sv} - \sigma_{sl}\right] A_{sv} - \left[P_v - P_l\right] V_v \tag{2.7}$$

If the bubble is assumed to be a spherical section, the bubble volume and interfacial areas can be expressed in terms of the radius of curvature, R, and contact angle, ϕ. From the geometry of Figure 2.1:

$$\frac{Z}{R} = \psi = \cos(\pi-\phi) = -\cos\phi \tag{2.8}$$

$$V = \frac{1}{3}\pi(R-Z)^2(2R+Z) = \frac{1}{3}\pi R^3\left[2-3\psi+\psi^3\right] \tag{2.9}$$

$$A_{lv} = 2\pi r(R-Z) = 2\pi R^2(1-\psi) \tag{2.10}$$

$$A_{sv} = \pi r^2 = \pi R^2\left[1-\psi^2\right] \tag{2.11}$$

By a force balance at the bubble edge,

$$\sigma_{sl} = \sigma_{sv}+\sigma_{lv}\cos(\pi-\phi) = \sigma_{sv} +\psi\sigma_{lv} \tag{2.12}$$

Hence,

$$\psi = \frac{\sigma_{sl}-\sigma_{sv}}{\sigma_{lv}} \tag{2.13}$$

Substituting equations 2.8 through 2.13 and the Laplace equation into equation 2.7 results in:

$$\Delta G^* = \frac{4}{3}\pi\sigma_{lv}R^2F \tag{2.14}$$

where:

$$F = \frac{2 - 3\psi + \psi^3}{4} \tag{2.15}$$

Equation 2.14 reduces to equation 2.4 with F = 1. An expression for the nucleation rate of the form similar to the combination of equations 2.6 and 2.4 can be obtained by substituting the ΔG^* of equation 2.14 for ΔG^* in equation 2.6. However, Blander and Katz (1975) suggest that J is proportional to $n^{2/3}$ rather than to n because molecules at the solid-gas interface are more likely to become potential bubbles than molecules within the volume of a liquid droplet. Thus:

$$J = \frac{n^{2/3} kT}{h} \exp\left(- \frac{\frac{4}{3}\pi\sigma_{lv} R^2 F}{kT} \right) \tag{2.16}$$

The ability of the above macroscopic model of Blander and Katz (1975) to predict the conditions necessary for heterogeneous incipient boiling and the resulting phase change dynamics is limited. For example, the microgeometry necessary for the determination of the F in equation 2.16 is unknown for most surfaces. In addition, the effects of gases adsorbed on the boiling surface are not accounted for in such a model.

Having examined the fundamental mechanisms of homogeneous and heterogeneous nucleation, the conditions influencing sustained heterogeneous incipient boiling in which bubble nuclei are formed or pre-exist during heating of the liquid will now be addressed. Models developed to predict incipient boiling have demonstrated limited degrees of success when compared with experimental measurements as a result of their inability to satisfactorily account for the following elements influencing the process:

(1) Surface microgeometry

(2) Surface energy

(3) Liquid temperature distribution

(4) Externally forced liquid motion

(5) Buoyancy induced liquid motion

The heater surface microgeometry, which is assumed to consist of microscopic crevices and pits, traps vapor and gases which become bubble nuclei. The heater surface energy affects the wettability of a surface by a liquid, and as a result, influences the ability of the surface microgeometry to trap vapor and gases. The liquid temperature distribution at the moment of incipient boiling depends on the presence of fluid motion, externally forced or resulting from density variations in a gravity field. These five elements will now be considered in some detail.

2.2.1 Surface Microgeometry

It is known, as indicated by the studies below, that nucleation and initial boiling are strongly affected by the surface microgeometry. Bankoff (1958), Griffith and Wallis (1960), Lorenz (1974), Winterton (1977), and Webb (1981), for example, purport that the role of microgeometry in incipient boiling is to trap gases and vapor, which then act as nuclei for bubbles. Howell and Siegel (1966) report that photographs of water boiling from artificial sites drilled in stainless steel surfaces show vapor remaining in the site after a bubble departs. The high speed photographic studies of surface boiling of pentane by Clark et al (1959) demonstrated that active nucleation sites were located at pits and scratches on the surface. Griffith and Wallis (1960) showed that the cavity mouth radius determines the superheat necessary for

conditions of isothermal incipient boiling, and that the shape of the cavity determines whether boiling will persist, once having begun.

Coeling and Merte (1968) presented experimental data for natural convection heat transfer and for boiling inception of LH_2 and LN_2. The experimental variables included heater surface material, surface roughness, and orientation. Stainless steel and copper surfaces were tested in both polished and lapped conditions. A surface coated with TFE teflon was also tested. Heater surface orientation, which included horizontal up, vertical, and horizontal down with respect to the direction of earth gravity, were test parameters. A stainless steel surface lapped with a 600 grit compound was found to be a more effective boiling surface for LH_2 than the same surface whether polished or lapped with a coarser 280 grit compound. In terms of vapor trapping in cavities, this experimental result indicated the existence of an optimum surface microgeometry for producing nucleate boiling with a minimum heater surface superheat. More recent works concerning the role of microgeometry in incipient boiling and nucleate boiling will be discussed below.

Webb (1981) presented a survey of the evolution of special surface geometries that promote high performance nucleate boiling covering the period from 1931 to 1980. The surface geometries described were designed with the intent of trapping vapor efficiently. These geometries included re-entrant cavities, porous coatings, and re-entrant grooves.

Forest (1982) presented a general free energy analysis of the equilibrium and stability of a gas-vapor nucleus inside of a surface cavity for a uniform temperature in the liquid. He demonstrated that the spontaneous growth of a pre-existing nucleus occurs when the radius of curvature reaches a minimum as the gaseous volume of the nucleus increases. This confirmed the earlier work of Griffith and Wallis (1960).

Tong et al (1990) described the influence of the dynamic contact angle on the liquid-gas trapping as related to boiling inception with highly wetting liquids.

Changes in the dynamic contact angle were shown to determine the trapped volume of gas in a heater surface crevice.

The major problem encountered in studying the role of surface microgeometry on incipient boiling for a "natural" boiling surface is how to satisfactorily quantify, in a collective manner, the micro-valleys, pits, and scratches present on such a surface. Surface roughness measurements are gross measurements for the length scale of the cavities being considered, which are on the order of 10^{-7} m. Surface roughness measurements do not necessarily detect vapor trapping re-entrant cavities or microscopic pits, while scanning the boiling surface at discrete locations may not reveal some potential boiling sites.

Chowdhury and Winterton (1985) studied the effect of surface roughness and contact angle on nucleate boiling using a quenching technique with aluminum or copper cylinders and saturated water or methanol. They concluded that the number of active sites, rather than the surface roughness as measured by a profilometer, influenced nucleate boiling. Consistent techniques for roughening different surfaces of the same materials produced remarkably similar boiling curves for surface-liquid combinations with the same measured contact angle.

2.2.2 Surface Energy

The importance of the surface energy, measured in terms of the contact angle, to the onset of boiling has long been known. However, surface energy is not well understood. It is not known explicitly how surface energy affects the formation of nuclei, nor how surface energy affects the stability of nuclei in potential boiling cavities. The contact angle between a solid and a liquid characterizes the wettability of a certain solid surface by a specific liquid. Parameters such as the volume of trapped air or gas in a surface cavity, the critical bubble radius and the resulting

incipient superheat are influenced by surface wettability. The description of this wetting phenomenon is difficult, as solid surfaces are surmised to have micro crevices and valleys of complex forms. In addition, chemical reactions may take place at liquid-solid interfaces and develop impurities which concentrate at the liquid-solid interface. The following studies examined the relationship between the contact angle and boiling incipience.

Cornwell (1982) maintained that boiling incipience was caused by the instability of pre-existing vapor-liquid interfaces in heater surface cavities. He proposed that the micro-roughness of the cavity walls results in a contact angle hysteresis between the advancing and receding contact angles which cause the meniscus within the cavity to invert from being convex to concave on the vapor side. This meniscus inversion provides an explanation for the trapping of vapor and gases. Surface heterogeneity in terms of spatially varying amounts of contaminants, including organic films and oxide layers, was purported to play a part in the contact hysteresis.

Winterton and Blake (1983) concluded that the liquid-vapor interface within a boiling surface cavity can adjust to external changes in liquid pressure on a time scale of less than a few seconds. They purported that boiling incipience on a heated surface induced by surface vibration can be explained in terms of the hysteresis between the advancing and receding contact angles.

In a theoretical investigation, Tong et al (1990) concluded that for highly-wetting fluids such as R113, the nucleus for boiling incipience lies below the cavity mouth radius. They also concluded that for such fluids, variations in the contact angle during bubble embryo formation and growth resulting from changes in the liquid-vapor interface velocity explain the wide variation in measured incipient superheat values. A method for calculating the wall temperature at boiling incipience was given, but depended on unknown values of the static equilibrium contact angle, the dynamic

contact angle, and the cavity geometry. As these values could not be measured, assumed values were used.

Because the heating surface microgeometry and surface energy are usually unknown, some studies have lumped these two effects in an energy reduction factor as a modification to classical expressions for homogeneous nucleation in order to predict boiling inception.

Nghiem et al (1981) attempted to determine the necessary conditions for transient incipient boiling with a step in power input using two test fluids, saturated water and R113 at atmospheric pressure, and using three test surfaces: a platinum wire (0.15 mm diameter x 24 mm length), a copper wire (0.2 mm diameter x 24 mm length), and a thin gold film (20 mm x 2 mm x 400 angstroms thick). It was observed that as the steady input heat flux was increased, the delay time for the onset of boiling decreased. This decrease in delay time was accompanied by higher wall superheats at the moment of boiling inception, up to 90 K at 0.9 sec for the R113. To incorporate the influences of convection, fluid properties, surface energy, and microgeometry of the heated surface on the delay time, an empirical factor was used in combination with an expression resulting from homogeneous nucleation theory. This factor was defined as:

$$F = \left[\frac{\Delta G_{het}}{\Delta G^*}\right] \tag{2.17}$$

where ΔG^*, the free energy required to form a vapor nucleus for the process of homogeneous nucleation, was defined in equation 2.4. ΔG_{het} was defined as the free energy required to form a vapor nucleus under conditions corresponding to heterogeneous nucleation. The expression of Fisher (1948) for the homogeneous nucleation rate of bubbles of critical size, given as equation 2.6 above, was used to

relate the nucleation rate to the observed nucleation delay time. Nucleation is considered to occur when a bubble of critical size forms and grows per unit volume in a reasonable time, t seconds, after the onset of heating. This t was termed the nucleation delay time, and J in equation 2.6 was taken as the inverse of this delay time, as a first approximation. Since the heterogeneous nucleation appeared to take place in the fluid immediately adjacent to the solid surface, the fluid temperature at the instant of nucleation was taken to be the same as the wall temperature. For a given fluid-surface combination, F was a function of the fluid properties and the measured heater surface temperature at the moment of incipient boiling. This particular treatment of incipient boiling will be considered in more detail in a later section.

A free energy reduction factor based on homogeneous nucleation theory paralleling that of Nghiem et al (1981) was also presented in Gerum et al (1979), where the value for the nucleation rate was taken as unity, using a form similar to equation 2.6. Calculated values of this energy reduction factor, based on measured quasi-steady heater surface temperatures at the onset of boiling, were correlated in terms of:

$$F = A \left(\frac{T_{crit} - T_w}{T_{crit}} \right)^B \tag{2.18}$$

for a number of different fluids, including R12, LN_2, R114, LO_2, R22, ethyl ether, and water. A and B were determined by curve fitting calculated values of F for a given substance as a function of the dimensionless temperature in equation 2.18. Critical heat flux heater surface temperature measurements were used in addition to the quasi-steady incipient boiling heater surface temperature measurements, as it was felt that the incipient boiling data alone were unreliable. However, this point is not clear.

2.2.3 Liquid Temperature Distribution

The role that the liquid temperature distribution in the vicinity of the heater surface has on incipient boiling will now be considered. Incipient boiling models which include the liquid temperature distribution will be examined first, followed by a discussion of the effect of the mode of heating.

Early models of initial boiling such as that of Griffith and Wallis (1960) and Corty and Foust (1955) assumed a liquid of uniform superheat. The predicted heater surface superheat at boiling inception by Griffith and Wallis agreed with the measurements only for a surface immersed in a uniformly heated bath. Furthermore, the two models referred to above placed no upper limit on the size of a potentially active cavity. It would appear reasonable that a cavity size must exist beyond which it could no longer become a nucleation site, since a cavity size large enough would be completely wetted.

Models for incipient boiling which attempt to incorporate the influence of liquid temperature distribution on the process assume a spherically shaped pre-existing vapor nucleus at the entrance of a heater surface cavity, and generally relate the difference between the internal vapor pressure of the nucleus and interface liquid pressure to the radius of curvature by equation 2.2. As was noted earlier, equation 2.2 is based on the assumption of a uniform liquid temperature and a nucleus of spherical geometry. This pressure difference is then related to the liquid superheat necessary by the Clausius-Clapeyron equation, which is based on equilibrium conditions. Analyses vary according to the equilibrium nucleus shapes assumed and the criteria necessary for the nucleus to grow, including the liquid temperature distribution. The growth criterion is usually that the local liquid superheat must attain a value greater than the saturation temperature of the vapor nucleus at some defined location.

The model of Hsu (1962) predicts a size range of potentially active heater surface cavities and will be described in some detail here since it incorporates the critical features of most nucleation models in varying temperature fields, and was one of the earliest to be presented. This model assumes the existence of a vapor nucleus of spherical cross-section geometry sitting at the mouth of a surface cavity. The origin of the nucleus is unclear. The liquid in a slab of thickness δ adjacent to the heater surface is taken to be heated in a transient conduction process by the solid heater surface. It was assumed that the temperature of the liquid at a distance greater than δ from the heater surface remained at T_∞. Figure 2.2a presents the coordinate system used and defined quantities. The model uses the following form of the energy equation:

$$\frac{\partial \theta}{\partial t} = \alpha \frac{\partial^2 \theta}{\partial x^2} \tag{2.19}$$

where $\theta = T - T_\infty$. The boundary and initial conditions for the constant temperature case of a heater surface are:

$$\theta(x,0) = 0 \tag{2.20}$$

$$\theta(0,t) = 0 \tag{2.21}$$

$$\theta(\delta,t) = \theta_w \tag{2.22}$$

The well-known solution is:

$$\frac{\theta}{\theta_w} = \frac{x}{\delta} + \frac{2}{\pi} \sum_{n=1}^{\infty} \frac{(-1)^n}{n} \sin\left[\pi n \frac{x}{\delta}\right] \exp\left[\frac{-\alpha t (n\pi)^2}{\delta^2}\right] \tag{2.23}$$

For a nucleus of height b above the heated surface, the nucleus is presumed to grow when θ equals θ_b at $x = \delta - b$. θ_b results from the Clausius-Clapeyron relationship and equation 2.2:

$$\theta_b = \theta_s + \frac{2\sigma T_s}{h_{fg}\,\rho_v\,r_n} \tag{2.24}$$

r_n is an effective bubble radius to be defined below. In this discussion, the saturation pressure corresponding to a flat liquid-vapor interface will be referred to as the "normal saturation pressure." T_s in equation 2.24 represents the saturation temperature in a system at a pressure corresponding to a flat interface and is similarly termed the "normal saturation temperature." $\theta_s = T_s - T_\infty$ and represents the bulk liquid subcooling. For a saturated liquid $\theta_s = 0$.

A relation among the bubble height, b, the radius of the bubble nucleus, r_n, and the cavity radius, r_c, was determined assuming that the vapor bubble was in the shape of a truncated sphere:

$$r_n = \frac{b}{c} = \frac{\delta - x_b}{c} \tag{2.25}$$

substituting equation 2.25 for r_n in equation 2.24:

$$\theta_b = \theta_s + \frac{2\sigma T_s}{h_{fg}\rho_v\left[\frac{\delta - x_b}{c}\right]} \tag{2.26}$$

where c was determined from the assumed geometry of the truncated sphere. δ was measured experimentally or estimated, as in Wiebe and Judd (1971). Dividing equation 2.26 by:

$$\theta_w = T_w - T_\infty \tag{2.27}$$

yielded:

$$\frac{\theta_b}{\theta_w} = \frac{\theta_s}{\theta_w} + \left(\frac{2\sigma T_s c}{h_{fg}\,\rho_v \delta\,\theta_w}\right)\left(\frac{1}{1-(x_b/\delta)}\right) \tag{2.28}$$

When the liquid temperature at x_b is equal to θ_b in equation 2.28, the bubble nucleus was said to begin to grow. For the transient conduction process within the liquid layer of thickness δ, this implies a tangency between the liquid temperature distribution curve and the equilibrium bubble temperature curve. Figures 2.2b through 2.2d present the sequence of events necessary for the bubble nucleus to grow as described above. Figure 2.2b presents the liquid temperature distribution before heating. Figure 2.2c shows the liquid temperature distribution during heating, but the liquid temperature distribution depicted does not yet pass through the equilibrium bubble temperature. Figure 2.2d presents the liquid temperature distribution passing through the equilibrium temperature, and the nucleus of equivalent radius r_n is now assumed to grow.

Cavities which required an infinite time to become active were considered to be inactive. At $t = \infty$, the temperature distribution in the liquid, from equation 2.23, is linear:

$$\frac{\theta}{\theta_w} = \frac{x}{\delta} \tag{2.29}$$

When equations 2.28 and 2.29 are set equal to each other at $x = \delta - b$, the upper and lower limits for a range of cavities which can be active may be found:

$$r_{C\,max} = \frac{\delta}{2c_1}\left[\left[1-\frac{\theta_s}{\theta_w}\right] + \sqrt{\left[1-\frac{\theta_s}{\theta_w}\right]^2 - \left[\frac{8\sigma T_s c_3}{h_{fg}\,\rho_v \theta_w \delta}\right]}\right] \tag{2.30}$$

$$r_{C\,min} = \frac{\delta}{2c_1}\left[\left[1-\frac{\theta_s}{\theta_w}\right] - \sqrt{\left[1-\frac{\theta_s}{\theta_w}\right]^2 - \left[\frac{8\sigma T_s c_3}{h_{fg}\,\rho_v \theta_w \delta}\right]}\right] \tag{2.31}$$

where:

$$c_1 = (1+\cos\phi)/\sin\phi \tag{2.32}$$

and

$$c_3 = 1+\cos\phi \tag{2.33}$$

Hsu used the values of 1.6 and 2 for the constants c_3 and c_1, respectively. The model of Hsu described above gives a range of cavities on a constant temperature boiling surface which are potential sites for boiling. For a saturated liquid:

$$\theta_s = 0 \tag{2.34}$$

$$r_{c\,max} = \frac{\delta}{2c_1}\left(1 + \sqrt{1 - \frac{8\sigma T_s c_3}{h_{fg}\,\rho_v \theta_w \delta}}\right) \tag{2.35}$$

$$r_{c\,min} = \frac{\delta}{2c_1}\left(1 - \sqrt{1 - \frac{8\sigma T_s c_3}{h_{fg}\,\rho_v \theta_w \delta}}\right) \tag{2.36}$$

For saturation conditions, it is required that:

$$\frac{8\sigma T_s c_3}{h_{fg}\,\rho_v \theta_w \delta} \leq 1 \tag{2.37}$$

for a physically reasonable cavity size range. With this in mind, Hsu gave a criterion for the boiling inception in terms of a critical θ_{wo} for the case with an imposed heater surface temperature:

$$\theta_{wo} = \theta_s + \frac{4\sigma T_s c_3}{\delta h_{fg} \rho_v} + \sqrt{\left[2\theta_s + \frac{4\sigma T_s c_3}{\delta h_{fg} \rho_v}\right]\left[\frac{4\sigma T_s c_3}{\delta h_{fg} \rho_v}\right]} \tag{2.38}$$

Boiling incipience occurred if the imposed heater surface temperature was greater than θ_{wo}. If δ were known by some measure, the surface temperature for incipient boiling could be predicted for a given subcooling from equation 2.38.

The case for a constant heater surface heat flux was also analyzed. The range of potentially active cavities for this situation was expressed by equations 2.30 and 2.31 by replacing θ_w with $q''\delta/k$. A criterion for the boiling inception in terms of a critical q''_o was also given for the case with an imposed heat flux:

$$q''_o = \frac{k}{\delta}\left[\theta_s + \frac{4\sigma T_s c_3}{\delta h_{fg} \rho_v} + \sqrt{\left[2\theta_s + \frac{4\sigma T_s c_3}{\delta h_{fg} \rho_v}\right]\left[\frac{4\sigma T_s c_3}{\delta h_{fg} \rho_v}\right]}\right] \tag{2.39}$$

For boiling incipience $q'' > q''_o$, where δ again must be determined in some manner in order to calculate q''_o.

A disadvantage associated with the Hsu model for incipient boiling is that the constants used in the model, including δ, cannot be measured, and must be assumed empirically to provide the best fit of the experimental data. Wiebe and Judd (1971) found that measured values of the heating surface temperature at boiling incipience agreed well with the θ_{wo} of equation 2.38. Shoukri and Judd (1975) found that although equation 2.38 predicted a surface superheat of 0.25 °C for the onset of boiling, no boiling was observed until a surface superheat of 5 °C was attained. Shoukri and Judd felt that boiling inception did not occur precisely at θ_{wo} because of

the nonexistence of sufficiently large cavities with the prerequisite trapped gas. They also found that measured boiling cavity radii data fell in the lower portion of the range of cavity radii predicted by the Hsu model.

A conduction model for boiling inception similar to that of Hsu is the model of Han and Griffith (1965). In this model the physical situation was formulated as a transient conduction problem in a semi-infinite liquid, where the temperature distribution has been solved by the Laplace transform method. The spatial derivative of the liquid temperature evaluated at the heating surface was set equal to the slope of an assumed linear temperature distribution in the liquid. The transient thermal boundary layer thickness was defined as:

$$\delta = \sqrt{\pi \alpha t} \tag{2.40}$$

The time from the onset of heating of the liquid to boiling initiation was defined as the waiting period, t_w. During the waiting period, the bubble nucleus was assumed to be hemispherical. The liquid temperature at a distance of 1.5 r_c from the heating surface, located on the interface of the vapor nucleus, was equated to the vapor bubble equilibrium temperature, yielding:

$$\delta = \frac{1.5\, r_c \left[T_w - T_\infty \right]}{\left[T_w - T_{sat} \left[1 - \frac{2\sigma}{r_c \rho_v h_{fg}} \right] \right]} \tag{2.41}$$

The distance 1.5 r_c, rather than a presumed cavity radius of r_c, comes from an analogy with potential flow, but this analogy is not clear. The effective cavity range was found

in a manner similar to that of Hsu (1962) and defined in terms of a maximum thermal boundary layer:

$$r_{c\,max} = \frac{\delta\left(T_w - T_s\right)}{3\left(T_w - T_\infty\right)}\left(1+\sqrt{1-\frac{12\left(T_w - T_\infty\right)T_s\sigma}{\left(T_w - T_s\right)\delta\,\rho_v\,h_{fg}}}\right) \tag{2.42}$$

$$r_{c\,min} = \frac{\delta\left(T_w - T_s\right)}{3\left(T_w - T_\infty\right)}\left(1-\sqrt{1-\frac{12\left(T_w - T_\infty\right)T_s\sigma}{\left(T_w - T_s\right)\delta\,\rho_v\,h_{fg}}}\right) \tag{2.43}$$

For $T_w = T_s$, $r_{c\,min}$ and $r_{c\,max}$ are both zero, which means that boiling does not occur.

The maximum thermal boundary layer thickness was considered to be capable of being determined from convection correlations. A disadvantage of the Han and Griffith model for the onset of boiling is the use of empirical constants, including r_c or δ. The heater wall temperatures computed from the Han and Griffith model were compared to the measured maximum transient wall temperatures in the work of Hall and Harrison (1966). The measured maximum wall temperatures were 30-40 °C higher than the computed wall temperatures at boiling incipience. Sakurai and Shiotsu (1977) claimed that Hall and Harrison should not have compared the measured maximum transient surface temperature with the incipient surface temperature as calculated by the Han and Griffith model, but rather felt that the measured incipient boiling surface temperature, which is not necessarily the maximum transient surface temperature, would more closely follow the Han and Griffith model. Ibrahim and Judd (1985) found that the Han and Griffith model does not correctly predict the bubble waiting time at high degrees of subcooling.

The Bergles and Rohsenow (1963) model of boiling initiation assumes a linear liquid temperature distribution near the heating surface, and relies on convection correlations for the determination of the active cavity range. Rohsenow (1970) later indicated that the trend predicted by this model could not be observed clearly in a large number of experimental data.

Sakurai and Shiotsu (1977) used a conduction model similar to those of Hsu, Han and Griffith, and Rohsenow, with different empirical constants to describe the geometry of the pre-existing nucleus. Experiments using an imposed exponential rise in heat flux with a horizontal platinum wire verified the predictions of their model.

The above conduction models neglect any turbulence effects which may be present in a flow field near a heating surface, and may explain the large errors observed when predicting the heater surface temperature at the onset of boiling.

2.2.4 Externally Forced Liquid Motion

The temperature distribution in the liquid adjacent to the heated surface is known to affect boiling inception. For example, the liquid temperature distribution produced by rapid transient heating is quite different from that as a consequence of quasi-steady heating. Homogeneous nucleation of various organic liquids initially at atmospheric pressure has been produced by heating a platinum wire immersed in the test fluids with an intense current pulse of short duration, in the studies of Simpson and Walls (1965-1966). However, what appears to be heterogeneous nucleation only has been obtained by quasi-steady heating from a solid surface immersed in organic fluids.

Externally forced liquid motion, as in forced convection boiling systems, influences the liquid temperature distribution. In a gravity field, the degree of this

influence is determined by the magnitude of the ratio of the buoyancy forces on the liquid to the inertial forces, and is expressed as the Richardson number:

$$Ri = \frac{Gr}{Re^2} \tag{2.44}$$

$Ri \equiv 1$: corresponds to "mixed" convection

$Ri >> 1$: corresponds to "natural" convection

$Ri << 1$: corresponds to "forced" convection

These parameters are defined in the List of Nomenclature. Figure 2.3 shows a solid surface with an imposed step in heat flux. Two mean liquid temperature distributions are presented: one mean temperature distribution in a flowing liquid and the other in a quiescent liquid. The effect of fluid velocity, regardless of the specific forces inducing the fluid motion, produces a temperature distribution which is lower than that of the liquid with zero velocity. The heater surface temperature at incipient boiling and the ensuing phase change dynamics are surmised to be different for the two temperature distributions.

Incipient boiling with forced convection and with transient heating of the surface is defined here for operational purposes as the appearance of the first visible bubble anywhere on the surface. Incipient boiling with forced convection as used here is distinctly different from what is generally termed incipient flow boiling, which usually refers to the quasi-steady heating of a flowing liquid until a vapor bubble appears either as the initial one on the heated surface or as an additional one at a location where no previous boiling had taken place. The latter will be referred to here as quasi-steady incipient boiling. Quasi-steady incipient flow boiling studies are reviewed in Yin and Abdelmessih (1977), Hino and Ueda (1985), and Lee et al (1988) and are not considered in the present work.

Few works have been reported on transient forced convection boiling, with even fewer reported for transient forced convection incipient boiling. Fabic (1964) used 4 mil thick nickel-iron (Deltamax) ribbons in flowing water to measure transient mean surface temperatures and measured the time from when the ribbon was energized to the appearance of the first bubble. The power input to the ribbon increased exponentially with time. Measurements of the mean surface temperatures by means of reading ribbon voltages from Polaroids of an oscilloscope had large uncertainties, on the order of $\pm$ 12 to 19 °C. Fabic presented a model based on a uniform temperature for incipient boiling which relied on assumed values of the advancing and receding contact angle. He also found that the heat flux predicted by the Bergles and Rohsenow (1963) correlation for incipient boiling with quasi-steady heating:

$$q''_l = 15.6\, P_l^{1.156} (Tw\text{-}Ts)^{(2.30/(P_l^{0.0234}))} \tag{2.45}$$

did not agree with the transient measured heat flux at the onset of boiling.

2.2.5 Buoyancy Induced Liquid Motion

When the local liquid temperature near the heating surface exceeds the saturation temperature by some amount, determined by the microgeometry of the solid surface, the surface-liquid properties, the surface temperature of the solid, and the temperature distribution in the liquid, incipient boiling occurs. The heater surface temperature and the liquid temperature distribution, in turn, depend on the heat flux and velocity distribution of the liquid as affected by gravity induced buoyancy. For forced convection boiling with Ri << 1, then the buoyancy forces are negligible. If Ri $\cong$ 1, then the buoyancy forces and the inertial forces acting are of similar importance.

Forced convection studies involving boiling inception were described above in the previous section.

For pool boiling in earth gravity, the liquid is initially stagnant. Buoyancy is the only force to initiate bulk liquid motion during the heating of the liquid with Ri >> 1. The onset of single phase natural convection is an instability phenomenon induced by buoyancy forces. Studies with the onset of natural convection occurring before boiling inception in a heated liquid pool at earth gravity or greater acceleration are reviewed in Ulucakli (1987). Additional works concerning the transient heating of a liquid pool in earth gravity include that of Oker and Merte (1978) and Nghiem (1980). In Oker and Merte (1978), the departure of the measured transient gold film temperature from the one dimensional conduction prediction was considered to be the onset of natural convection. For a flat rectangular heater surface horizontal up in earth gravity, a semi-empirical correlation for the onset of natural convection was found and is referred to in Chapter 5. In Nghiem (1980), transient boiling in water and R113 with various heater surfaces was investigated experimentally with an imposed step in heat flux. Prior to boiling, the onset of natural convection was observed with holographic interferometry for heated wires and a narrow (20 mm x 2 mm) thin gold film heater. Nghiem proposed an empirical heterogeneous nucleation factor which also included natural convection effects, and was described above in section 2.2.2.

2.3 Relationship to Proposed Research

The influences of surface microgeometry, surface energy, liquid temperature distribution, externally forced liquid motion, and buoyancy induced liquid motion in previous studies have been presented above in section 2.2. Information lacking in previous studies but pertinent to the objectives of this work is now discussed.

In Oker (1973), it was shown that fluid velocity as a consequence of gravity induced buoyancy can affect initial boiling and the early motion of the newly formed vapor phase. In Figure 2.4, incipient boiling with transient heating occurred at a considerably larger surface temperature for the horizontal up orientation than with microgravity, with all other test conditions held constant. This difference in surface temperature at initial boiling demonstrates that the temperature distribution in the liquid, which is effected by the fluid velocity, influences incipient boiling. The effect of a known liquid temperature distribution at the moment of boiling inception and the resulting phase change dynamics has not been previously examined and is an objective of the present study.

In transient pool boiling in the absence of buoyancy, an initially quiescent fluid remains stagnant upon heating until the onset of boiling. The transient temperature distribution at the moment of initial boiling in a motionless fluid can be determined from a conduction heat transfer analysis with a high degree of certainty. A heated liquid in microgravity does not have buoyancy induced fluid velocities, and thus, microgravity provides a known liquid temperature distribution at boiling inception.

Microgravity conditions may be obtained with drop towers, aircraft in parabolic flight trajectories, and sounding rockets. Although the available time in drop towers is short, up to a maximum of five seconds, a high vacuum drop environment can provide high quality microgravity, down to $a/g = 10^{-5}$. The time available for reduced gravity in aircraft flying a parabolic trajectory is typically greater than the time of microgravity in drop towers, up to 25 seconds. The quality of the reduced gravity when compared to microgravity conditions of a drop tower is considerably less, on the order of $a/g = 0.02$. In addition, the initial quiescent states required to obtain a well defined temperature distribution for studies of incipient boiling are not possible since operation requires large gravity fields preceding each trajectory, in addition to the normal disturbances associated with aircraft in flight. Sounding rockets

have been used to achieve high quality microgravity, claimed to be on the order of a/g = 10^{-4} for up to 140 seconds. The small size inherent in such vehicles requires limitations in the size of the heating surface and in the ability to obtain precise measurements. Repeated rocket launches are costly, and the possibility for non-reproducibility of the experimental conditions between tests is increased, particularly if new test equipment must be fabricated because of damage during retrieval. The present study is concerned with incipient boiling, and Merte and Littles (1971) presented a summary of incipient boiling work in microgravity.

Table 2.1 presents a survey of transient incipient boiling experimental studies. Oker (1973) examined the results of initial boiling of saturated R113 and LN2 in a drop tower (a/g = 0.004 for 1.4 seconds) using a semi-transparent gold film on pyrex glass. Oker was the first to measure the transient heater surface superheat required for boiling inception in microgravity and in earth gravity for various orientations. The degree of initial temperature uniformity was unknown, and special consideration was not taken to absorb the infrared radiation from the 200 watt mercury arc lamp used for the high speed filming. In addition, the system pressure was not controlled.

Straub et al (1990) summarized the results of a German microgravity boiling test program from the mid 1970s to the present which used sounding rockets and parabolic aircraft flights. Many of the tests were performed using heated wires. The diameters of these wires were of the same size as the thermal boundary layer surrounding the heated wires and comparable to the size of the vapor bubbles which nucleated on them. Surface tension effects on vapor motion were quite different for wires as compared to flat surfaces. Often the wires were completely enveloped by vapor at boiling inception, and subsequent surface tension effects maintained a "pseudo film" boiling only because of the wire geometry. Straub et al concluded that the effect of buoyancy on pool boiling was very small. This conclusion, however, was based largely on the results of the small diameter wire experiments (Weinzierl (1982),

Zell et al (1984)). In addition to the small heated wires, Straub et al also used thin film resistance surface heaters for boiling tests.

In transient heating, different boundary disturbances result in different temperature distributions. An imposed step increase in heat flux has a constant temperature gradient at the heater surface and provides an elementary boundary disturbance: all other boundary disturbances can be constructed from a series of steps in heat flux. An imposed heater surface temperature is another elementary boundary disturbance important in heat transfer and produces a temperature distribution in the liquid quite different from that of a step increase in heat flux. In Table 2.1, it may be noted that no previous study used an imposed surface temperature to study transient incipient boiling, as was used in the work described here.

The present work is the first experimental study of incipient boiling with transient heating in microgravity where the quiescent fluid had an initial known uniform temperature, and the pressure of the system was precisely controlled for various subcoolings. The microgravity tests involved a single step in heat flux imposed on a large flat heating surface for a five second duration with $a/g \cong 10^{-5}$. As a result of the well defined initial conditions of the tests and the single step in heat flux, the temperature distribution in the liquid near the heating surface was computed with certainty not previously possible. The present study is also the first to utilize an imposed surface temperature to specifically examine incipient boiling.

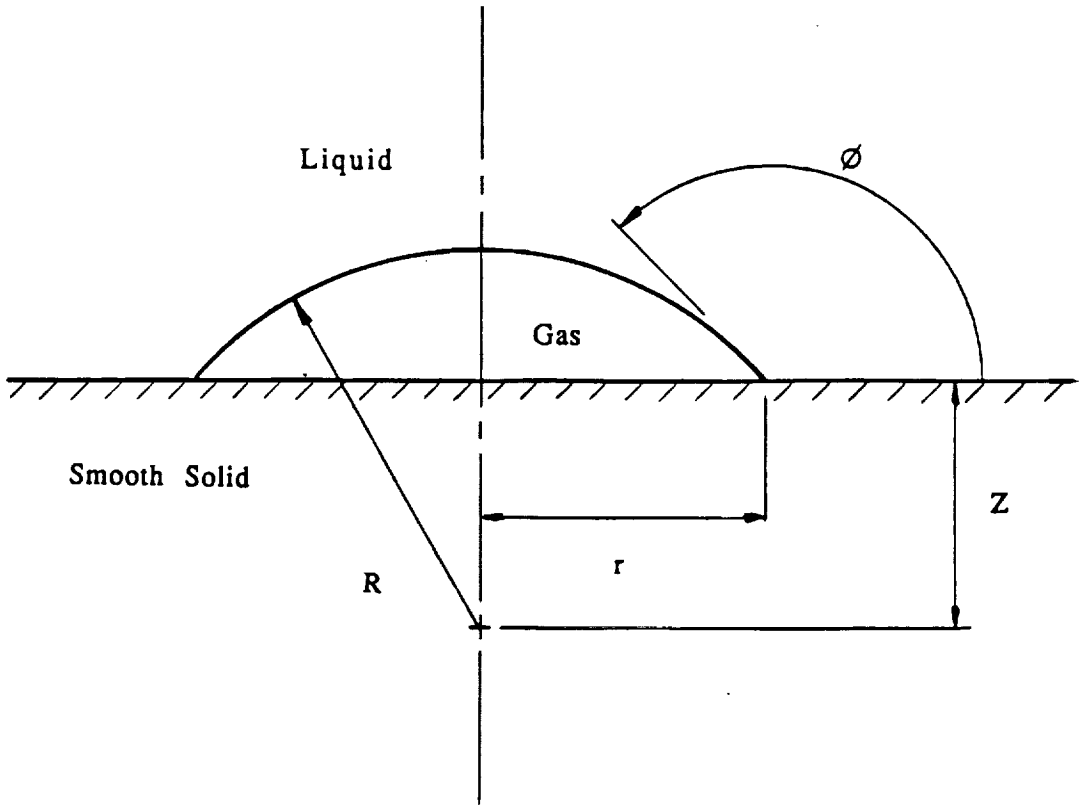

Figure 2.1 Gas bubble at a solid-liquid boundary

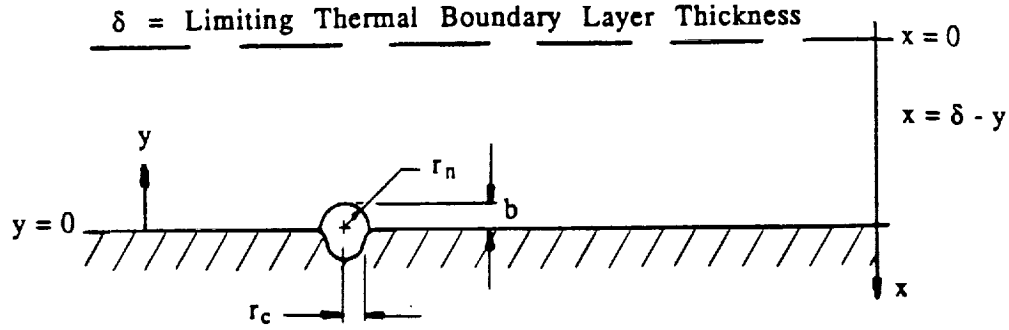

Figure 2.2a Pre-existing vapor nucleus protruding from a cavity

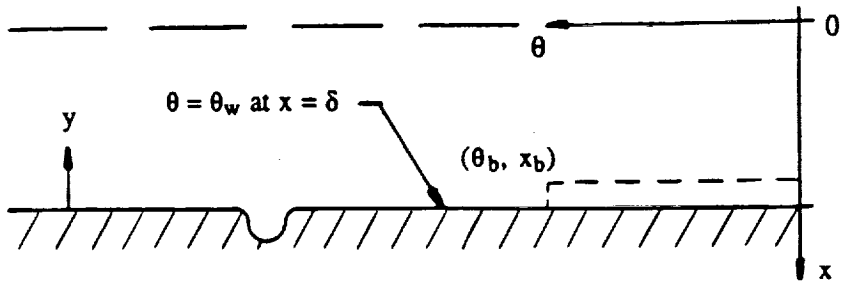

Figure 2.2b Initial liquid temperature distribution

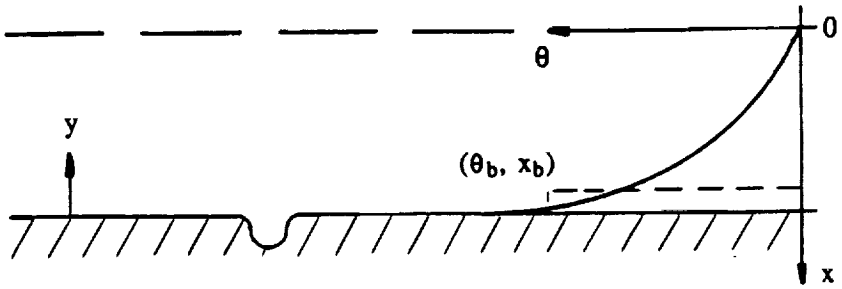

Figure 2.2c Liquid temperature distribution after heating, but below the equilibrium bubble temperature, equation 2.28

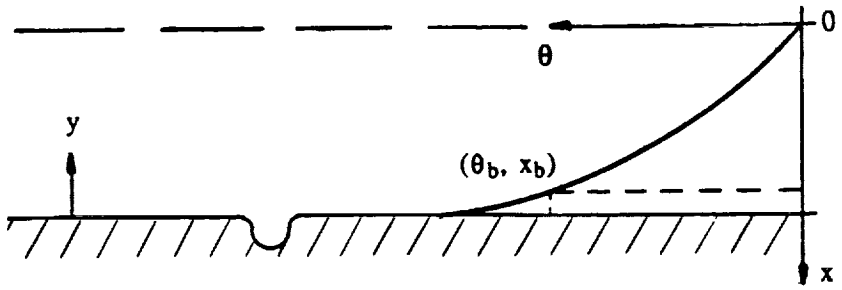

Figure 2.2d Liquid temperature distribution tangent to the equilibrium bubble temperature, and nucleus now begins to grow

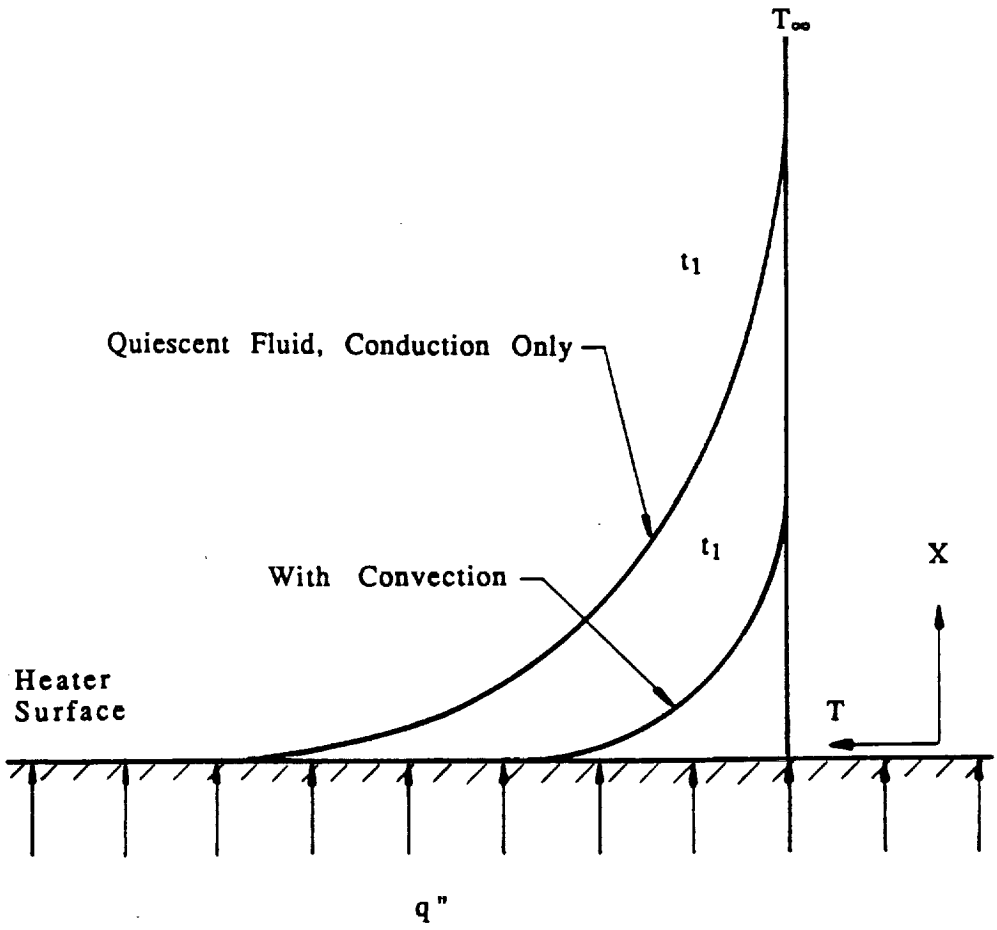

Figure 2.3 Influence of convection on mean liquid temperature distributions

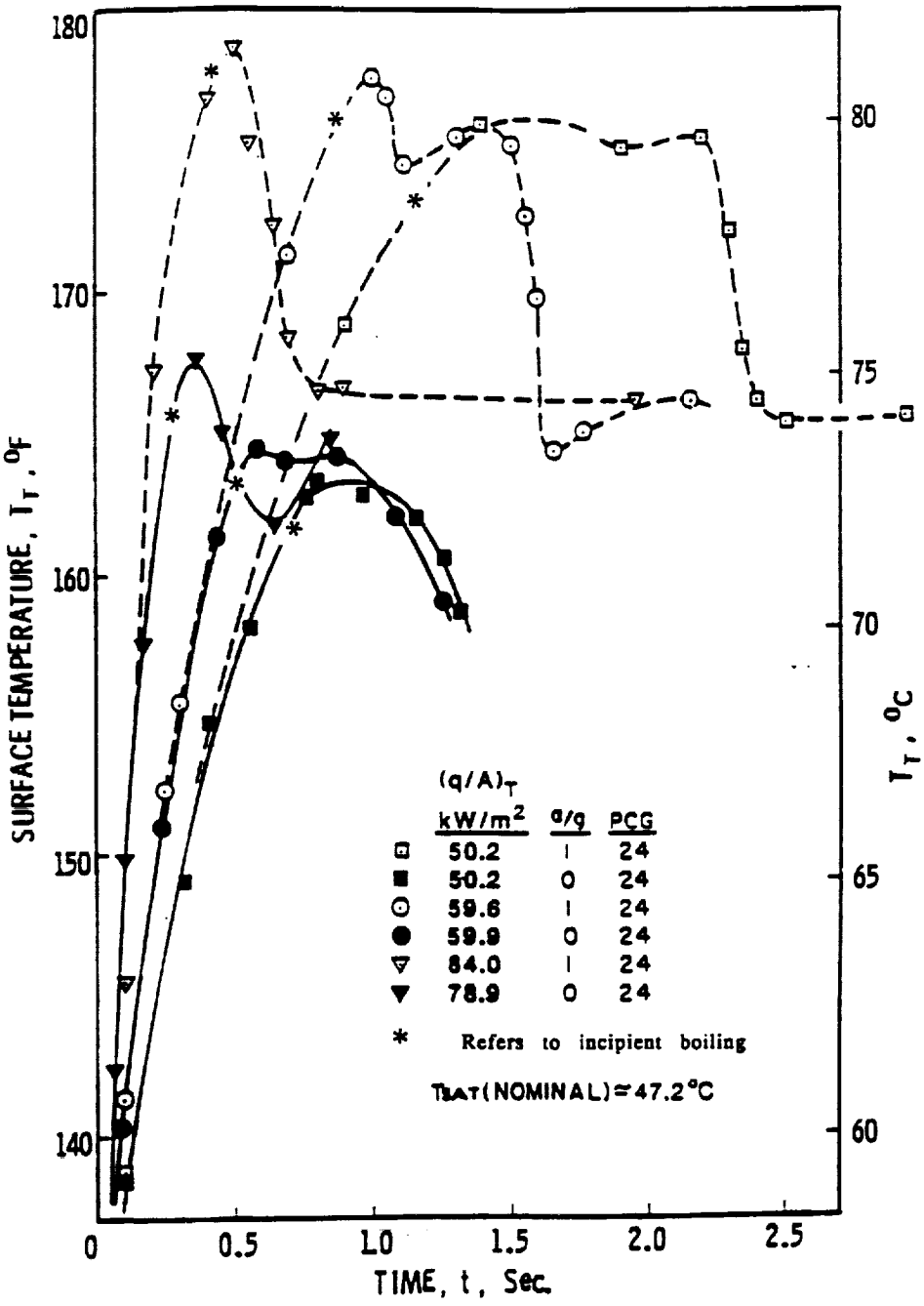

Figure 2.4 Transient surface temperature for gold film heater in R113, horizontal up in a/g = 1 and microgravity

Table 2.1 Transient experimental incipient boiling data

Heat Flux	Fluid/Surface	Geometry	a/g	High Speed Photos	Reference	Subcooling Deg. C	P level atm
Step	R113/Gold	Flat Surface	1	X	Ngheim (1980)	0	1
Step	R113/Gold	Flat Surface	0,1,-1	X	Oker (1973)	0	1
Step	LN2/Platinum	Wire	1		Sinha (1980)	0	
Step	LN2/Platinum	Wire	1	X	Tsukamoto et al (1980)	0	1
Step	LN2/Gold	Flat Surface	0,1,-1	X	Oker (1973)	0	1
Step	H2O/Copper	Wire	1	X	Ngheim (1980)	0	1
Exponential	H2O/Platinum	Flat Surface	1		Hall & Harrison (1966)	0-80	
Step	H2O/Iron-Nickel	Flat Surface	Vertical	X	Lurie & Johnson (1962)	0,62	1
Exponential	H2O/Platinum	Wire	1		Sakurai et al (1977)	25-75	1
Step	R113/Copper	Flat Surface	1	X	Okuyama et al (1988)	30	3.0-18
Step	Water/Platinum	Wire	1	X	Derewnicki (1985)	75-155	1.0-10
Linear	Water/Platinum	Wire	1	X	Faw et al (1986)	0-30	1-4.8
Stepped	R113/Platinum	Wire	0	X	Weinzierl & Straub(1982)	0-50	1
Stepped	R113/Gold	Flat Surface	0,1	X	Zell & Straub (1987)	0-48	1
Stepped	R12/Platinum	Wire	0,1	X	Zell & Straub (1987)	0-48	1
Linear Temp	LHe/Carbon	Flat Surface	Vertical		Giarratano et al (1980)	0	0.82
Step	LN2/Platinum	Wire	1	X	Okuyama & Iida (1990)	0	1

CHAPTER 3

EXPERIMENTAL APPARATUS

This is an experimental study of incipient boiling with variable subcooling for pool boiling. Pool boiling experiments were conducted in both earth gravity and microgravity, Two different test vessels were used: a pool boiling vessel for earth gravity studies (designated as the laboratory pool boiling vessel) and a pool boiling vessel for microgravity tests in a drop tower (designated as the drop vessel). The heat flux, heater surface temperature, pressure near the heating surface, and liquid bulk temperature were measured in both test vessels. High speed video recordings for the earth gravity experiments and high speed black and white movies for the microgravity tests were obtained. The videos and movies were recorded using two orthogonal views, across and through each test surface.

3.1 Common Experimental Elements

The heat transfer test surfaces, heater surface power controllers, test fluid, data acquisition systems, thermocouples, optics, pressure control system, camera synchronization, and vessel power supply were common to both of the test vessels and will be discussed before the unique details of each of the individual vessels are given.

3.1.1 Heat Transfer Test Surfaces

Two different kinds of heating surfaces were used in the experiments: a thin gold film deposited on a quartz substrate and a massive gold coated copper surface. Two types of boiling tests were performed in this study, transient and quasi-steady. The gold film heaters were used in both the transient and the quasi-steady tests, while the large thermal mass of the copper heater restricted it to the quasi-steady heating tests.

Figure 3.1 presents the concept of the gold film coated quartz heating surface. A 400 angstrom thick gold film is sputtered on a quartz substrate which was pre-sputtered with a 30 angstrom tantalum layer for improved gold adhesion. Before the tantalum layer was applied, the surface was cleaned by ion bombardment to remove about 10 angstroms of the quartz substrate. The thin film served simultaneously as a heater and a resistance thermometer, and had a negligible time constant associated with the transient temperature measurement. The temperature of the thin film thus is identical to that of the surface of the quartz substrate. The quartz substrate was highly polished by the manufacturer, using a 1.4 micron pitch polish. The semi-transparent gold surface consisted of a rectangular shape 1.91 cm by 3.81 cm (0.75 inches by 1.5 inches), and was expected to be considerably larger than the size of the bubbles to be formed above it. This semi-transparent gold surface had a higher resistance than the 10,000 angstrom thick gold surface near the power taps, which acted as the current connection. The voltage measuring leads also consisted of 10,000 angstrom thick gold films. Kovar screws passing through holes drilled in the quartz were used as power and voltage taps. The low linear thermal expansion coefficient of Kovar closely matched the linear thermal expansion coefficient of the quartz substrate, which was mounted in a Teflon holder.

As in the work of Oker (1973, 1981), it was found that the electrical resistance of the gold surfaces varied with time, but that the slope of the linear relationship of surface resistance and temperature, dR/dT, for each particular surface remained constant. This resistance change was attributed to an aging effect. Following the suggestion of Oker (1973), the surfaces were tempered at a temperature of about 275 ^{o}C for 20 minutes, which accelerated the aging to a stable level. It was also found in early testing that sputtered gold surfaces were more durable than those deposited by vacuum evaporation. The temperature-electrical resistance relation for each thin gold film surface was determined by calibration, and the details are presented in Appendix B.1. On the day an experiment was to be performed, the thin film heater was calibrated in place within the test vessel before heating the vessel and the test fluid to the test temperature level. This calibration is referred to here as the single point calibration. The single point calibration consisted of passing a small current, on the order of 20 milli-amps, across the thin film heater to produce negligible ohmic heating while simultaneously measuring the differential voltage across the heater surface and the differential voltage across a heater shunt, which was in series. With the differential voltage across the heater surface and the differential voltage across the shunt known, together with the calibrated shunt resistance, the heater surface resistance was determined from Ohm's relationship. Since the test vessel and fluid remained at the ambient temperature, the temperature of the heater surface during the resistance measurement was known from the calibrated test vessel thermocouples. Because the slope of the linear temperature-resistance relationship remained constant from previous calibration, this single measured heater surface resistance and corresponding measured fluid temperature determined the constant required for the temperature-resistance relationship. Additional details of the single point calibration are given in section 3.1.4.

Figure 3.2 shows the design of the typical metal heater used for the study of initial boiling under quasi-steady heating. The heater consisted of a copper block with a film heater imbedded in a Stycast electrical encapsulating potting compound. A copper foil, 0.00254 cm (0.001 inch) thick was soldered to the copper block and to the stainless steel holder to expose a continuous surface to the heated fluid, thereby preventing preferential boiling at the crevice that would otherwise be present. The copper foil was sputtered with gold to provide the identical heater surface-liquid energy combination as the gold deposited on the quartz. A chromel-constantan thermocouple with a bead of 0.025 inches was inserted into a 0.030 inch diameter hole in the copper heater in order to determine the temperature of the copper foil. The hole for the thermocouple was filled with a thermally conducting copper compound. The tip of the thermocouple was about 0.030 inches from the gold sputtered copper foil and was essentially at the same temperature as the heating surface. To prevent any air trapped between the stycast and the foil from expanding and deforming the foil during the period when a vacuum was imposed on the upper surface (as required for gold deposition and for the charging of the test vessel with the test fluid), it was necessary to embed an evacuation tube passing through the stycast to a point just under the copper foil. The other end terminated in a "quick-disconnect" fitting which could be attached to a vacuum pump when required.

3.1.2 Heater Surface Power Controllers

Two modes of heating were used in this study, transient and quasi-steady. For the transient heating studies two different conditions were imposed on the heater surface: a step increase in heat flux and a step increase in temperature. A heater surface controller was designed for use with both the step increase in heat flux and the

quasi-steady heating, and a different heater surface controller was designed to provide the step increase in surface temperature.

The power supply for the step increase in heat flux and the quasi-steady heating maintained a nominally constant voltage across the thin film surface for the boiling tests. Since the resistance of the thin film test surfaces during heating changed on the order of a few percent, the product of the current and voltage remained essentially constant. The constant voltage power supply could accept either a microprocessor input or a manual voltage pot signal as an input, and provided an output signal to the base of the power transistors, which in turn powered the thin film surface heater or copper block heater. The heater surface voltage was used as a feedback signal, compared with the set point voltage, and the difference amplified to furnish the appropriate signal to the power transistors. Details of the heater surface controller circuit for the step in heat flux and quasi-steady heating are given in Appendix E.1.

The imposed step increase in surface temperature tests, performed only in the laboratory pool boiling vessel, required a power supply different than that for the constant voltage heater surface controller. With the heater surface inverted in earth gravity for heating periods on the order of milliseconds, conduction heat transfer from the heater surface to the liquid may be used to determine the transient heat flux required to impose a constant heater surface temperature. The solution of equation 2.19, the one dimensional transient conduction equation, together with the boundary condition of an imposed step in heater surface temperature for two semi-infinite media with heat generation at their common plane, is well known. The result is a two domain solution, a temperature distribution for each of the two media. The partial derivative of the solution for each domain was evaluated at the common plane and multiplied by the respective thermal conductivity to obtain the heat flux from the plane of energy generation to each of the semi-infinite media. The transient heat flux to

each of the two domains was summed to obtain the required total energy input to the thin gold film heater:

$$q''_T = \left(\left[\sqrt{k \rho c_p} \right]_l + \left[\sqrt{k \rho c_p} \right]_{qtz} \right) \frac{T_w - T_\infty}{\sqrt{\pi t}} \qquad (3.1)$$

The details of the above analysis resulting in equation 3.1 are given in Appendix F. In the present experiment, a series of 24 imposed steps in heat flux were used as an approximation to equation 3.1. An illustration of this approximation to the exact expression for the total imposed heat flux is shown in Figures 3.3 and 3.4. The total heat flux-time curve initiated at a pre-set maximum total heat flux for 400 microseconds, then decreased in 23 discrete steps ranging in time intervals from 22 microseconds to 1.4 seconds, so that equation 3.1 was approximately followed.

A set of nichrome wire dropping resistors was fabricated to vary the voltage across the heating surface. The initial connection with the thin film heater was a direct connection to the power supply, providing the maximum power to the heater. The subsequent resistance steps reduced the power to the heating surface according to the time schedule given in Table 3.1, which apply for an initial maximum voltage. Each successive power level was produced by a different resistor and switch in series with the heater. One side of each resistor was connected to the supply voltage, and the other side was connected to a switch which was in series with the heater. Figure 3.5 illustrates the arrangement of the switches, resistors, electronic controls, and power generator.

The times for switching each resistor to approximate equation 3.1 were used in a microprocessor program written in assembly language to provide the switching signals, at the appropriate times, to the switching circuits. The switching currents

ranged from 37.5 amps to about one amp. Twenty-four MOSFETs were used as the solid state switching devices with the capability to perform the actual switching process in less than one microsecond. The MOSFETs were actuated by the output port controlled by the microprocessor, using timing pulses. (A MOSFET is a metal oxide semi-conductor field effect transistor.) Details of the circuitry for the imposed step in surface temperature are given in Appendix E.2.

3.1.3 Test Fluid

Commercial grade R113 (Refrigerant 113 or trichlorotrifluoroethane, CCl_2FCClF_2) was used for all of the experiments. This fluid, with a normal boiling point of 47.6 °C, was chosen as the test fluid because of its well established thermodynamic properties. The low normal boiling point permitted variation of subcooling by the control of system pressure. R113 is also electrically non-conductive, which prevented "deplating" of the thin gold film heater as would occur if water were used. Because of its vapor pressure and surface tension characteristics, R113 is representative of "space fluids" such as cryogens and other fluorocarbons.

A degassing and purification unit was necessary because of the high solubility of air in R113. For example at 25 °C and 1 atm, R113 saturated with air has a mole fraction of air dissolved nearly equal to 1.15×10^{-3} or a volume fraction of air dissolved of about 0.23 Dupont (1990). The degassing unit was fabricated of 304 SS, and a sketch of the system is shown in Figure 3.6. The concept of the degassing system involved a combination of distillation at room temperature, leaving behind the high boiling point components such as oils and solids, and freezing the R113 on the fins by LN_2 within the inner vessel. A sufficiently low pressure was maintained such that the air components, except for water vapor, were removed by a vacuum pump. Davison Chemical molecular sieves made from synthetic silico aluminate zeolite, with

a four angstrom effective pore size, were used to remove the water vapor, and also served as a mechanical filter.

3.1.4 Data Acquisition Systems

Because of the large differences required for the rate of heating in the imposed constant heat flux experiments and the imposed surface temperature experiments, two different voltage measuring systems were used for data acquisition: the CR7X and the Codas system.

The Campbell Scientific Co. CR7X (Serial No. 1448) is a programmable digital measuring and controlling device used to measure differential voltages from the thermocouples and the pressure transducer and across the heater surface and the heater shunt, in addition to sequencing events involving the drop vessel. The CR7X could record data within eight voltage intervals from $\pm$ 1.5 mV (with a resolution of 50 nanovolts) to $\pm$ 5 V (with a resolution of 166 microvolts) at two different speeds, designated as fast or slow. The CR7X sampled the voltage input channels sequentially in time.

Four tests were performed to determine the performance characteristics of the CR7X under various measuring conditions. The results of these tests are summarized here, with the details given in Appendix C. The maximum uncertainty in voltage on the fast sampling rate mode, the mode in which all tests were run, was $\pm$ 0.6 microvolts. This maximum uncertainty in voltage readings corresponded to an uncertainty in temperature as indicated by the thermocouples of about $\pm$ 0.01 ^{o}C for the 15, 50 and 150 mv ranges at the bulk liquid temperature level of 49 ^{o}C. The 15 mV and 50 mV voltage measurement ranges were the most desirable in terms of stability and accuracy in the 20 to 60 ^{o}C ambient temperature range, and had the smallest errors when compared to a standard reading from a potentiometer at the slow

sampling rate. It was determined that an ice reference junction for thermocouples provided more accurate temperature measurements than when the internal reference junction compensation of the CR7X was used. The dynamic measurements of the heater shunt and the heater surface voltages as measured by both the CR7X and the 7700 series 8 channel Sanborn recorder, which was used as a standard, were compared. The CR7X dynamic voltage measurements agreed with the Sanborn recorder measurements.

A schematic of the voltage measurement circuit for the determination of the surface temperature of the thin gold film is shown in Figure 3.7. The heater power supply set the voltage level for the circuit. Voltage differentials across the shunt and surface were measured with the CR7X in all of the tests except for the experiments involving the imposed step in surface temperature, where the Codas system was used. A calibrated shunt, 0.016314 $\pm$ 0.000002 Ω, was used for the determination of the current in tests in the laboratory pool boiling vessel. For the single point calibration in all of the laboratory tests, the National Bureau of Standards calibrated standard resistor (Leeds and Northrup Model No. 4221-B), with a resistance of 0.1000008 $\pm$ 0.000001 Ω was used. In the drop vessel, a relay was used to switch voltage difference measurement from a calibrated shunt, 0.014788 $\pm$ 0.000002 Ω, used for the drop tests to a calibrated resistor, 3.770 $\pm$ 0.001 Ω, used for the single point surface calibration. Figure 3.8 presents a schematic of the drop vessel heater surface experimental run and calibration circuit.

In order for the CR7X to sample in the fast mode, it was desirable to have voltages from the heater surface divided proportionately so as to be in the same voltage range as the shunt (150 mV). The heater surface voltages in all of the tests were divided by stable calibrated resistors.

For the imposed surface temperature experiments, the Codas system was used to measure differential heater and shunt voltages, in addition to the CR7X, because the

initial portion of the power transient was too rapid for the CR7X to sample. The Codas system consists of the software on an IBM PS/2-30 286 for acquiring data, an analog and digital interface card, and 16 single-ended (8 differential) analog input channels. The analog-to-digital converter has a 12-bit resolution, 1 part in 4096, with a conversion time of 20 microseconds (including acquisition) and a maximum throughput rate of 25 kHz for two channels. The full scale voltage input range of the Codas was -2.5 to +2.5 volts. The Codas software permitted programmable data acquisition and waveform analysis (integration, differentiation, rectification, and filtering) of the acquired data. The uncertainty in the Codas voltage measurements is $\pm$ 1.0 millivolts, presented in Appendix C.

3.1.5 Thermocouples

Chromel-constantan teflon sheathed thermocouples with ungrounded junctions were used for the measurement of the R113 temperature. These thermocouples were fabricated from a 30 gage thermocouple spool from Omega Engineering Co. The measuring junctions of the thermocouples were carefully welded to produce a 0.051 $\pm$ 0.013 cm (0.020 $\pm$ 0.005 inch) bead. The thermocouple reference junction was maintained in a dewar containing crushed ice and water, and each of the thermocouple wires and extension wires were numbered for identification purposes. The dewar for the drop vessel had an o-ring seal to avoid leakage under the external vacuum conditions. Copper wires were used as extension wires from the ice junction to the CR7X terminals. The thermocouple spool was calibrated with a platinum resistance thermometer, and the details of this calibration are given in Appendix B.2 The final accuracy of the temperature measurement as determined by a calibrated thermocouple was on the order of $\pm$ 0.01 ^{o}C, as discussed in Appendix D.2.

3.1.6 Optics

Two views of the heating surface were recorded in all of the transient experiments for purposes of determining the incipient boiling time and for observation of phase change dynamics. No images of the heating surface were recorded for the quasi-steady heating tests.

The optical arrangement for the laboratory pool boiling vessel and the drop vessel were essentially the same. Figure 3.9 shows the optical arrangement for the two orthogonal views of the heating surface. Light passed across the heater surface and simultaneously through the surface for the two simultaneous views. The light sources, labelled L1 and L2, were 360 watt bulbs powered by a 110 volt a.c. transformer to set the desired light intensity in the case of the laboratory pool boiling vessel. For the drop vessel, L1 and L2 were 80 watt lights. It was found that neither the 360 watt lights, set at their highest intensity in combination with the water cooled infrared filter (which contained water as an infrared absorbing media) for use with the laboratory pool boiling vessel, nor the 80 watt lights, used in combination with the cold mirrors of the drop vessel, produced any detectable increase in R113 temperature as measured by the vessel thermocouples over a 3 minute period (a much longer time period than any of the transient tests). Milk glass or ground glass was used to diffuse the light to permit improved imaging. Three mirrors, M2, M3, and M5, and a prism, P1, directed the light to the high speed camera. A light block reduced the amount of light entering the camera across the heater so as to produce a picture of the same brightness as the image formed from the light which passed through the surface. The mirrors and prisms, fixed to a vessel-mounted frame, were adjusted so that the two light paths were nearly equal.

The laboratory pool boiling vessel and the drop vessel had different imaging cameras. The high speed camera for the laboratory pool boiling vessel was a Kodak

Ektapro 1000 Image System, which was operated at speeds up to 1000 frames per second. This high speed camera system made video recordings which were stored on magnetic tape cartridges. A D.B. Milliken high speed camera (Model DBM 3A RFI, 28 volts d.c.) recorded boiling phenomena in the drop vessel on black and white film at 400 pictures per second with timing marks at 100 Hz for reference.

3.1.7 Pressure Control System

A schematic of the pressure control system is shown in Figure 3.10, and was essentially the same for both test vessels. The pressure system actively maintained and measured the pressure level of the liquid within each of the test vessels, and consisted of four main parts: a bellows, valves, electronic control circuits, and a pressure transducer.

A seven inch diameter stainless steel bellows isolated the test fluid, located on the inner side of the bellows, from the air (or nitrogen in the case of the drop vessel) on the external side of the bellows. The valves, which opened or closed as directed by signals from the electronic control circuits, admitted high pressure air to the bellows to increase the system pressure or released air from the bellows to lower the system pressure. The valves included two (four in the case of the laboratory pool boiling vessel) pneumatic solenoid valves (Kip Inc. No. 0141013, 12 volts d.c.), a proportional valve (Skinner valve No. BP2EV0035, 24 volts d.c. supply, 0-5 volts d.c. control), and a needle valve.

A description of the electronic control circuits for controlling the pressure is presented here, while the circuit diagrams are given in Appendix E.3. The pressure control card received a set point either from a microprocessor, in the case of the drop vessel, or from a manual input, for the laboratory pool boiling vessel and. The output signal from the pressure transducer is also transmitted to the control card. The set

point voltage is compared with the actual pressure transducer signal, and their difference, suitably conditioned, used as inputs for actuating the vent and fill solenoid valves and the proportional valve. While the proportional valve operated continuously, the vent and fill solenoid valves were normally closed. They were actuated only when the pressure error exceeded a pre-determined value. The vent and fill solenoid valves controlled the large pressure transients while the proportional valve controlled small pressure fluctuations. The vent and fill solenoid valve controllers opened the valves at a given error level and caused them to remain open until the error was reduced to half the original error. The proportional valve controller used a combination of proportional and integral controller modes. The proportional mode responded to pressure transients while the integral controller mode attempted to drive the steady state error to zero. The proportional valve was operated within its linear range of operation by adjusting the needle valve on the "fill side" so that as voltage to the proportional valve was increased or decreased, the flowrate from the bellows changed in direct proportion to the voltage.

A Heise Model 623 pressure transducer was used for the measurement and the pressure control in the laboratory pool boiling vessel. The Heise pressure transducer had a maximum pressure rating of 344.74 kPa (50 psia) and a sensitivity of 0.01724 kPa (0.0025 psi). The Heise pressure transducer provided a pressure measurement with an uncertainty of $\pm$ 0.028 kPa ($\pm$ 0.004 psi). The pressure level was controlled to within $\pm$ 0.172 kPa ($\pm$ 0.025 psi) of the set point pressure, corresponding to $\pm$ 0.06 ^{o}C ($\pm$ 0.1 ^{o}F) of the saturation temperature The pressure transducers were mounted horizontally at the center of rotation on the laboratory pool boiling vessel so that compensation for the change in hydrostatic pressure at the heater surface on test package rotation took place requiring only a sign change, provided by the software which translated the transducer signal into a pressure measurement.

The pressure system of the drop vessel was similar to the laboratory drop vessel, except for a few minor differences. The gas side of the bellows in the drop vessel was pressurized by an on board high-pressure nitrogen tank supply rather than by a building air supply as for the laboratory pool boiling vessel . Instead of a calibrated Heise 623 pressure transducer, a calibrated Setra model 270 pressure transducer which could withstand a 50 g impact was mounted on the top vessel wall and provided pressure determination within the desired uncertainty range of $\pm$ 0.172 kPa ($\pm$ 0.025 psi). In addition, as a guarantee against the possible detrimental effects of the drop tower vacuum, the CR7X was mounted in a pressurized box. A complete pneumatic diagram for the drop vessel is shown in Figure 3.11.

A discussion of the uncertainty estimates in the pressure transducer measurements is presented in Appendix D.3. For pressure calibration of the Heise and Setra pressure transducers, a Ruska Pressure Dead Weight Calibration System (2400 series dead weight gage) was employed, and the details of this calibration are given in Appendix B.3 The Ruska system was also used for calibrating a Heise Bourdon tube gage which in turn was used for in-place periodic check calibrations of the pressure transducers.

3.1.8 Camera Synchronization

The camera was synchronized with the powering of the heater surfaces to establish a time reference for the observation of incipient boiling phenomena. The description of the synchronization apparatus for each of the vessels will now be presented, beginning with the laboratory pool boiling vessel.

To synchronize the high speed video system with the switching on of the heater power for the constant heat flux tests in the laboratory pool boiling vessel, a light emitting diode was placed in the field of view of the camera. The light emitting diode

was in parallel with a copper knife switch to the 24 volt power source. When this knife switch was closed, the quartz heater and diode were simultaneously powered. A five millisecond delay exists until the light emitting diode provides sufficient illumination for viewing by the camera. As a result of this delay, there was an uncertainty of $\pm$ 6 milliseconds in the time interval between heater powering and visible light emitting diode illumination.

For the imposed step in surface temperature experiments in the laboratory pool boiling vessel, a light emitting diode was placed in the field of view of the camera to synchronize the camera with the powering of the thin gold film heater. The light emitting diode, which was powered by a nine volt battery, was switched on by the same signal that turned on the first MOSFET switch of the heater driver. The uncertainty in the time interval between the powering of the heater and recording of the light emitting diode at 1000 fps is $\pm$ 1.5 ms. This uncertainty in the time interval is smaller than that associated with the imposed step in surface heat flux because the voltage switching for the diode was done by electronic components rather than by a copper knife switch.

As in the case of the laboratory pool boiling experiments, a light emitting diode was placed in the field of view of the camera for the synchronization of the high speed camera with the powering of the thin film heater for the drop vessel experiments. The CR7X powered the light emitting diode with a 5 volt signal 2.9 milliseconds after the thin film heater was energized. The diode took 5 milliseconds to reach maximum intensity. The uncertainty in the time interval between powering of the diode and of the heater was $\pm$ 7 milliseconds.

3.1.9 Vessel Power Supply

For the imposed step in heat flux tests, with the lab pool boiling vessel an essentially noise-free 24 volt d.c. power supply consisting of two 12 volt batteries connected in series was used. A Sorenson three phase 240 volt a.c. power converter supplied up to 150 d.c. volts to the power heater supply for the step in surface temperature experiments. The $\pm$ 5 and $\pm$ 15 d.c. volts required for the control circuits were supplied by a 110 volt a.c. converter. An additional 110 volt a.c. converter supplied 12 volts for the operation of the solenoid valves.

The 24 volt d.c. power supply for the drop vessel heater and pressure controls were provided by batteries mounted on the drop bus. The $\pm$ 5 and $\pm$ 15 volt d.c. power supply consisted of a 24 volt d.c. power converter mounted on the heater surface controller cards. The 12 volt d.c. supply needed for the operation of the solenoid valves was provided by batteries mounted on the drop bus.

3.2 Laboratory Pool Boiling Vessel

The laboratory pool boiling experiments were conducted at a/g = $\pm$ 1. This variation in body forces was achieved by inverting the test vessel from horizontal up (a/g = + 1) to horizontal down (a/g = -1). Heat flux, liquid subcooling, surface type, and orientation of heating surfaces were the test parameters.

The laboratory vessel shown in Figure 3.12 contained two heater test surfaces, both located on the same surface of the vessel. Trunions located on opposite sides of the vessel permitted rotation between the horizontal facing up and the horizontal facing down orientations with respect to the earth body force direction. The laboratory vessel was vacuum helium leak tested and was found to be leak free for the system pressurized with R113.

The inner part of the laboratory vessel containing the R113 was surrounded on all sides, except where the heating surface and windows were located, by a circulated mixture of water and ethylene glycol (50% ethylene glycol by volume). This mixture was used as it had desirable viscosity and heat transfer characteristics. A precision constant temperature bath (Neslab Endocal RTE-210) pumped the thermostatically controlled water-ethylene glycol mixture through the laboratory vessel. The temperature stability of the bath was $\pm$ 0.02 °C. The temperature non-uniformity was 0.08-0.11 °C (0.15-0.20 °F) at the operating level of 49 °C, as determined by twelve boiling chamber thermocouples. The circulation system of the laboratory pool boiling vessel is shown in Figure 3.13.

The heating surface and viewing windows were surrounded by thick aluminum walls to help provide uniform temperature conditions at the start of a test. The viewing windows were made of optical quality quartz, and were enclosed by a glass cover to minimize convection losses. Fins were located in the annular space between the inner and outer sections of the laboratory vessel to promote heat transfer and to guide the flow of the circulating water-ethylene glycol mixture. Fins were also welded to the inner walls of the inner vessel to increase the heat transfer to the test fluid.

3.3 Drop Vessel

The drop vessel experiments were performed in the evacuated 132 meter drop tower at the NASA Lewis Research Center, which provided 5.18 seconds of free fall at accelerations of 10^{-5} g. All of the experimental hardware associated with the drop vessel were loaded on a one meter diameter "bus" for the drop. The drop chamber was evacuated by a series of pumps to a final pressure near 10^{-2} torr. The bus was decelerated in a 6.1 meter deep cylinder filled with polystyrene pellets.

The drop vessel and associated electronics were designed to take a 50 g impact at the bottom of the drop tower under the conditions of a vacuum. The drop vessel was made of aluminum and of essentially the same design as that of the laboratory pool boiling vessel, except that the drop vessel was not double-walled and, consequently, did not rely on external ethylene glycol and water circulation to maintain a uniform R113 temperature at the start of a test. Temperature uniformity was achieved through the use of film heaters mounted externally to the drop vessel. The drop vessel was vacuum leak tested with helium and found to be leak free for a pressurized system. An overview of the drop vessel is shown in Figure 3.15.

The desired uniform temperature of the test fluid before the drop was achieved by film heaters attached to the external surfaces of the test vessel. A laboratory test to determine the amount of temperature stratification in the liquid when using the external wall film heaters was performed. After a time period of 5 hours following the switching off of the external wall film heaters, the temperature stratification was 0.47 ^{o}C from the bottom surface to the top surface of the insulated vessel. A smaller temperature stratification (about 0.2 ^{o}C) was expected for the vessel in the drop tower before the drop, during the drop tower evacuation period for the following two reasons: (1) the dominant mode of heat loss in the evacuated drop tower was radiation, which was less than the convective heat loss during the laboratory stratification test, (2) the time from the switching off of the drop vessel external film heaters was less than 2 hours, as compared to five hours for the laboratory stratification test.

The temperature of the six sides of the vessel were controlled automatically and independently: the temperature of the bottom surface was set with respect to the ice thermocouple reference junction, while the temperatures of the other five surfaces were controlled relative to the bottom surface. A thermopile summed the voltages of the individual chromel constantan thermocouples distributed on the vessel wall. Mean

values of temperatures for a wall were obtained by the average of the thermocouple voltages on the wall. Since each of the vessel walls was heated with respect to the bottom wall, a differential thermopile measurement was made using the bottom surface as the reference junction. Power was supplied to the wall film heaters by an a.c. current heater drive. A schematic of the external film heating system is presented in Figure 3.15. Diagrams of the associated circuits appear in Appendix E.5.

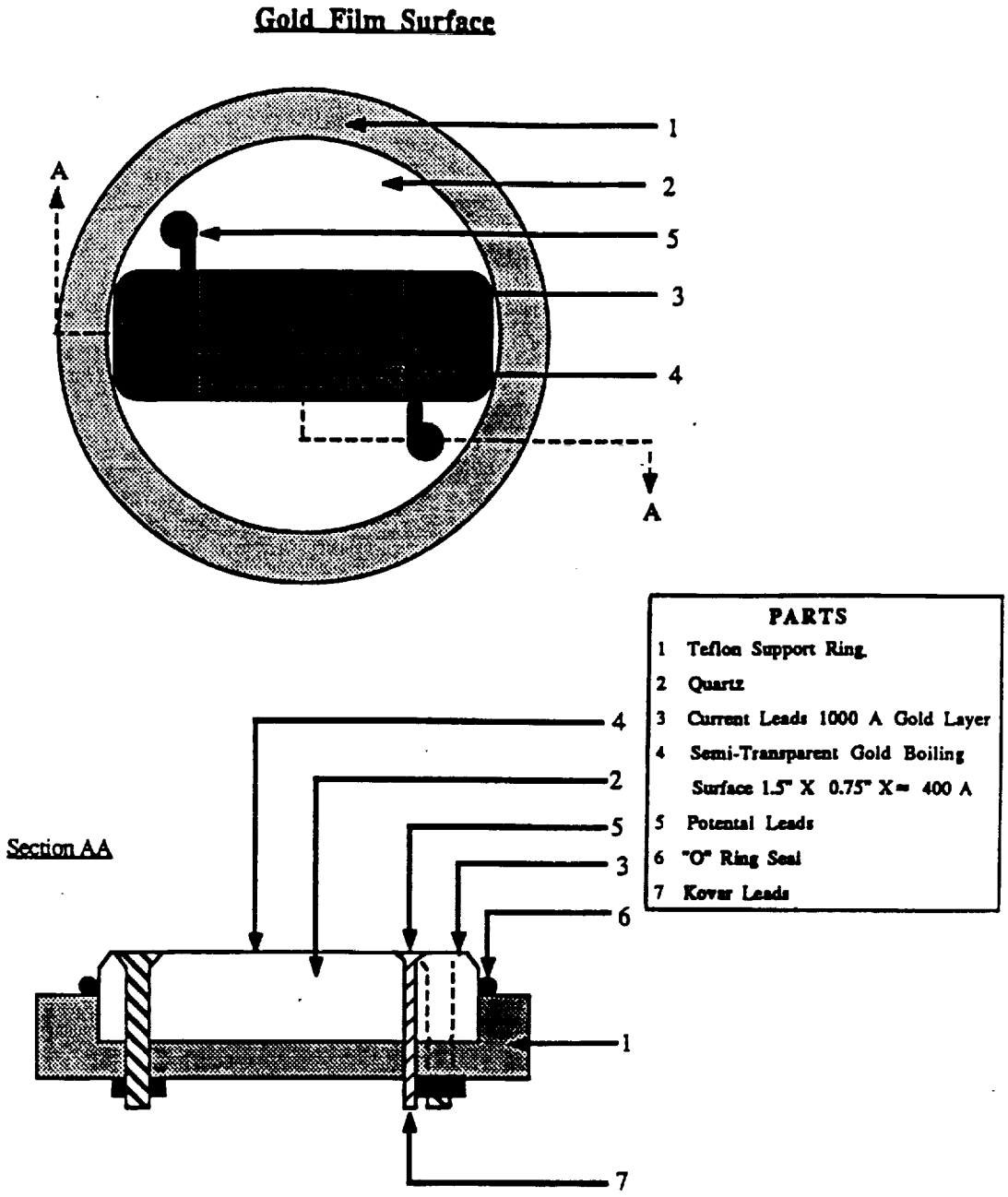

Figure 3.1 The gold film heating surface for transient and quasi-steady experiments

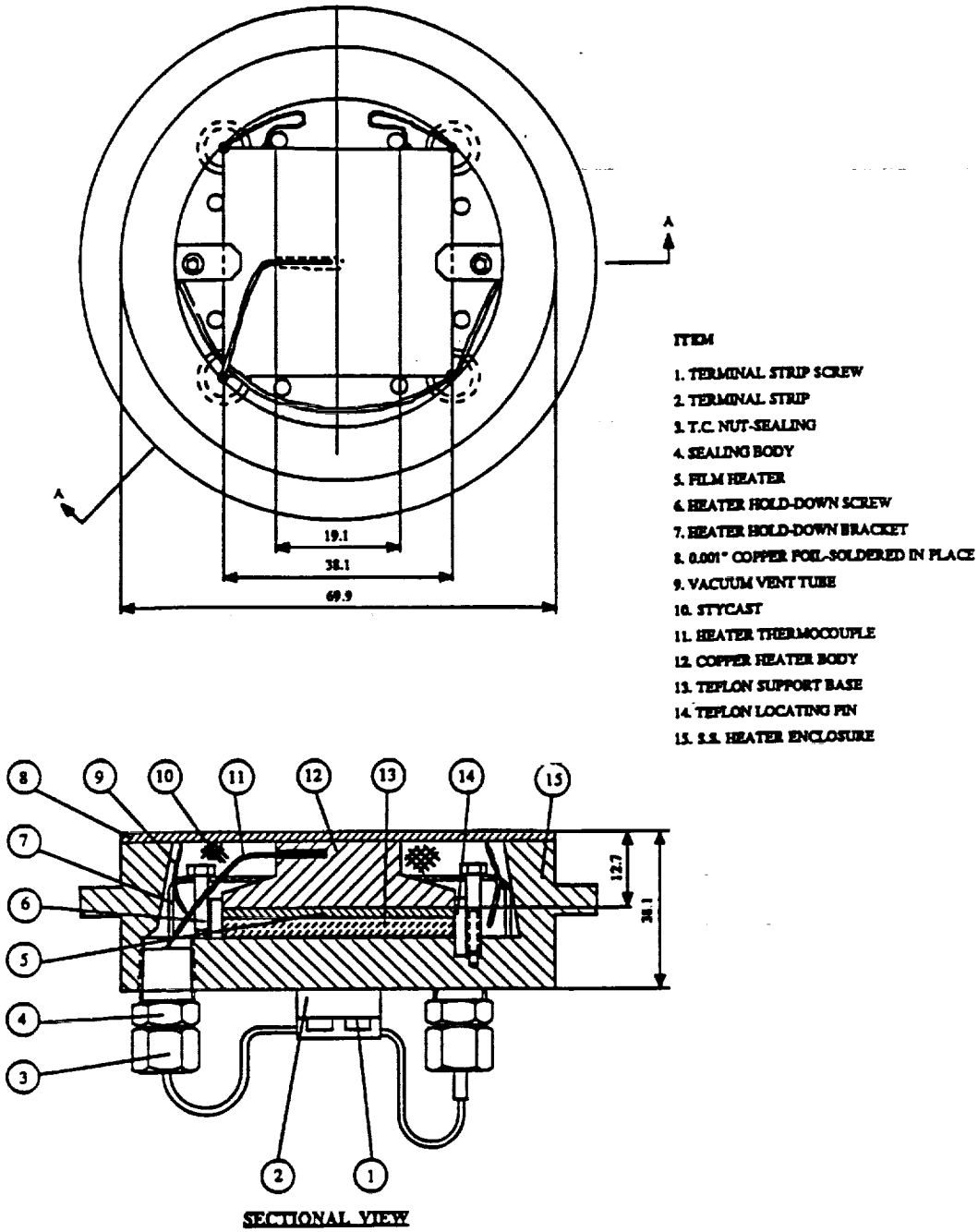

Figure 3.2 Copper block heater for the quasi-steady tests

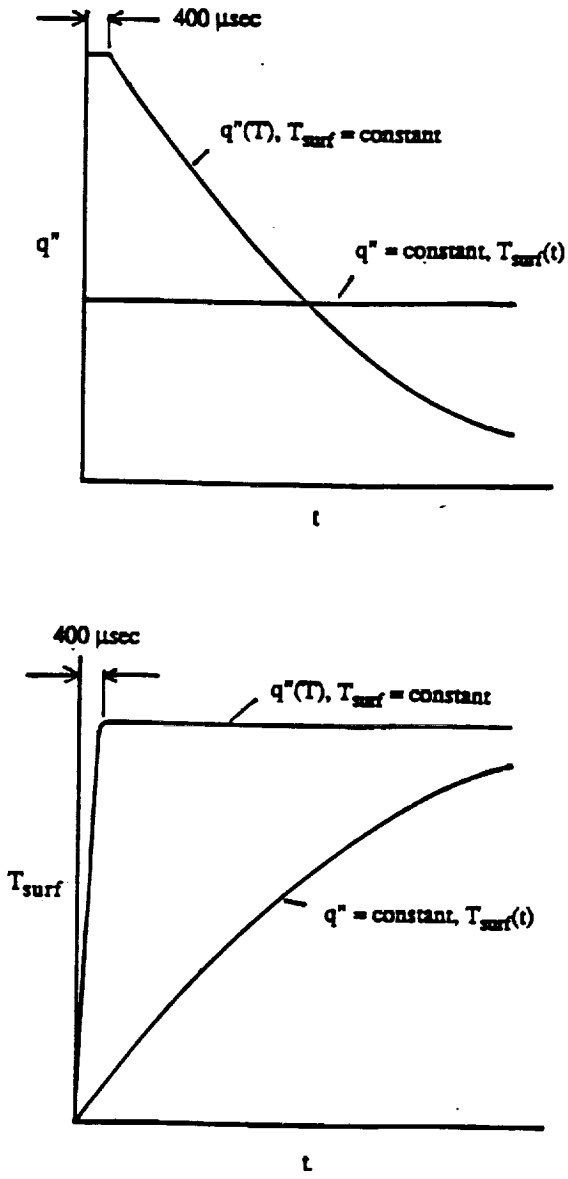

Figure 3.3 Concept of imposed heat flux and imposed heater surface temperature

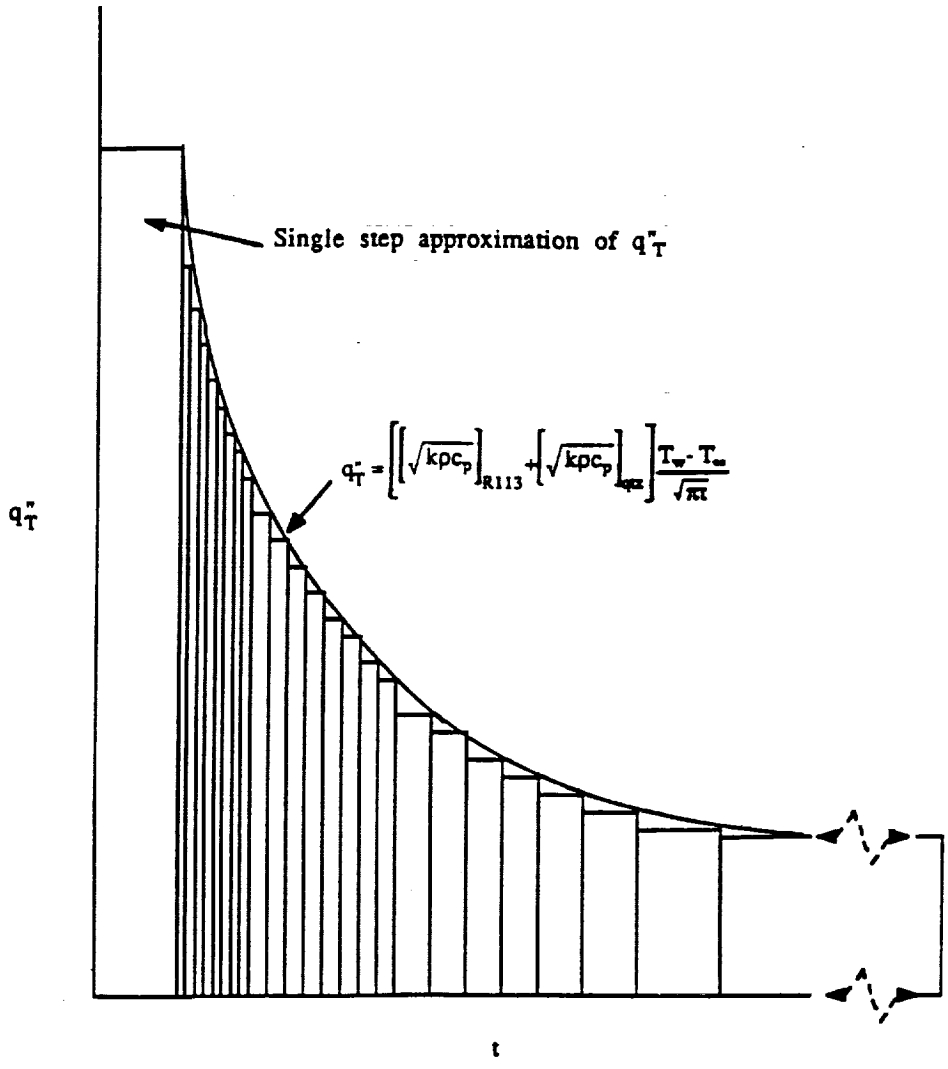

Figure 3.4 Series of steps in q''_T as an approximation of the analytical q''_T for a step increase in surface temperature

Table 3.1 Power Schedule for Imposed Surface Temperature

% Of Initial Power	Step Number	Resistance (Ohms)	Time Step (Seconds)
100	1	0	4.47E-04
95	2	0.103	1.96E-05
90	3	0.216	2.29E-05
85	4	0.338	2.71E-05
80	5	0.471	3.23E-05
75	6	0.618	3.90E-05
70	7	0.78	4.76E-05
65	8	0.96	5.90E-05
60	9	1.163	7.44E-05
55	10	1.392	9.57E-05
50	11	1.656	1.26E-04
45	12	1.961	1.70E-04
40	13	2.323	2.38E-04
35	14	2.76	3.47E-04
30	15	3.301	5.34E-04
25	16	3.998	8.86E-04
20	17	4.942	1.63E-03
15	18	6.325	3.52E-03
10	19	8.646	1.01E-02
5	20	13.884	5.43E-02
4	21	16	4.07E-02
3	22	19.088	8.80E-02
2	23	24.28	2.52E-01
1	24	36	1.36E+00

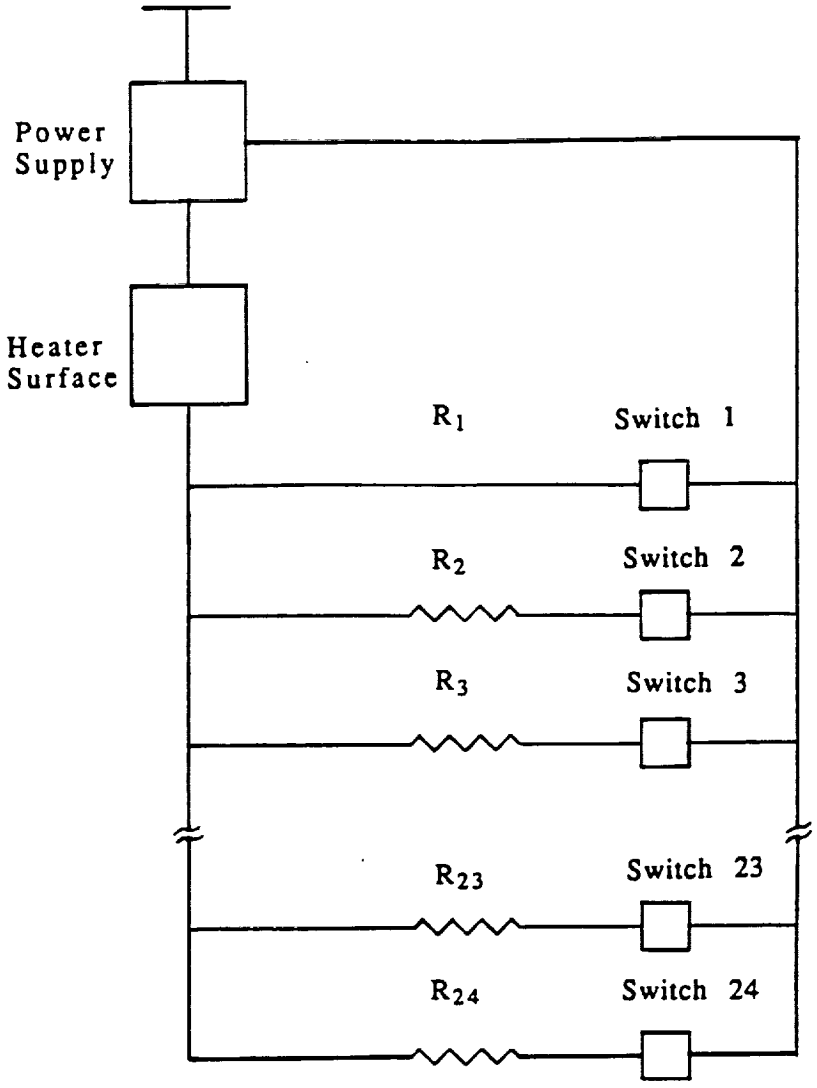

Figure 3.5 Schematic of switches and resistors for imposed heater surface temperature

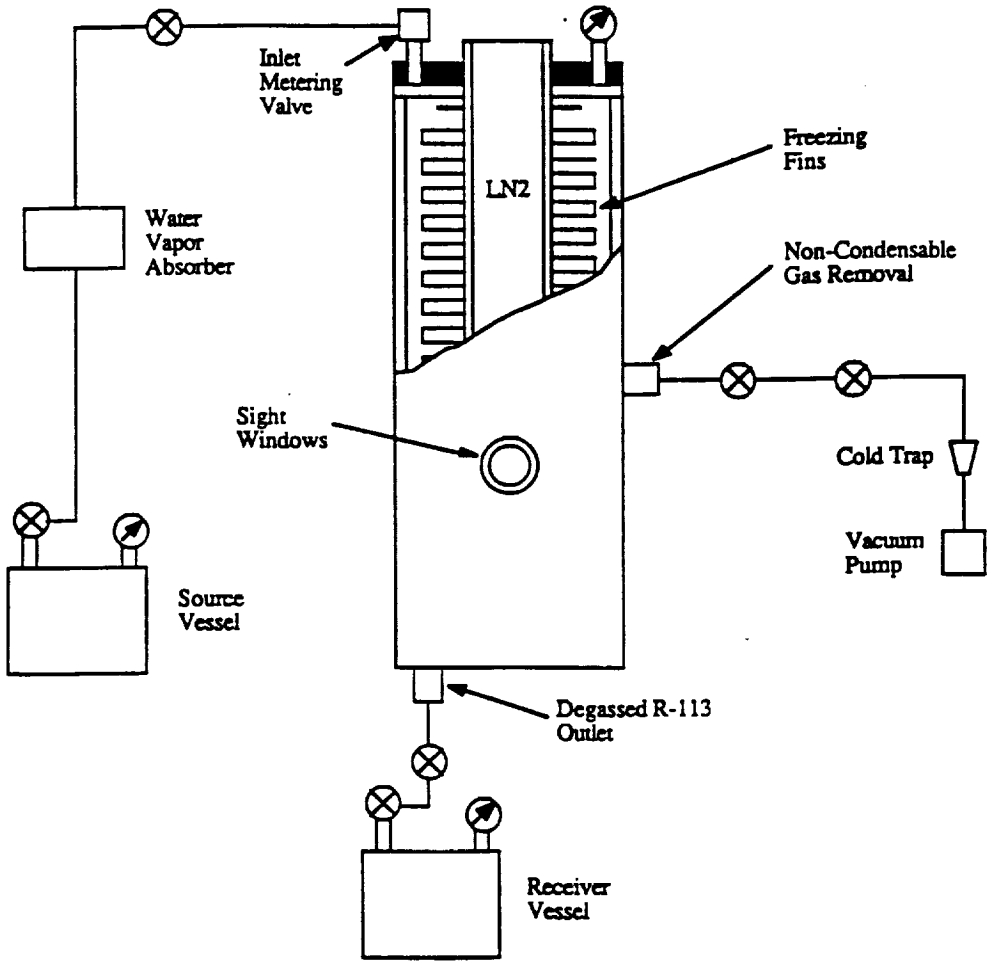

Figure 3.6 Schematic of R113 degassing unit

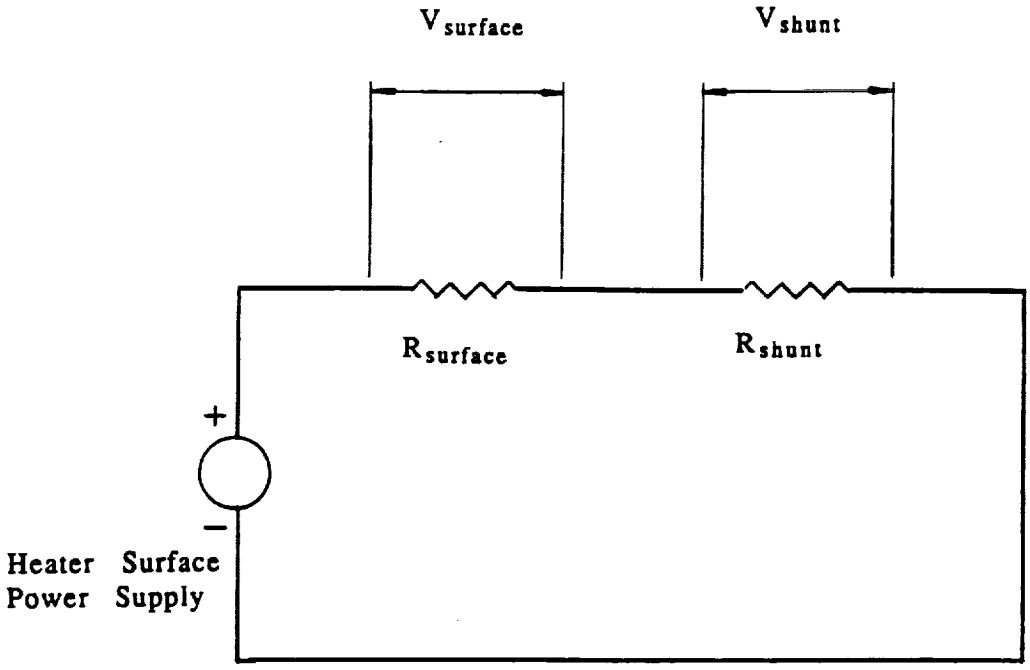

Figure 3.7 Schematic of the voltage measurement circuit in the determination of the gold film temperature

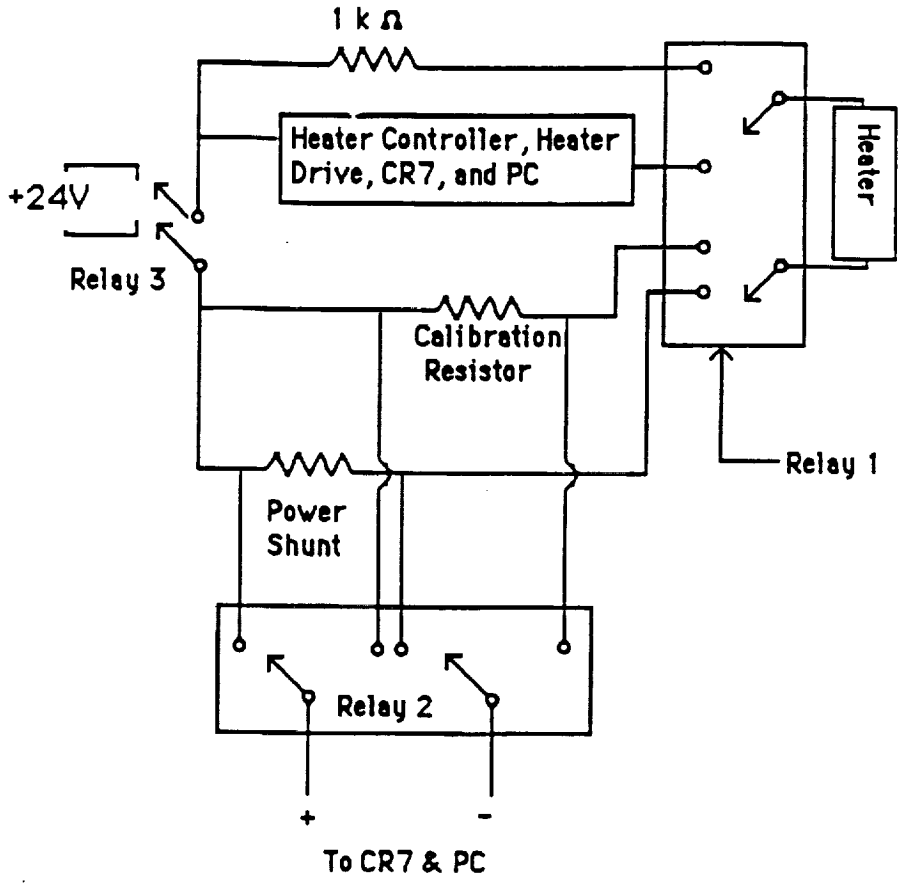

Figure 3.8 Schematic of the drop vessel calibration and power circuit

FIRST SURFACE MIRRORS
M2, M3, M5

REFLECTING PRISM, 45°
P1

LIGHT SOURCES,
L1, L2

COLD MIRRORS
M1, M4

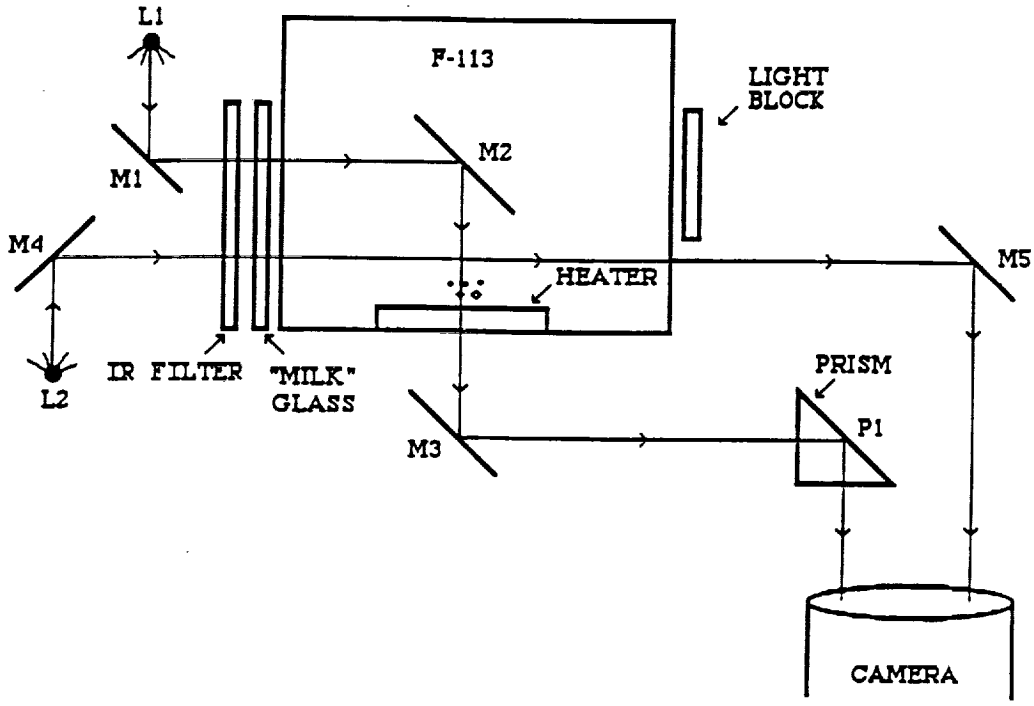

Figure 3.9 Schematic of the optical system for orthogonal views in the laboratory pool boiling vessel and the drop vessel

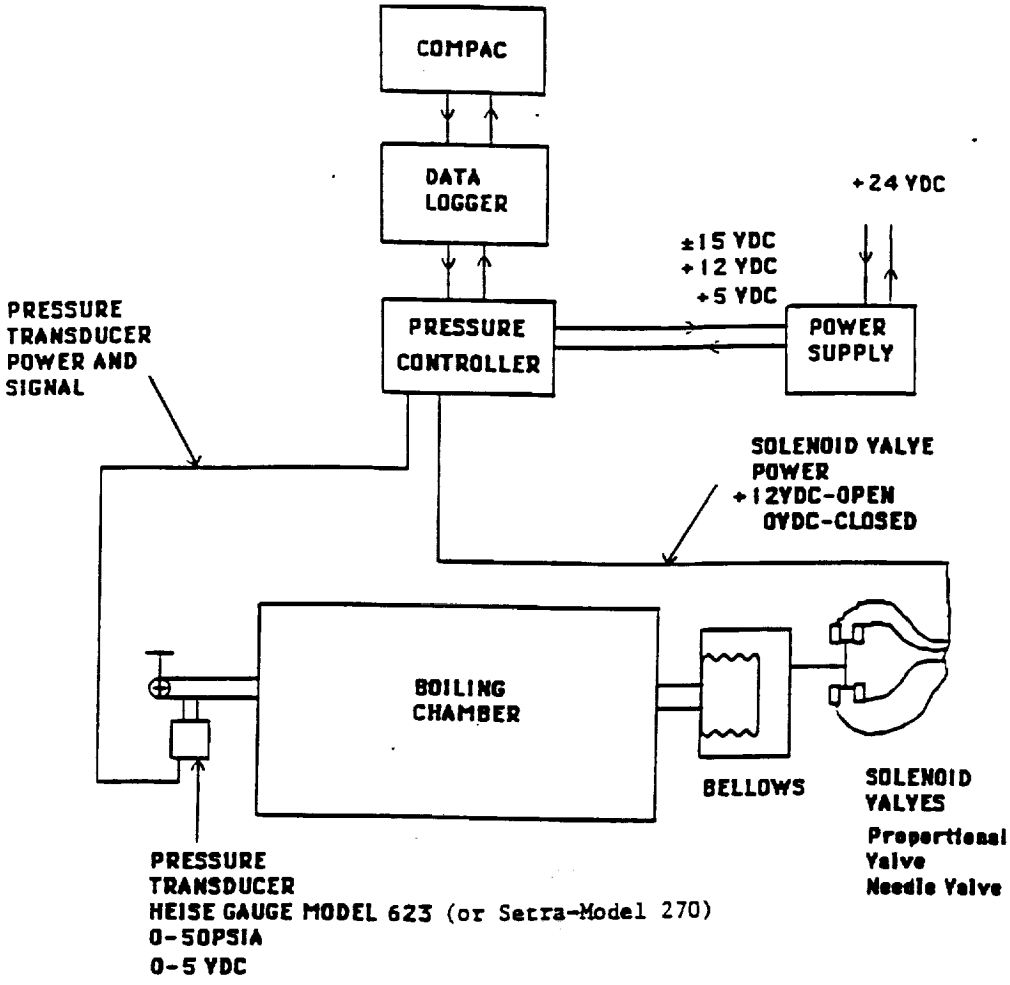

Figure 3.10 Schematic of the pressure control system

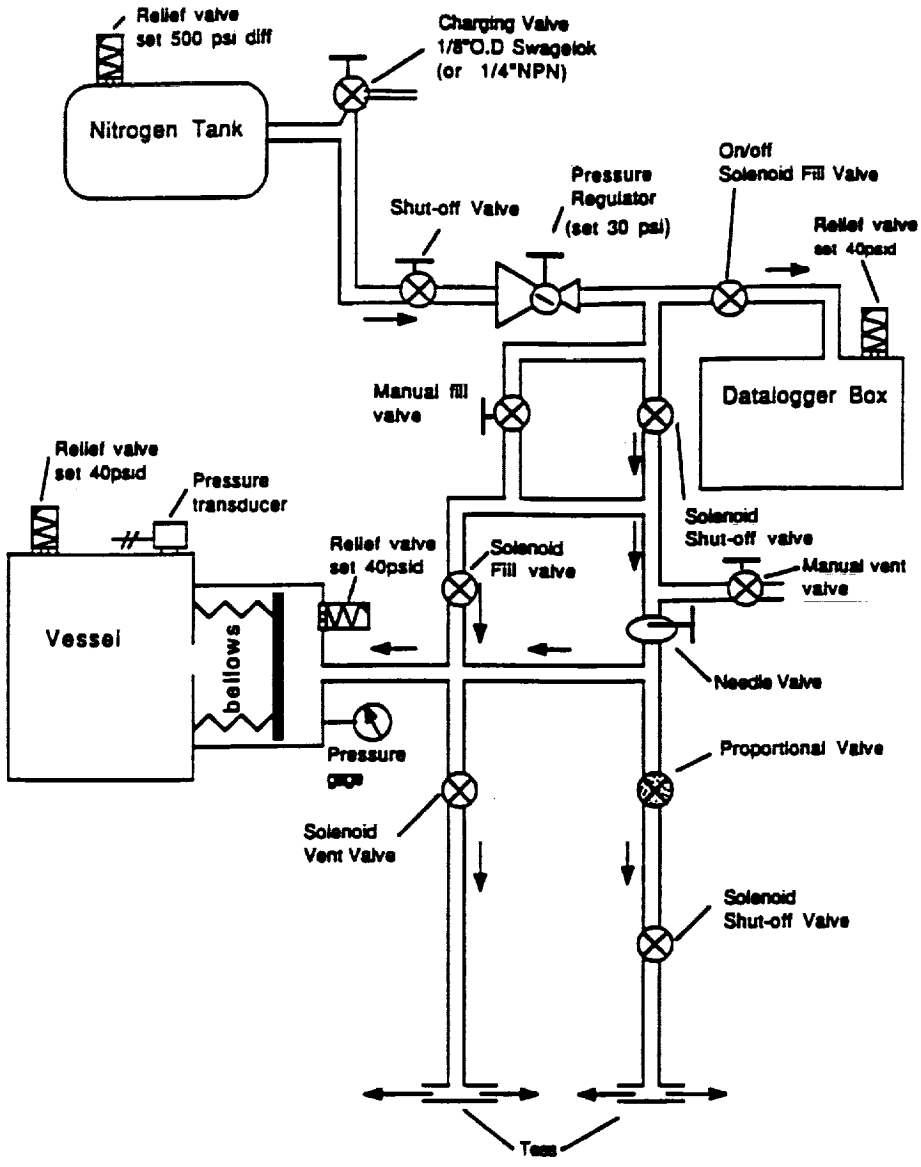

Figure 3.11 Drop vessel pneumatic diagram

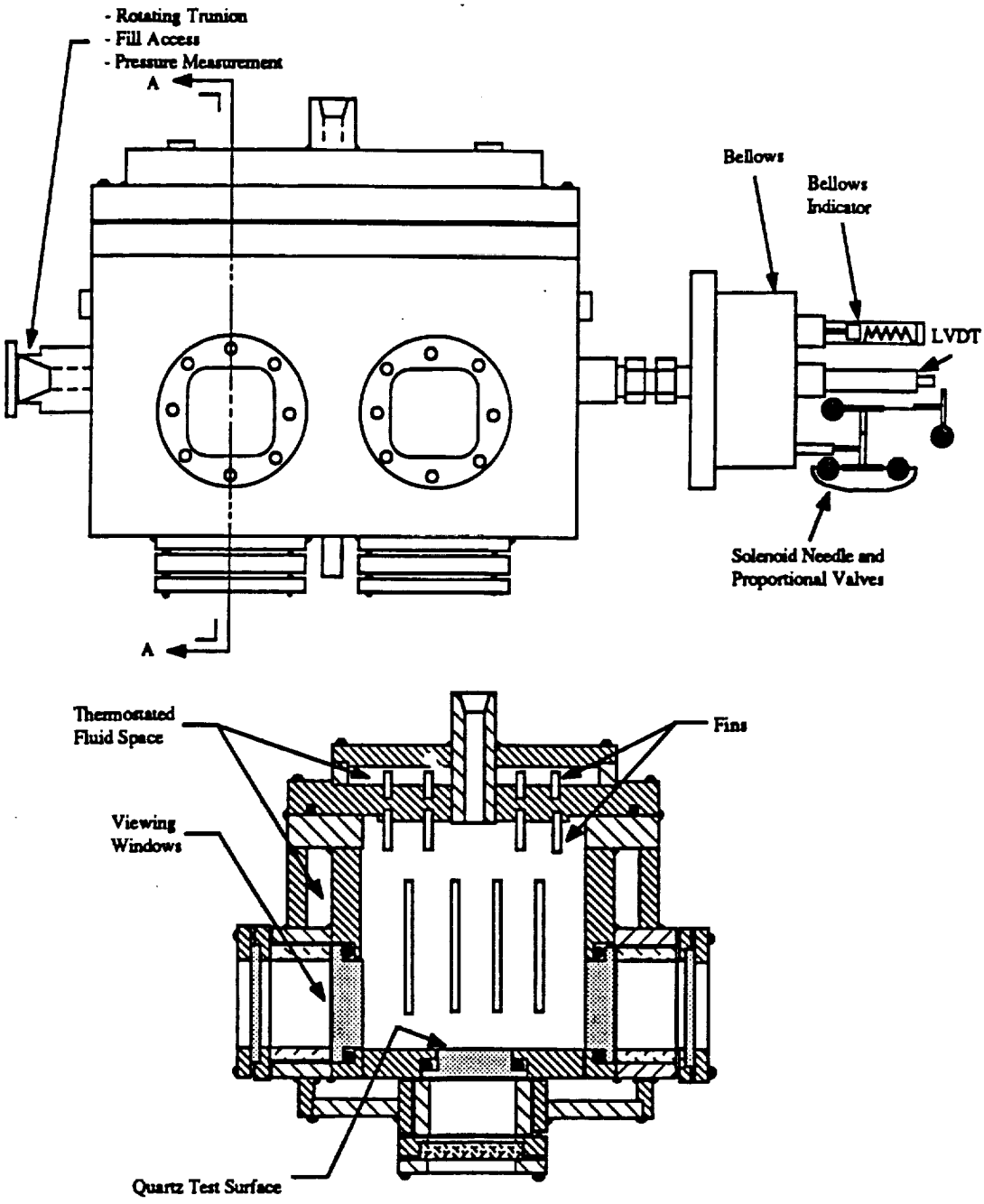

Section A-A

Figure 3.12 Laboratory pool boiling vessel

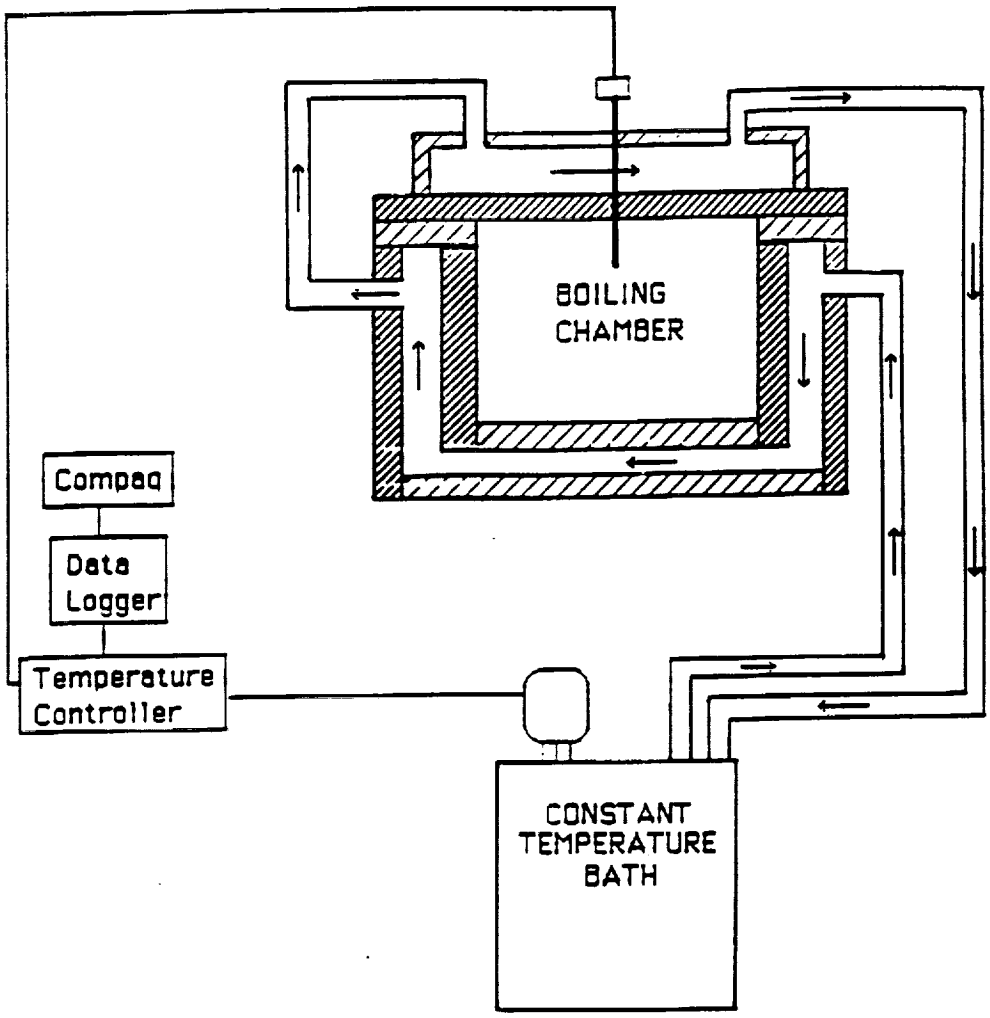

Figure 3.13 Laboratory pool boiling vessel temperature control system

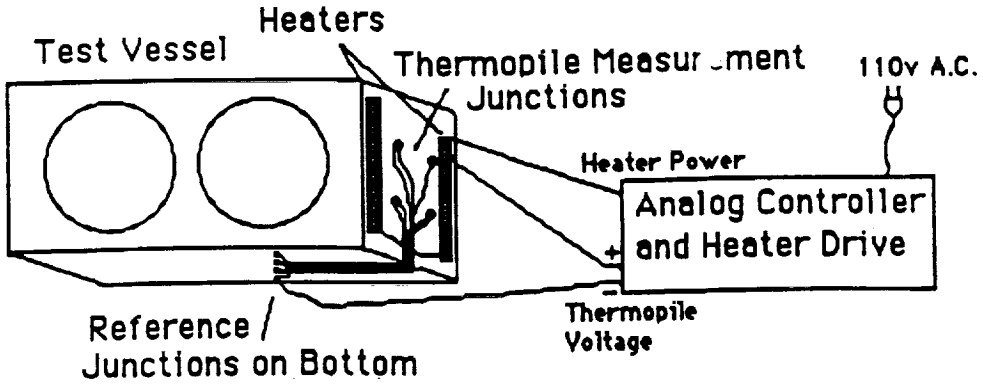

Figure 3.14 Drop vessel temperature control system

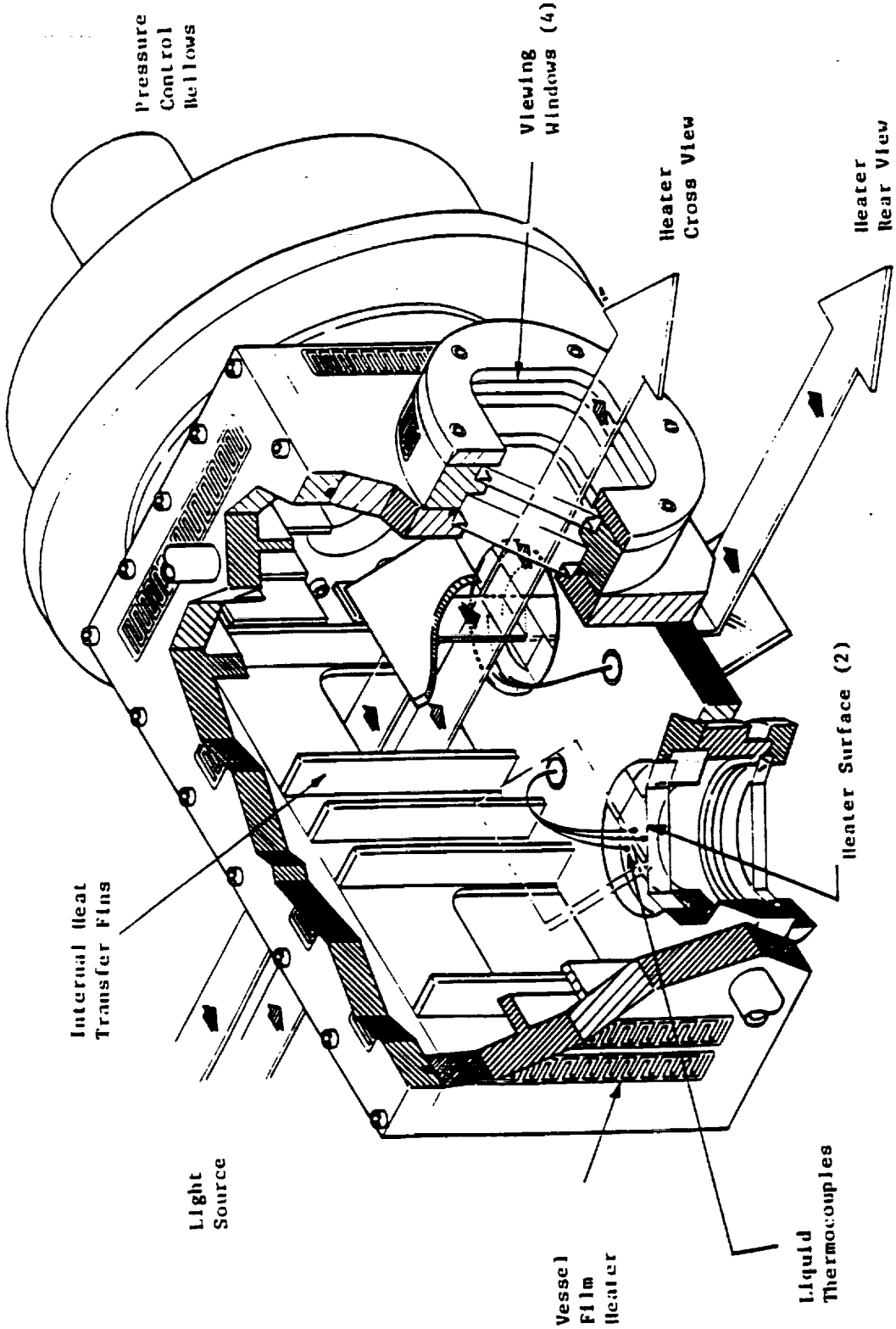

Figure 3.15 Drop vessel

CHAPTER 4

EXPERIMENTAL PROCEDURE

The experimental procedures that were followed are described below. Several of the test procedures are common to both test vessels used and are presented first: the charging of the vessels and the calibration of the thin film heater surfaces. The filling of the test vessels will be described first.

4.1 Common Procedures

Because of the high solubility of air in R113, precautions were taken in the filling process to insure that no contact was permitted between the degassed R113 and air. The description of the degassing system was given previously in Section 3.1.3. A filling cart fabricated from angle iron held a vacuum pump, a valve system and associated piping, and a pressure gage. The vacuum pump was used for the evacuation of the test vessel and the connecting line to the test vessel. The piping connected the test vessel to the tank holding the degassed R113, and the valve system permitted the evacuation of the test vessel and piping without opening the valve of the R113 container. The vessel and associated piping and valves were evacuated with a vacuum pump for eight hours to remove air and water vapor. The pressure gage provided an approximate vacuum indication before the R113 was allowed to flow from the storage container. In addition, this filling cart supported the elevated storage tank of the degassed R113 which provided the hydrostatic pressure for filling the test vessel.

The storage container was irradiated with heat lamps to maintain a positive pressure relative to the atmosphere. When the pressure gage mounted on the storage container indicated a gage pressure of 34.47 kPa (5 psig), the valve between the storage container and the stainless steel lines was opened and R113 flowed into the test vessel. The system was flushed with R113 vapor several times before filling with the liquid, to further remove any possible residual gases. To avoid contamination of the degassed R113 by atmospheric air, the pressure in the boiling vessels was always maintained above the ambient, either by the bellows actuated pressure system or by heating.

For every test, a single point calibration of the thin film heater surface was performed before heating the test fluid to the operating temperature of the experiment. As discussed in Section 3.1.1, the linear temperature-resistance relationship changed with time, with observable changes occurring after about a week. However, the slope of the temperature-resistance relationship remained constant, and hence, only a single calibration point was necessary for the determination of the new temperature-resistance relationship. Prior to the heating of the test fluid, the surface temperature was known with certainty since the entire test package was at the accurately known ambient temperature, determined with the calibrated thermocouples of the vessel. This known surface temperature was determined simultaneously with the heater surface resistance for the calibration point data. The procedure for the single point calibration of the gold film heating surface was described in detail in Section 3.1.1.

The experimental procedures required for conducting the experiments with the laboratory pool boiling vessel and the drop vessel were slightly different from one another due to the variation in vessel instrumentation. Observation of the boiling inception times, phase change dynamics, and natural convection phenomena were obtained with the high speed camera recordings in the transient experiments. Subcooling in all of the tests refers to the difference between the saturation

temperature corresponding to the system pressure and the bulk liquid temperature. In the following experiments, the total heat flux, q''_T, refers to the total thermal power generated in the heating surface divided by the area of the heater surface.

4.2 Laboratory Pool Boiling Vessel

Transient and quasi-steady experiments were performed in the laboratory pool boiling vessel following the calibration of the thin film heating surface. The laboratory pool boiling vessel required two hours to reach a steady-state uniform R113 temperature distribution within the vessel, nominally 48.5 °C (with a spatial variation of $\pm$ 0.06 °C as indicated by the internal calibrated thermocouples), as ethylene glycol and water circulated in the outer vessel jacket from the constant temperature bath. The nominal operating temperature of 48.5 °C was selected since this is slightly above the R113 saturation temperature (46.7 °C) corresponding to atmospheric pressure.

Subcooling can be obtained by one of two methods: (1) with a constant liquid temperature by pressurizing the liquid above the saturation pressure corresponding to the constant temperature or (2) with a constant pressure by cooling the liquid below the saturation temperature corresponding to the constant liquid pressure. At the beginning of a run, the desired liquid subcooling level of either 0, 2.8, or 11.1 °C, was set by the former method with the pressure controller, with the pressure maintained constant for each test.

After the desired subcooling was attained, the camera lights were switched on with water circulating through the double-walled infrared water filter, necessary to eliminate the heating of the R113. A cool-down period of 45 minutes between tests provided the same reproducibility of the boiling inception surface temperature (within 5% of the previous value) as that obtained by waiting 36 hours. This cool-down period allowed the heating surface to cool to the original liquid temperature before

energization of the heater, and permitted the observable vapor bubbles to collapse. The procedures for the transient heating measurements will be presented first, followed by that for quasi-steady heating.

4.2.1 Transient Heating Measurements

The transient experiments performed in the laboratory pool boiling vessel imposed either a step in the heater surface heat flux or a step in the heater surface temperature. The purpose of using these two different types of transients was to examine the effect of the heating rate on the incipient boiling process, as manifested by the heater surface temperature at the appearance of the first vapor bubble, and by the associated delay time from the onset of heating.

4.2.1.1 Imposed Constant Heat Flux

For the transient imposed constant heat flux tests, a light emitting diode was placed in the high speed video camera field of view to synchronize the time when the thin film heater was energized with the operation of the camera. A copper knife switch connected the heater controller to the heater surface. The 1.5 volt diode was in parallel with the knife switch such that when the switch was closed, the diode lighted.

A command given to the CR7X data acquisition unit via a portable computer initiated the data acquisition, and the camera was then switched on. At this point the knife switch was closed, and the thin gold film heater and diode were energized. Shortly after boiling was initiated and the data taken, the heater circuit was opened at the knife switch, and the video recording and data acquisition terminated.

The independent variables in the imposed heat flux tests were: surface orientation, horizontal up and horizontal down with respect to earth gravity; surface

type, four different quartz surfaces; bulk liquid subcooling, nominally 0, 2.8, or 11.1 °C; and total heat flux, nominal levels of 2, 4, 6, and 8 W/cm^2. The total heat flux is the power input to the heater divided by the heater surface area. The dependent test variables were the voltage across the heater surface and the voltage across the heater shunt, which provided the instantaneous mean heater surface temperature and heat flux. The bulk liquid temperature near the heater surface and the system pressure were also recorded.

4.2.1.2 Imposed Constant Surface Temperature

All tests conducted with the step increase in surface temperature were performed with the thin film heating surface in the horizontal down orientation. With heating at a given heat flux in the horizontal down position, the onset of natural convection is delayed for a considerably longer period of time than that for heating with the identical heat flux in the horizontal up position. The temperature distribution in both the liquid and the quartz substrate can thus be determined from a conduction analysis with a reasonable certainty, since each experiment is completed before the onset of natural convection occurs. This is discussed in detail in Oker (1973).

As stated in Section 3.1.2, the software for acquiring data in the fast portion of the power transient, together with the analog and digital interface card and analog input channels, are referred to as the Codas system. With the maximum sampling rate limited to 25 kHz per each of two channels, the Codas system was programmed to sample the differential voltages across the heater surface and shunt sequentially. The CR7X, as previously described in Section 3.1.2, sampled the shunt and heater surface voltages only for the slow part of the power transient, but with much greater accuracy than was possible with the Codas system. The measurement accuracy was thus compromised with the use of the Codas system for the high sampling rate, while the

high sampling rate was compromised by using the CR7X for the measurement accuracy. Details of the measurement accuracy are given in Appendices C and D1. The pressure transducer voltage and bulk fluid temperature thermocouple voltages were also recorded by the CR7X at the start and end of a given test. The onset of boiling and initial vapor dynamics were recorded by the high speed video camera. The imposed steps in heater surface temperature were in the range of 0.5-25 °C.

An experiment was initiated by turning the camera on, followed by execution of the switching program on the first computer, which caused a light emitting diode on one of the circuit boards to flash, indicating that the heater surface would be powered in one second. At the time of the one second warning, the Codas data acquisition process began on the second computer. The test was terminated after heating for 1.8 seconds by the switching software, which opened the heating circuit automatically.

The independent variables in the imposed heater surface temperature tests were: surface type, two different quartz surfaces; bulk liquid subcooling, nominally 0, 2.8, or 11.1 °C; and the initial heater surface voltage level, which governed the level of the step increase in heater surface temperature. The dependent test variables were the voltage across the heater surface and the voltage across the heater shunt, which provided the instantaneous mean heater surface temperature and heat flux. The bulk liquid temperature and system pressure were also recorded.

4.2.2 Quasi-Steady Heating

Both the thin gold film heater on quartz and the solid metal heaters were used for the quasi-steady measurements. The desired power setting was set, and the system was allowed to reach a steady-state surface temperature. If boiling inception did not occur, the heater input voltage was increased by 10% of the previous level, and another steady-state heating surface temperature was obtained. Following the point of

boiling initiation, the power was switched off and the surface allowed to cool for more than 45 minutes. Power at a slightly lower level than that which produced the previous boiling inception point was then applied to the surface to obtain a non-boiling steady-state surface temperature. The power was then increased slightly again in steps, until boiling occurred. This incremental approach was iterated to determine more precisely the temperature and heat flux at which incipient boiling occurs.

Because of the large uncertainties as to when incipient boiling would take place with quasi-steady heating, high speed photographs were not taken. The CR7X recorded the shunt and heater surface voltages, for the calculation of the heat flux (and mean heater surface temperature in the case of the gold film heater on quartz), the pressure transducer voltage, for the determination of the pressure level, and the voltage output of the thermocouple imbedded in the copper block near the heater surface for the determination of the metal heater surface temperature. The bulk fluid temperature increased by no more than 0.25 °C during any of the quasi-steady heating tests.

The independent test variables in the quasi-steady heating tests were: surface orientation, horizontal up or horizontal down with respect to earth gravity; surface type, quartz substrate or metallic surface; and bulk liquid subcooling, nominally 0, 2.8, or 11.1 °C. The dependent test variables were the voltage across the heater surface, the voltage across the heater shunt, and the metal heater thermocouple voltage, which provided the mean heat flux and heater surface temperature. The bulk liquid temperature and system pressure were also recorded.

4.3 Drop Vessel

Following charging with degassed R113, the drop vessel, cameras, lights, and associated electronics were placed on the drop bus, which was then balanced with lead

weights. Only one of the two thin film heaters installed in the drop vessel was used for a particular test.

The day before a drop test, the single point calibration of the heater surface resistance-temperature was performed, since the entire drop vessel was at the accurately known and uniform ambient temperature. The measured shunt, surface, and thermocouple voltages acquired by the CR7X during the surface calibration were stored in a portable computer. The a.c. temperature controller regulating the power to the thin film heaters mounted on the outer drop vessel walls was switched on, and the vessel was then covered with an insulating blanket. The controller was adjusted to provide a temperature of approximately 58 °C when the vessel was to be prepared for installation in the drop tower on the following day.

Preparation for the drop test the next day then required that the a.c. heaters be disconnected from the power source. The heat loss to the ambient at about 20 °C during the 20 minute period required to transfer the vessel to the actual drop location and during the two hour period required for the evacuation of air from the drop tower resulted in a decrease in temperature of the test vessel and its contents from the initial 58 °C to the desired level of about 47.7 °C.

Three tests were performed sequentially in connection with each drop experiment: a pre-drop test with the high speed photography, a drop test with high speed photography, and a post drop test with no photography. The pre-drop test was identical to the drop test, using the drop tower control room circuitry, but was conducted at earth gravity. This test provided a direct comparison between the boiling process in earth gravity and boiling in microgravity, and included the transient heater surface temperature, heat flux, pressure, and photographic measurements. The exposed film was removed for developing after completion of the pre-drop test, and the data downloaded from the CR7X to a portable computer. The camera was then reloaded for the drop test. After the test package was dropped and retrieved from the

bottom of the drop tower, the film was again removed for processing, and the drop data downloaded from the CR7X to a portable computer. The post drop test was then performed to verify the proper operating condition of the circuitry and mechanical hardware following a drop test, and was identical to the pre-drop test except that no movies were filmed.

The actual drop test procedure will now be described in greater detail. Following the pre-drop test, the camera was reloaded, the pre-drop data was downloaded to the portable computer, and the batteries were recharged. Data acquisition and control instructions were transferred from the portable computer to the CR7X mounted on the drop bus. The software instructed the CR7X to measure the bulk liquid temperature and then set the specified subcooling level, based on this measured bulk liquid temperature, by adjusting the pressure level inside the vessel through actuation of the bellows pressure control system described previously. The CR7X also set the voltage level to be applied to the heater surface to produce the desired heat flux. The CR7X control instructions also checked that appropriate voltage signals were being received from the drop tower control room by means of the drop bus umbilical. The protective outer skins were installed on the drop bus, and the bus placed into position at the top of the drop tower, at which time evacuation began.

At the desired tower vacuum level and R113 temperature, the control room sent a signal to the drop vessel (called the energize signal) which caused the CR7X to set the pressure level based on the current vessel temperature in order to achieve the desired subcooling level. The CR7X sampled the pressure transducer signal and calculated the pressure based on the pressure transducer calibration. The pressure set point (command voltage) was adjusted until the measured pressure was near the desired pressure. At this point, the CR7X transmitted a five volt signal to the control room, indicating that the R113 in the vessel was at the desired subcooling. The control room then switched on the camera lights and started the high speed camera, which was

followed by the release of the drop bus in the drop tower. The onset of the free fall then disconnected the umbilical from the test package, which in turn produced an open circuit signal called the drop signal. The drop signal was an indication to the CR7X to (1) power the heater at the pre-determined voltage level by sending a calibrated set point signal between zero and five volts to the heater controller and to (2) begin data acquisition. A diode powered by a three volt digital signal from the CR7X in the field of view of the camera was used to synchronize the application of power to the heater surface with the camera operation. After five seconds, the CR7X stopped measuring the shunt, heater surface and pressure transducer voltages, and terminated power to the heater surface. In some of the drops, the voltage of a thermocouple in the liquid near and over the center of the heater surface was sampled. The camera continued to film during impact. An outline of the free fall drop sequence is presented in Figure 4.1.

The independent variables in the drop vessel tests were: surface type, two different quartz surfaces; bulk liquid subcooling, nominally 0, 2.8, or 11.1 °C; and total heat flux, nominal levels of 4, 6, and 8 W/cm^2. The low heat flux level of 2 W/cm^2 used in the laboratory pool boiling experiments was not used in the drop experiments because it was observed that the time required for the onset of boiling at a power input of 4 W/cm^2 in microgravity was apparently greater than the five second microgravity period available in the drop tower. The dependent test variables were the voltage across the heater surface, the voltage across the heater shunt, and the pressure transducer voltage, which provided the mean instantaneous heater surface temperature, heat flux, and system pressure. As will be noted in the results, short pressure variations occurred during some of the more dynamic nucleation processes, although attempts were made to maintain a constant pressure level. At times, a liquid temperature measurement near the heater surface was also included.

4.4 Data Reduction

The procedures for the calculation of the thin film heater surface temperature, the metal heater surface temperature, the bulk liquid temperature, the liquid pressure, and the heat flux from the recorded data are presented below, along with the uncertainties in the determination of these quantities.

4.4.1 Spatial Mean Film Heater Surface Temperature

The spatial mean thin gold film heater surface temperature, T_w, is determined from the measured test surface resistance, R_w, the single point calibration resistance, R_C, with its corresponding calibration temperature, T_C, and the slope of the calibration curve, $\frac{dT}{dR}$, in the following equation:

$$T_w = T_C + \frac{dT}{dR}\left[R_w - R_C\right] \tag{4.1}$$

For the constant heat flux tests, R_w, R_C, T_C, and $\frac{dT}{dR}$ were determined with representative values and uncertainties of $2.9985 \pm 0.0008\ \Omega$, $2.6266 \pm 0.0002\ \Omega$, $20.00 \pm 0.01\ ^oC$, and $214.83 \pm 0.23\ ^oC/\Omega$, respectively, as given in Appendix D.1. As a result of the uncertainties in these quantities, the heater surface temperatures were determined with an uncertainty of $\pm 1.0\ ^oC$, as described in Appendix D.1.

For the imposed step change in surface temperature tests using the Codas system during the fast portion of the power generation curve discussed earlier, R_T, R_C, T_C, and $\frac{dT}{dR}$ were determined with representative values and uncertainties of $2.7989 \pm 0.020\ \Omega$, $2.6266 \pm 0.0002\ \Omega$, $20.00 \pm 0.06\ ^oC$, and $214.83 \pm 0.23\ ^oC/\Omega$, respectively. The calculation of these uncertainties is also described in Appendix D.1. As a result of these uncertainties, the heater surface temperatures were determined with an

uncertainty of ± 6 °C. When the CR7X was used during the slow portion of the power generation curve, the heater surface temperature was determined with an uncertainty of ± 1 °C, as shown in Appendix D.1.

4.4.2 Metal Heater Spatial Mean Surface Temperature

The metal heater surface temperature was determined from the chromel-constantan thermocouple imbedded in the copper heating block near the heater surface, as shown in Figure 3.2. The error in assuming that the temperature at the location of the thermocouple was equal to the surface temperature was estimated to be less than 0.002 °C, by assuming one dimensional conduction in the copper block and negligible contact resistance between the soldered copper foil and the copper block. An error of this magnitude is less than the uncertainty of ± 0.01 °C associated with the thermocouple temperature measurement and, as a result, was neglected.

4.4.3 Bulk Liquid Temperature

The liquid bulk temperature was measured by calibrated chromel-constantan thermocouples, described in Chapter 3. The CR7X was used for all measurements of bulk liquid temperature in all three vessels, and the uncertainty of ± 0.6 microvolts for the thermocouple voltage determination translates to a ± 0.01 °C uncertainty in the liquid bulk temperature. A detailed discussion of the estimate of this uncertainty in the temperature determination from a thermocouple voltage measurement is in Appendix D.2.

4.4.4 System Pressure

The liquid pressure near the heater surfaces in all three vessels was measured by calibrated transducers. The calibration and resulting calibration equations of the pressure transducers are described in Appendix B.3 The uncertainty of the pressure measurement in the laboratory pool boiling vessel, the drop vessel, and the forced convection boiling loop was less than the desired uncertainty of $\pm$ 0.172 kPa ($\pm$ 0.025 psi). The details of the estimate of the uncertainty in the pressure measurements are given in Appendix D.3.

4.4.5 Heat Flux

The total power input per unit area, q''_T , for both the quasi-steady heating tests and the constant heat flux tests was calculated from:

$$q''_T = \frac{V_T V_{sh}}{A R_{sh}} \tag{4.2}$$

The voltages were in volts, the resistance in ohms, the heater surface area in cm^2 , and q''_T in W/cm^2. The maximum uncertainty in q''_T was $\pm$ 0.18 W/cm^2. The details of the estimate in the uncertainty associated with q''_T are presented in Appendix D.4.

The heat transfer to the liquid, q''_l, could be calculated from the measured total heat flux, q''_T, under circumstances which permitted reasonable analytical assumptions. For the transient constant heat flux tests in the pool boiling vessels q''_l can be determined by a one dimensional, semi-infinite media conduction analysis provided two conditions were met. The first condition for a valid semi-infinite media

conduction analysis is the absence of significant natural convection while the fluid is being heated. This condition was met for all of the microgravity boiling tests up to the point of the onset of boiling. The conduction analysis was valid for experiments conducted in earth gravity where boiling occurred in times less than that required for the onset of natural convection. The time for the onset of natural convection for a heated surface horizontal up in earth gravity was given by Oker (1973) in a semi-empirical equation for the combination of a pyrex substrate and R-113 at atmospheric pressure, where q''_T is in W/cm^2 and t_{nc} is in seconds:

$$\left(q''_T\right)^{\frac{1}{2}} t_{nc} = 0.77 \tag{4.3}$$

For illustrative purposes, a q''_T of 8 W/cm^2 corresponds to a time, t_{nc}, of 0.27 seconds required for the onset of natural convection. Equation 4.3 is based on the fluid near the heating surface reaching a certain critical Rayleigh number. This condition was not met by most of the pool boiling experiments conducted here in earth gravity and, as a result, q''_l was not computed for most of these earth gravity tests. The second condition necessary for a valid semi-infinite media analysis is that the thermal penetration depth be less than the thickness of the heated substrate material. An acceptable thermal penetration depth in this study corresponds to periods of heating that are less than six seconds. All of the microgravity tests were completed in less than six seconds, as were many of the laboratory pool boiling experiments with the heating surface horizontal down.

Using the one dimensional semi-infinite media solutions presented in Appendix G, for a constant plane heat source, the ratio of the heat flux transferred to the liquid and to the quartz is a constant, given by:

$$\frac{q''_l}{q''_T} = \frac{1}{1+\frac{q''_{qtz}}{q''_l}} \tag{4.4}$$

where

$$\frac{q''_l}{q''_{qtz}} = \frac{k_l}{k_{qtz}} \sqrt{\frac{a_{qtz}}{a_l}} \tag{4.5}$$

Evaluating the properties of quartz and R113 at a mean temperature of 70 °C, the fraction of the total input heat flux to the liquid becomes, from equations 4.4 and 4.5:

$$\frac{q''_l}{q''_T} = 0.175 \tag{4.6}$$

The heat flux to the test fluid is then evaluated from equation 4.6 using the measurement of q''_T. The uncertainty in the calculation of heat transfer to the liquid as given by equation 4.6 comes from the uncertainties in the tabulated property values and the uncertainty involved in using a representative mean temperature for the selection of the tabulated properties. The total uncertainty in q''_l calculated from equation 4.4 is $\pm$ 4%. In the non-boiling portion of the quasi-steady tests q''_l is computed from subtraction of the losses from the total power input to the heater. The losses are estimated from the following natural convection correlations (Incropera and Dewitt (1984)) for the test surfaces heated in air:

$$Nu = 0.15\ Ra^{\frac{1}{3}} \quad \text{(horizontal up)} \tag{4.7}$$

$$Nu = 0.27\ Ra^{\frac{1}{4}} \quad \text{(horizontal down)} \tag{4.8}$$

The uncertainty in q''_l results primarily from the uncertainty in the calculation of the losses computed from the natural convection heat transfer correlations, which are on the order of $\pm$ 20%.

Drop Sequence

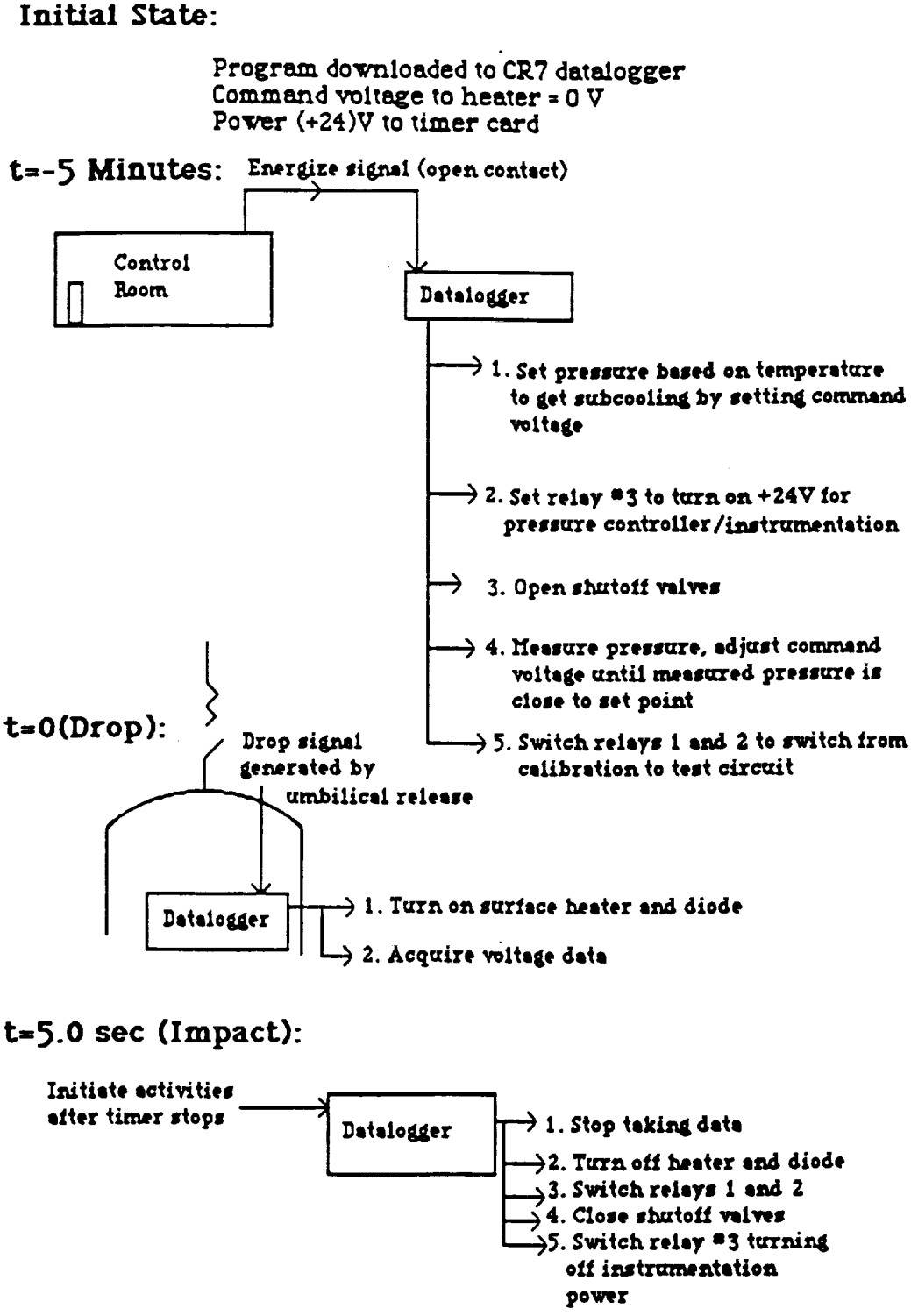

Figure 4.1 Sequence of events during a free fall microgravity test in the NASA Lewis RC drop tower

CHAPTER 5

EXPERIMENTAL RESULTS

The experimental results obtained during the current study are presented below. The transient experimental results are presented first, followed by the quasi-steady heating results.

5.1 Transient Boiling

The transient boiling experiments were performed in both the laboratory pool boiling vessel and the drop vessel. A step in heater surface heat flux was used in the drop vessel. Both step increases in heat flux and in surface temperature were used in the laboratory pool boiling vessel, as well as the quasi-steady heating process which will be presented in Section 5.2 below. A step change in heat flux is the most elementary form of imposed heat flux variation possible, as all other time varying imposed surface heat fluxes can be constructed from a series of steps in heat flux. These two basic and elementary thermal boundary disturbances, step changes in heat flux and in temperature, produce distinctly different liquid temperature distributions, which determine the heater surface temperature at the moment of boiling inception and the resulting phase change dynamics. The transient pool boiling results are presented first, followed by the transient forced convection boiling results.

5.1.1 Pool Boiling-Imposed Constant Heat Flux

5.1.1.1 Transient Heater Surface Temperature

Since the resistance of the gold film heater surface is computed from the measured current and voltage drop across the entire heater surface, the resulting calculated surface temperature is a spatially averaged temperature. The non-uniformity of the surface temperature was estimated by solving the three dimensional transient conduction model for the quartz substrate-R113 system using a finite difference solution technique. The conduction assumption with R113 is valid for short times in earth gravity and in microgravity up to the point of incipient boiling. The Crank-Nicholson finite difference method was used, with a uniform spatial grid size of 0.79375 mm (0.03125 inches). The procedure is described in Appendix H. Figure 5.1 shows the computed surface temperature rise for a total heat flux input of 8 W/cm^2 at one second, the approximate time from the onset of heating for boiling inception. Because of symmetry, only one quarter of the film surface is shown, and the computed surface temperature is noted to be quite uniform except near the heater surface edges.

In the remainder of this section, selected representative heater surface temperature-time plots are presented in order to demonstrate the distinguishing features in common for the same body force magnitude and orientation. The identical heater surface, designated as Q-5, is used in all of the results presented here.

The transient heater surface temperature for Run 79 is shown in Figure 5.2, along with a tabulation of the test conditions, and applies to the case where the heater surface is facing horizontal up in earth gravity. The onset of natural convection, appears as an irregularity in the temperature-time plot. The time from the energization of the heater to the onset of natural convection is designated as t_{nc} . Experimental values for this t_{nc} were obtained by the appearance of two independent phenomena,

which coincide with the irregularity; the observed onset of fluid motion above the heater was characterized by a wave-like disturbance recorded by the high speed video camera, and by the departure of the heater surface temperature from the one dimensional semi-infinite media transient conduction solution.

Oker (1973) found a semi-empirical relationship for t_{nc} based on the critical Rayleigh number predicted by instability theory for the case of a semi-infinite surface in the horizontal up position in earth gravity with an imposed heat flux:

$$t_{nc} = \frac{k_l \nu}{\alpha_l \beta g q''_l} \left(Ra_c\right)^{\frac{1}{2}} \tag{5.1}$$

Ra_c is the critical value of the Rayleigh number for the onset of fluid motion, where the Rayleigh number is defined as:

$$Ra = \frac{g \beta \left[T_w - T_\infty\right] \delta^3}{\alpha_l \nu} \tag{5.2}$$

δ is the approximation to the penetration depth of the thermal disturbance, and was taken as $\sqrt{6at}$ in the work of Oker, from the integral solution of the one dimensional transient conduction equation with a step in heat flux for a media of semi-infinite extent. With the properties evaluated at a mean temperature of 66 °C and Ra_c taken as 800, as suggested by Sparrow et al (1964) for a semi-infinite surface with an imposed step in heat flux without an upper rigid boundary, equation 5.1 becomes:

$$t_{nc} = \frac{0.342}{q''^{\frac{1}{2}}_{l}} \tag{5.3}$$

In Figure 5.3, the prediction of Oker for t_{nc}, equation 5.3, is less than the experimentally measured t_{nc} of this study. When δ is taken as $2\sqrt{at}$ from the exact one dimensional solution to the conduction equation for an imposed surface heat flux with the properties also evaluated at a mean temperature of 66 °C, the following equation is obtained:

$$t_{nc} = \frac{0.463}{q''^{\frac{1}{2}}_{l}} \tag{5.4}$$

Equation 5.4 predicts times for the onset of natural convection which are also lower than the corresponding experimentally measured times. Using a larger Ra_c of 3600, with δ taken as $2\sqrt{at}$, gives:

$$t_{nc} = \frac{0.982}{q''^{\frac{1}{2}}_{l}} \tag{5.5}$$

and describes the experimental measurements better than the previous expressions. Since the heating surface is not semi-infinite (w/l = 0.5), the edge effects of the film heater during heating can be expected to affect the onset of natural convection, requiring a Ra_c different than that predicted by the earlier analyses based on a semi-infinite heating surface.

In an earlier study, Ngheim (1980) observed the onset of natural convection from a narrow gold film heater (w/l = 0.1) on a large quartz substrate in R113 with high speed holographic interferometry simultaneously with the measurement of the

film heater resistance. The resulting temperature-time plots, similar to that in Figure 5.2, also showed the same type of disturbance at t_{nc}, and were also correlated well by equation 5.5.

The next significant event in Figure 5.2 following the onset of natural convection is incipient boiling, as indicated. Incipient boiling, or the onset of boiling, is defined as the appearance of the first vapor bubble on the heating surface. In some tests, this incipient boiling takes place at the point when the mean heater surface temperature reaches a maximum, while in other tests, the onset of boiling occurs prior to this point. For tests in which the latter took place, the level of the ensuing maximum heater surface temperature depended on the manner in which the boiling propagated across the heated surface. If incipient boiling occurred as an almost explosive event over the entire heater surface, then the temperature associated with boiling incipience was the maximum surface temperature. If incipient boiling occurred at a location near a corner of the heater, for example, the heater would become cooled locally while the remainder of the heater surface continued to rise in temperature. The heater surface temperature measurement is a spatially averaged quantity, as described earlier, and the measurement would continue to rise until the boiling spread sufficiently to produce a subsequent decrease in the mean value. This boiling propagation will be defined in more precise terms later.

Following the onset of boiling, a quasi-steady boiling region is noted in Figure 5.2. In this domain of the temperature-time plot, boiling has spread across the entire heating surface, and the quasi-steady boiling temperature level is less than the maximum heater surface temperature, but above the saturation temperature for the liquid at the system pressure, as expected.

The heater surface temperature-time plot of test Run 75 is presented in Figure 5.4 with the experimental conditions as indicated. These experimental conditions are virtually identical to those of Figure 5.2, except that the heater surface is inverted, or

horizontal down (a/g = -1). As can be seen, the temperature-time curve is quite different from that for heating in the horizontal up position. The departure from the one dimensional conduction prediction marks the onset of natural convection, t_{nc}, as was also observed in Figure 5.2 for the horizontal up surface orientation. In this case the fluid flow that eventually takes place with heating results in a lateral outward flow for the heated surface in the horizontal down position, and depends on the dimensions of the heater surface and on the geometry of the enclosure. The buoyancy force tends to hold the liquid against the heated surface. A uniformly heated semi-infinite surface with this orientation produces a stable configuration with no liquid motion, and heat transfer by conduction alone exists. Heaters of finite size, however, produce lateral temperature gradients in the liquid, which induce subsequent lateral liquid motion. In the present study, the edge effects on the liquid temperature resulting from the finite extent of the heater surface were such that the t_{nc} for a heater horizontal down, with the same imposed heat flux and initial conditions as a horizontal up heater, was larger than t_{nc} for a horizontal up heater (1.9 seconds versus 1.2 seconds in Figures 5.4 and 5.2). Similar observations were reported in the transient experimental work of Oker (1973).

The incipient boiling point is indicated in Figure 5.4, and appears as a disturbance in the temperature-time plot. The initial phase change and propagation of this phase change across the heated surface causes a drop in the spatial average temperature. Once boiling has spread across the entire heating surface, the vapor bubble covers the heater, since buoyancy holds the R113 vapor at the heater surface with a/g = -1, unlike heating with a/g = +1 where the buoyancy force lifts the vapor from the heated surface. Since the thermal conductivity of R113 vapor is much less than that of the liquid, the heater becomes, in effect, insulated from the liquid. As a consequence, the temperature of the heater will rise, if permitted, until the heater reaches an unduly high temperature or is destroyed. This process is sometimes

referred to as dryout, or heater burnout. Boiling with a surface horizontal down (a/g = -1) in the absence of forced liquid motion will result only in an unsteady heater surface temperature. Periodicities superimposed on the mean surface temperature are observed in Figure 5.4 because the vapor slug continuously collapses and grows near the edges of the heater.

Transient heating in microgravity is different from that in earth gravity, regardless of whether heating horizontal up or horizontal down. Figure 5.5 presents the spatial mean temperature-time plot for microgravity drop vessel experiment PBMT1115.605, which used a heated thin gold film surface. The measured temperature follows the one dimensional semi-infinite media conduction solution reasonably well until incipient boiling takes place. At the level of microgravity present in these initially quiescent experiments (a/g = 10^{-5}), there was effectively no liquid motion resulting from the heating of the liquid. Following the onset of boiling, the surface temperature decreases and then immediately rises, as was expected after the drop tower movie films were viewed. Following the initial boiling, a single large vapor bubble covered the heater surface, effectively insulating the heater surface. Similar to boiling in earth gravity in the horizontal down orientation, boiling on a flat surface in microgravity is unsteady.

Figure 5.6 presents the predicted and measured thin gold film surface temperature rise for a variety of tests with surface Q-5, a nominal q''_T of 6 W/cm^2 and nominal subcoolings of nominally either 0 or 11 °C. The final two digits of the test names listed in Figure 5.6 give the subcooling in degrees Fahrenheit. The results are scaled by the total heat flux to both the R113 and the quartz substrate, and plotted as a function of the square root of time. The predicted heater surface temperature rise is from the solution to the one dimensional transient heat conduction problem for two semi-infinite media with constant energy generation at the plane separating the two media given in Appendix G and evaluated at the common plane:

$$T_w - T_\infty = \frac{2q''_T}{k_l}\sqrt{\frac{\alpha_l t}{\pi}} \qquad (5.6)$$

Measurements from tests with heater surface orientations of both horizontal up and horizontal down in earth gravity are included along with data from two microgravity tests. Departure from the linear prediction results either from the onset of liquid motion arising from the buoyancy effects during heating or from the onset of boiling. Although heating of the film surface is not truly one dimensional, the departure from the one dimensional linear prediction shown in Figure 5.6 provides a conservative estimate for the onset of natural convection with a surface in the horizontal up or horizontal down orientation in earth gravity, as was demonstrated in Figure 5.2. For the microgravity experiments PBMT1101.600 and PBMT1121.620, the departure from the conduction predicted surface temperature was the consequence of incipient boiling. The lack of departure from the linear prediction earlier than at incipient boiling gave credence to the technique used for heater surface temperature measurement.

Figure 5.7 presents the results of constant imposed heat flux tests in the laboratory pool boiling vessel, with a surface orientation of horizontal up. The tests were all conducted with the same heat flux but with three different levels of subcooling. For the early times the curves are superimposed on one another, as anticipated. However, at later times they were expected to separate because of the differences in subcooling and delay times to incipient boiling. Figure 5.7 confirms this expectation, and provides an indirect check on the heater surface temperature measurement. Because of the difference in subcooling, the quasi-steady surface boiling temperature is different for each of the surfaces by roughly the amount of the liquid subcooling, as indicated.

5.1.1.2 Transient Liquid Temperature

The measured heater surface temperatures provide data with which the calculated temperatures can be compared. In the absence of liquid motion, it is also possible to compute the transient temperature distribution in the liquid. A calibrated thermocouple was included in the drop vessel, and transient measurements obtained which can be compared with the computations. Figure 5.8 shows the temperature rise determined by the thermocouple located at a nominal distance of 1.6 mm above the center of the heater surface. The uncertainty in the location of the thermocouple relative to the heating surface was $\pm$ 0.2 mm, and the calculated temperature variations are presented for the possible locations of the thermocouple at 1.4 mm, 1.6 mm, and 1.8 mm above the heater surface. The calculations for the liquid temperature at these locations are from the solution to the one dimensional transient conduction equation for two semi-infinite media given in Appendix G. The measured thermocouple temperature variation is closest to the liquid temperature variation at 1.6 mm, the nominal location of the thermocouple.

5.1.1.3 Transient Pressure Measurements

The laboratory pool boiling vessel and the drop vessel pressure transducers measured the transient pressure of the liquid near the heating surface during the experiments. This section presents representative results of the transient pressure measurements, which give an indication of the quality of the pressure control possible with set pressure levels in the laboratory and drop vessel pool boiling experiments.

Figure 5.9 shows representative pressure measurements for boiling tests performed in the laboratory pool boiling vessel at the three pressure levels used to

obtain three different subcooling levels with an initial liquid temperature of 48 °C. The pressure level was maintained within ± 0.34 kPa (± 0.050 psi) of the set point except at boiling incipience, where the pressure increased by as much as 15 kPa (2.2 psi) as a result of the sudden generation of a considerable amount of vapor. This spike in the pressure measurement, when it was large enough to be observed, always correlated with the incipient boiling observed on the recorded videos. When the boiling incipience was particularly violent, as seen on the recorded videos, a pressure system oscillation was observed. The response time of the pressure control system required to restore the pressure to the original level before boiling was less than 30 milliseconds, except for the more violent incipient boiling events.

Figure 5.10 shows representative pressure measurements obtained with the drop vessel experiments in microgravity. The three pressure levels necessary to produce the three different subcooling levels used in microgravity are presented, and one pressure level from a pre-drop test measured with the heater surface horizontal up in earth gravity is included for comparison. In the drop vessel pressure measurements, as in the laboratory pool boiling measurements, a spike of as much as 6.8 kPa (1 psi) sometimes occurred at incipient boiling. The pressure level in the drop vessel otherwise was maintained to within ± 0.6 kPa (± 0.09 psi) of the set point. On occasion, however, an initial small decrease in pressure occurred in changing from earth gravity to microgravity on release of the test package before the pressure reached a nearly constant level, because of the dynamics of the pressure control system. Incipient boiling occurred after this initial pressure disturbance, so this anomaly in pressure was not detrimental to the results obtained.

5.1.1.4 Transient Heat Flux Measurements

Figure 5.11 illustrates representative examples of transient total heat flux data for boiling tests performed in the laboratory pool boiling vessel and in the drop vessel. The heater controller maintained the heat flux constant to within ± 3% of the set point for most of the laboratory pool boiling vessel experiments, and to within ± 5% of the set point for most of the drop vessel experiments.

5.1.1.5 Heater Surface Superheat at Boiling Inception

Four different gold thin film surfaces were used in the tests conducted with an imposed constant heat flux and were designated by: Q-1, Q-2, Q-5, and Q-6. Surfaces Q-5 and Q-6 were used in both the laboratory pool boiling vessel and the drop vessel, while surfaces Q-1 and Q-2 were used only in the laboratory pool boiling vessel. The heat flux imposed on these surfaces, q_T'' , the delay time to incipient boiling, t*, and the heater surface superheat temperature at the time of boiling inception, ΔT^*_{sup}, are related to one another. The following figures will attempt to demonstrate these relationships in a variety of ways. It will become obvious, of course, that as t* is reduced for whatever reason, in the absence of natural convection effects ΔT^*_{sup} will also be reduced for a given level of q''_T. Certain data points shown are flagged, and represent the heater surface superheat at the time of boiling inception. The flagged data point is connected by a dashed line to an unflagged data point, which in turn represents the heater surface superheat measured at the time when the boiling begins to propagate across the surface. Data points with no flags or connecting lines represent data where the onset of boiling resulted in virtually the immediate spread of the boiling process. This amounted to a delay of less than 1 millisecond for tests conducted in the laboratory pool boiling vessel, and of less than 3 milliseconds in the

drop tower. This latter figure is greater because of the uncertainty associated with the lower camera speed. Nominal subcoolings of 0, 2.8, and 11.1 °C were used in all of the tests. With the heater surface horizontal up, a q_T" of 2 W/cm^2 resulted in a boiling inception delay time of more than five minutes. As a result, this combination of orientation and heat flux was not used in any of the laboratory vessel boiling tests. The lower bound of the heat flux range for the microgravity tests was set by the limited fall time of 5.18 seconds in the drop tower. In two drop vessel microgravity experiments with a nominal $q"_T$ of 4 W/cm^2, boiling inception did not occur. As a result of these two preliminary tests, the heat flux range for the microgravity tests was limited to 6 to 8 W/cm^2.

The heater surface superheat results for surface Q-1 shown in Figure 5.12 were obtained in the laboratory pool boiling vessel with the heater surface in either the horizontal up or the horizontal down position. For the initial test conditions as indicated, Figure 5.12 implies a significant time interval between boiling inception and boiling spread at the lower heat flux of $q"_T = 4$ W/cm^2 which was not observed for any of the other surfaces. Figure 5.12 also indicates a trend of a decrease in the heater surface superheat associated with the spreading of the boiling process as the heat flux is increased. This decrease was not observed with the other heating surfaces, where the other corresponding heater surface superheats tended to remain constant as the heat flux increased. The onset of boiling with Q-1 always occurred at a large visible scratch on the thin gold film. From the presence of this scratch and the inconsistency between these data and that from the other surfaces, the results in Figure 5.12 are considered to be an anomaly. Since the thin gold film was undamaged prior to installation, it is surmised that the heater surface was accidentally scratched as it was placed in the vessel.

Figure 5.13 shows the results of wall superheat at boiling inception from the laboratory pool boiling experiments for surface Q-2. The initial conditions are given.

Larger heater surface superheats at boiling incipience resulted for a/g = -1 than for a/g = + 1 with q_T" near 4 W/cm^2 , but not near 8 W/cm^2, for tests with the same nominal subcooling. The wall superheat for most tests fell into a band of data between 40 and 55 °C, except for wall superheats corresponding to q_T" near 8 W/cm^2 which produced lower heater surface superheats.

Figure 5.14 presents the heater surface superheat incipient boiling results for surface Q-5 for a/g = $\pm$ 1 and microgravity, with different subcoolings. A nominal initial fluid temperature of 49 °C was used for the a/g = $\pm$ 1 tests and a nominal initial fluid temperature of 47 °C was used for the microgravity tests. For total heat flux levels of 2, 4, 6, and 7.5 W/cm^2 , the maximum superheats at boiling incipience occurred at a/g = -1 or microgravity, and at a nominal subcooling of either 0 or 2.8 °C. Boiling inception followed by a measurable time delay to boiling spread occurred for q_T" greater than 7 W/cm^2 . It appears from the surface Q-2 and Q-5 data in Figures 5.13 and 5.14, respectively, that the time delay to boiling spread is most pronounced at the higher heat flux levels. Except for the initial boiling phenomena near the heat flux of 8 W/cm^2, all of the heater surface superheat at boiling inception fall within a range of 50 to 75 °C.

For all tests conducted with surface Q-5 after 10/13/89, the superheats for boiling incipience consistently fell in the range of 50 to 75 °C. Before this date, the superheat level increased continually from about 10 to 38 °C. The boiling incipience character of the surface was somehow changing during this interval, after which the heater surface superheat at the onset of boiling became consistent. Similar behavior was observed by Tong et al (1990) in an experimental study of boiling of R113 with thin platinum thin films. Tong et al speculated that the R113 had somehow broken down above 100 °C and formed deposits on the heater surface. However, the decomposition temperature of R113 is greater than the observed heater surface temperatures of the present tests: a trace decomposition of R113 exposed to quartz for

30 seconds was found to first occur at a temperature of 299 °C in a testing described by E.I. DuPont de Nemours (1969). It is believed that the surface became more "regular" in incipient boiling character after the first few tests and the resulting boiling removed some of the adsorbed gases and impurities.

Figure 5.15 shows the heater surface superheat at incipient boiling for surface Q-6 as a function of total heat flux with a/g = $\pm$ 1 and microgravity with different subcoolings. The tests at a/g = -1 were conducted in the laboratory boiling vessel, while those in microgravity were conducted following the tests for surface Q-5. Surfaces Q-5 and Q-6 were installed in the drop vessel at the same time. The nominal initial fluid temperature for the earth gravity tests was 49 °C and 47 °C for the microgravity experiments. Except near 8 W/cm^2, the heater surface superheats lie in a range between 48 and 62 °C. The lower level of this heater surface superheat range is close to the lower range of heater surface superheats for surface Q-5. The heater surface superheat at incipient boiling is lower than that for the undamaged surfaces Q-2 and Q-5, at the high heat flux levels.

The incipient boiling heater surface superheat levels for surfaces Q-5 and Q-6 were similar, but greater than those of Q-1 and Q-2. The similarity of behavior for surfaces Q-5 and Q-6, compared to surfaces Q-1 and Q-2, is presumed to be due to their having been fabricated together by sputtering, while surfaces Q-1 and Q-2 were vacuum deposited with gold at the same time. Surface Q-2 shows a more constant superheat range than does Q-1, most likely because of the presence of the scratch observed on Q-1. In all of the plots of ΔT^*_{sup} , the delay from incipient boiling to the onset of boiling spread is most pronounced near the heat flux of 8 W/cm^2.

In the present pool boiling experiments with an imposed heat flux at the heater surface, the subcooling level, from near saturation to 11 °C, had little influence on $\Delta T^*_{sup.}$ As is shown below, the present subcooling range also had little effect on the incipient boiling delay time, t*.

Figures 5.16 through 5.19 show the incipient boiling delay time, t*, as a function of the total heat flux. Figure 5.16 is for the damaged surface Q-1 and Figure 5.17 for heater surface Q-2. It may be noted that t* decreases with increasing $q"_T$. It is also noted that the onset of a significant time interval between incipient boiling and boiling propagation is first observed at $q_T"$ of 4 W/cm^2 on Q-1 and $q_T"$ of 6 W/cm^2 on Q-2. Further, the incipient boiling delay times with the surface orientation that is horizontal up are greater than those with a horizontal down orientation, for the same conditions. This is to be anticipated since the fluid motion induced by buoyancy transfers energy from the horizontal up heater surface at a rate greater than from the horizontal down heater surface. As a result, for a given total heat flux more time is required for the horizontal up heater surface to reach the heater surface temperature range in which incipient boiling is expected. On the other hand, no particular influence of bulk liquid subcooling on the incipient boiling delay time is to be observed.

The incipient boiling delay times for three subcooling levels and with $a/g = \pm 1$ and microgravity are presented in Figures 5.18 and 5.19 for surfaces Q-5 and Q-6, respectively. Similar to the data with surfaces Q-1 and Q-2, t* decreases with increasing $q"_T$, and the experiments associated with $a/g = +1$ have greater delay times for incipient boiling for the same heat flux than either $a/g = -1$ or microgravity for $q"_T \leq 7$ W/cm^2. It is also observed in Figures 5.18 and 5.19 that for $q"_T \geq 7$ W/cm^2, the values of t* for the heater in the horizontal up orientation approach the values of t* for the heater in the horizontal down position or in microgravity. Also, for $q"_T \geq 7$ W/cm^2, boiling inception occurs before the onset of significant natural convection. As in the tests performed with surfaces Q-1 and Q-2, the time interval between the onset of boiling and boiling propagation is greatest near 8 W/cm^2. t* measured for surfaces Q-1 and Q-2 in the horizontal down orientation for $q"_T > 4$ W/cm^2 were similar to the t* determined from the drop tower experiments at the same heat flux. This

reproducibility of t* between the horizontal down tests and the microgravity tests indicates that the determination of the incipient boiling delay time of heater surfaces may be done with the heater surface in the inverted position rather than in the more expensive microgravity conditions. The slopes of the curves of the incipient boiling delay times for surfaces Q-5 and Q-6 were similar to each other, but different than that for surfaces Q-1 and Q-2. Since surfaces Q-5 and Q-6 were sputtered at the same time, they should have physical characteristics similar to each other but different from those of surfaces Q-1 and Q-2, which were vacuum deposited at the same time, as was pointed out earlier.

The quartz surfaces are representative of "smooth" boiling surfaces, and the metal surfaces are representative of "rough" boiling surfaces. The smoothness of the quartz surfaces is characterized below using the measured surface superheats. The thin film surfaces were polished before sputtering with a 1.4 micron pitch polish by the manufacturer. Heater surface superheat levels ranged from 75 °C to 12 °C in the microgravity tests. The Laplace equation, equation 2.2, taken together with the Clausius-Clapeyron relationship for equilibrium conditions give an estimated cavity radii range of 0.02 microns to 0.8 microns. Scanning electron microscopy of the thin film on quartz surface Q-9 revealed minute scratches which had widths of approximately 0.2 microns. This width is in the above cavity radii range.

5.1.1.6 Incipient Boiling and Boiling Propagation

Of the earlier transient boiling studies described in Chapter 2, none had photographed simultaneous orthogonal views of the heating surface, across and from beneath the heating surface, using high speed cameras. A single view of the heating surface is inadequate for distinguishing the characteristics of the vapor dynamics since much of the interfacial motion is obscured by other vapor motion. In the current

experiments, the boiling inception and the resulting vapor motion was observed from two orthogonal views: directly across the heater and through the bottom of the quartz substrate. Distinctly different categories of vapor dynamics were observed in both the laboratory and the drop vessel pool boiling experiments. This section will present types of behavior, some previously unobserved, which will be referred to here as boiling spread or boiling propagation. Boiling spread may be classified into two distinct categories: (a) The first is the formation or nucleation of vapor ahead of a moving liquid-vapor front, which is sometimes pushed ahead by this front and is at other times absorbed into the front. (b) The second is the growth of an interface similar to that of vapor bubble growth due to evaporation at the interface, regular in some cases and in other cases chaotic, but without the formation of vapor bubbles ahead of the interface. The parameters under which these differences in behavior occurred will be described, but their detailed origins are as yet unknown.

The following discussion includes photographs which show the chronological sequences of the behavior observed. The measured initial conditions, including the applied power input, system pressure, bulk liquid temperature, a/g level, and orientation are given in the first figure of each chronological sequence. Six different categories of boiling spread are listed and then described below:

A. Advancement of vapor by irregular protuberances

B. Formation of mushroom-like vapor mass followed by spreading

C. Single pancake-like bubble with a "smooth" interface

D. Orderly growth followed by onset of interface disturbances

E. Explosive growth of a vapor mass

F. Marangoni motion of bubbles toward region of higher temperature

A. Advancement of vapor by irregular protuberances

The first category of boiling propagation is the advance of the vapor mass by irregular protuberances from bubbles, shown in the sequence of Figures 5.20a through 5.20e. The upper photo is through and from beneath the heating surface, and the lower portion presents the view across the heating surface. In the first figure of this series, a vapor bubble has already appeared. The onset of natural convection may be seen in Figure 5.20a, in both the view through the bottom of the heating surface and in the view across the heating surface. In the view across the heating surface, the onset of natural convection is characterized by the newly formed thermal plumes, parallel to and slightly above the heater surface. In the view from beneath the gold film heater, a disturbance around the periphery of the heater surface is visible. In the next figure, 5.20b, three bubbles are now present, and the peripheral disturbance, a result of natural convection, may be seen in the view from beneath the gold film heater. In Figure 5.20c, the boiling has spread over a large area of the heating surface, and bubbles depart from the heating surface as a result of buoyancy as the boiling propagates over the heating surface. The last figures of this boiling sequence are Figures 5.20d and 5.20e. In Figure 5.20e, boiling covers most of the heater surface, and bubbles coalesce near the edge of the outwardly growing bubble front. This type of boiling spread was observed only with the heating surface in the horizontal up position at $a/g = +1$, and for the total power input to the gold film heating surface ≥ 7 W/cm^2.

B. Formation of mushroom-like vapor mass followed by spreading

The second category of boiling spread presented in Figures 5.21a through 5.21d shows the formation of a mushroom-like vapor mass in the center of a thin vapor layer, which rises above the thin vapor layer due to buoyancy, while the thin

vapor layer moves outward beneath the large mushroom-like vapor mass. The first figure of this series, Figure 5.21a, shows the appearance of the first bubble in both views. The upper photo is through and from beneath the heating surface, and the lower photo of the figure looks across the heating surface. Convective stagnation lines are clearly observable in the lower portion of the photo. Figure 5.21b shows a thin vapor layer surrounding the large mushroom-like bubble. The bubble in the center of the thin outward growing vapor layer becomes larger in Figure 5.21c. The vapor layer has vapor bubbles on its surface. Figure 5.21d shows that boiling has covered most of the heater, and in the view across the heating surface, the large bubble is departing from the heater surface. The upward bubble motion entrains liquid and causes more disturbances over the outward growing vapor layer. This kind of spreading was observed only for $a/g = +1$ with $2 \leq q''_T \leq 7$ W/cm^2.

Okuyama et al (1988) observed this type of vapor motion using a large step in heat flux (q''_l on the order of 20 W/cm^2 to 40 W/cm^2) applied to a 7 μm thick copper foil (0.4 cm wide by 4 cm long) that was laminated to an epoxy plate, in R113 at $P <$ 0.5 MPa. A horizontal up heater orientation was used. In the present study, by contrast, the heat flux to the liquid is considerably smaller, with the largest q''_l on the order of 1.4 W/cm^2.

C. Single pancake-like bubble with a "smooth" interface

A third category of boiling spread consists of a single pancake-like bubble with a "smooth" interface. In Figures 5.22a through 5.22d, using the laboratory pool boiling vessel, the heater surface orientation is horizontal down. The upper portion of each figure is a view through the heater surface from above, and the lower portion of each figure is a view across the heating surface. The initial bubble grew outward in an orderly manner from one location near the edge of the heating surface. This initial

bubble eventually moved away from the location at which it first originated, and a second bubble formed at this location, as shown in Figures 5.22a and 5.22b. In the underside view of Figure 5.22b, the smaller second bubble is in front of the larger bubble (in the darker region of the heater surface), but in the side view of Figure 5.22b, the smaller bubble is behind the larger one. Figure 5.22c shows only one bubble in both views. The larger bubble of the previous two figures expended the available thermal energy for both bubbles while growing, and this large bubble eventually coalesced with the smaller bubble. The rate of growth of the larger bubble varied linearly with the square root of time, until the bubble reached the outer edge of the heater, an indication that the growth of the bubble was thermally controlled. After the bubble had grown past the edges of the film heater as shown in Figure 5.22d, it collapsed at some peripheral locations, and the liquid rewetted the gold film heater. This category of boiling spread was observed only in earth gravity with the heating surface oriented horizontal down, such that the upward buoyancy force flattened the bubble and held the vapor against the heating surface.

D. Orderly growth followed by onset of interface disturbances

The fourth category of boiling propagation consists of initially orderly growth of either a hemispherical bubble, in the case of microgravity, or a pancake-like one for a/g = -1. This orderly growth then gives way to violent growth, for some as yet unknown reason. The initially smooth bubble interface was observed to rupture either on the surface or at the base of the bubble at the beginning of the violent growth. Figures 5.23a through 5.23d show the history of violent boiling spread associated with the rupturing of the bubble occurring at the periphery of the bubble base. The bubble was initially smooth, but this is not shown. The heater surface shown is in the laboratory pool boiling vessel in the horizontal down position. The upper photo

presents the view across the heater surface, and the lower photo presents the view through the heater surface from above. Figure 5.23a shows a ruptured bubble one frame after boiling inception. In Figure 5.23b, the violently growing vapor mass develops large-scale satellite interface bubbles, which sometimes break away from the vapor mass. The view across the heater surface (oriented horizontal down) shows that the vapor is being pushed down into the subcooled liquid away from the heating surface. This motion was simultaneously accompanied by a spike increase in the pressure transducer reading. These two observations suggest that this later vapor motion is driven by pressure forces arising from the phase change. The heating surface is eventually covered by the vapor mass, as shown in the subsequent two photos, Figures 5.23c and 5.23d.

The type of violent boiling spread by the rupturing of an initially smooth and symmetrical bubble surface is shown in the photo sequence of Figures 5.24a through 5.24d. In these photos, the heater surface is again in the horizontal down position with the view through the heater surface from above in the upper portion of the photo and the view across the heater surface in the lower portion of the photo. Rupturing of the surface of the bubble is beginning in Figure 5.24a. The breaking of the liquid-vapor interface occurs on the bubble periphery near the warmest part of the heater, the heater center. The following two figures, Figures 5.24b and 5.24c, show smaller bubbles on the outwardly moving interface of the larger bubble. In the last photo of this sequence, Figure 5.24d, the vapor mass with the bubbles at the liquid-vapor interface has nearly covered the heater surface.

Category D phase change dynamics were observed to occur either in microgravity or in earth gravity with the heater surface in the horizontal down position. The heat flux producing category C boiling spread was greater than that associated with the category D boiling propagation, for the heater surface in earth

gravity in the horizontal down orientation, with the same subcooling and heater surface.

E. Explosive growth of a vapor mass

The fifth category of boiling spread is referred to as the explosive or energetic boiling propagation, characterized by initially uniform small scale protuberances over the entire liquid vapor interface. The sequence of photos in Figures 5.25a through 5.25g are from the drop vessel experiment PBMT1101.600 and illustrate the phase change dynamics associated with this kind of boiling propagation. In these figures, the upper photo of the figure is the view across the heating surface, and the lower photo of the figure is the view through and from beneath the heating surface. In the first of these figures, the upper part in Figure 5.25a, the conduction thermal boundary layer is visible as the line parallel to and slightly above the heater surface. This photo shows the onset of incipient boiling. In the view from beneath the heater surface, two slight shadows are seen on the heater surface. In the upper corresponding view at the same location, a shadow is present within or at the edge of the thermal boundary layer. The next photo, Figure 5.25b, shows boiling at five locations in the view from beneath the heating surface, and a large vapor mass above the thermal boundary layer in the view across the heater surface. Small scale protuberances are visible, but are blurred because of the high initial growth rate. The protuberances are more distinguishable in Figures 5.25c and 5.25d, and they are still present in Figure 5.25e. Figure 5.25f shows that the vapor has coalesced into a single large vapor mass, and some small bubbles have separated from this vapor mass. The protuberances are also larger. The vapor mass is observed to lift off the heater surface in the last photo, Figure 5.25g. The pressure disturbance associated with the initial rapid growth of the vapor mass imparts momentum to the liquid bulk which then lifts the vapor off the heating surface.

It is believed that the small scale protuberances, which may be the result of local pressure disturbances related to instabilities, greatly increase the liquid-vapor interface surface area, which then results in a large mass evaporation rate. The pressure disturbances resulting from this large mass flux create more protuberances which drive the unstable growth of the vapor mass across the heating surface. This type of boiling spread was observed only in microgravity, and only near saturation conditions with $q''_T \leq 6.5$ W/cm^2. A lower limit for this boiling propagation category could not be established at this time because the time available in microgravity was too short for boiling incipience to take place at the low heat flux level. In the drop tower tests, a q''_T of 4 W/cm^2 did not result in incipient boiling. A space experiment is required to obtain information concerning the lower limit of total heat flux for this explosive type of boiling spread. This category of boiling spread will be discussed in more detail in Chapter 6.

F. Marangoni motion of bubbles toward region of higher temperature

The final type of boiling propagation observed in the pool boiling experiments consisted of small bubbles forming and then moving toward the center of the thin film heater, the warmest part, and coalescing there as shown sequentially in time in Figures 5.26a through 5.26e. In these figures, the upper part of the photo is the view across the heater surface, and the lower part of the photo presents the view through the heater surface from beneath. The following photos resulted from the drop vessel pool boiling experiment PBMT0131.820, with the test conditions as given in the first figure. In Figure 5.26a, the first bubble appears at the edge of the heater, and the thermal boundary layer is not yet visible as in the case of Figure 5.26b. In Figure 5.26b, the first bubble has moved away from the heater edge, and two more bubbles have formed at the original incipient boiling location. Another location on the left side of the heater

surface has become activated as a boiling site with the thermal boundary layer now visible. In the next photo, Figures 5.26c and 5.26d, a number of additional bubbles have emanated from the two boiling locations. Some of the smaller bubbles have coalesced with larger ones, and new bubbles form at the edges of the vapor mass. In the last figure, Figure 5.26e, one large vapor mass finally results, which covers the heater surface. Some vapor has separated from the vapor mass and formed individual bubbles floating in the R113. The growth of these bubbles was orderly and slow. This type of boiling spread was observed for microgravity and for a/g = -1. q''_T for these instances was > 7.2 W/cm^2.

Table 5.1 summarizes the total heat flux ranges, subcooling levels, and body forces which characterize the conditions necessary for the aforementioned types of boiling propagation as known to date.

5.1.2 Imposed Heater Surface Temperature

5.1.2.1 Comparison of Measurements and Conduction Prediction

An imposed step in heater surface temperature, like an imposed step in surface heat flux, provides a simple and known temperature distribution in the test fluid, in the absence of buoyancy induced liquid motion. In order to observe the effects of different liquid temperature distributions on the resulting incipient boiling, these two different elementary liquid temperature distributions were used. The results with the imposed surface heat flux have been presented, and the results with a step increase in heater surface temperature will now be presented. The theory behind the design of the equipment for imposing a step in the heater surface temperature is presented in Appendix F, and a description of this equipment was given previously in Chapter 3.

Two different gold film surfaces, Q-6 and Q-14 were used in the tests conducted with an imposed increase in surface temperature. Both surfaces were heated in the horizontal down orientation, and the results from the two different surfaces were similar. Figure 5.27 presents the heater surface temperatures and uncertainties, as measured by the Codas system during the initial, rapid, portion of the heater power transient, and for the later part of the heater power transient as measured through the use of the CR7X. As discussed in Chapter 3, this later portion of the heater power transient was longer than the earlier portion. Because the initial series of steps in heat flux comprising an approximation to the heat flux necessary to impose a constant heater surface temperature were of short duration while the later steps were of much longer duration, two different measuring devices were used to verify that the system imposed a step in heater surface temperature. The less accurate Codas system measurements indicated that the surface resistance was constant, with an uncertainty in the resistance measurements of $\pm$ 2%. This uncertainty in heater resistance translates as a large uncertainty in the measured heater surface temperature, on the order of $\pm$ 7 °C, resulting from the small slope of the resistance-temperature linear relationship. The CR7X provided more precision in the measured heater surface temperatures for the slower portion of the heater power transient, on the order of $\pm$ 2.5 °C. The discussion concerning the estimation of the uncertainties in temperature measurement using the Codas and the CR7X is presented in Appendices C and D.1. The initial liquid temperature, T_i, and the computed heater surface temperature are shown for reference.

Figure 5.28 shows the comparison of the measured heater surface temperature with the computed one dimensional conduction heater surface temperature prediction, as presented in Appendix F. The measured heater surface temperatures for surface Q-6 shown in this figure were determined with the CR7X, and follow the one

dimensional prediction well until near the value of $E^2_{input}/100 = 15$. At this input voltage level, the larger disagreement between the measured and predicted heater surface temperature may be a result of multi-dimensional heating effects. The one dimensional predicted heater surface temperatures are greater than the measured heater surface temperatures, as would be expected, since the edge effects are neglected in the one-dimensional prediction.

Figure 5.29 shows the incipient boiling delay times for the step increase in heater surface temperature experiments performed in the laboratory pool boiling vessel for surface Q-14. The initial system temperature was 49 °C, and the liquid was subcooled by increasing the system pressure above the saturation pressure for R113 corresponding to 49 °C. As the initial voltage E_{input} , which corresponds to the imposed step increase in heater surface temperature, was increased, the delay time from the energization of the heater to the onset of boiling decreased somewhat. This decrease in the delay time to incipient boiling is expected intuitively since more energy goes into the liquid with a larger step in temperature. The delay times associated with incipient boiling are similar in magnitude for both surfaces tested here.

Figure 5.30 presents a comparison between the incipient boiling delay times and heater surface temperatures at incipience for both imposed surface temperatures and imposed surface heat fluxes for surface Q-14. The initial system temperature was 49 °C, and the liquid was subcooled by increasing the system pressure to a value greater than the saturation pressure corresponding to 49 °C. As demonstrated in Figure 5.30, the constant surface temperature experiments always resulted in boiling inception occurring at significantly lower surface temperatures and delay times when compared to the corresponding values of the constant heat flux tests. It thus may be concluded from these results that the manner of heating, and not merely the heater surface temperature, as viewed by some, affects boiling inception. Although Figure

5.30 only shows surface temperatures rather than surface superheat temperatures, the temperature differences are greater than those represented by different subcoolings.

The type of boiling propagation observed with the imposed heater surface temperature experiments always consisted of a single pancake type bubble, category C, described in section 5.1.1.6 for boiling propagation observed in the constant heat flux experiments. This observation is related to the consistently small superheated thermal boundary layer formed in the imposed surface temperature tests and will be discussed in Chapter 6.

5.2 Quasi-Steady Heating

Quasi-steady heating was performed in the laboratory pool boiling vessel using both the gold film heater, Q-2 and the copper block heater, SH-2. The liquid temperature in the laboratory pool boiling vessel was 49 °C and the liquid was subcooled by increasing the liquid pressure above the saturation pressure corresponding to 49 °C. The intent of these tests was to find the minimum heater surface temperature and heat flux for which the onset of boiling would just occur. The following figures show the heat flux to the liquid as a function of the difference between the heater surface temperature and the bulk liquid temperature. q''_l was determined, as discussed in Chapter 4, through natural convection correlations. Figure 5.31 is for surface Q-2 in the horizontal up orientation. Figures 5.32 and 5.33 are for the quasi-steady heating tests in the horizontal up and the horizontal down orientations involving the copper block heater, SH-2. Measurements at subcoolings of 1.23, 3.19, and 11.03 were obtained for the horizontal up orientation, and measurements at subcoolings of 4.08 and 11.87 were obtained for the horizontal down position.

For surface SH-2 which had the gold-sputtered copper foil exposed to the test liquid, the heater surface superheat temperatures associated with the minimum power

input to the heater at which incipient boiling would just occur were in the narrow range of 39.0 to 44.8 °C for both the horizontal up and horizontal down orientations regardless of the nominal subcooling levels of 1, 3, and 11 °C. The heater surface superheat temperatures for surface Q-2 corresponding to the minimum power input to the heater at the point where incipient boiling would occur were in the range of 32.0 to 39.6 °C irrespective of the nominal subcooling levels of 1, 3, 11, and 16 °C. The minimum heater surface superheat range required for incipient boiling was slightly greater for the metal foil surfaces rather than for the "smoother" quartz surfaces. This might at first appear contradictory to previous observations as described in Chapter 2. However, the measured heater surface temperatures of the present experiments are spatially averaged temperatures, and the local heater surface temperatures are estimated to vary by as much as 25 °C from each other, which can account for this discrepancy. (This variation in local heater surface temperature in earth gravity with the presence of buoyancy can be contrasted with the variation in local heater surface temperature in the microgravity tests with essentially no buoyancy. The local film temperature variation in microgravity was estimated to be less than 2 °C for locations 1mm inward from the film heater edge.) The tests using the quartz surface and the metal foil surface were conducted with the same initial conditions. Prior to the experiments, both test surfaces were placed together in the laboratory pool boiling vessel as described in Chapter 3.

For heater surface Q-2, the transient tests using an imposed step in heat flux resulted in larger mean heater surface temperatures at boiling inception for heat flux levels less than 7 W/cm^2 than in the case of quasi-steady heating for the same initial conditions. A step in heat flux of less than 7 W/cm^2 resulted in a mean gold film temperature of surface Q-2 at incipient boiling in the range of 42.0 to 62.9 °C.

Figure 5.34 presents natural convection data obtained before boiling inception during quasi-steady heating. The Nu calculated from the heat flux using the thin film

surface had larger uncertainties than those computed for the metal heater. This larger uncertainty in the Nu of the quartz surface is a consequence of the relatively greater uncertainties in the corresponding heat loss estimates. The natural convection correlation of Merte and Clark (1961) describe the measured data better than equation 4.7. Natural convection data is also shown for the metal heater surface in the horizontal down orientation. The Nu for the inverted metal surface are quite different from the Nu of the horizontal up orientation, as anticipated, because of the lateral fluid motion which results from buoyancy effects.

Figures 5.1 - 5.34 follow.

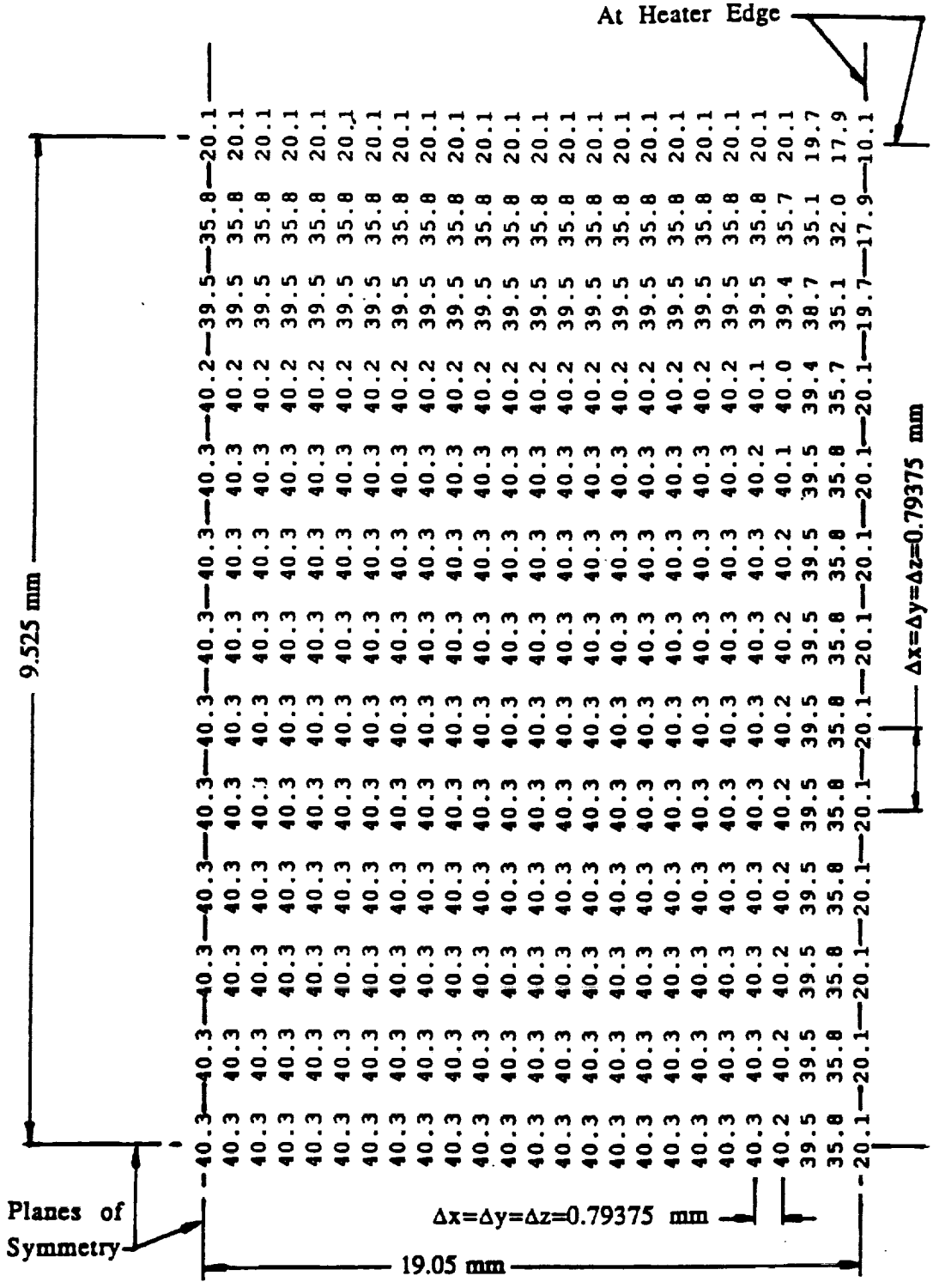

Figure 5.1 Gold film temperature rise for one fourth of the film surface for q''_T = 8 W/cm^2 at one second ($\Delta x=\Delta y=\Delta z=0.79375$ mm)

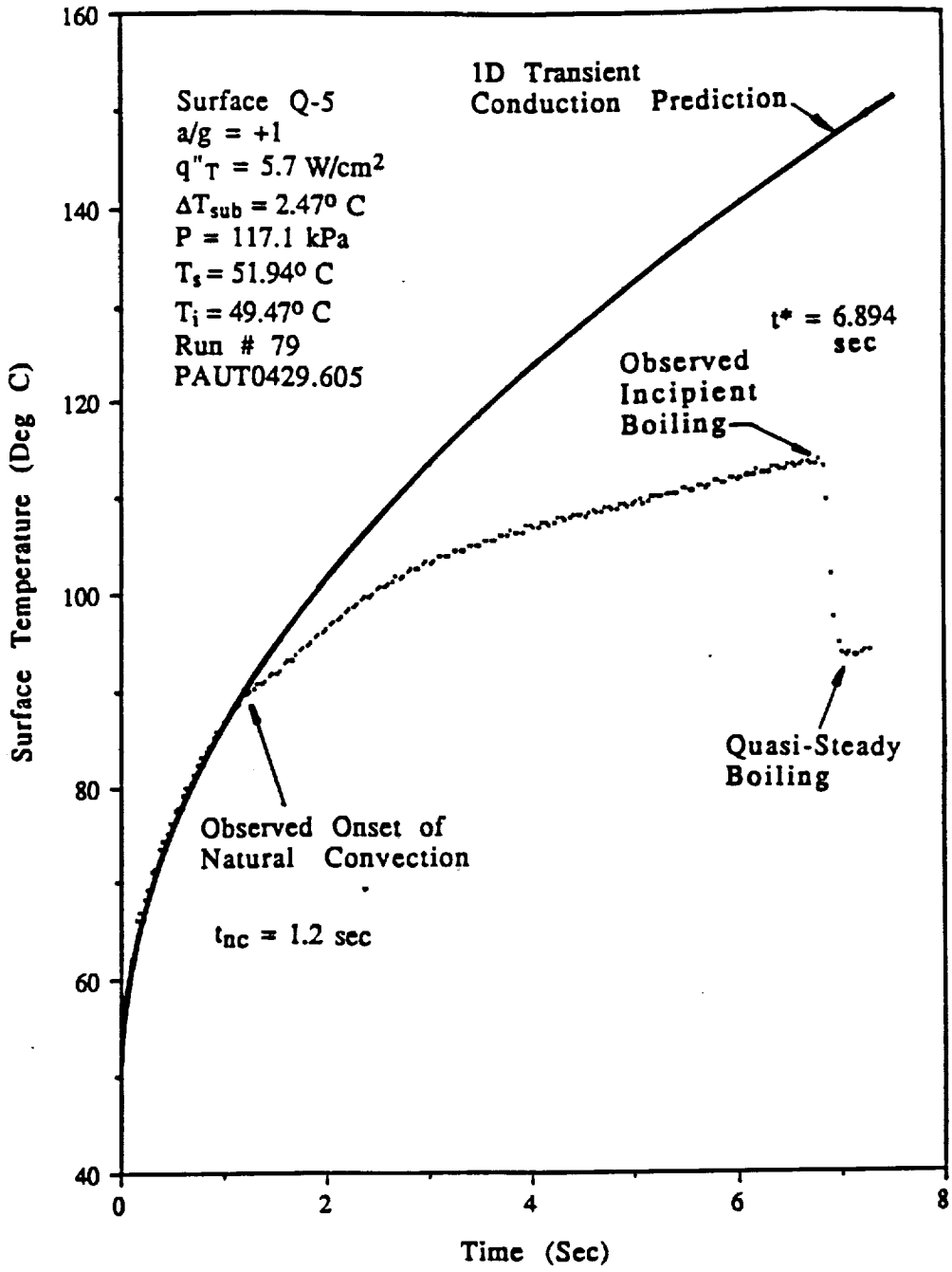

Figure 5.2 Thin gold film temperature with onset of natural convection, a/g = +1

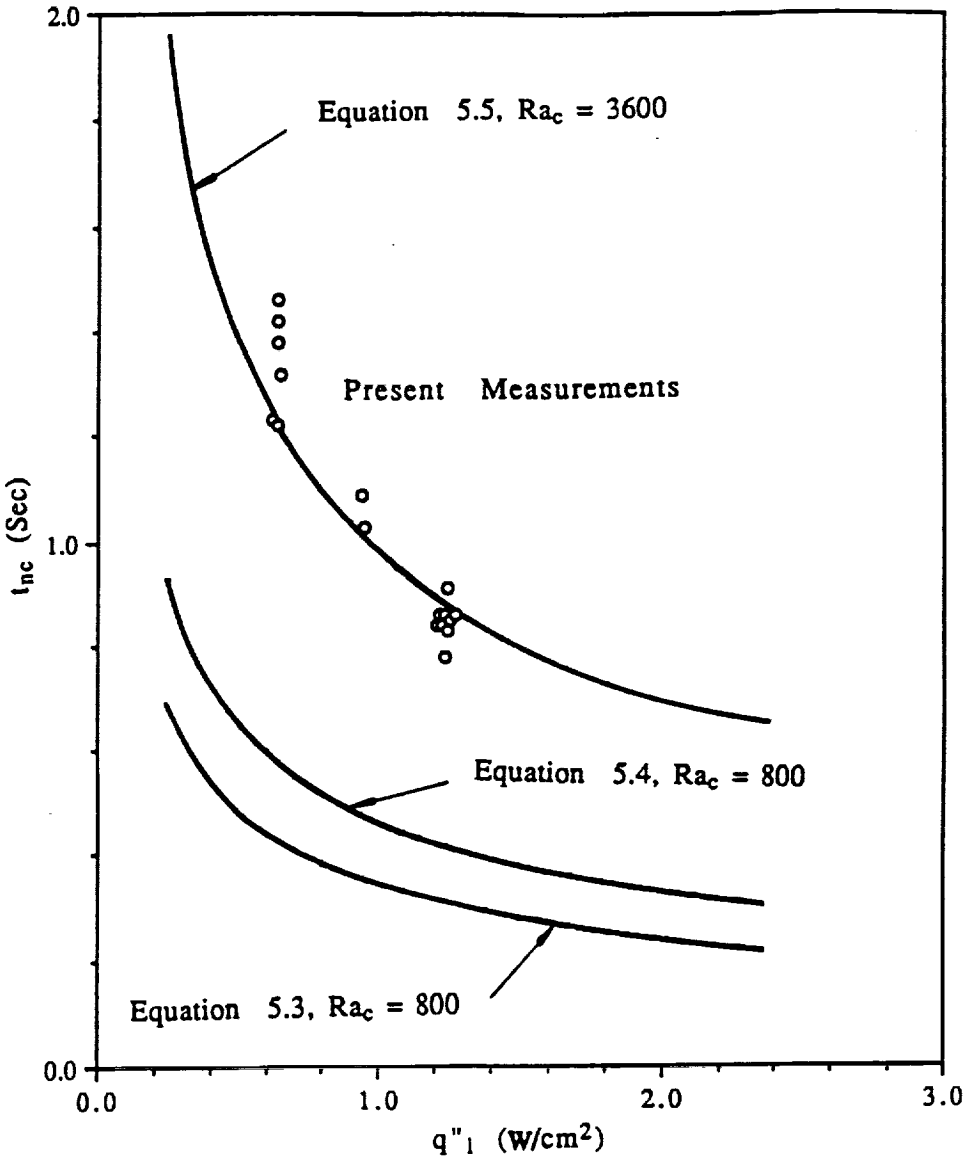

Figure 5.3 Predicted and measured time for the onset of natural convection, $a/g \cong 10^{-5}$

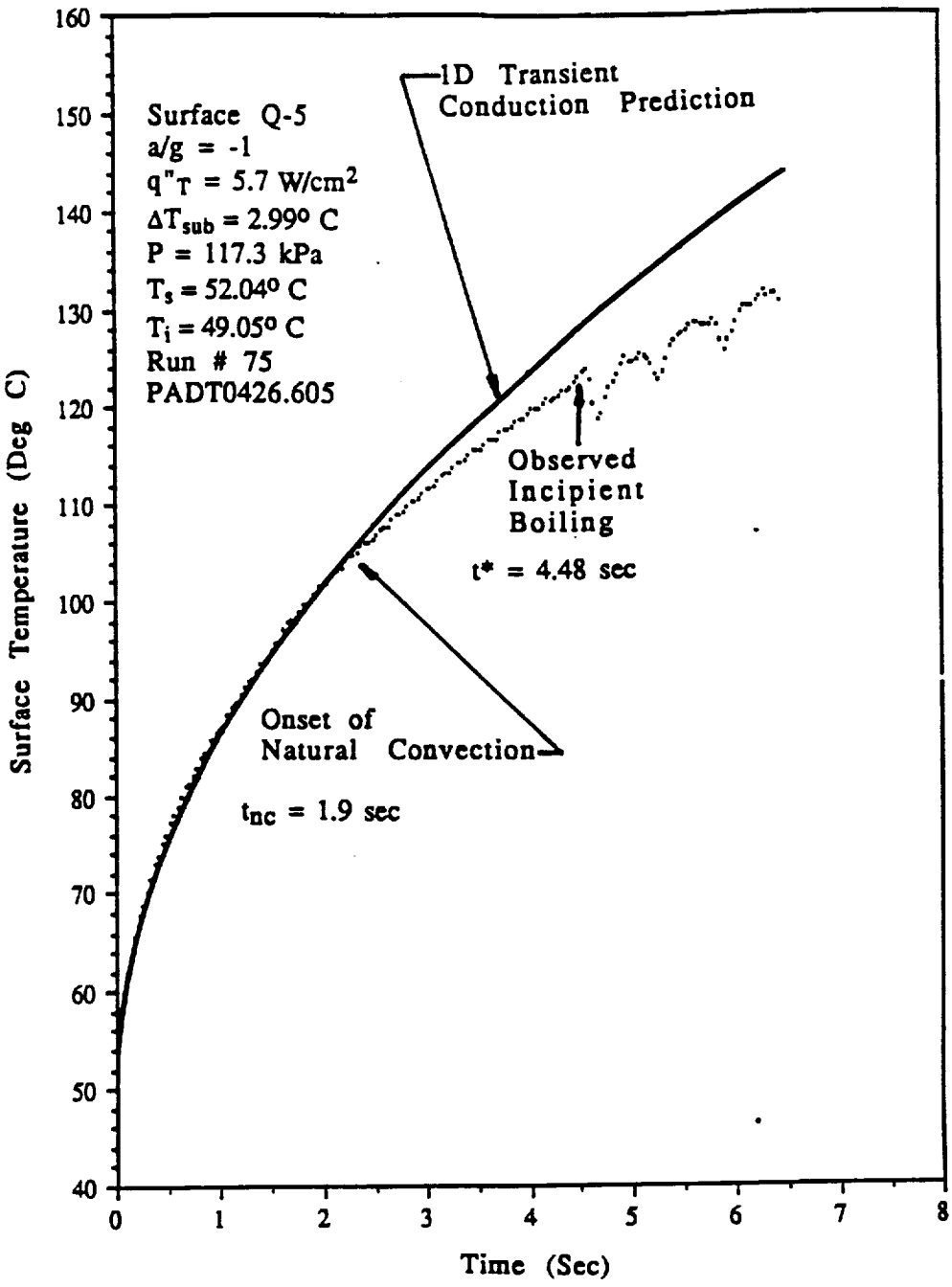

Figure 5.4 Thin gold film temperature with onset of natural convection, a/g = -1

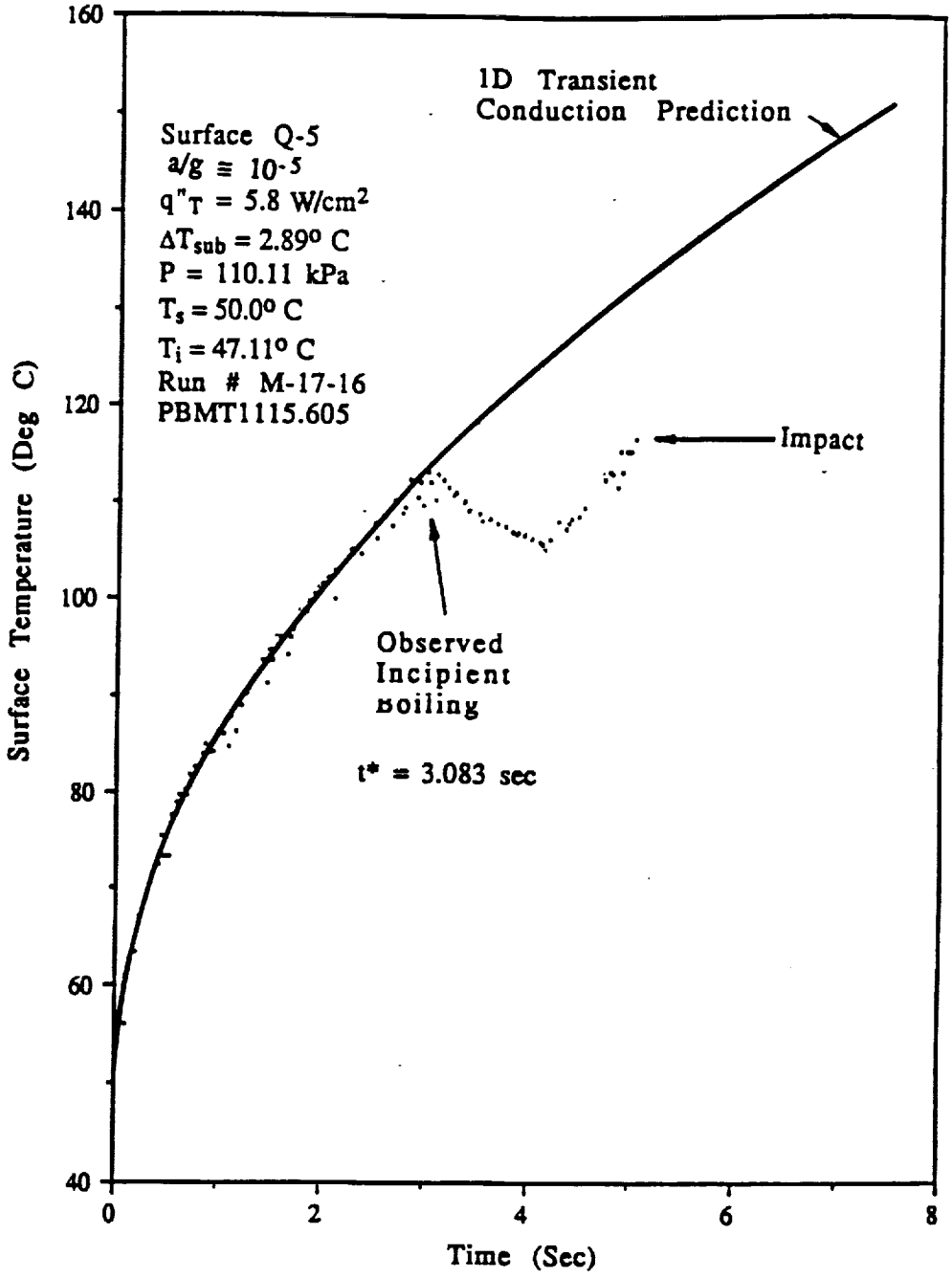

Figure 5.5 Thin gold film temperature with heater surface dryout, a/g ≡ 10^{-5}

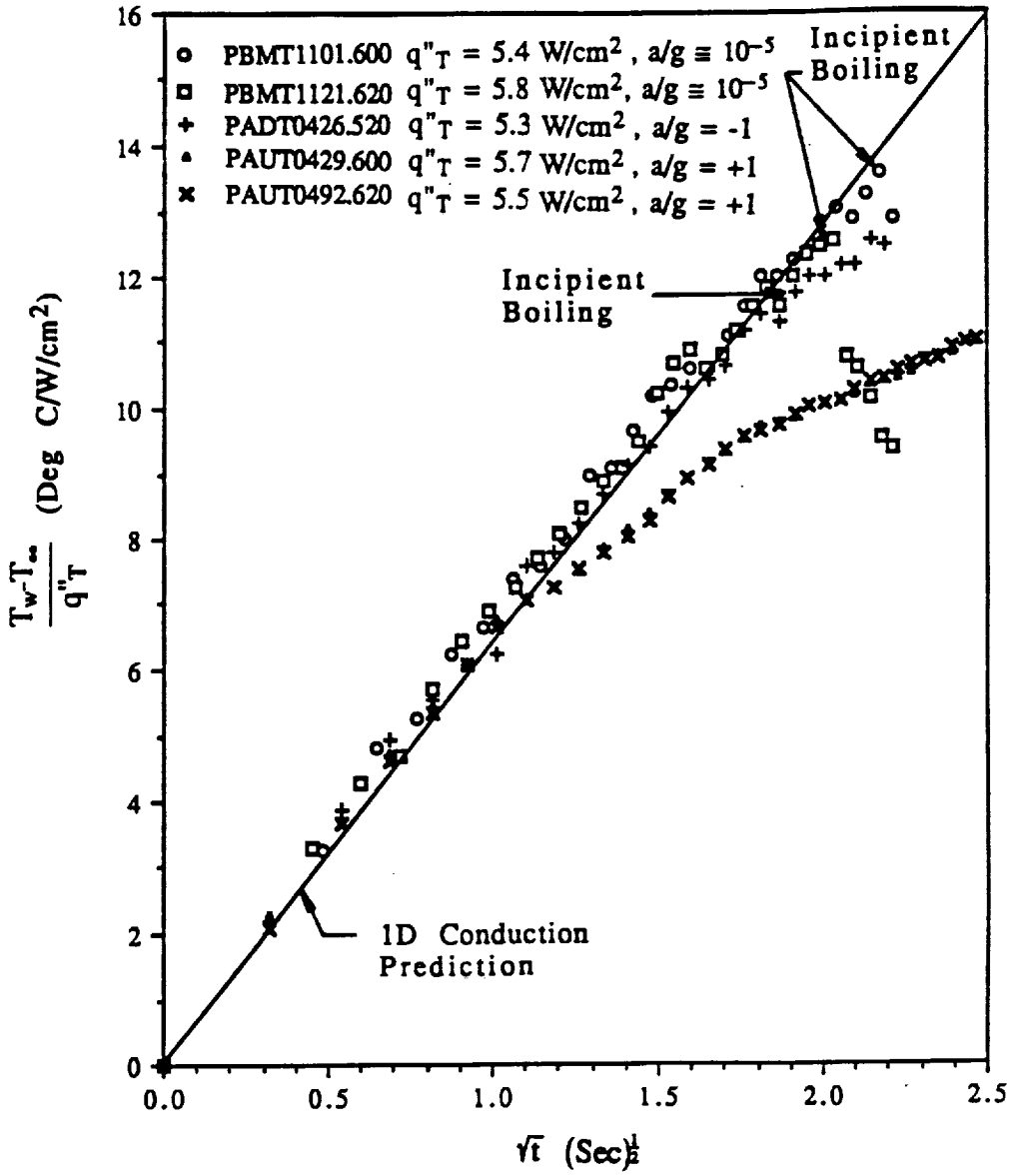

Figure 5.6 Departure of measured surface temperature from the 1D semi-infinite media prediction

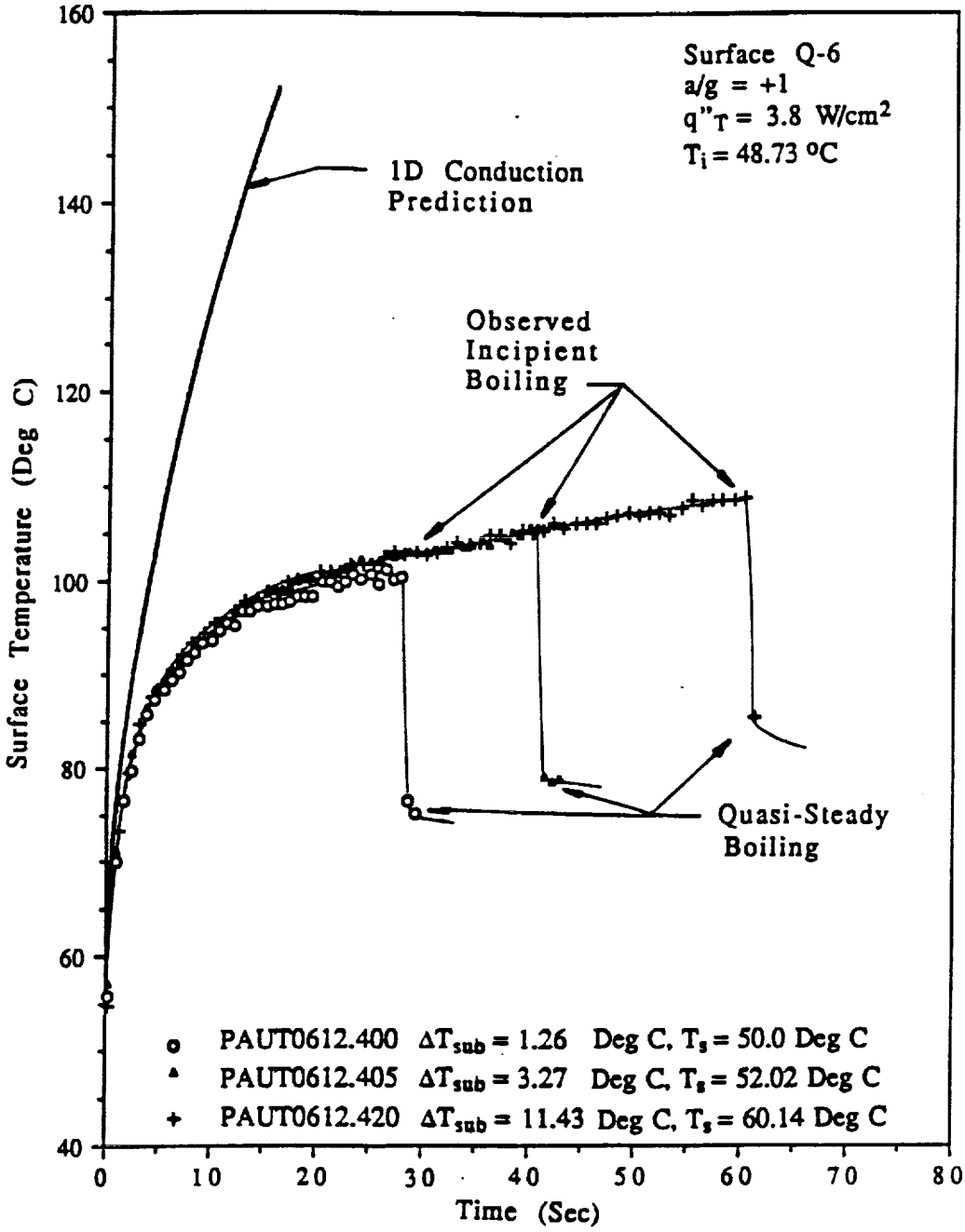

Figure 5.7 Effect of subcooling on the thin film surface temperature with a/g = +1

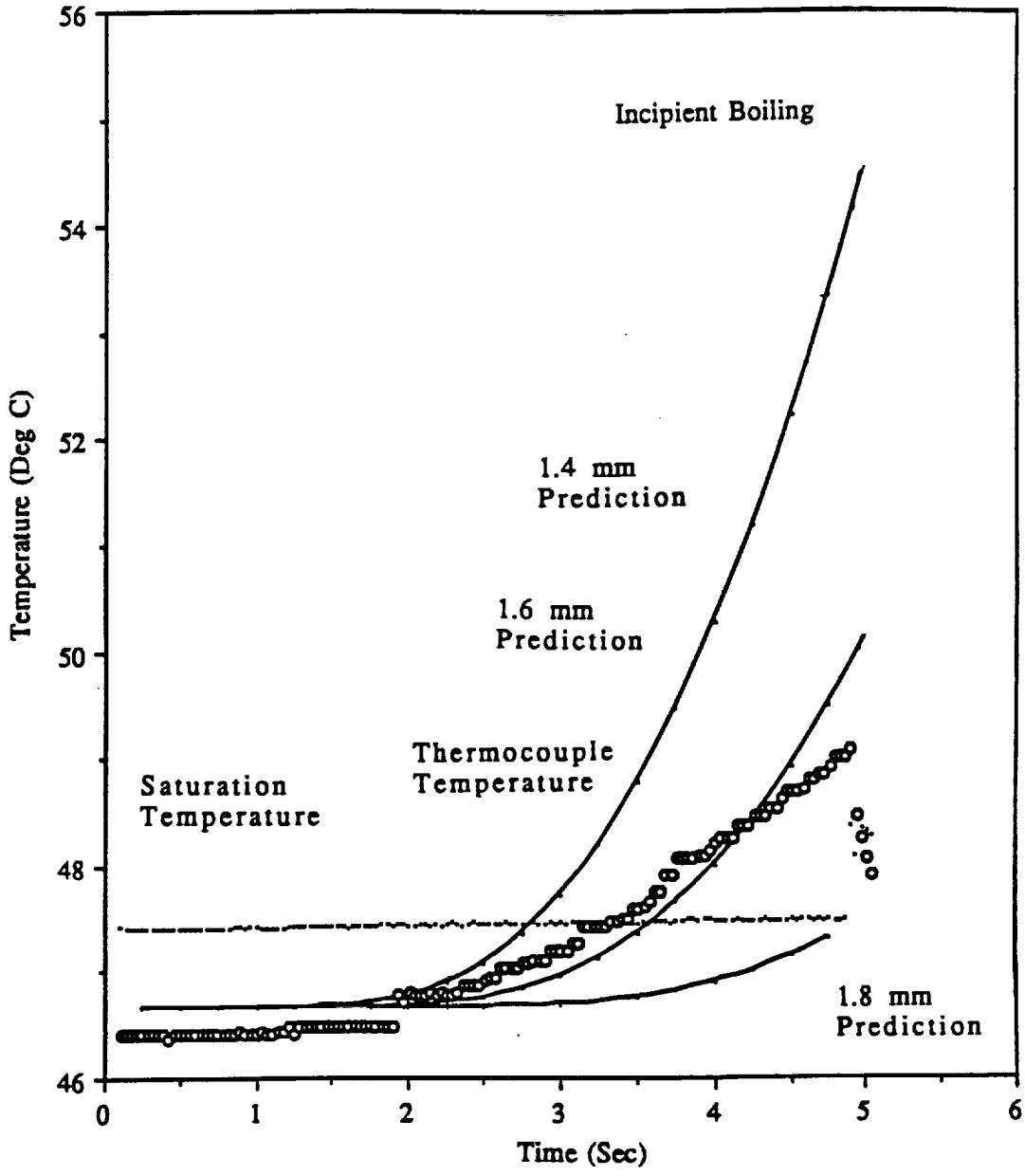

Figure 5.8 Effect of uncertainty in thermocouple location on computed liquid temperature with measured thermocouple temperature

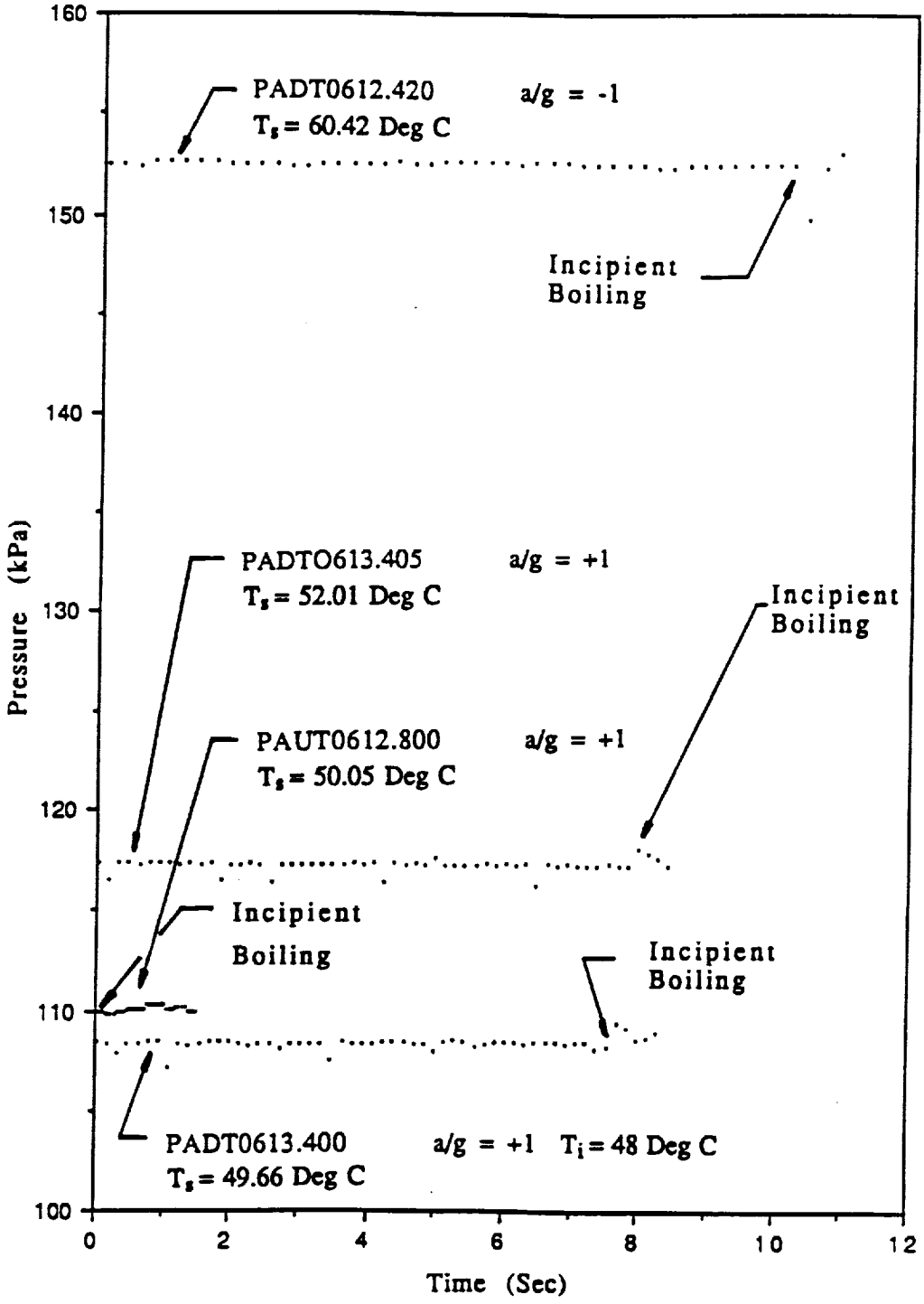

Figure 5.9 Representative pressure transducer measurements from the laboratory pool boiling vessel

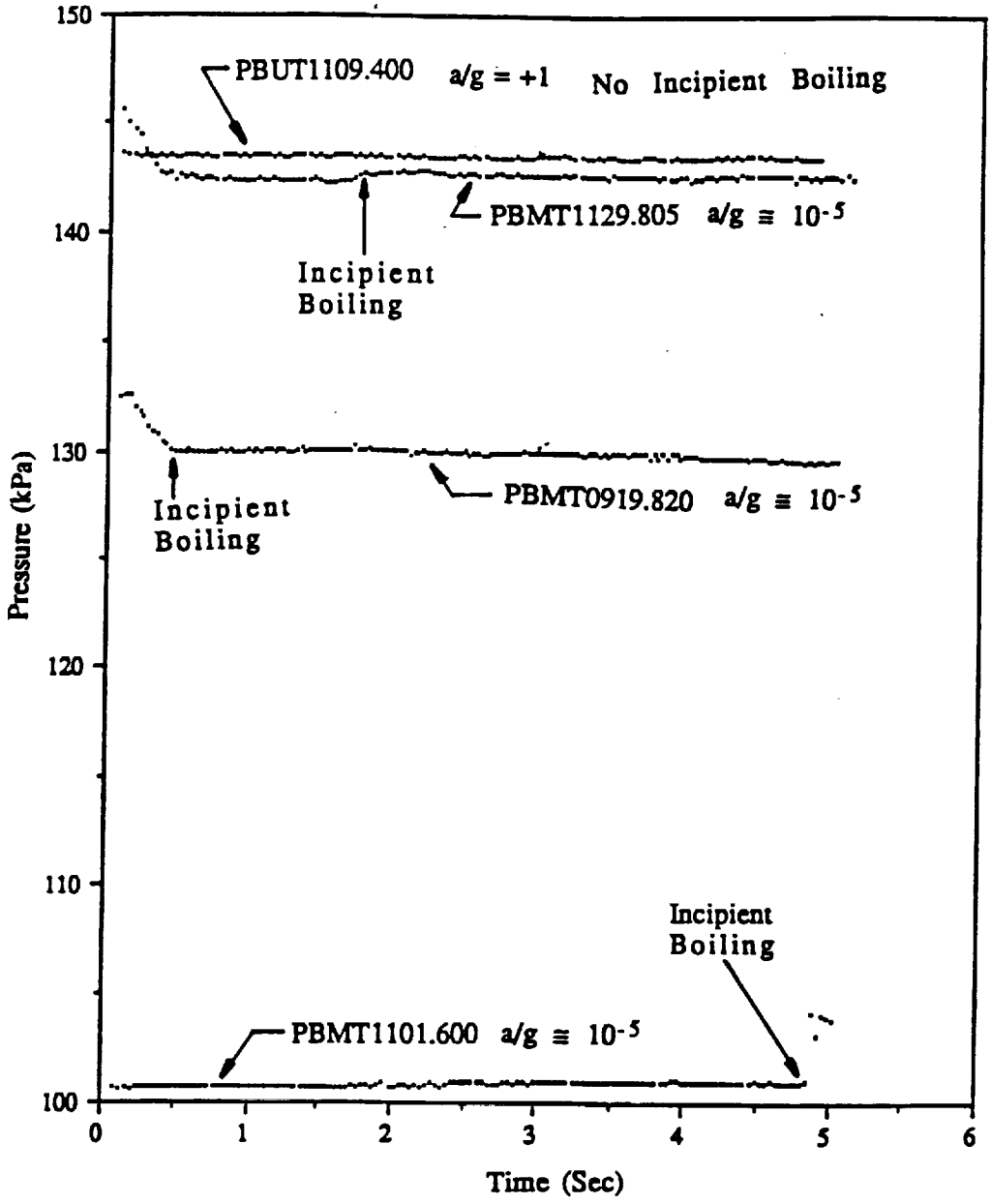

Figure 5.10 Representative pressure transducer measurements from the drop vessel at $a/g \equiv 10^{-5}$ and $a/g = +1$

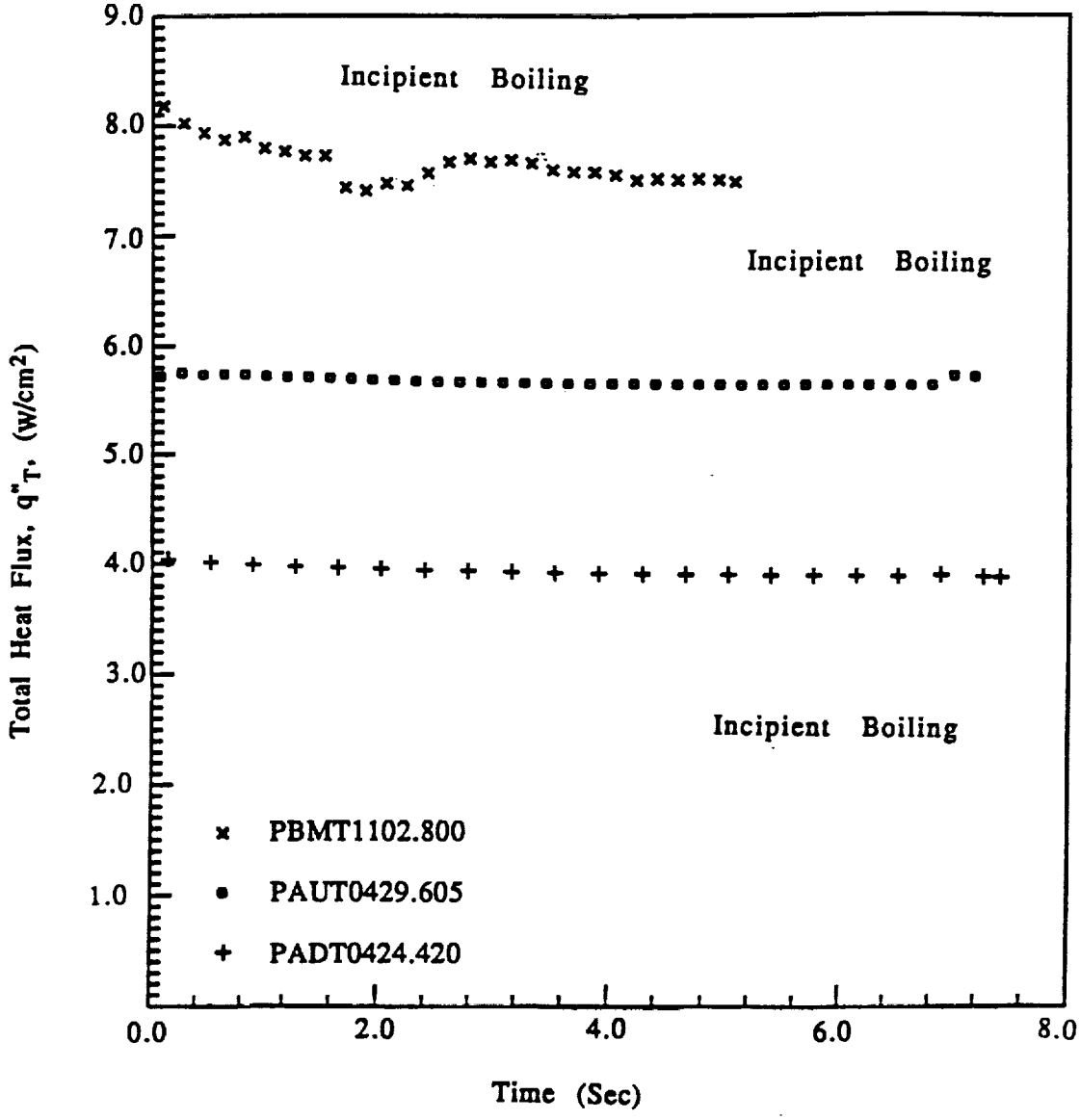

Figure 5.11 Representative measurements of the constant imposed total heat flux from the laboratory and drop vessels

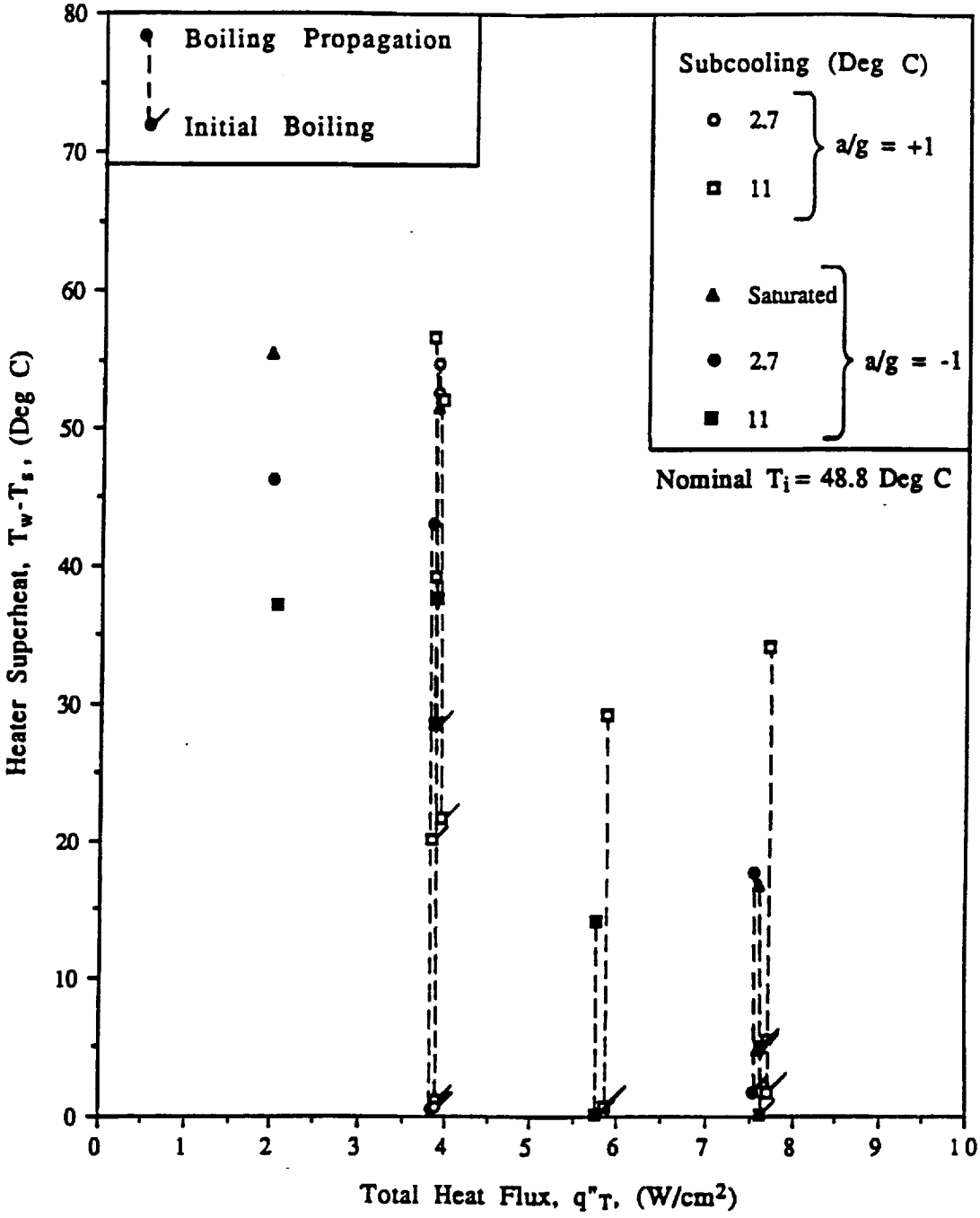

Figure 5.12 Heater surface superheat at incipient boiling with constant imposed heat flux, surface Q-1

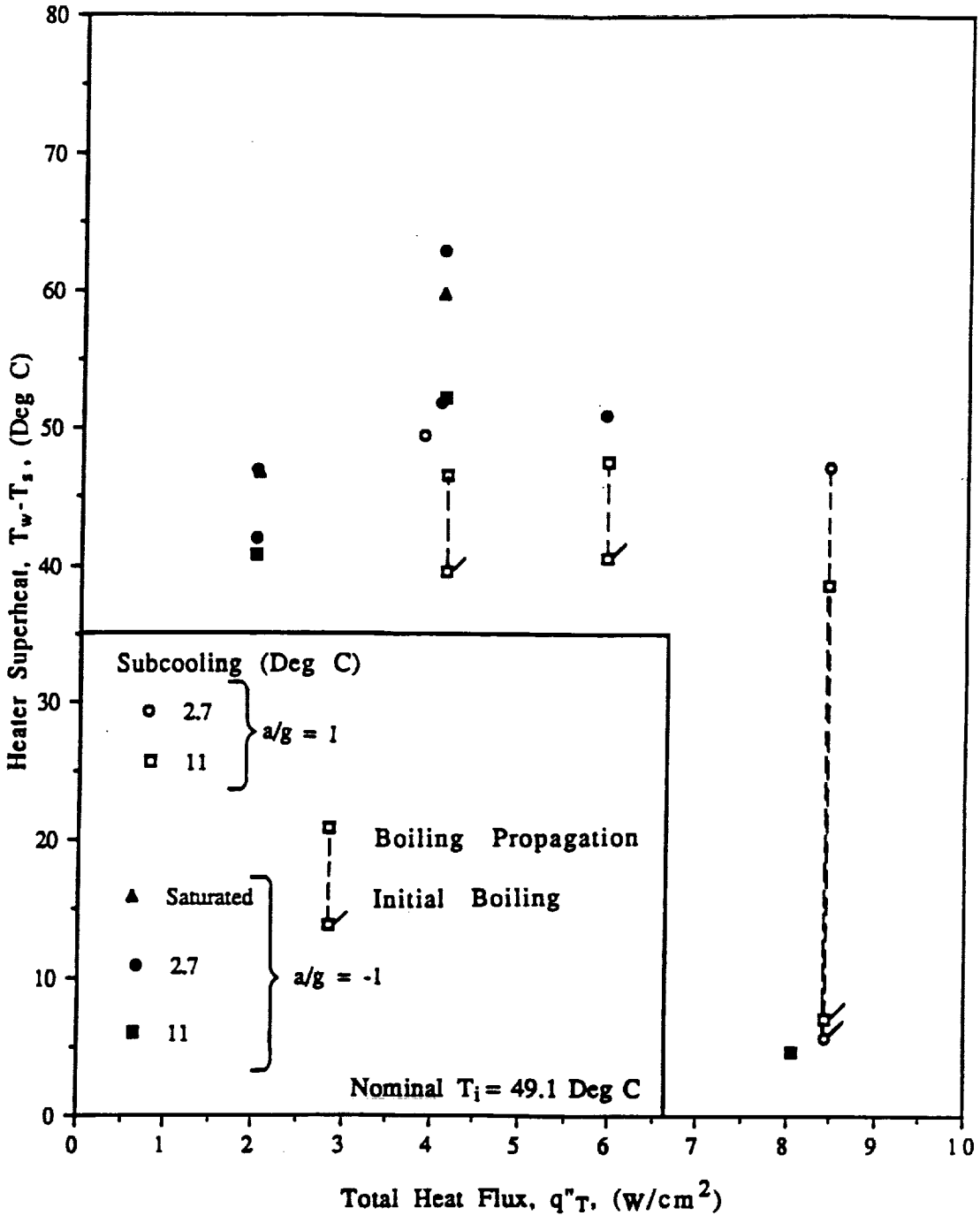

Figure 5.13 Heater surface superheat at incipient boiling with constant imposed heat flux, surface Q-2

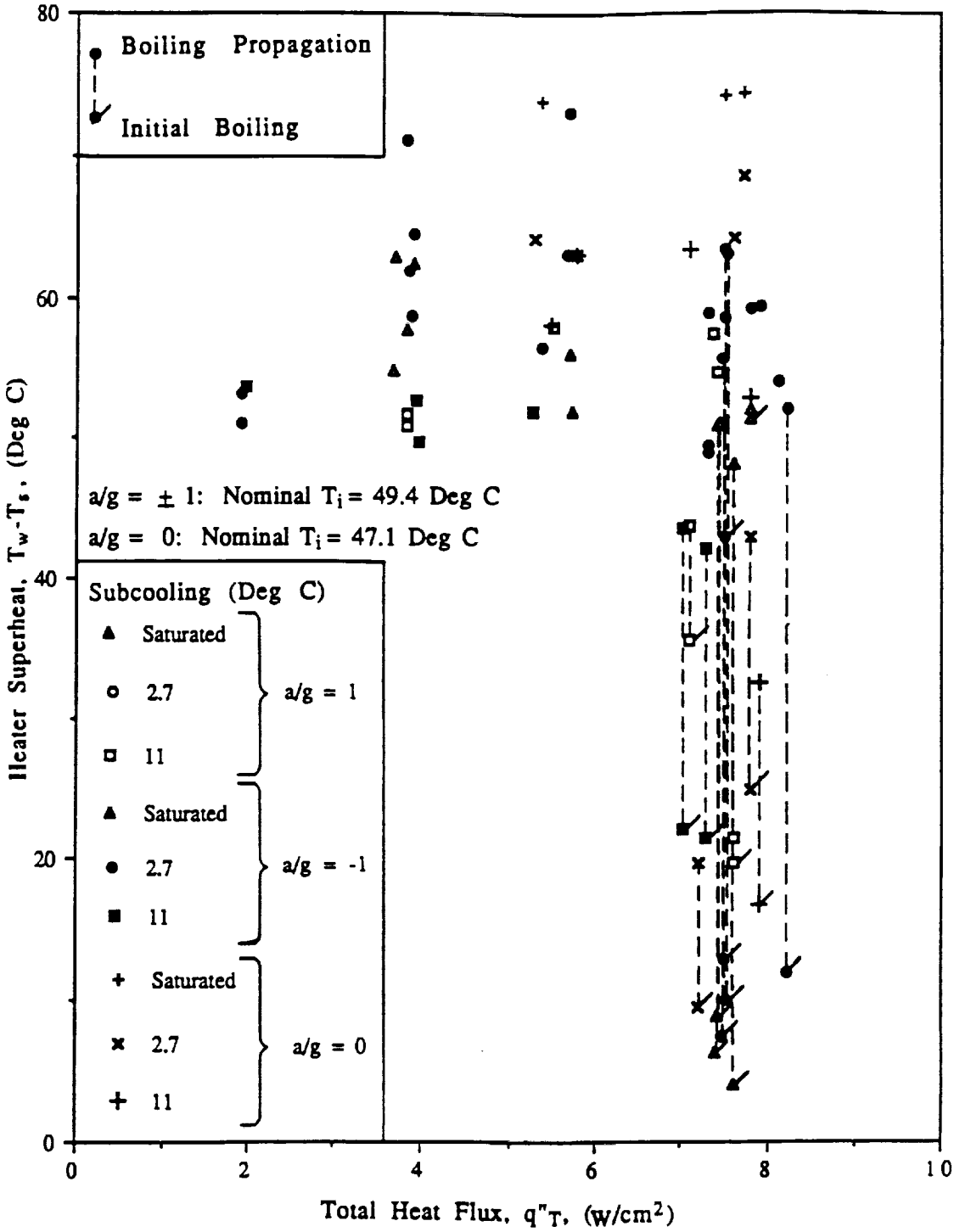

Figure 5.14 Heater surface superheat at incipient boiling with constant imposed heat flux, surface Q-5

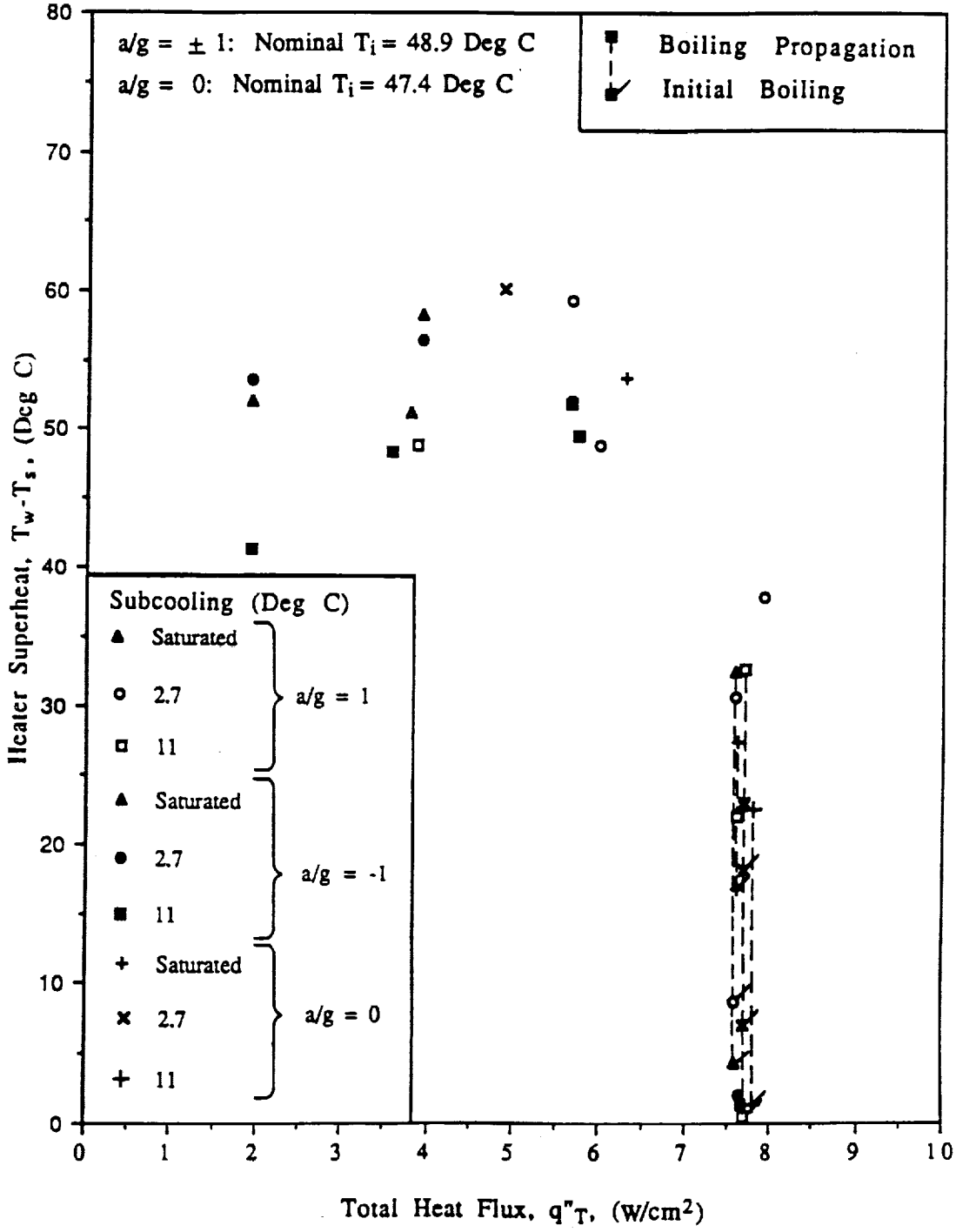

Figure 5.15 Heater surface superheat at incipient boiling with constant imposed heat flux, surface Q-6

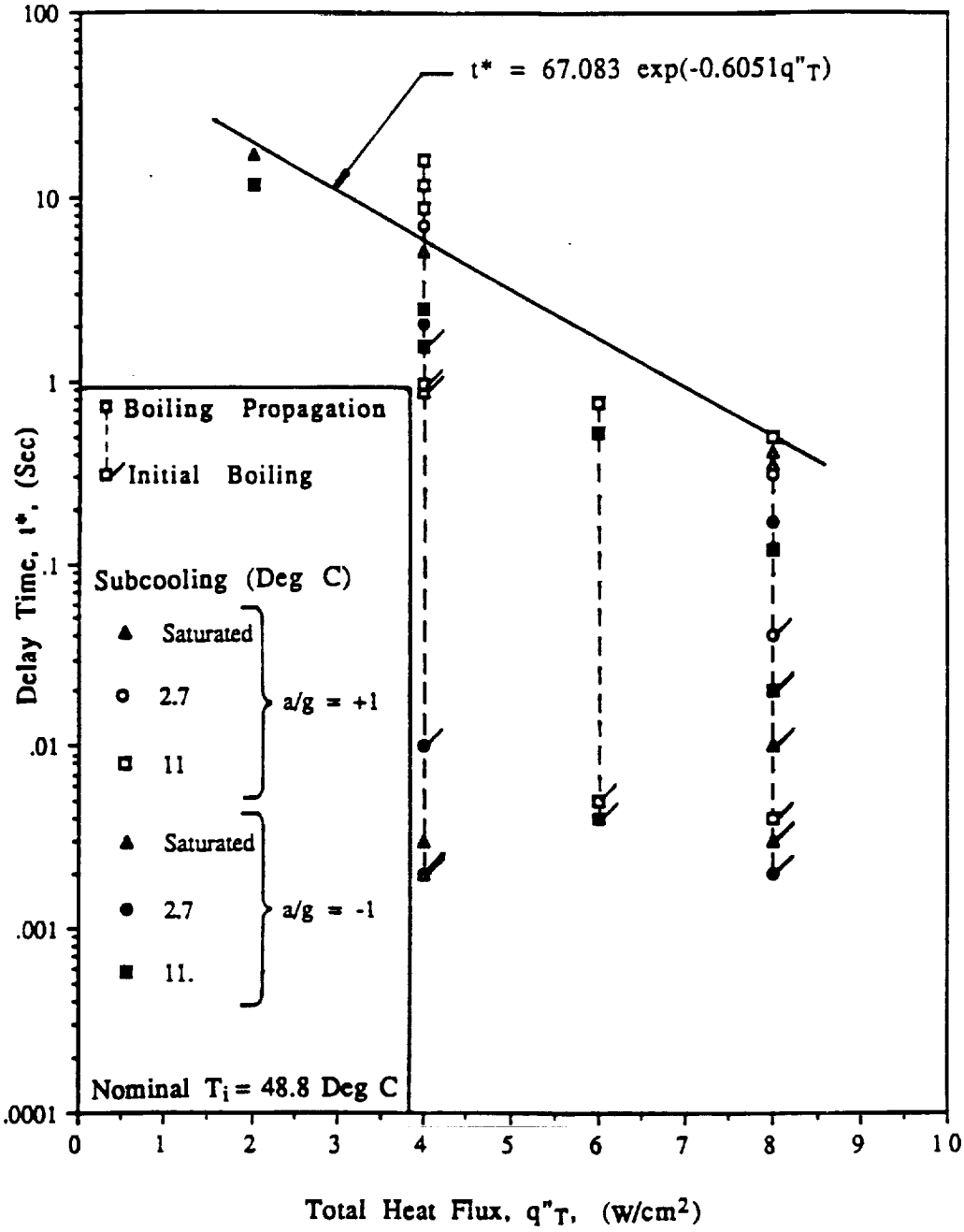

Figure 5.16 Incipient boiling delay time with constant imposed heat flux, surface Q-1

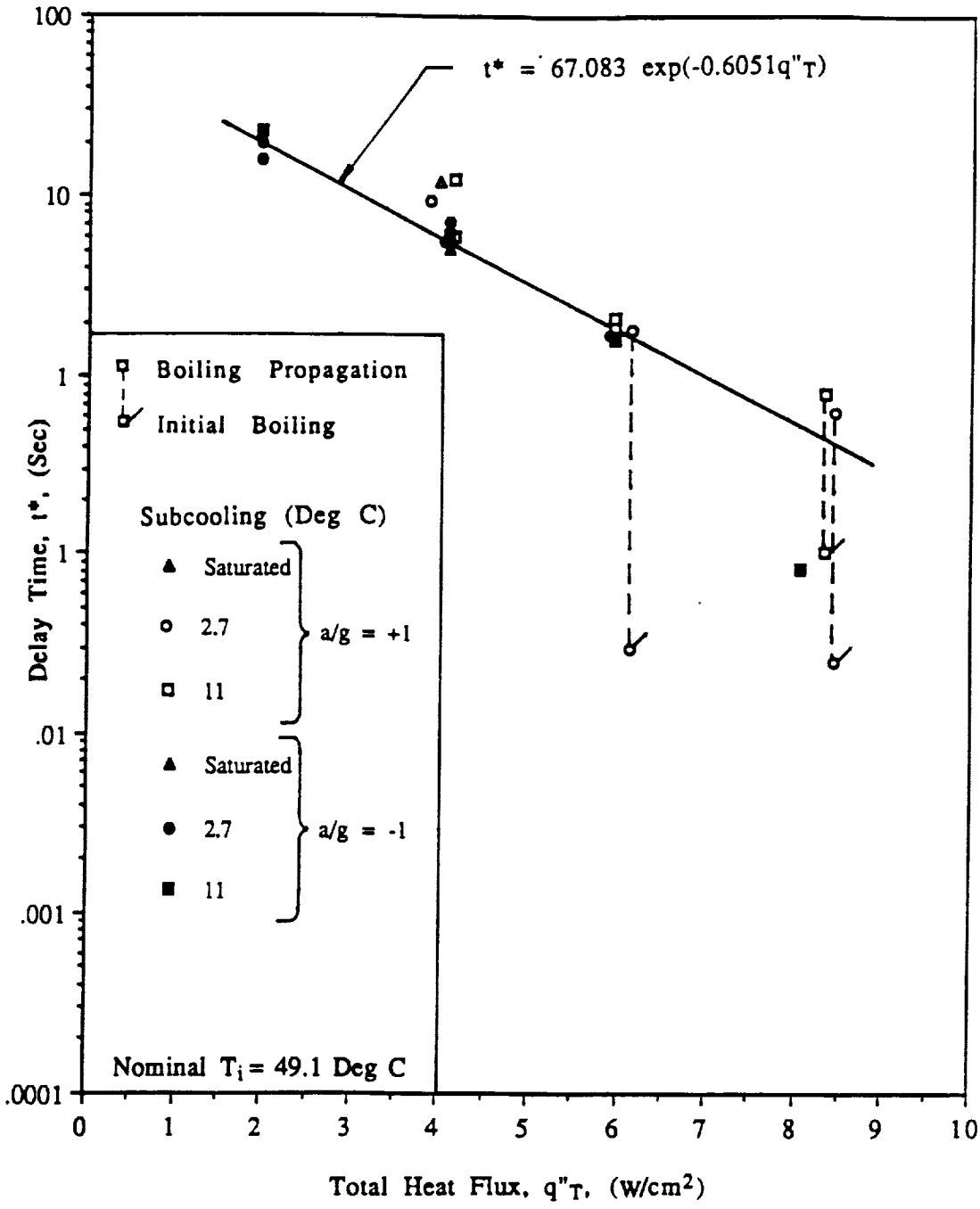

Figure 5.17 Incipient boiling delay time with constant imposed heat flux, surface Q-2

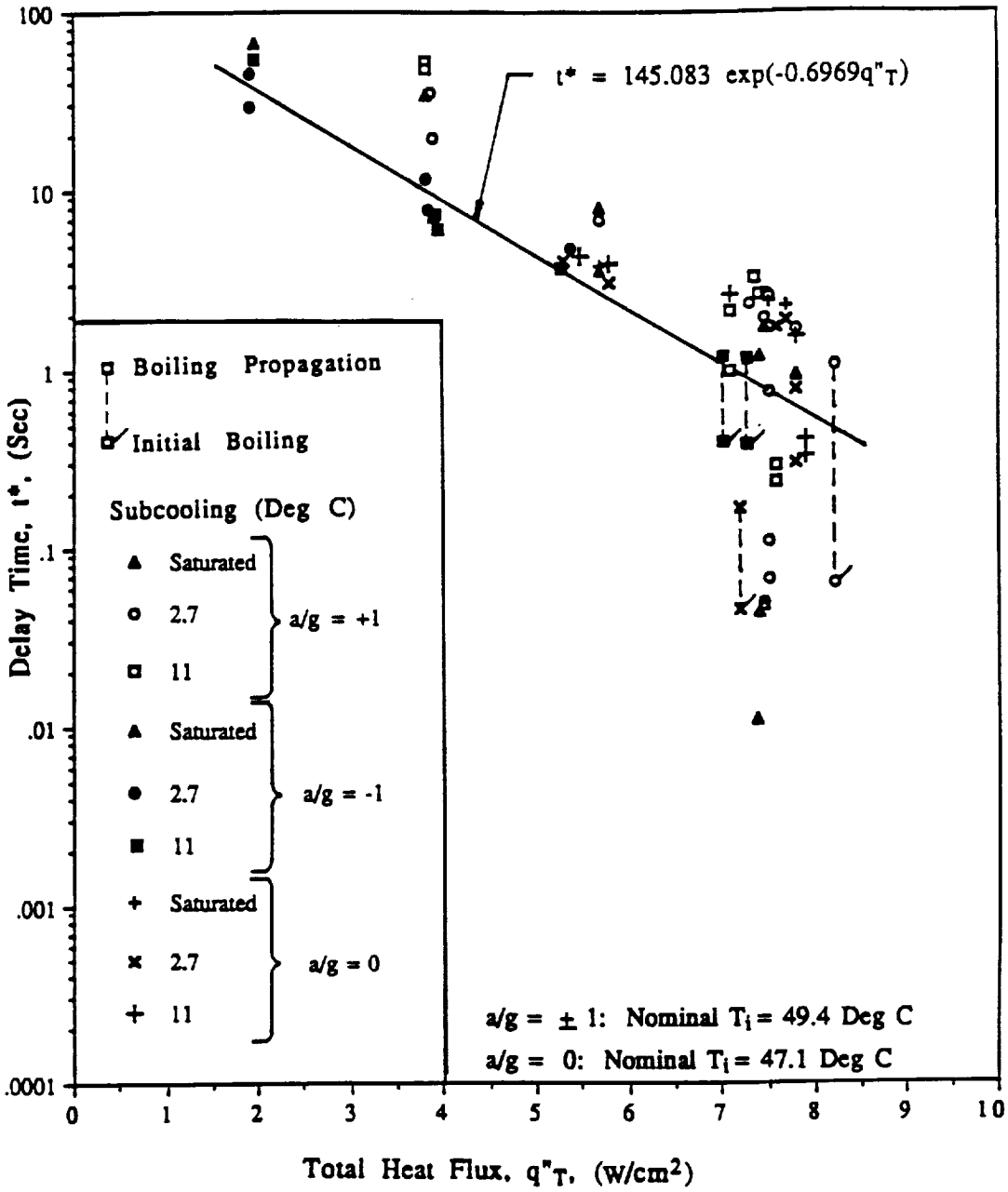

Figure 5.18 Incipient boiling delay time with constant imposed heat flux, surface Q-5

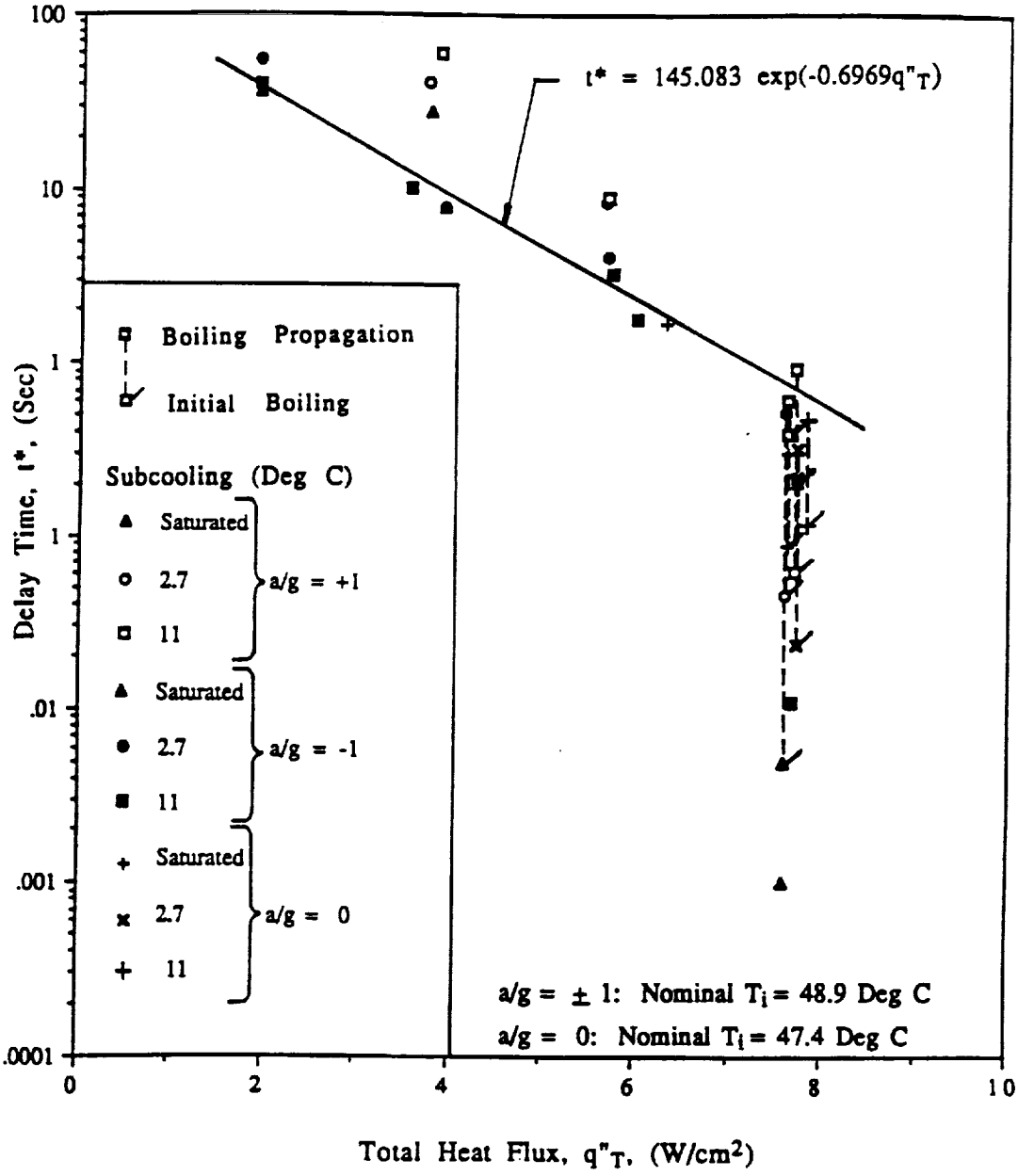

Figure 5.19 Incipient boiling delay time with constant imposed heat flux, surface Q-6

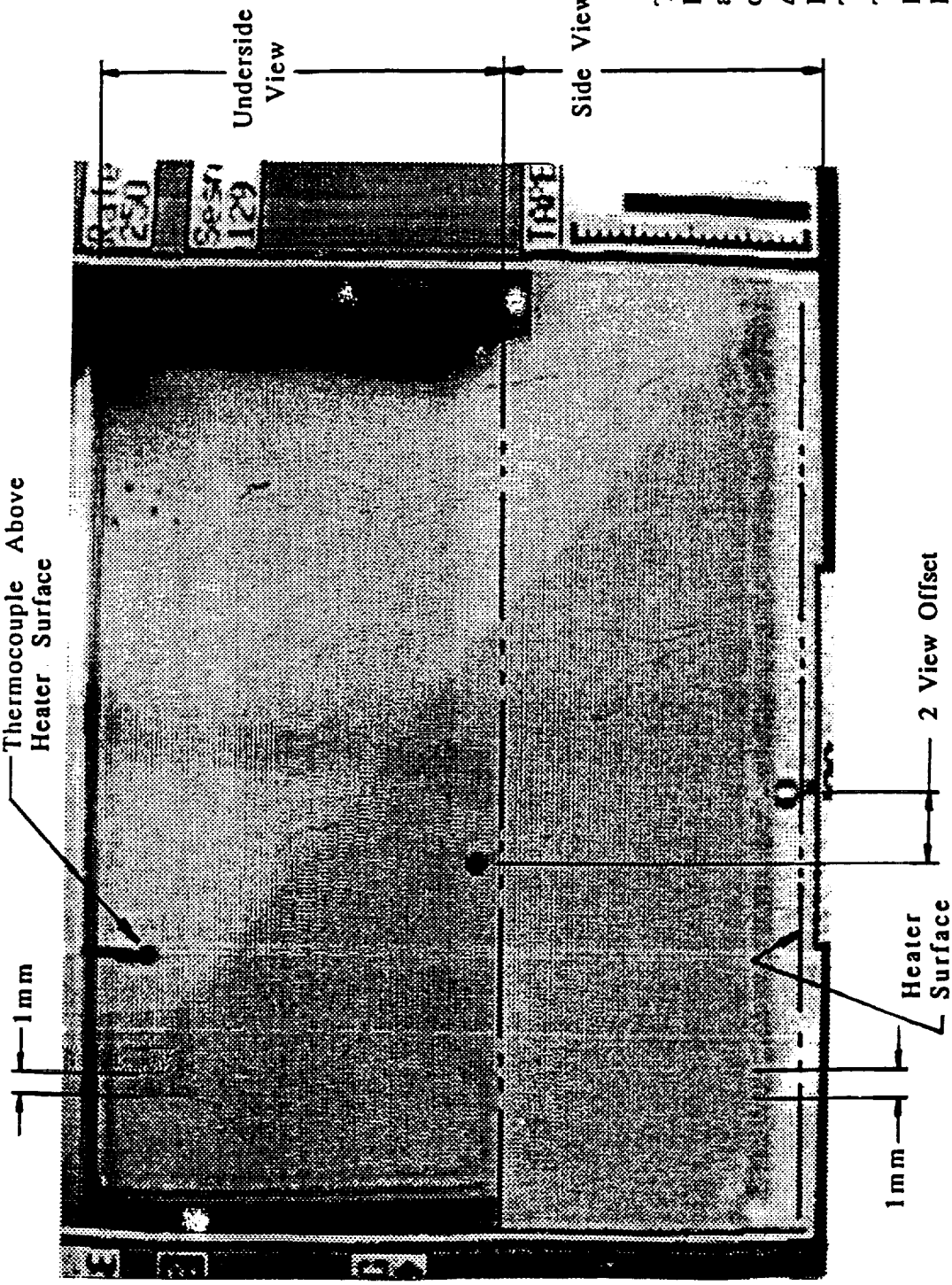

Figure 5.20a Category A: appearance of the initial vapor bubble, time = 0.894 sec

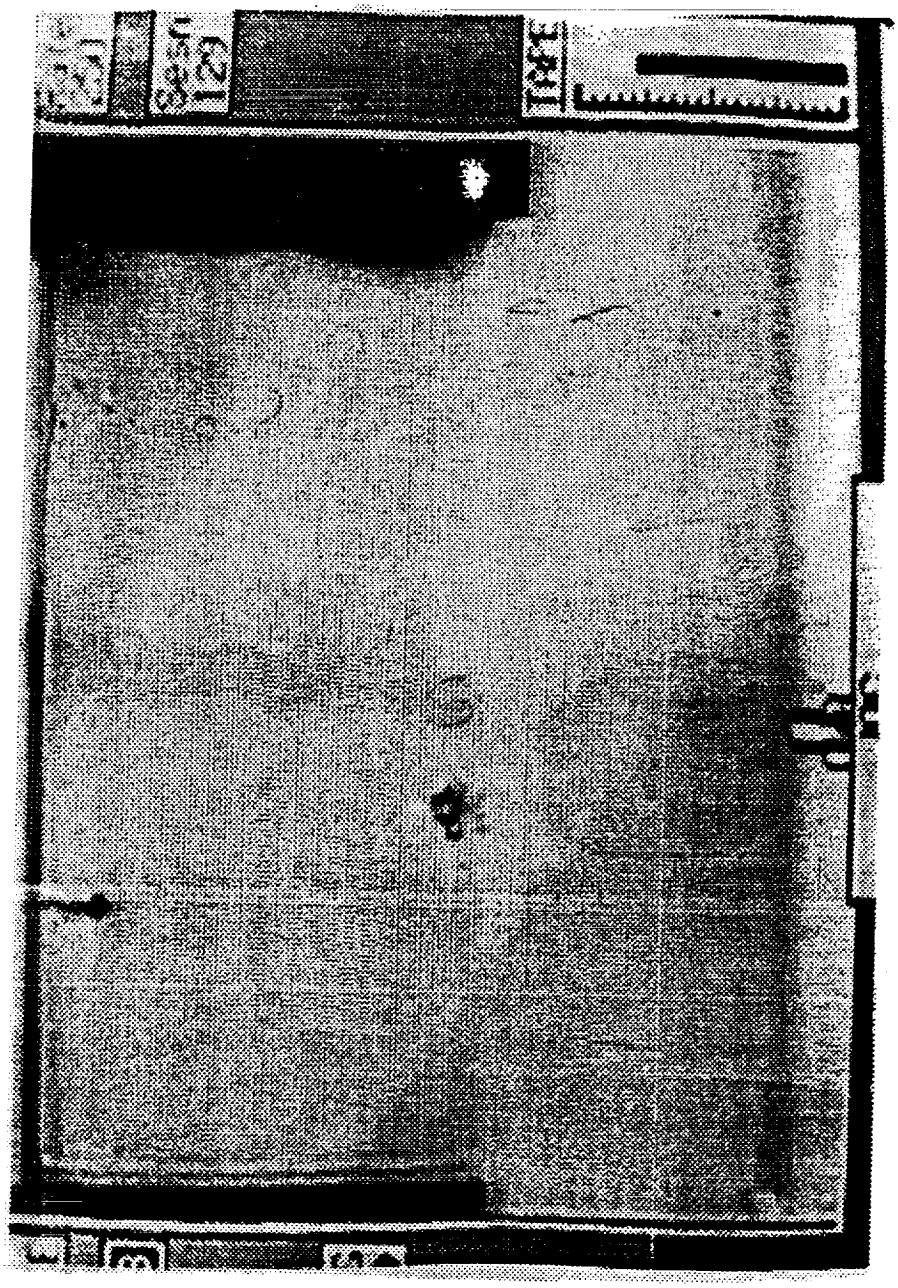

Figure 5.20b Category A: vapor bubbles immediately after the boiling propagation has begun, time = 0.934 sec

Figure 5.20c Category A: convection cells with propagating vapor, time = 1.126 sec

Figure 5.20d Category A: vapor propagating outward, time = 1.306 sec

Figure 5.20c Category A: vapor covering nearly the entire heating surface. Large bubbles visible from coalescing of smaller ones, time = 1.498 sec

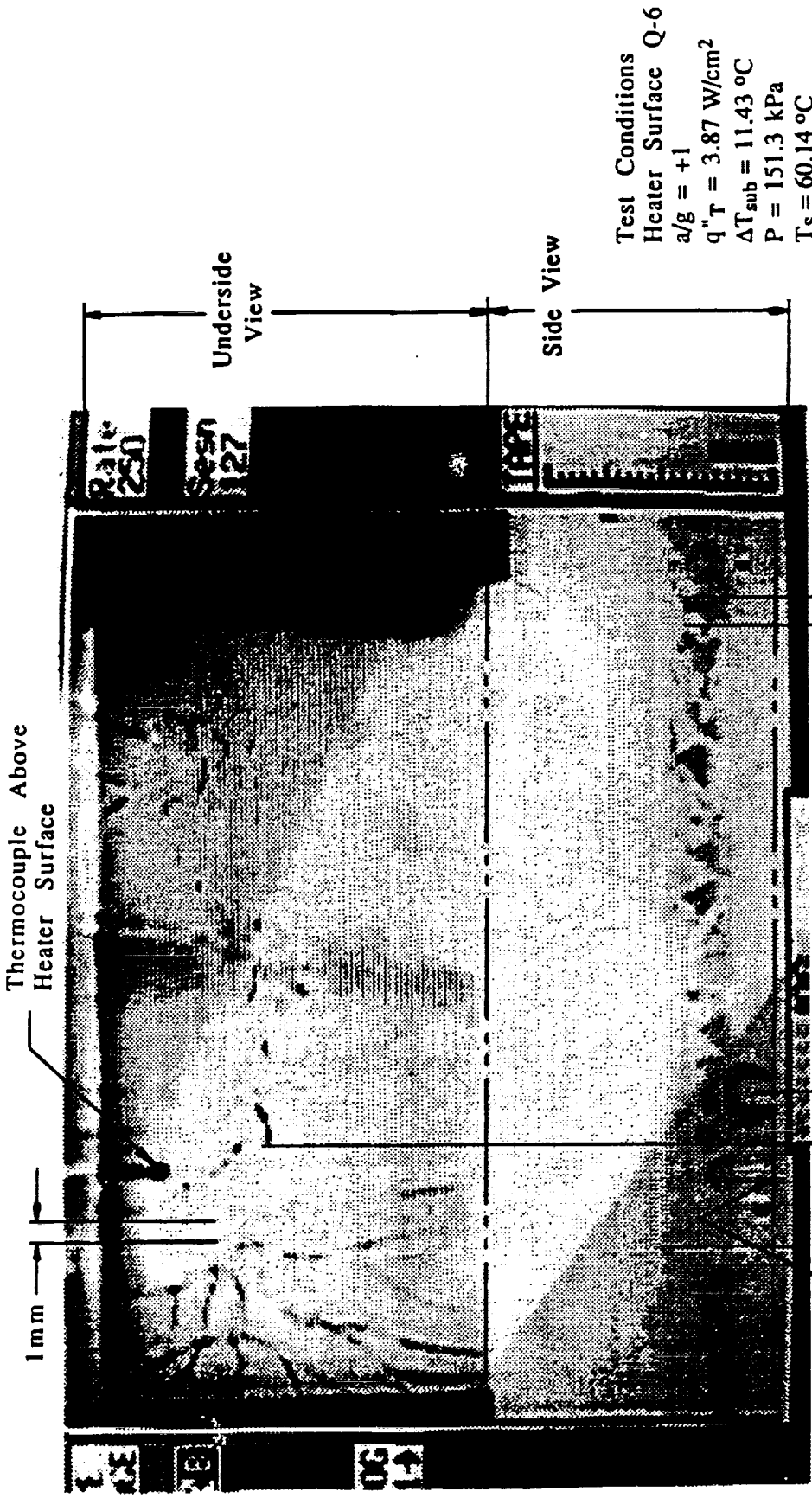

Figure 5.21a Category B: appearance of the initial vapor bubble with convection cells, time = 0.237 sec

Figure 5.21b Category B: boiling propagation with large bubble at the center of thin vapor layer, time = 0.249 sec

Figure 5.21c Category B: the thin vapor layer has advanced outward radially, time = 0.257 sec

Figure 5.21d Category B: heater surface is nearly covered by vapor mass and the large bubble departs upward from the surface, time = 0.289 sec

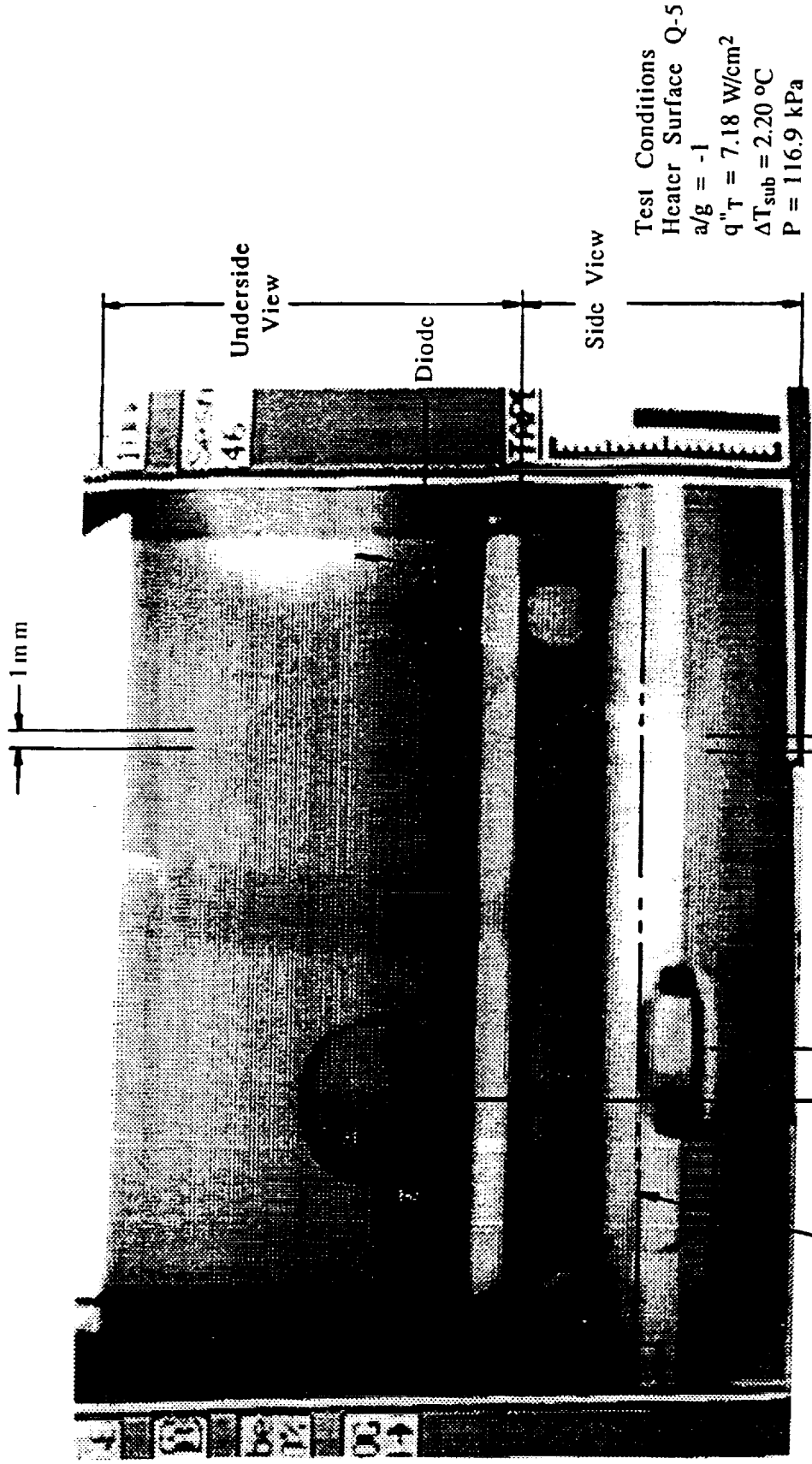

Figure 5.22a Category C: initial bubble with "smooth" interface growing with another smaller bubble located at the site of origin of the initial bubble, time = 0.335 sec

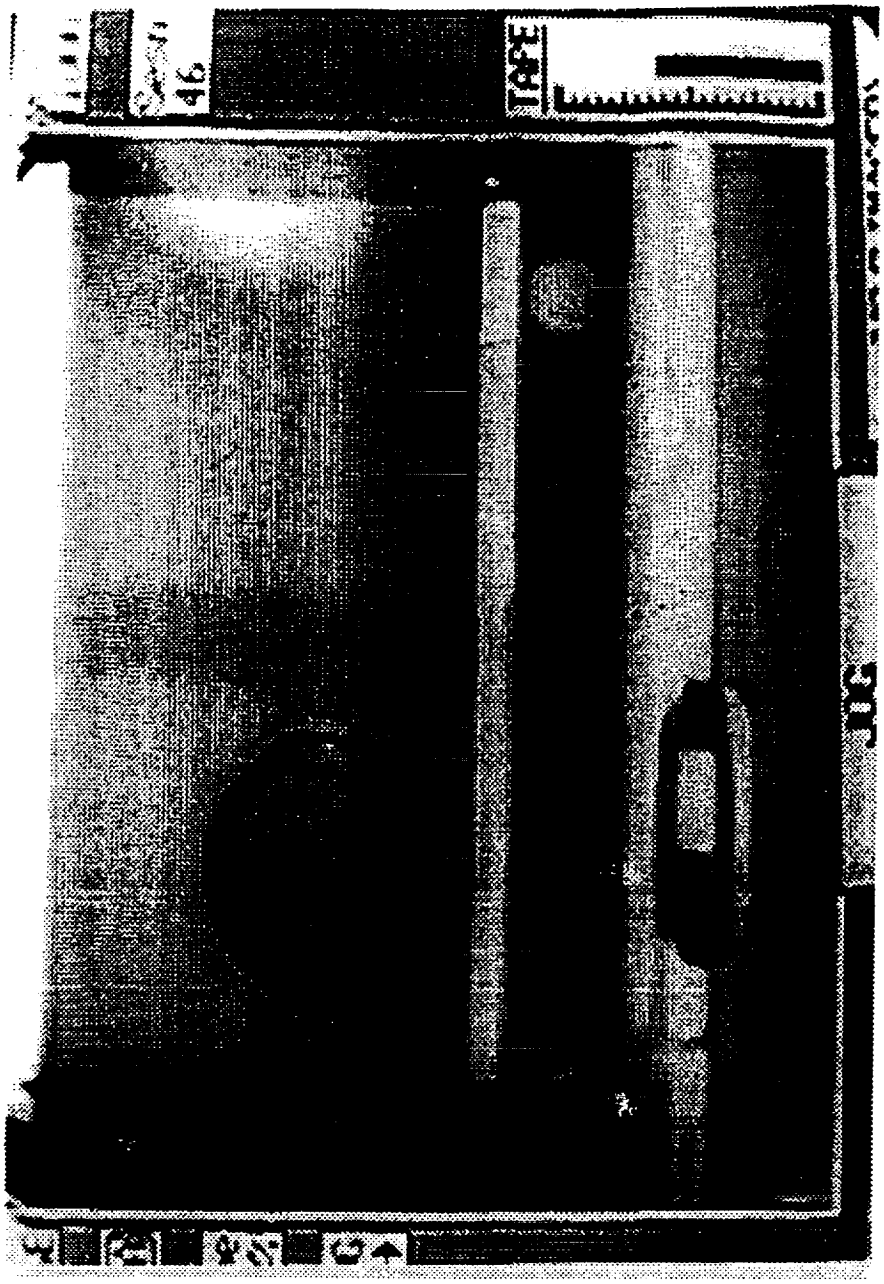

Figure 5.22b Category C: the two bubbles growing and moving from their site of origin, time = 0.419 sec

Figure 5.22c Category C: the two bubbles have coalesced into one, time = 0.505 sec

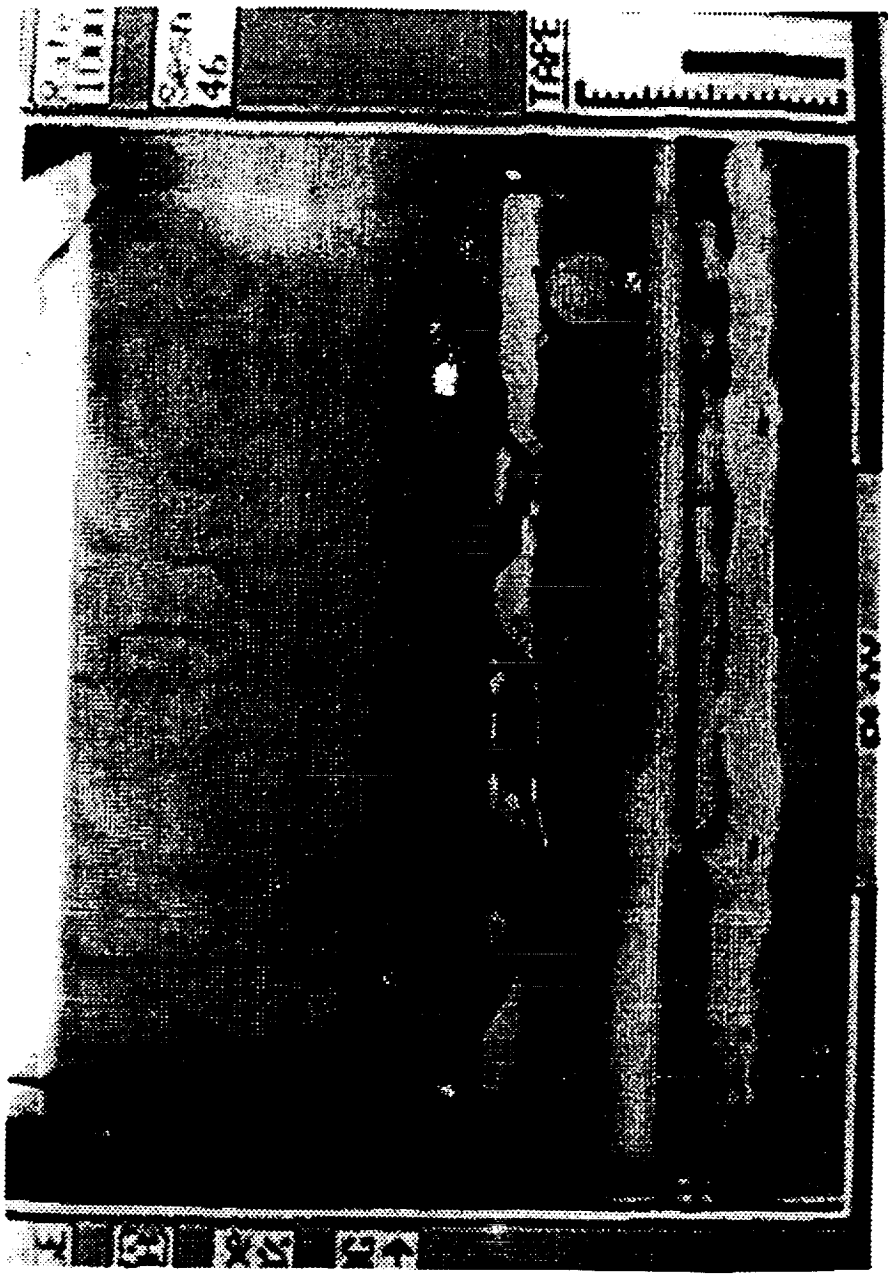

Figure 5.22d Category C: the single vapor bubble with a "wavy" interface remains at the heated surface, time = 1.151 sec

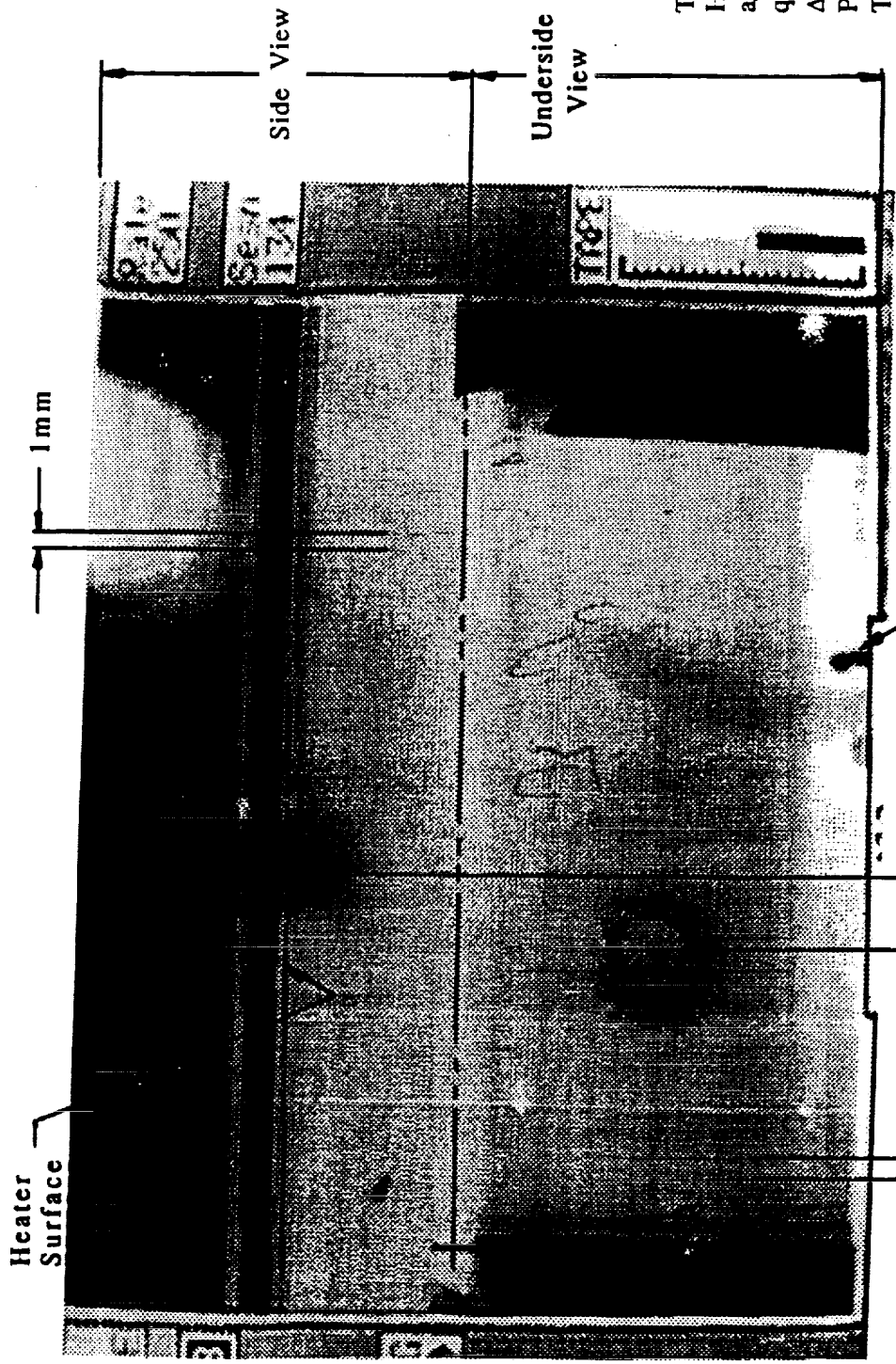

Figure 5.23a Category D: the single bubble has ruptured at the periphery of the bubble base and boiling propagation has started, time = 10.214 sec

Figure 5.23b Category D: large-scale satellite interface bubbles with the vapor pushed downward away from the heating surface, time = 10.226 sec

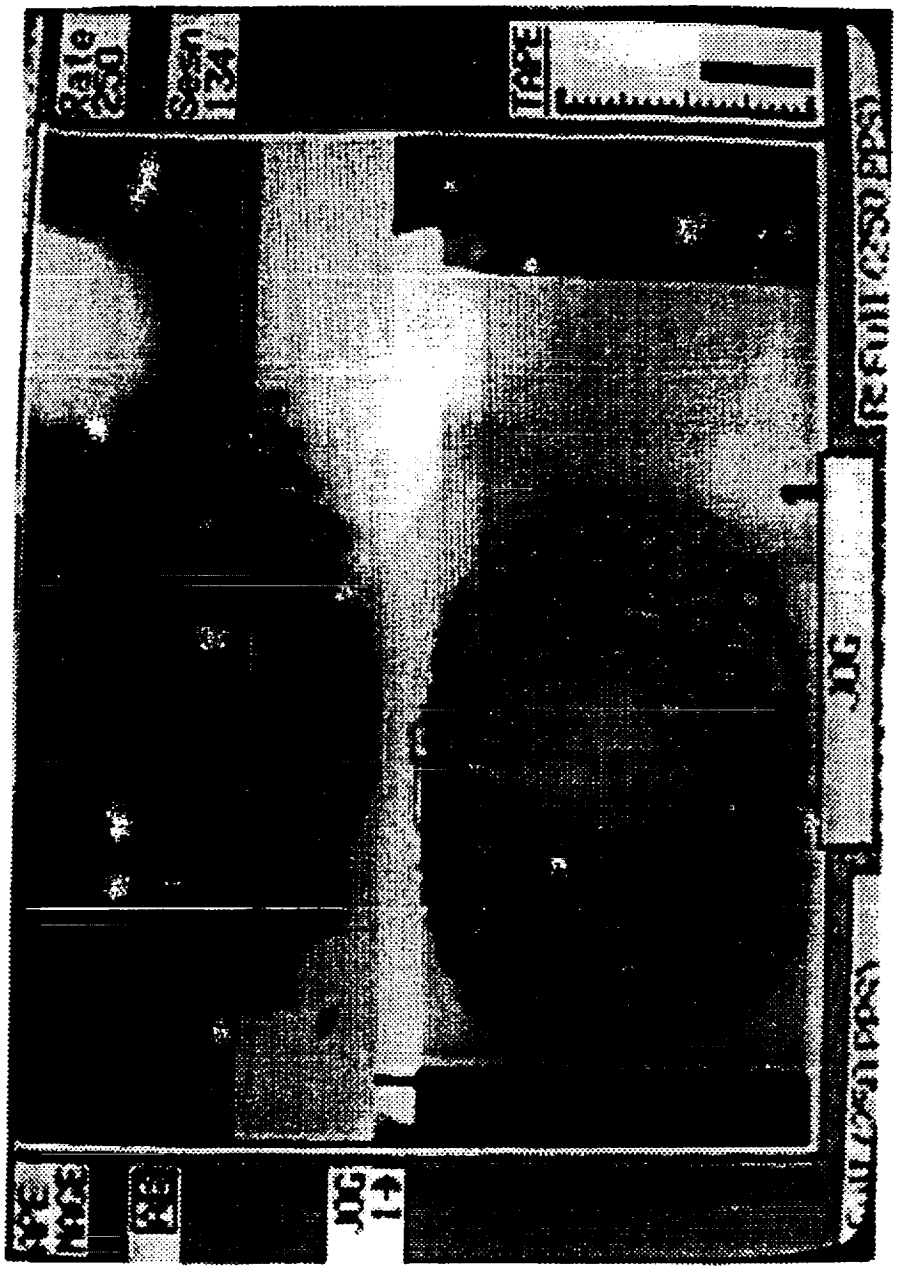

Figure 5.23c Category D: the heater surface is nearly covered by vapor, time = 10.238 sec

Figure 5.23d Category D: the single bubble remains at the heated surface with bubbles on parts of the larger bubble interface, time = 10.270 sec

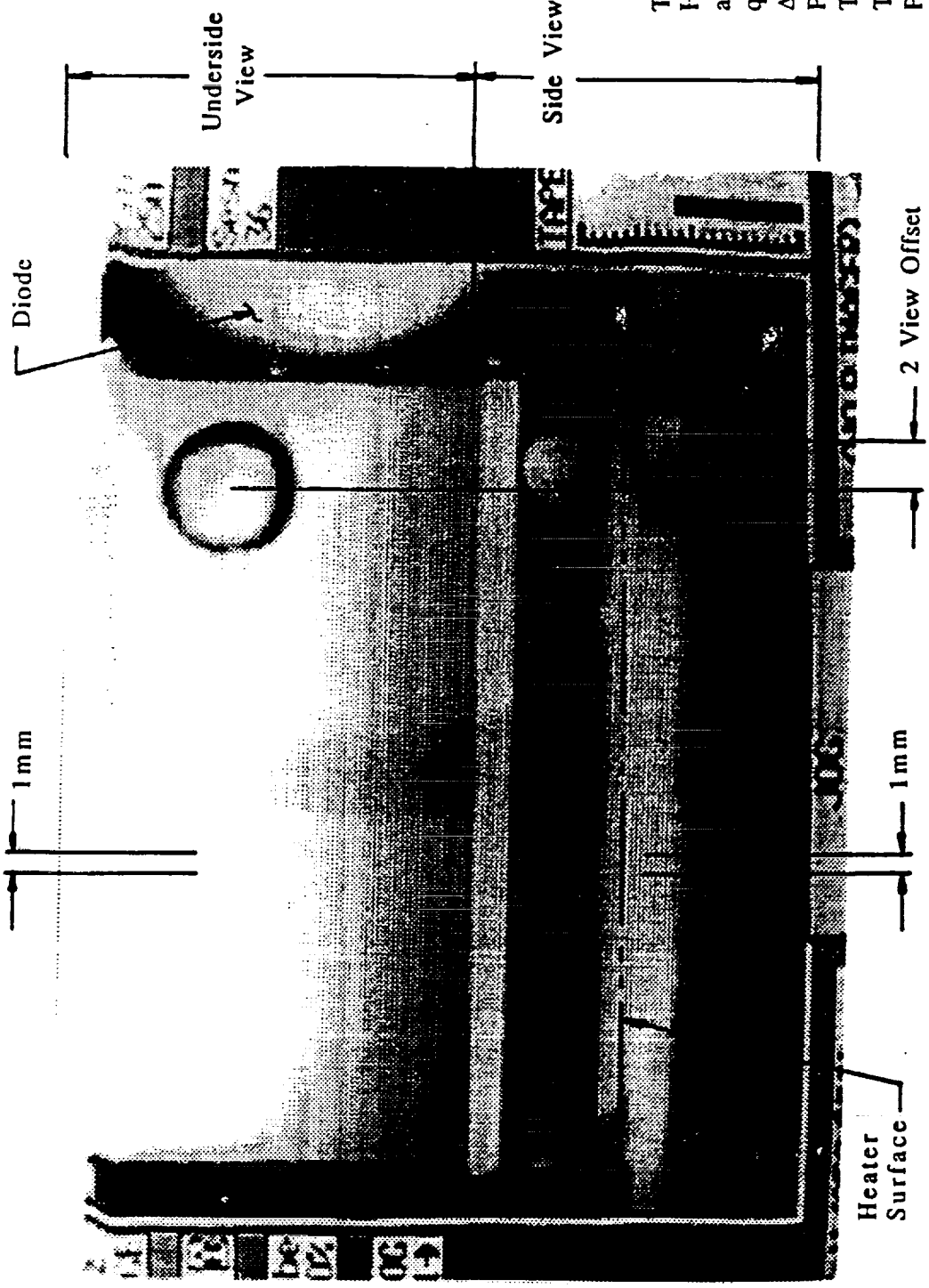

Figure 5.24a Category D: rupturing of the bubble interface is beginning, time = 28.890 sec

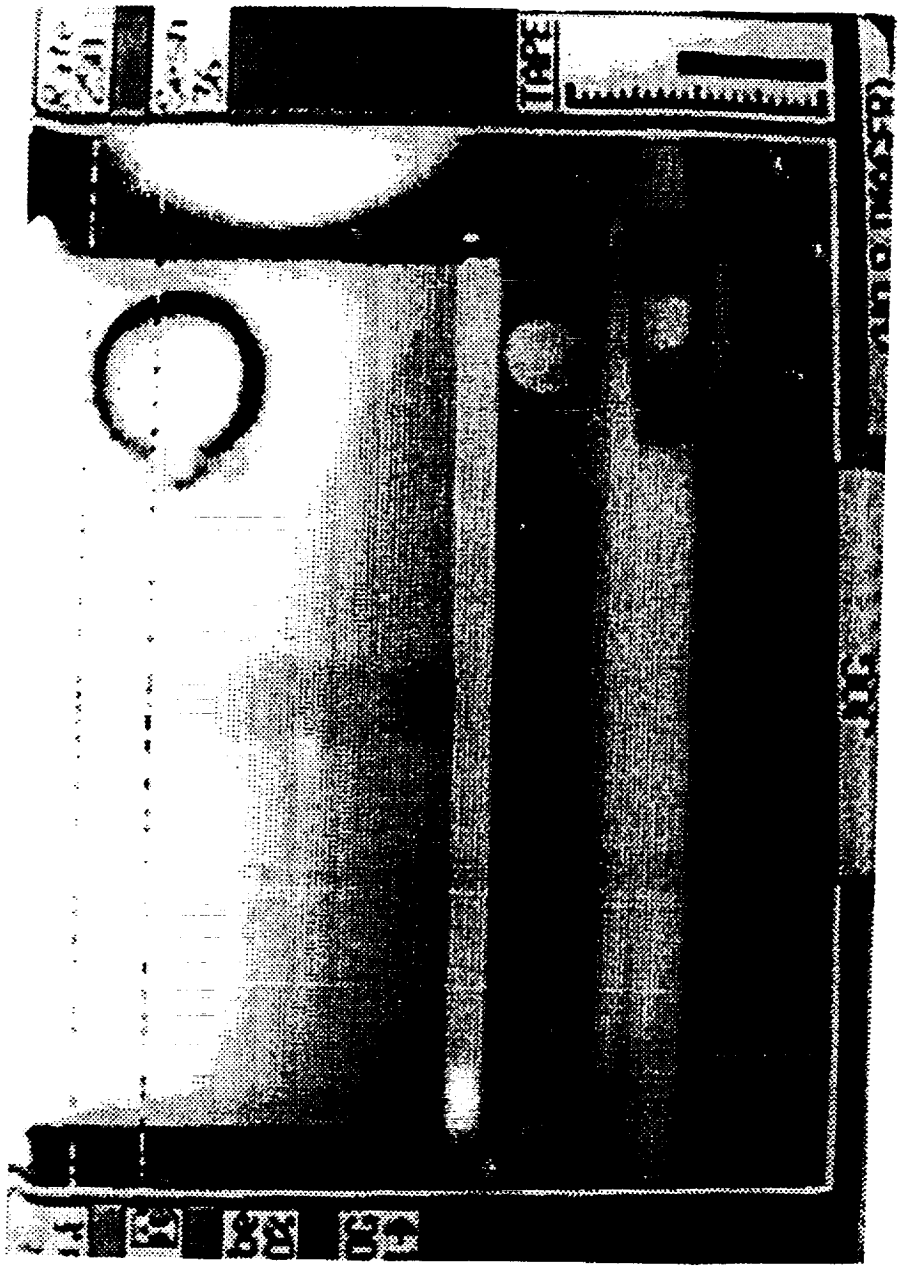

Figure 5.24b Category D: vapor moves outward from bubble interface disturbance, time = 28.894 sec

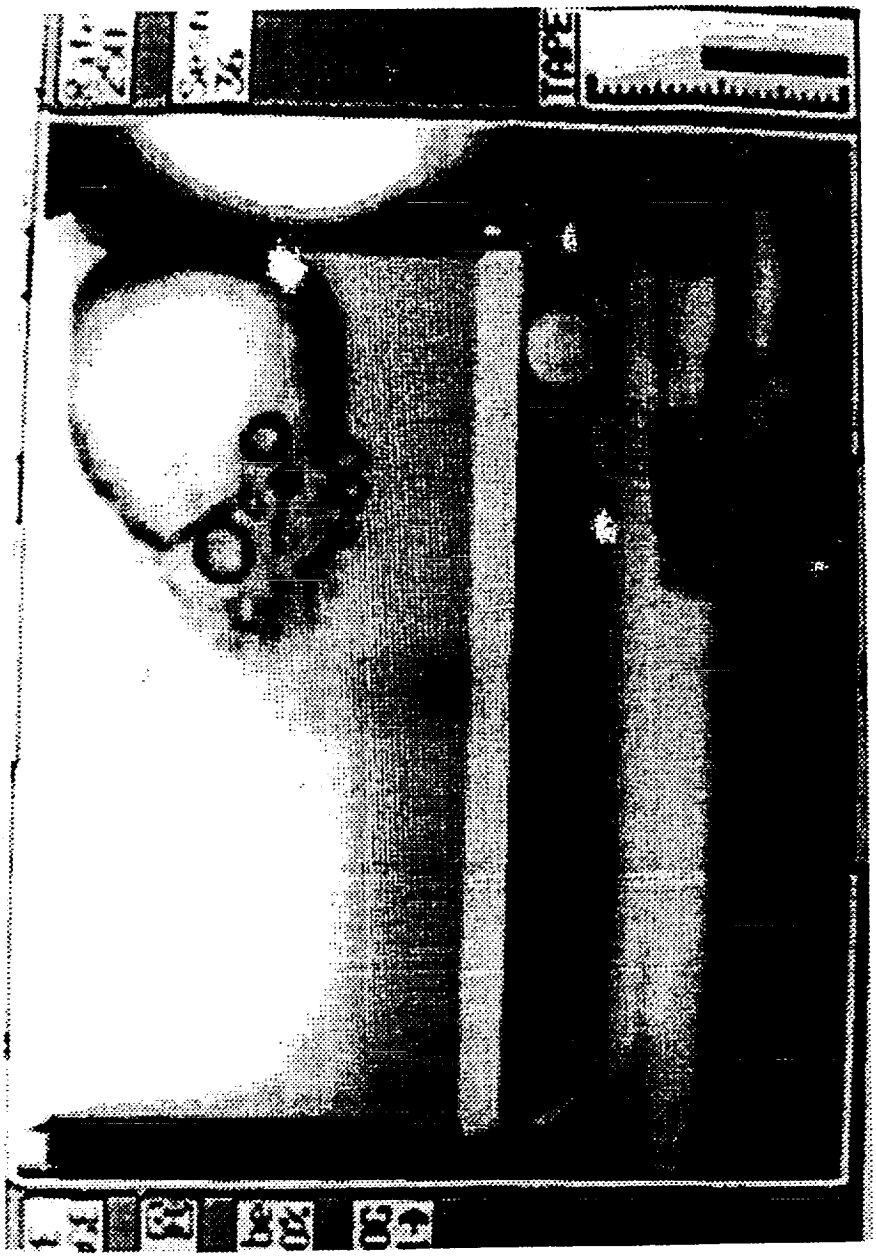

Figure 5.24c Category D: smaller bubbles are on the outwardly moving vapor mass, time = 28.910 sec

Figure 5.24d Category D: the vapor mass with interface bubbles has nearly covered the heater surface, time = 28.946 sec

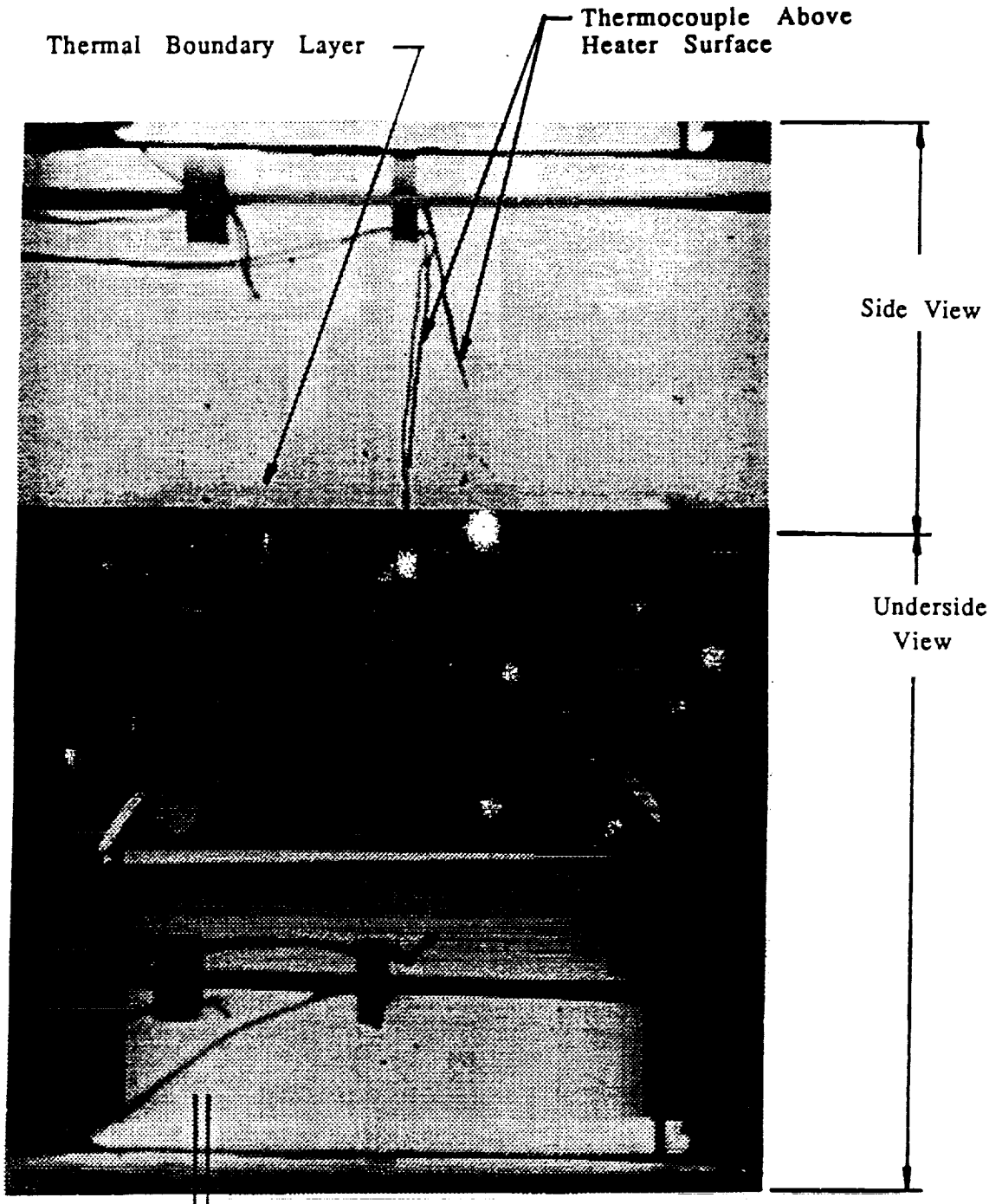

Figure 5.25a Category E: incipient boiling in the presence of the conduction thermal boundary layer, time = 1.130 sec

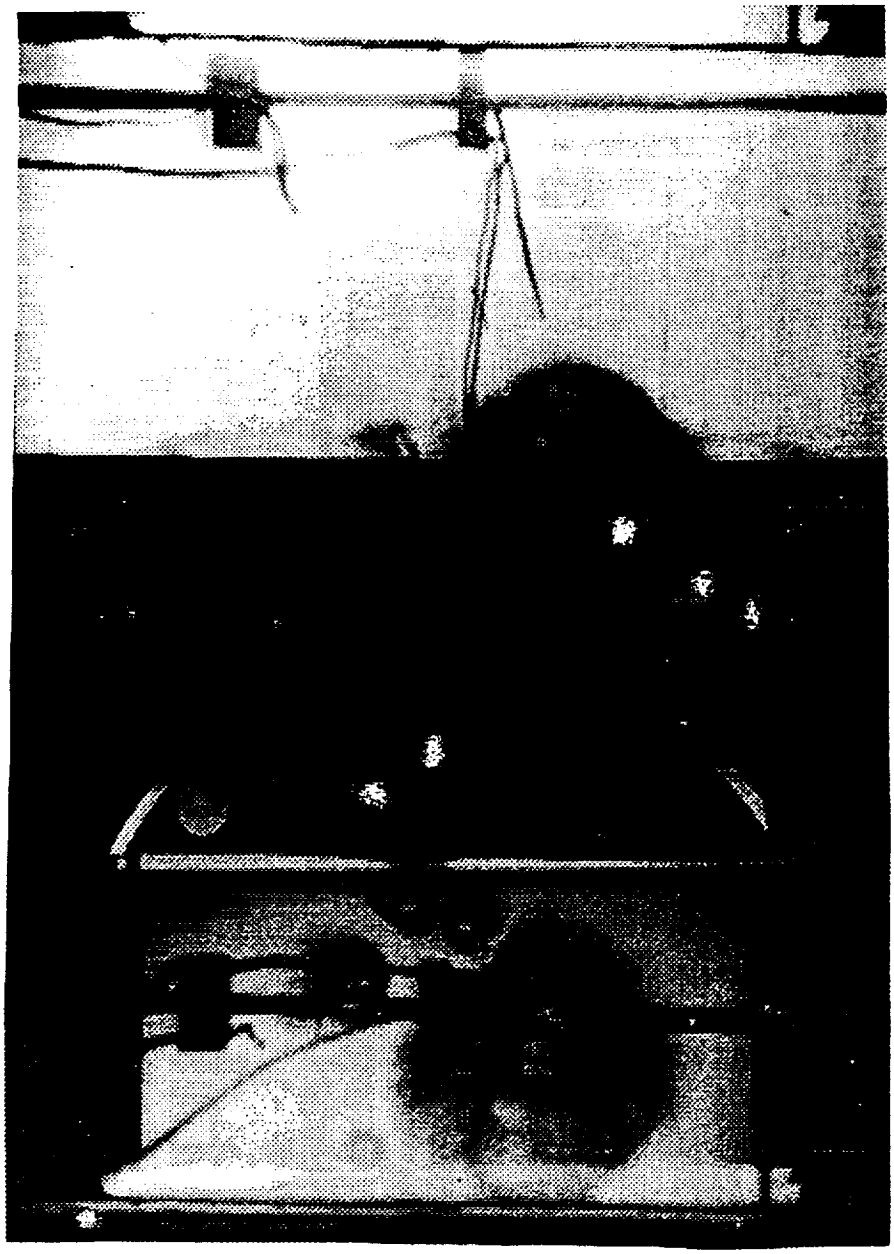

Figure 5.25b Category E: boiling at five different locations, time = 4.813 sec

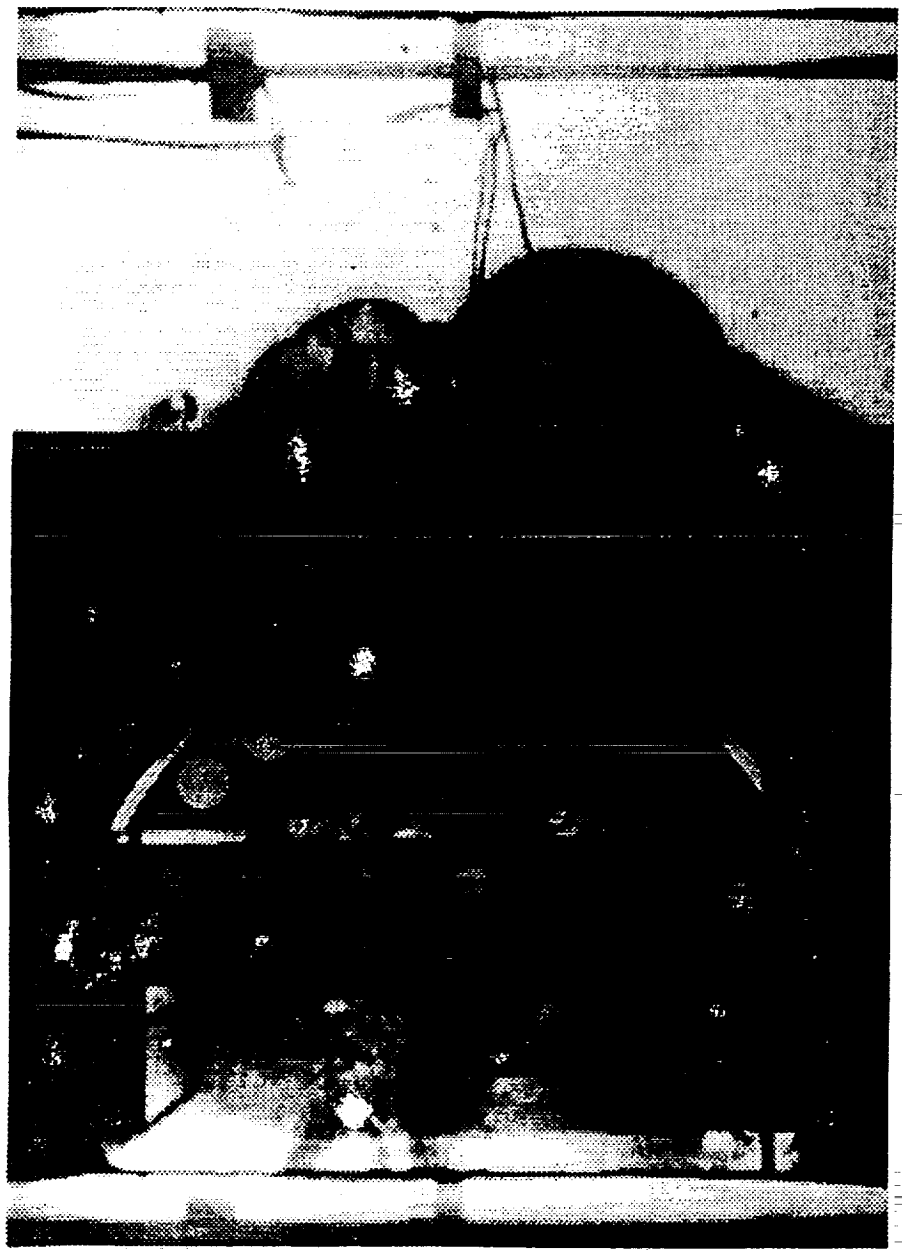

Figure 5.25c Category E: the vapor mass covers nearly the entire heater surface, time = 4.818 sec

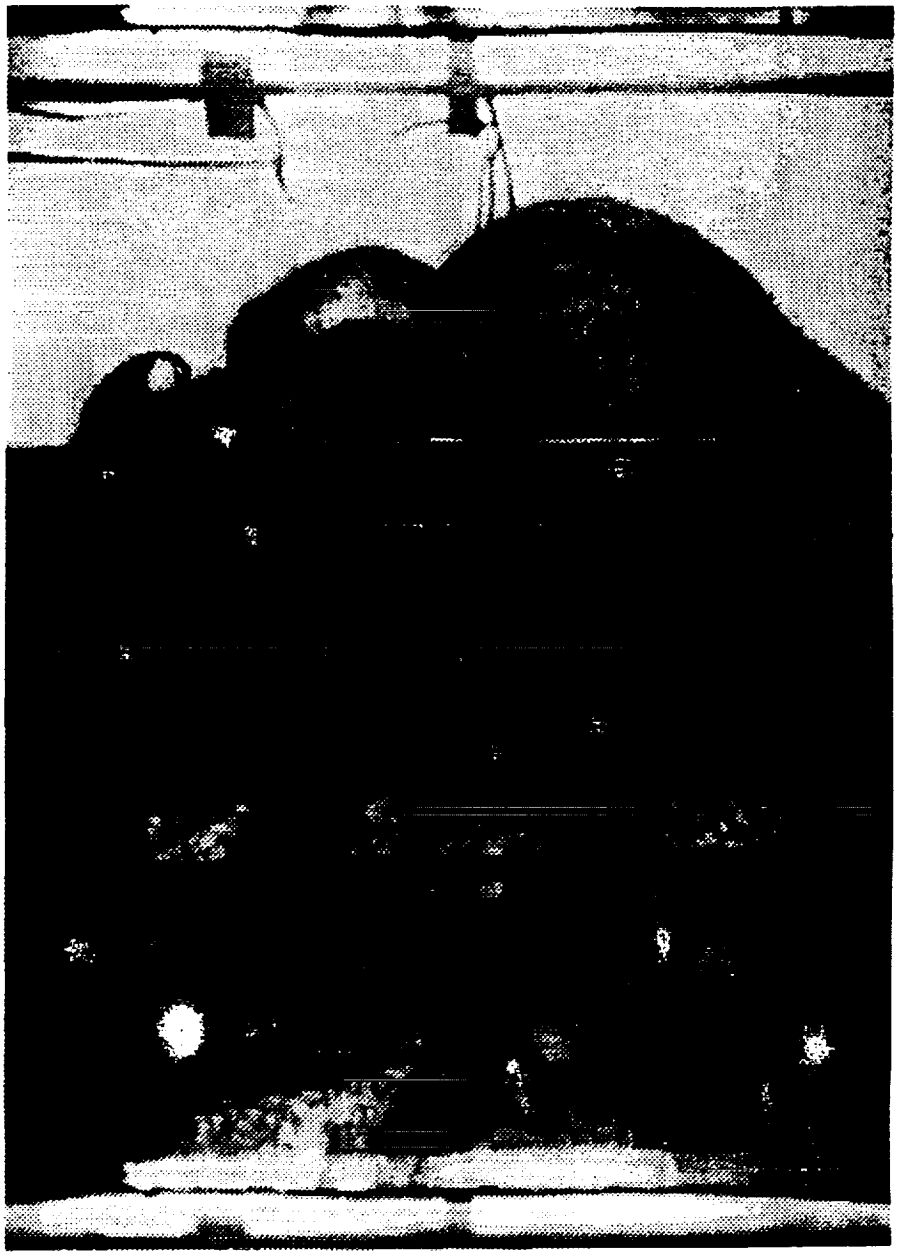

Figure 5.25d Category E: the small scale protuberances are more distinguishable, time = 4.820 sec

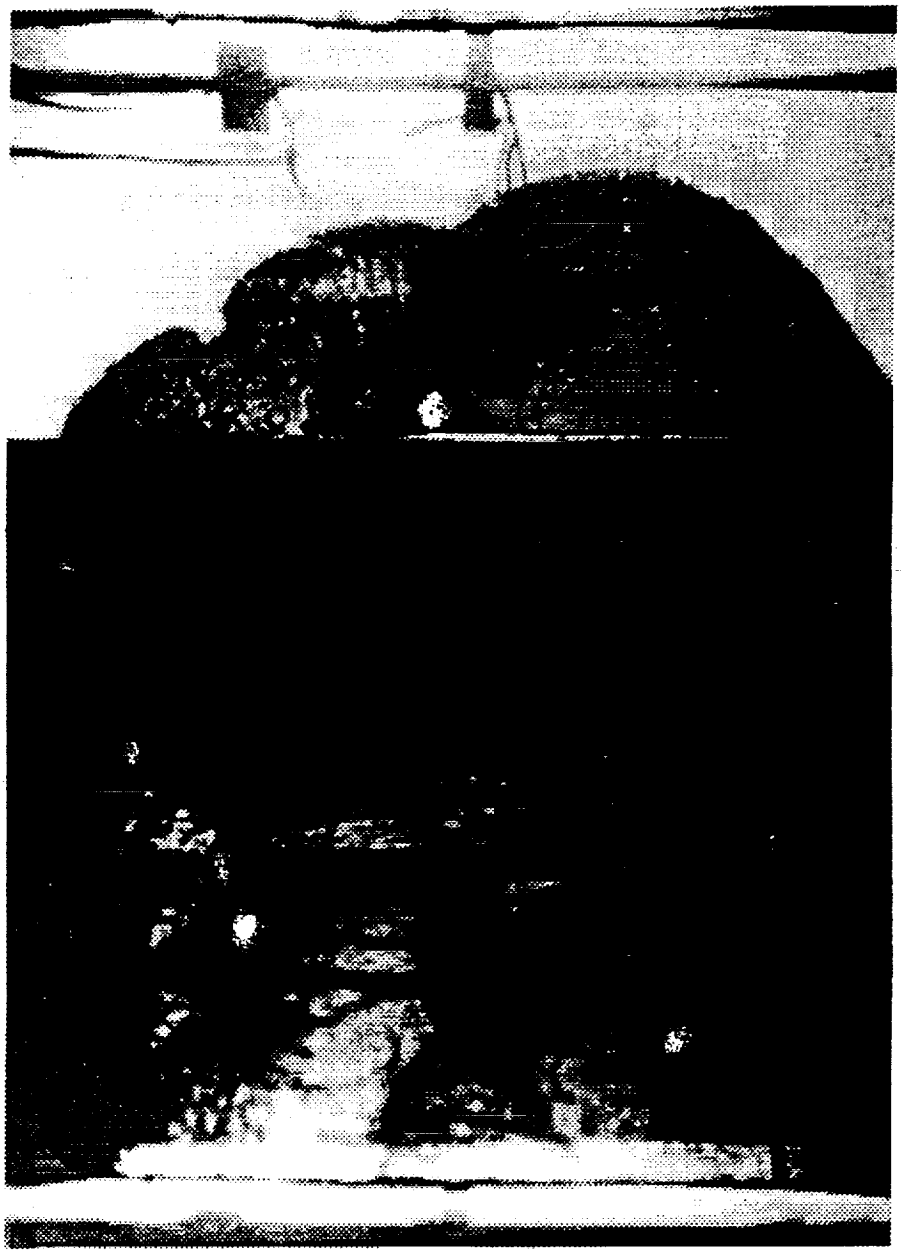

Figure 5.25e Category E: the vapor mass with small scale interface protuberances engulfs vertical thermocouple wires, time = 4.823 sec

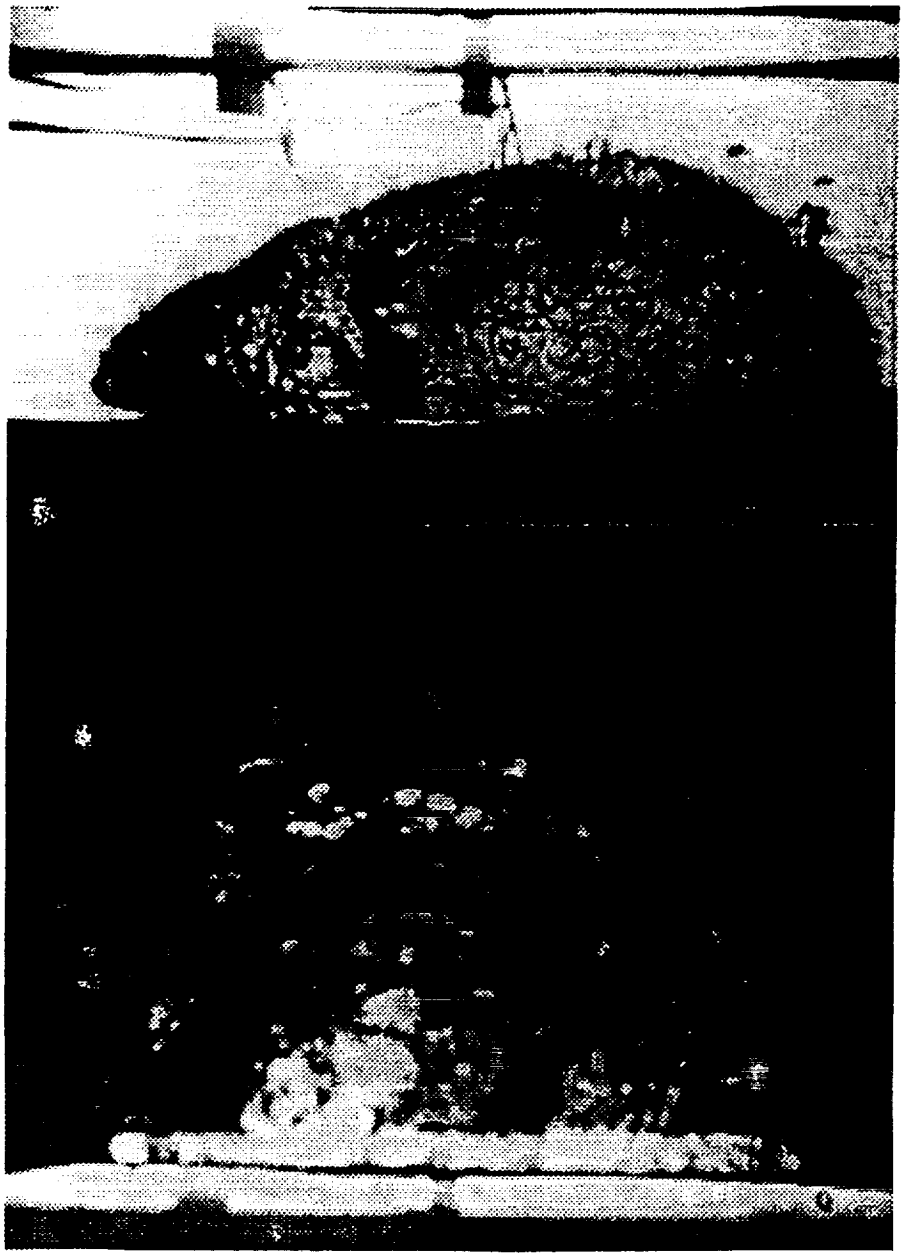

Figure 5.25f Category E: large scale protuberances are visible, time = 4.828 sec

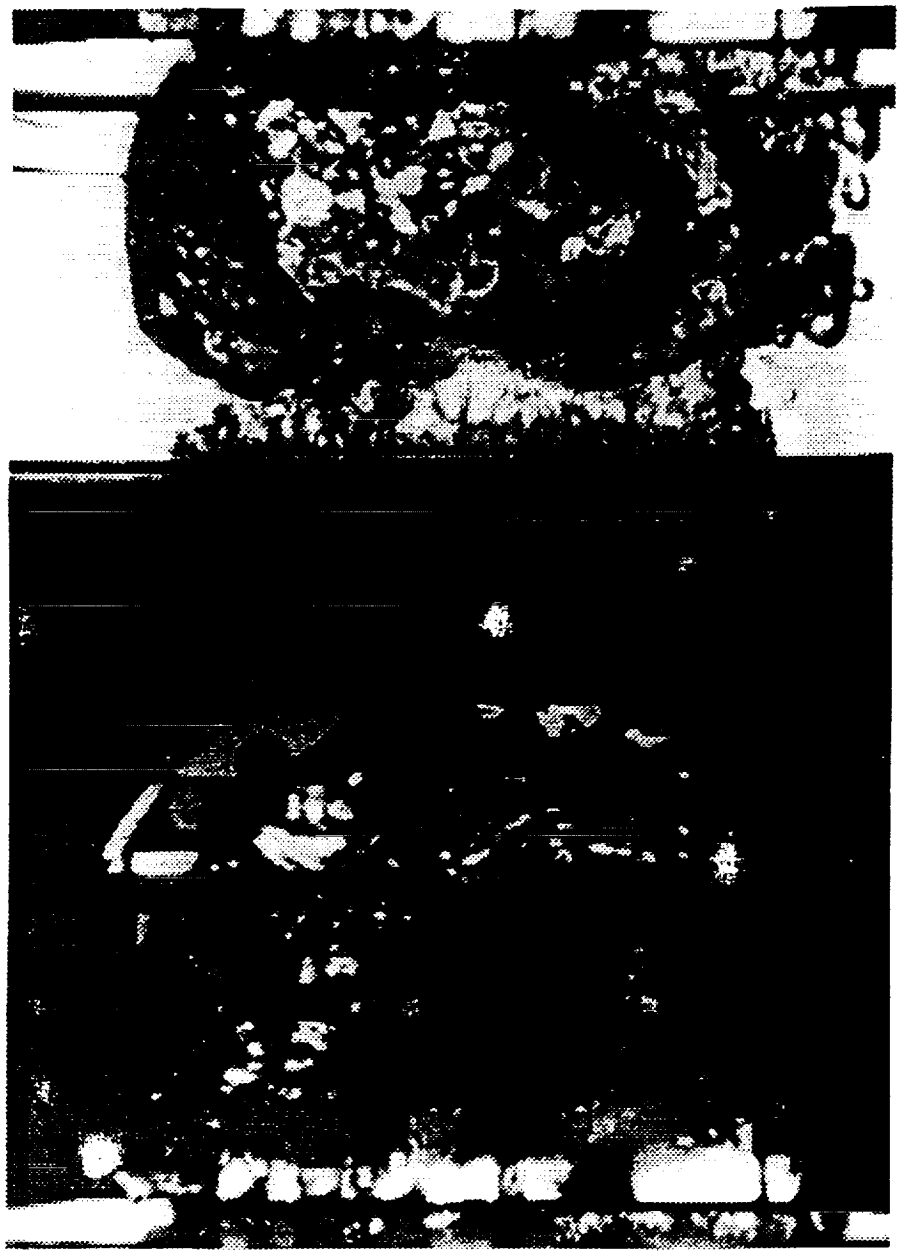

Figure 5.25g Category E: liquid bulk momentum lifts the vapor mass off the heating surface, time = 4.973 sec

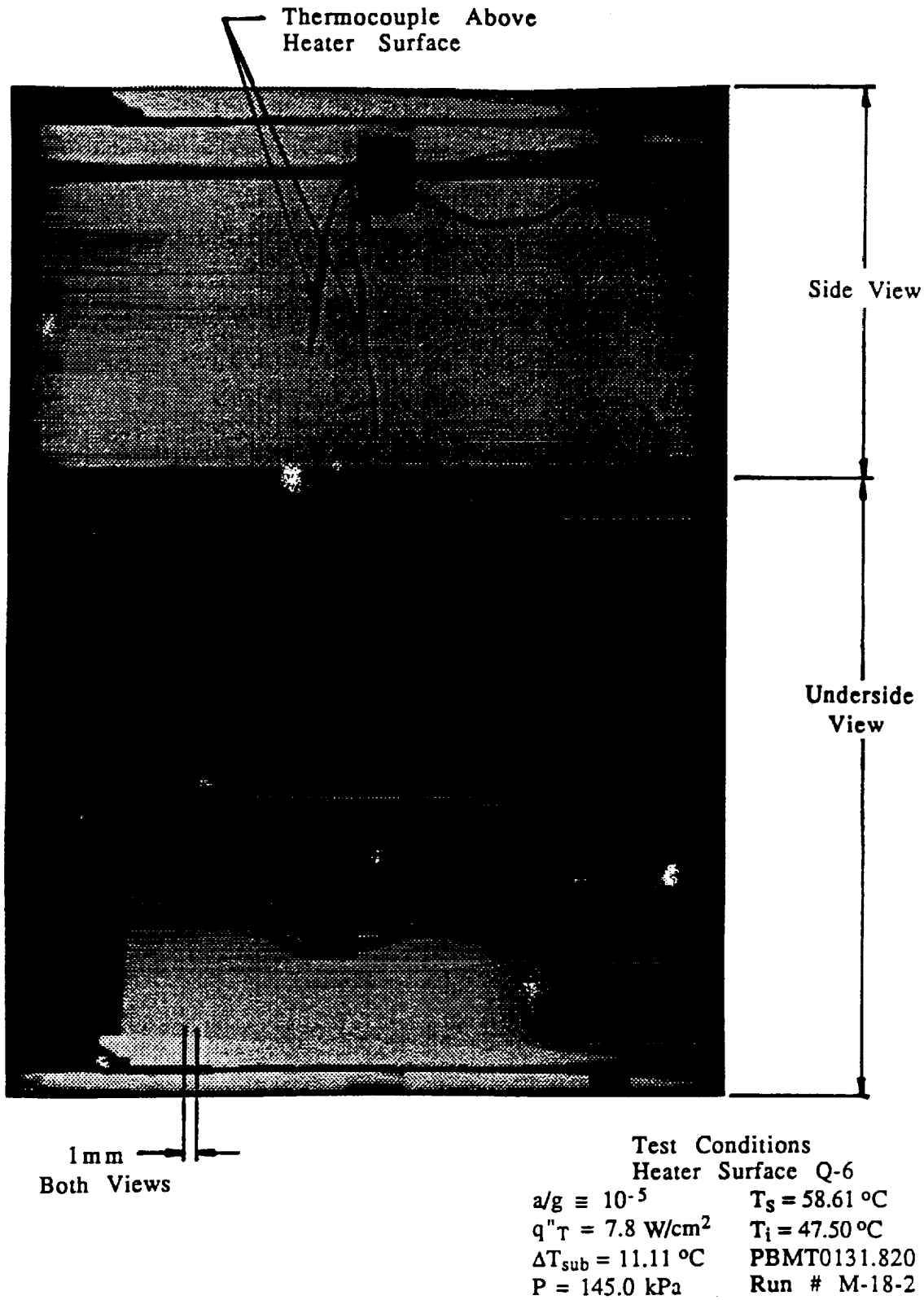

Figure 5.26a Category F: the initial bubble at the edge of the heater surface, time = 0.513 sec

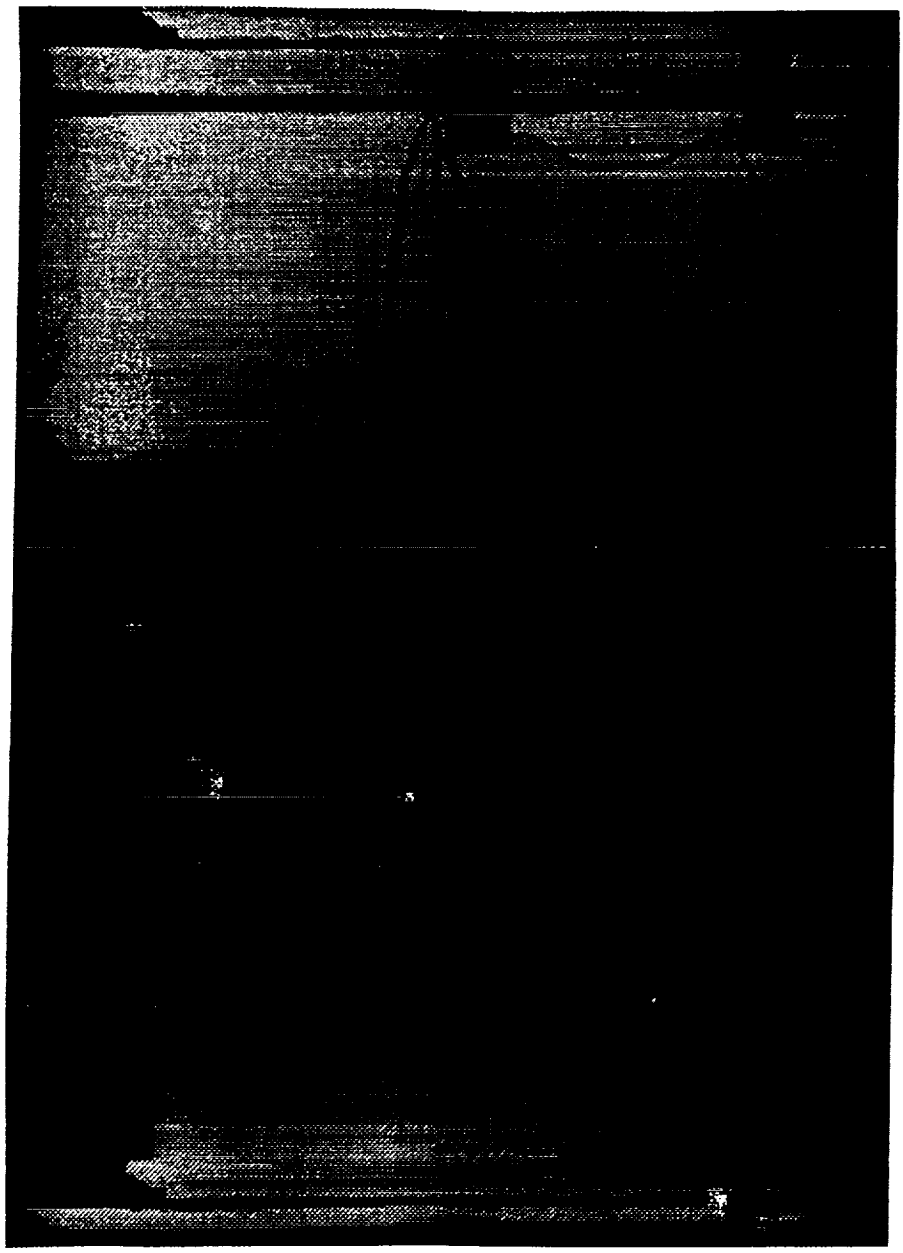

Figure 5.26b Category F: the initial bubble moves toward the heater surface center with two additional bubbles formed at the initial boiling site, time = 0.628 sec

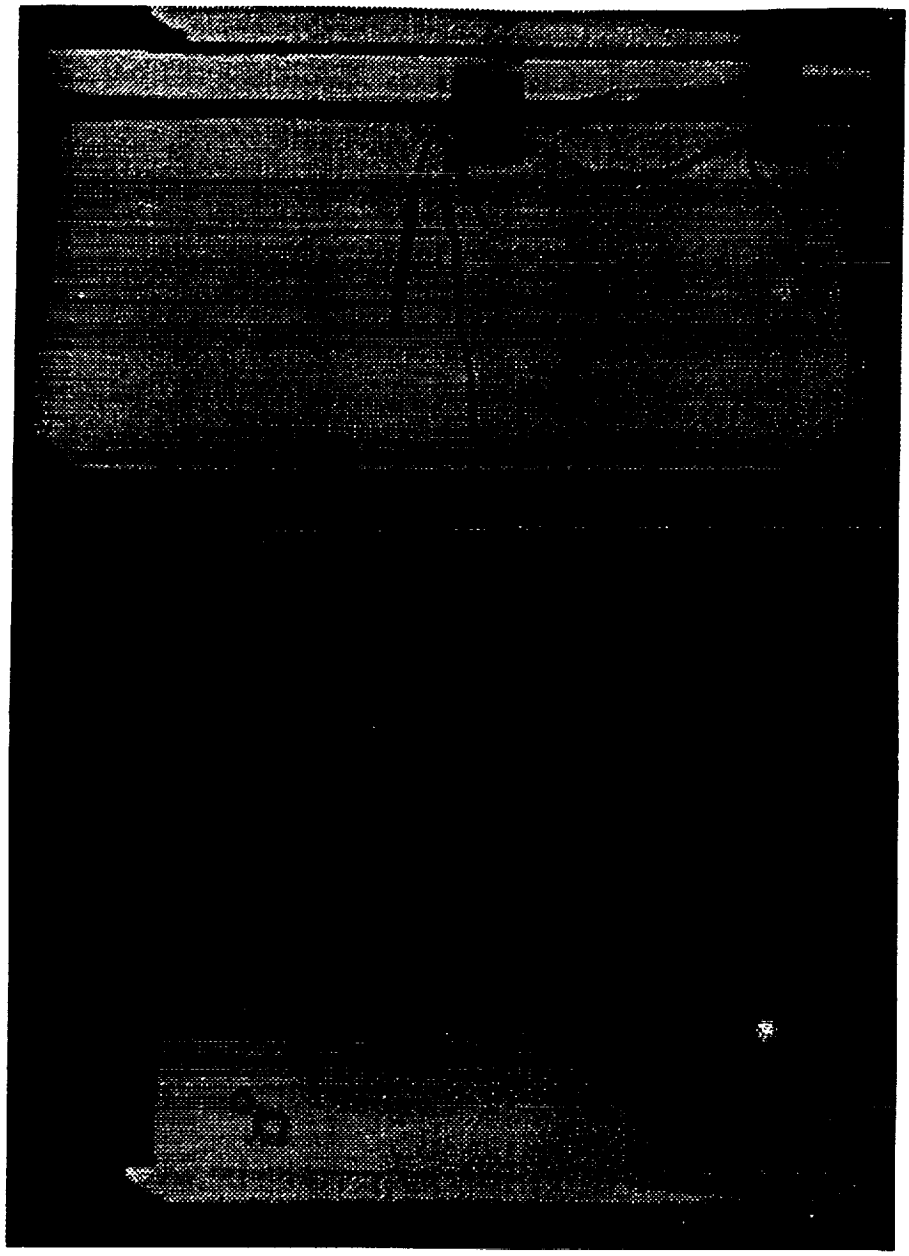

Figure 5.26c Category F: more bubbles grow from both sites and move toward the heater surface center, time = 0.718 sec

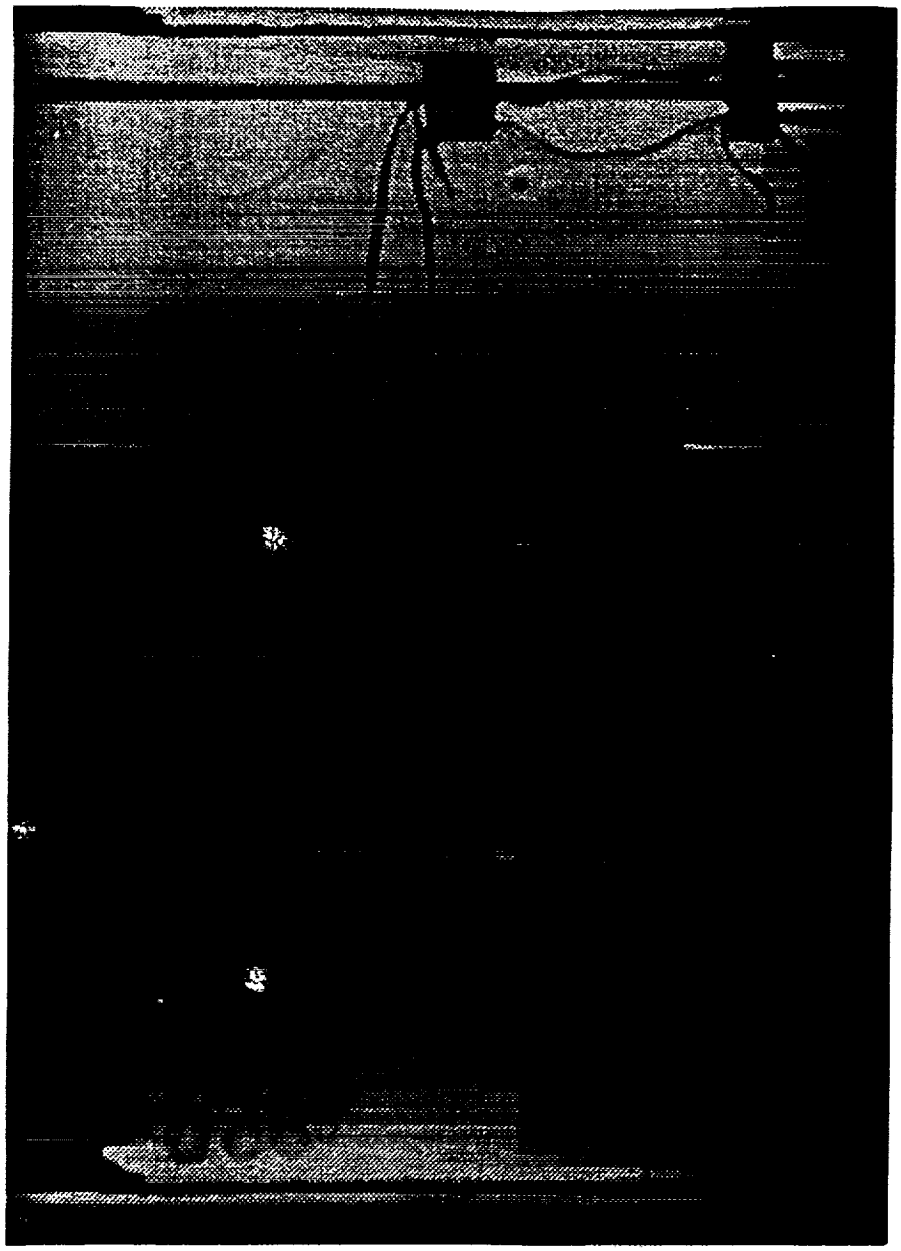

Figure 5.26d Category F: additional bubbles from the two boiling sites, time = 0.920 sec

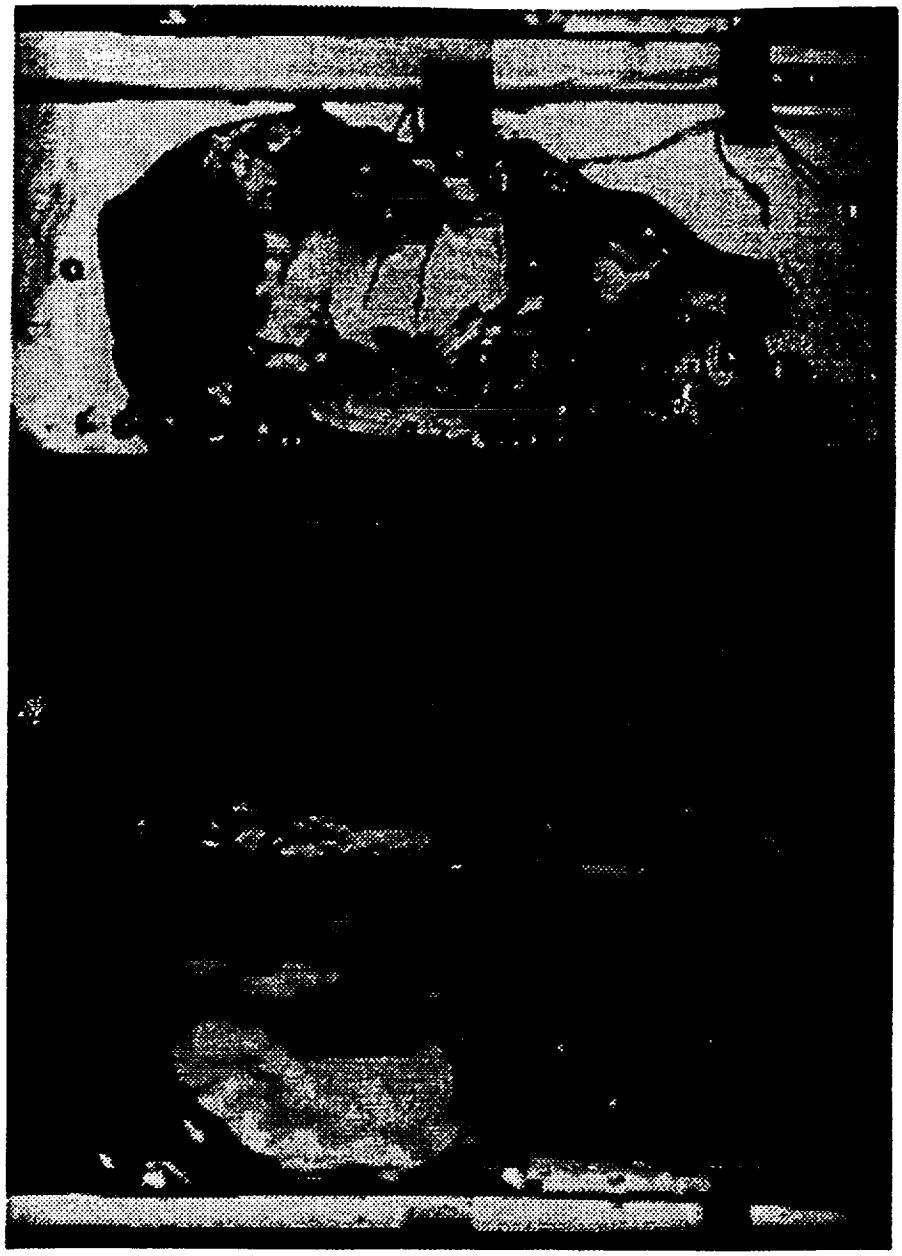

Figure 5.26e Category F: one large vapor mass covers the heater surface and some vapor has separated from this vapor mass to form individual bubbles in the R113, time = 3.608 sec

Table 5.1 Summary of independent variables and resulting measurements associated with observed incipient boiling categories, pool boiling

	Observed Incipient Boiling Categories					
	A	B	C	D	E	F
Body Force (a/g = −1, v, +1)	1	1	−1	0, −1	0	0, −1
Subcooling (Deg C)	0 .1−11.8	0.1−13.0	0.1−11.7	0.1−11.4	0.4−0.5	0.1−11.7
Total Heat Flux (w/sq cm)	6.1−8.2	3.6−8.1	> 7.0	1.93−8.0	5.4−7.7	> 7.0
Surface	Q−2, Q−5 Q−6, Q−14	Q−2, Q−5 Q−6, Q−14	Q−2, Q−5 Q−6, Q−14	Q−2, Q−5 Q−6, Q−14	Q−5	Q−2, Q−5 Q−6, Q−14

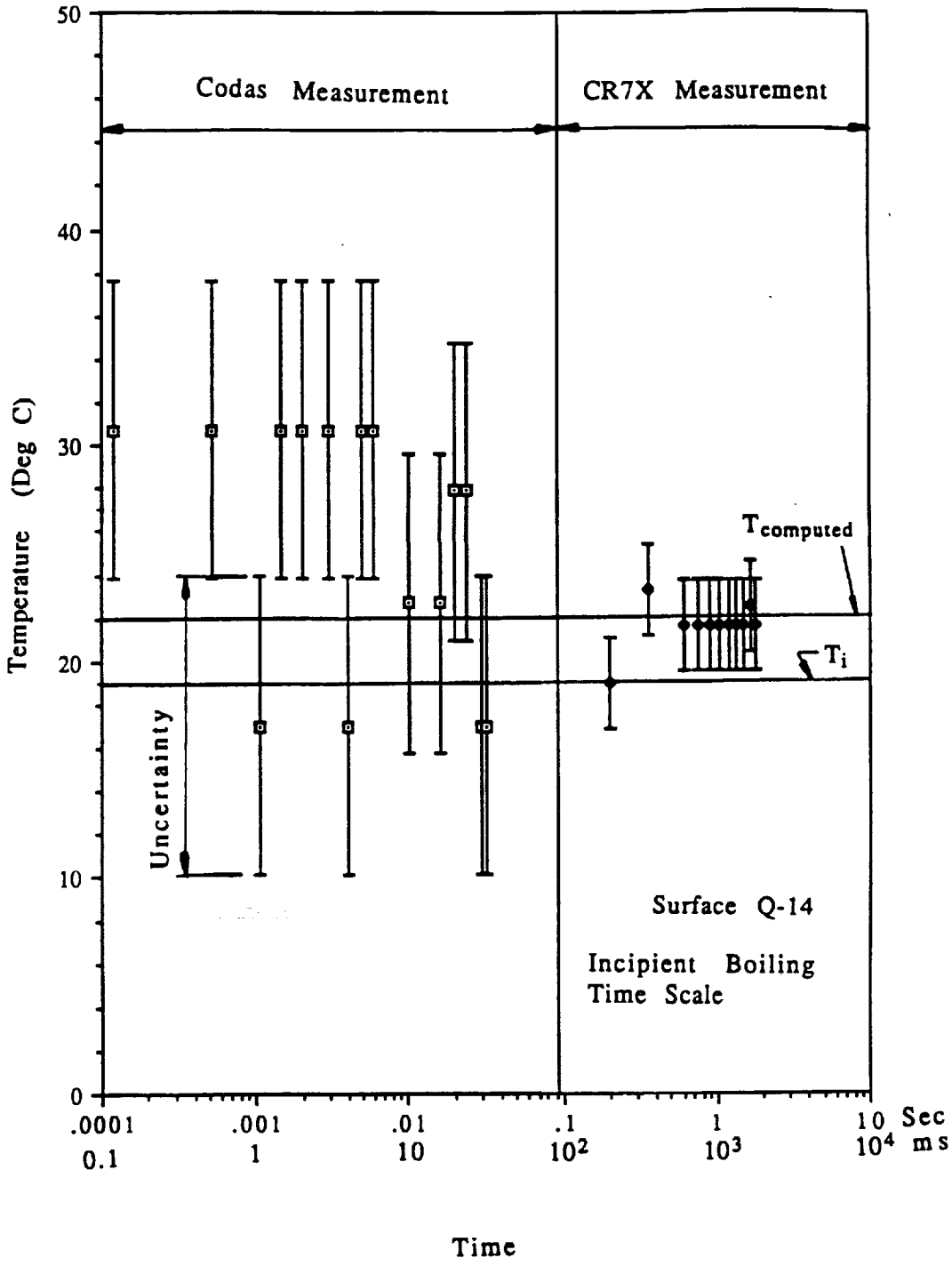

Figure 5.27 Demonstration of transient thin gold film temperature measured with the Codas and the CR7X systems

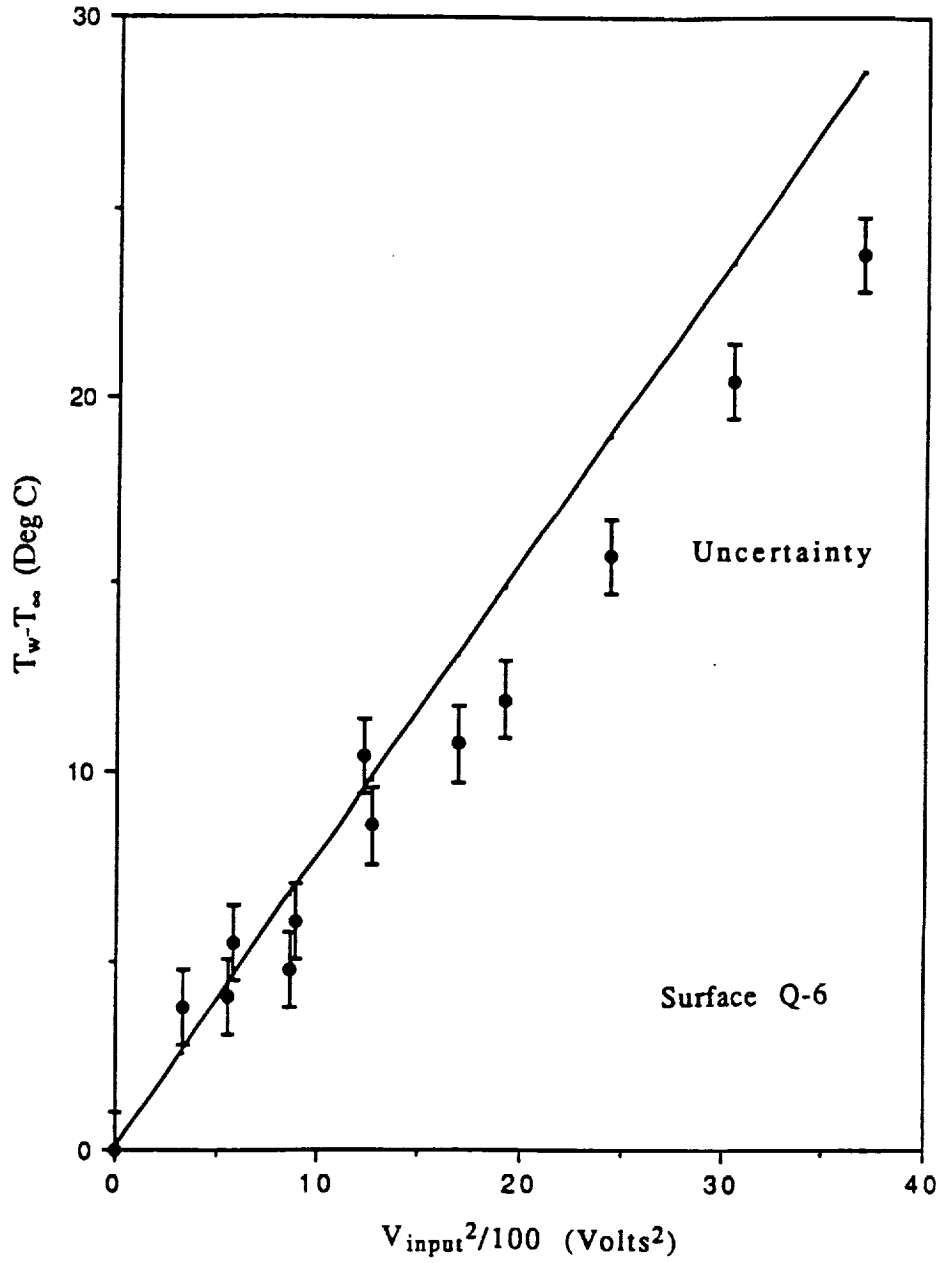

Figure 5.28 Comparison of predicted and measured step rise in surface temperature for various levels of power input

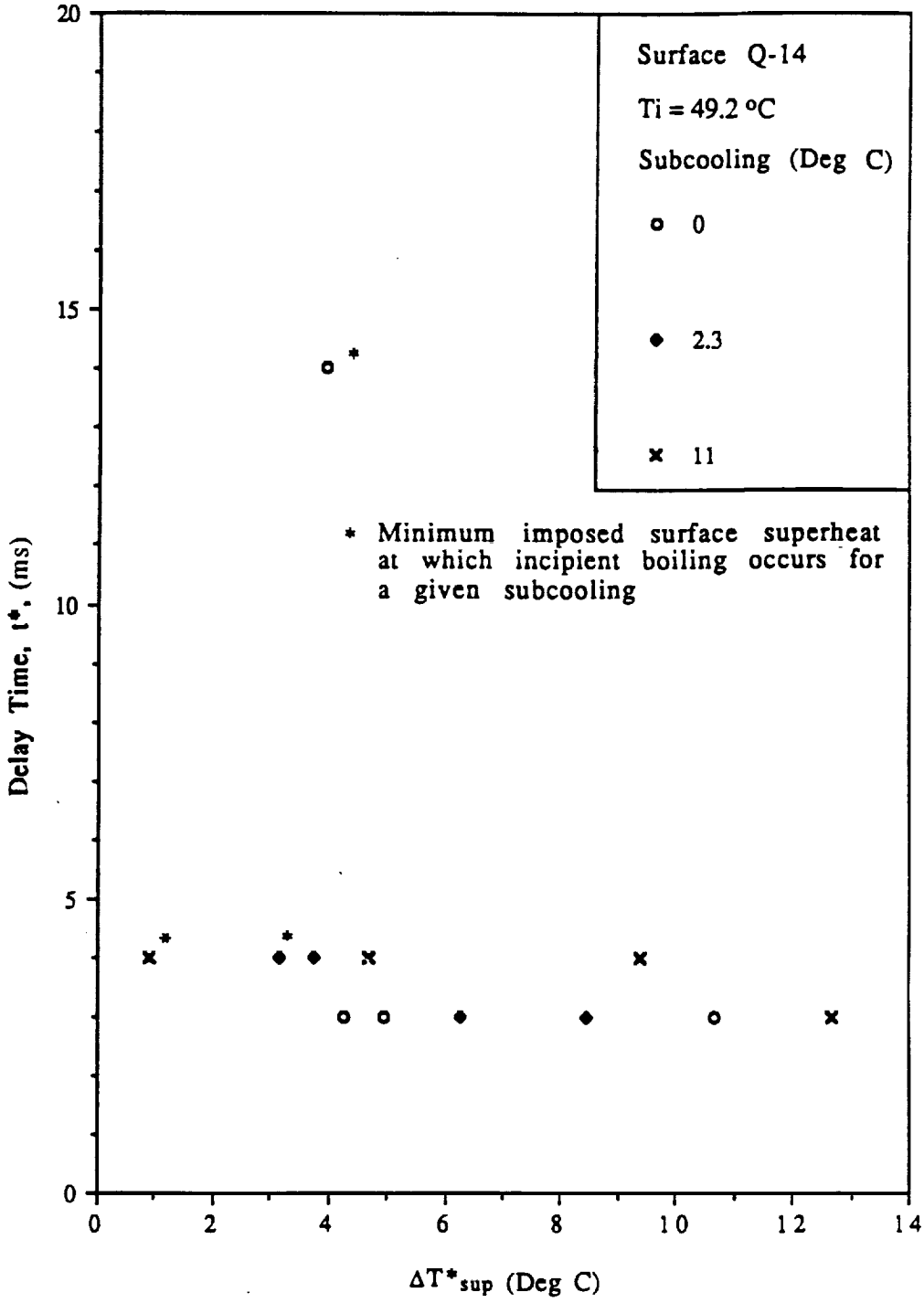

Figure 5.29 Measured incipient boiling delay times with step change in surface temperature

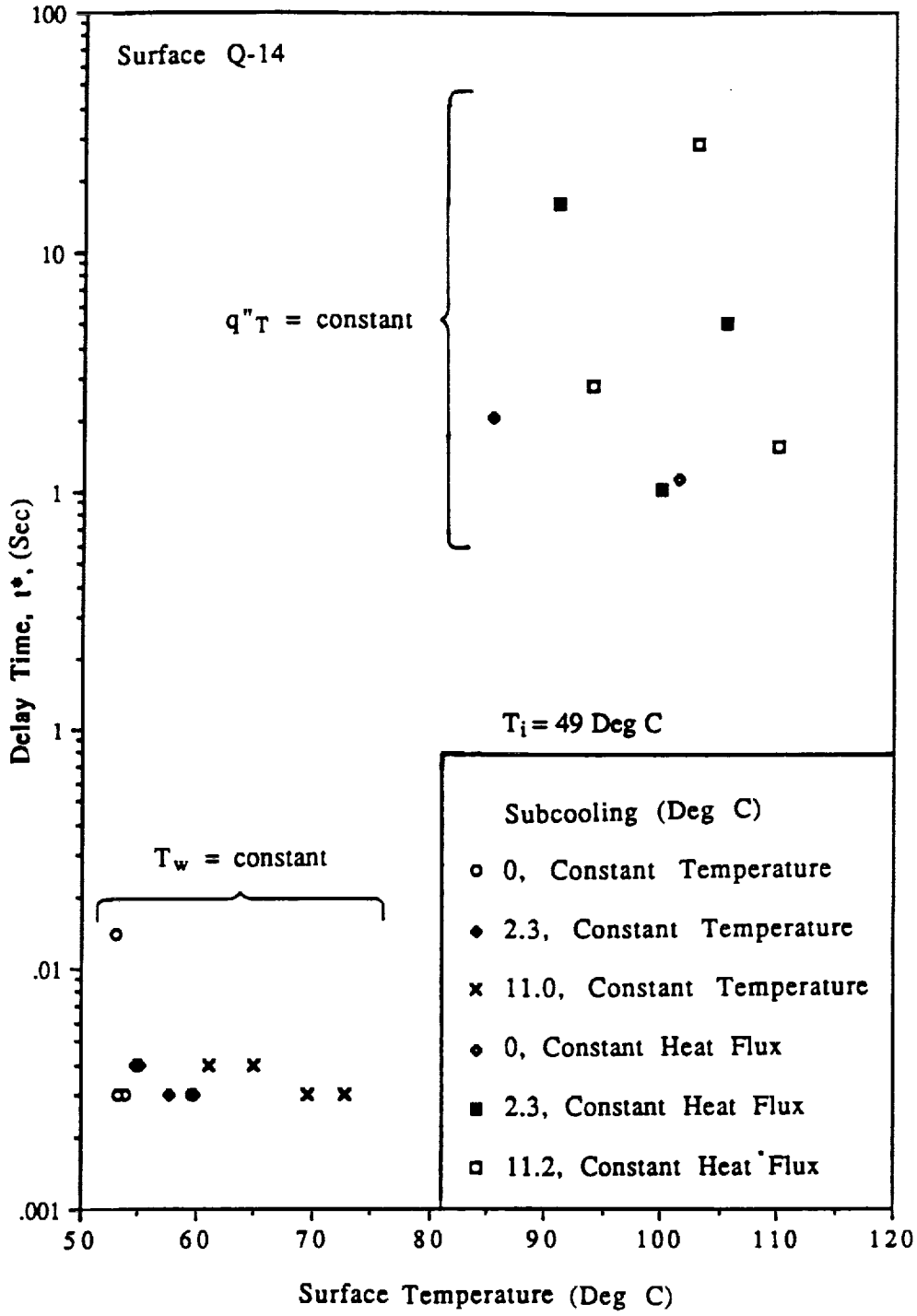

Figure 5.30 Measured incipient boiling delay times and the corresponding surface temperature at boiling inception

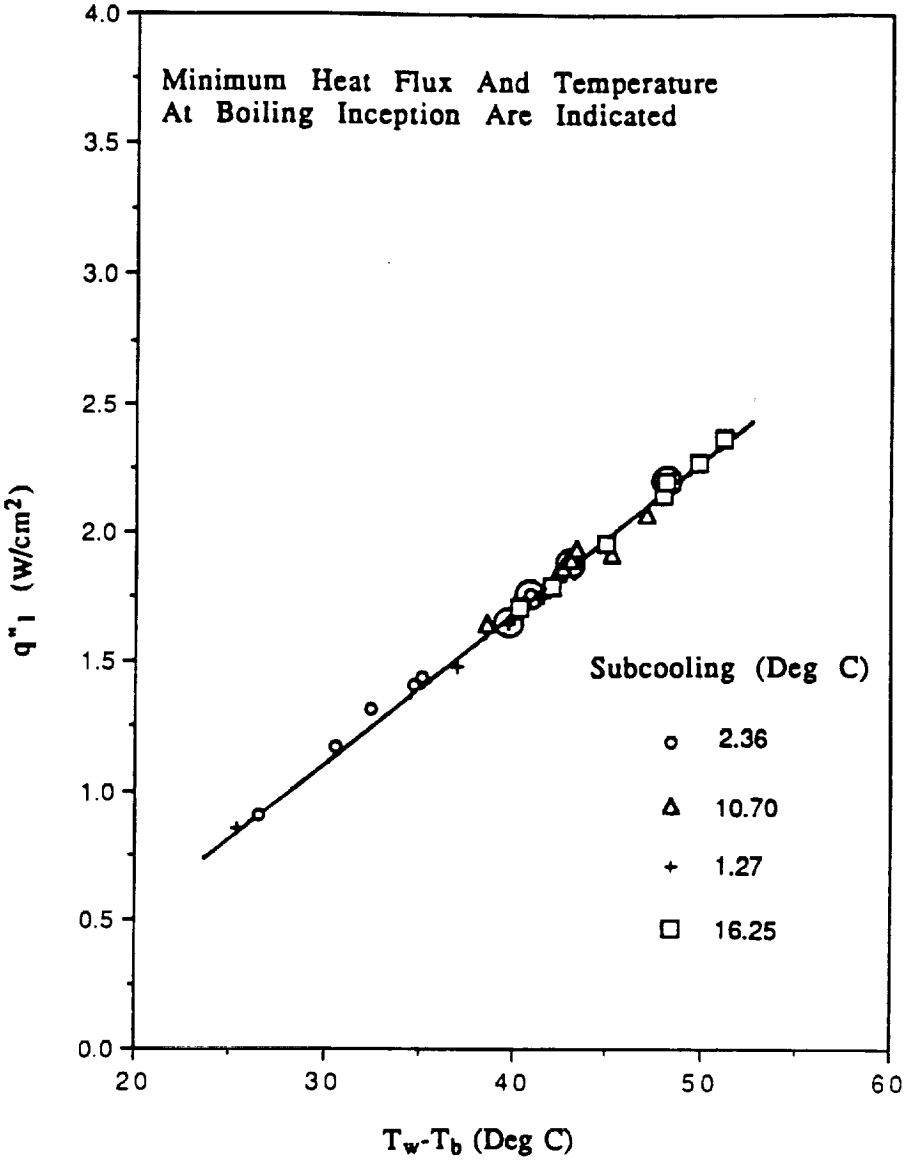

Figure 5.31 Quasi-steady heating prior to incipient boiling for surface Q-2 with horizontal up orientation

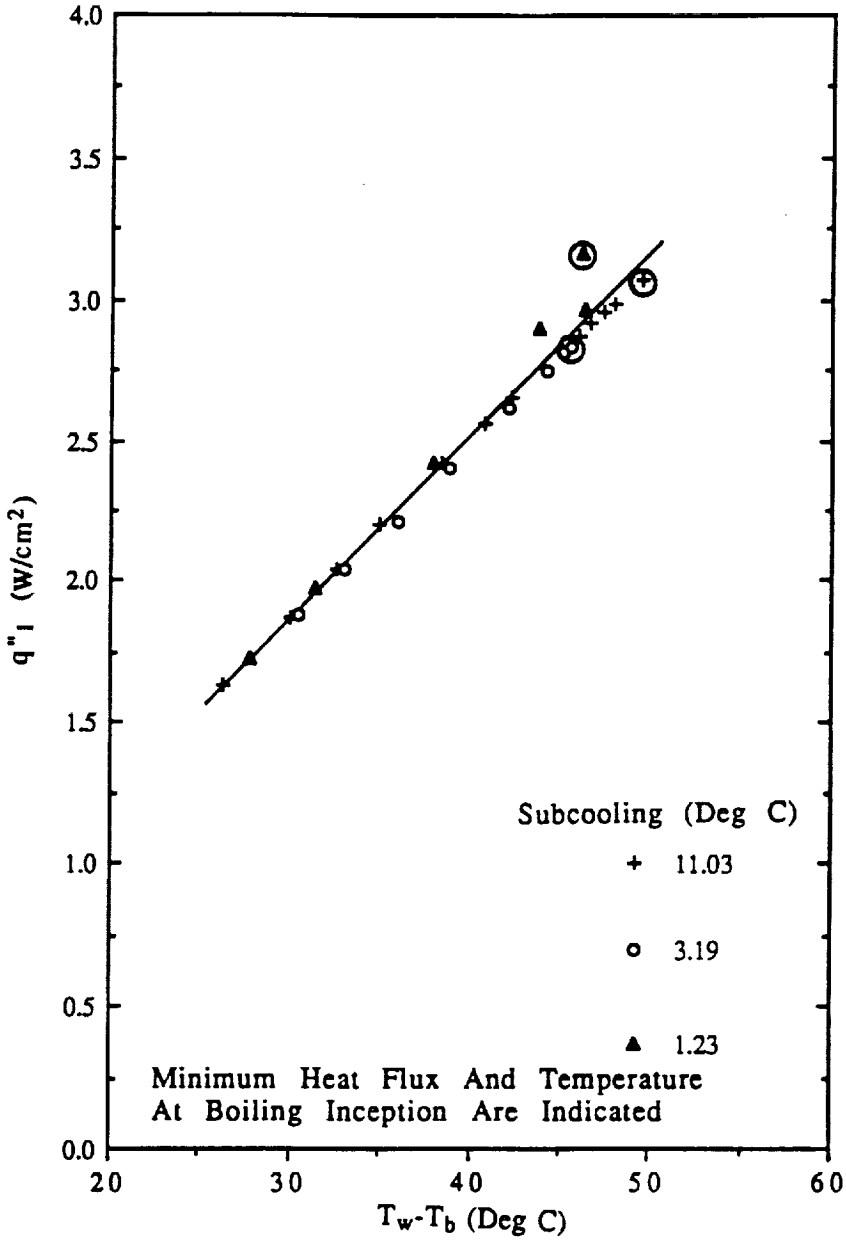

Figure 5.32 Quasi-steady heating prior to incipient boiling for surface SH-2 with horizontal up orientation

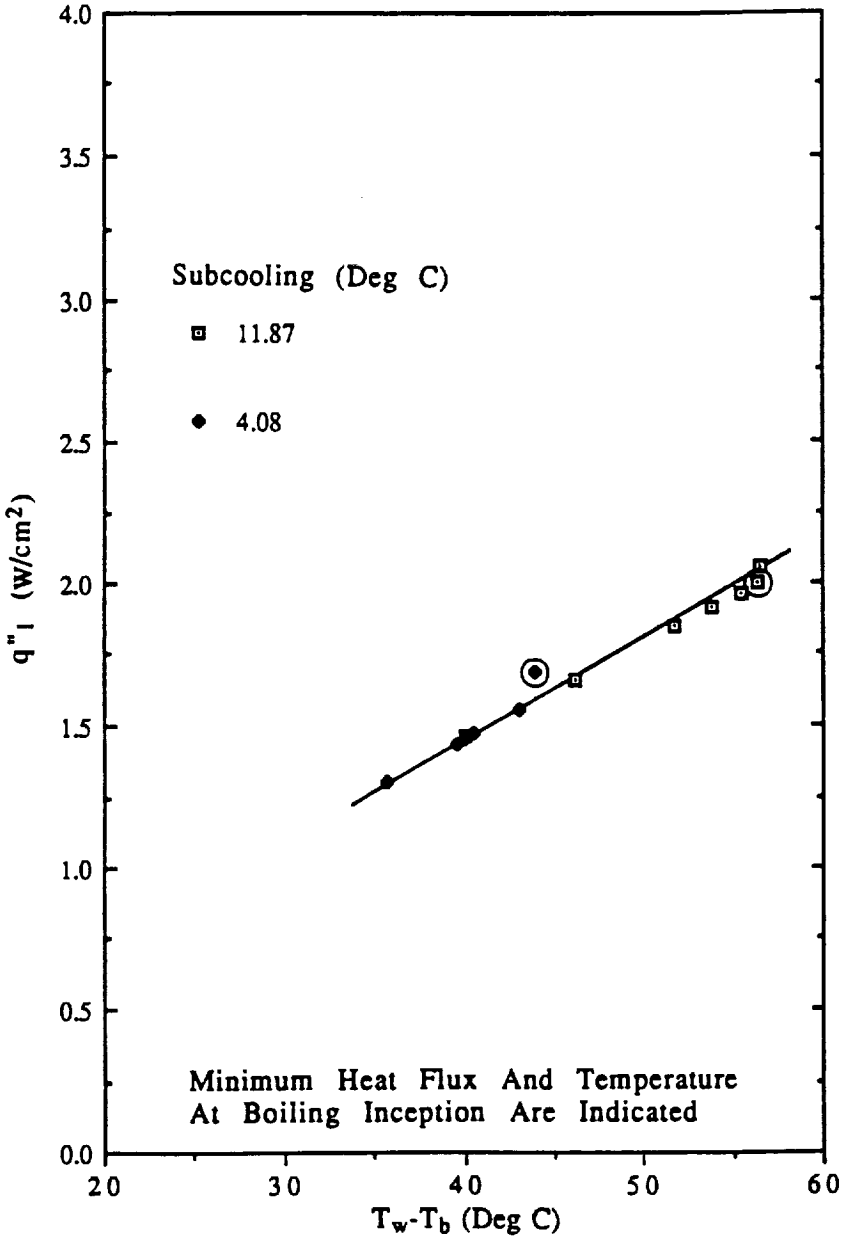

Figure 5.33 Quasi-steady heating prior to incipient boiling for surface SH-2 with horizontal down orientation

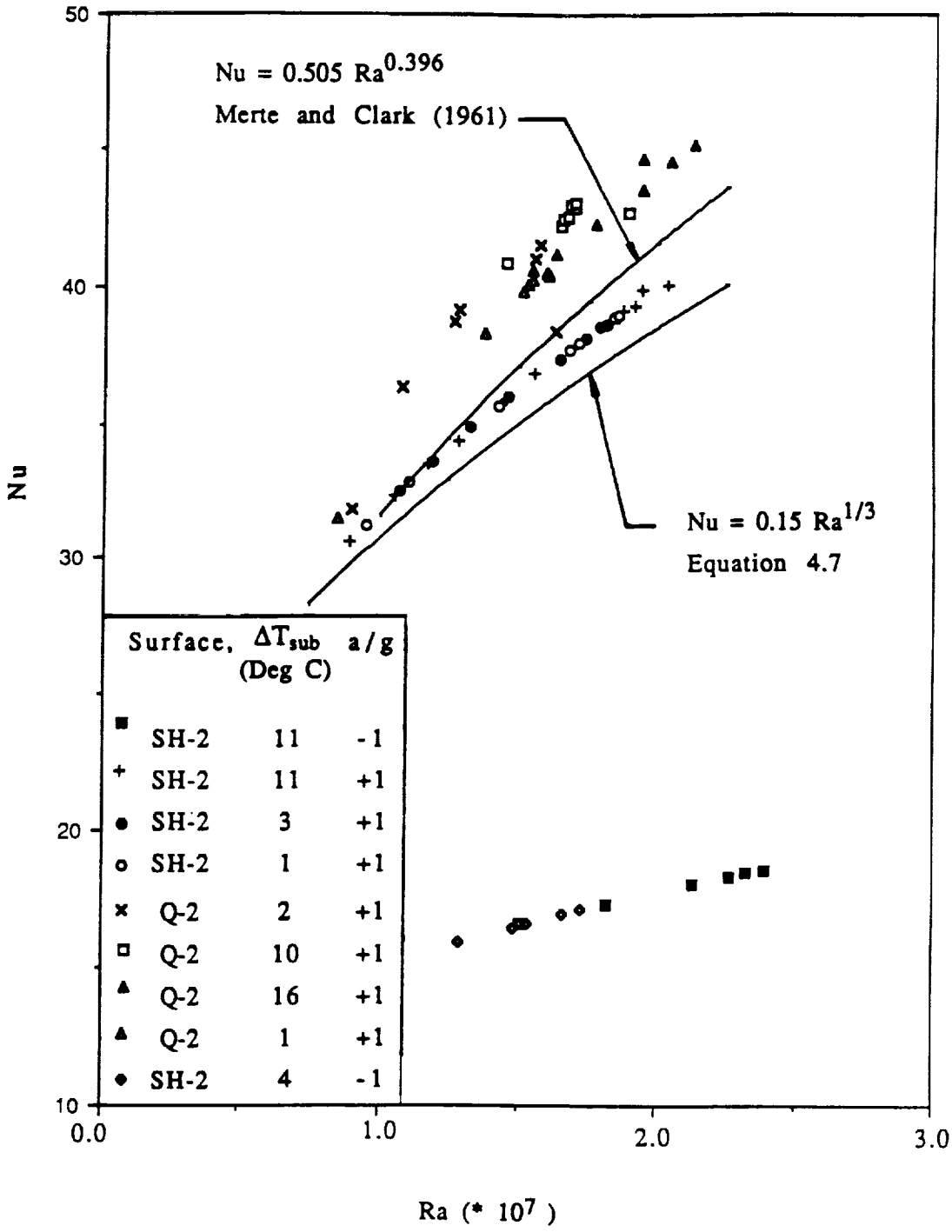

Figure 5.34 Natural convection heat transfer results

CHAPTER 6

DISCUSSION AND CONCLUSIONS

In Chapter 5, measured transient surface temperatures were presented for two different basic thermal disturbances at the heat transfer surface: a step increase in imposed heat flux and a step increase in imposed temperature. In the absence of convection, these permit the computation of the temperature distribution within the liquid, using well-known mathematical techniques. The influence of the liquid temperature distribution at the onset of boiling on the resulting phase change dynamics will be demonstrated, using the calculated liquid temperature distribution, together with the measured heater surface temperature, both at the moment of incipient boiling, to explain the type of subsequent boiling propagation observed, especially the explosive type of boiling propagation occurring at the low heat flux levels. Additionally, an examination of previous concepts concerning an empirical heterogeneous nucleation factor will be presented. In conclusion, the underlying concepts of the present work will be summarized.

6.1 Computed Superheat Temperature Distributions at Boiling Inception: Imposed q_T''

Figures 6.1 through 6.6 present the computed liquid superheat temperature distributions at the moment of incipient boiling together with the measured heater surface superheat temperatures in microgravity conditions obtained with the drop tower tests. The coincidence between the measured and computed heater surface

superheat temperatures confirms the accuracy of the calculated liquid superheat temperature distributions. The superheat temperature distributions, using the known total power flux input to the gold film, were calculated with the one dimensional semi-infinite media solution. For the case of a known imposed heat flux to the liquid, the expression for the transient one dimensional temperature rise is obtained by the Laplace transform solution of equation 2.19 as:

$$\Delta T_i = T(x) - T_i = \frac{2q''_l}{k_l}\sqrt{\frac{\alpha t}{\pi}}\exp\left[\frac{-x^2}{4\alpha t}\right] - \frac{q''_l x}{k_l}\,\mathrm{erfc}\left[\frac{x}{2\sqrt{\alpha t}}\right] \qquad (6.1)$$

The initial test conditions, which were nearly identical for tests with two different surfaces, Q-5 and Q-6, are included in the figures in order to demonstrate how the results obtained may differ with different test surfaces. The tests were conducted at two or three levels of heat flux with three nominal subcooling levels, obtained by increasing the system pressure above the saturation pressure corresponding to the initial liquid temperature.

For a given figure, the largest calculated superheated thermal boundary layer thickness at incipient boiling, δ^*, is denoted for illustrative purposes in addition to the computed liquid temperature distributions at the time of boiling inception. δ the total thermal boundary layer, or more simply the thermal boundary layer, is defined as a layer of liquid near the heating surface in which there is a significant increase in the liquid temperature above that far from the heating surface, with the liquid far from the heating surface remaining at the initial temperature. δ is always $\geq \delta^*$. The superheated thermal boundary layer is the layer of liquid near the heater surface where the liquid temperature is greater than the saturation temperature corresponding to the

system pressure. Both the thermal boundary layer and the superheated thermal boundary layer are shown for illustrative purposes in Figure 6.7.

Figures 6.1 and 6.2 are for the R113 initially near saturation conditions for surfaces Q-5 and Q-6, respectively. It may be noted that in both tests PBMT1012.800 in Figure 6.1 with a q_T" of 7.4 W/cm^2, and PBMT0125.800 in Figure 6.2 with a q_T" of 7.6 W/cm^2, which were conducted at the high heat flux levels, the lowest superheat distributions existed at incipient boiling. The superheated thermal boundary layer is the region within the liquid adjacent to the heater surface where the liquid temperature is above the saturation temperature corresponding to the initial, constant liquid pressure level, and it can be observed from these two figures that the high heat flux levels have the smallest superheated thermal boundary layers. The boiling spread associated with these two tests was the "slow growth," category F type described earlier in Chapter 5. Tests PBMT1025.800, PBMT1026.600, PBMT1102.800 with q_T" of 7.5, 5.7, 7.7, W/cm^2 respectively, in Figure 6.1 and Test PBMT0207.600 with a q_T" of 6.3 W/cm^2 in Figure 6.2 had the next larger liquid superheat distributions and the next larger superheated thermal boundary layers. These tests were characterized by the rapid unstable boiling spread pictured in Section 5.1.1.6, corresponding to category D. Test PBMT1101.600 in Figure 6.1 with surface Q-5, was the most violent of all of the microgravity tests and was referred to as violent or explosive boiling propagation, category E, in Section 5.1.1.6. This test resulted in a heater surface superheat temperature at incipient boiling nearly equal to that of tests PBMT1025.800 and PBMT1102.800, but with a liquid superheat distribution considerably above these two tests and with the largest superheated thermal boundary layer of all of the microgravity tests.

Figures 6.3 and 6.4 show the corresponding results using surfaces Q-5 and Q-6 in R113, with a subcooling of approximately 2.8 °C. In Figure 6.3, tests PBMT0914.805 and PBMT1013.805 had q_T" of 7.8 and 7.2 W/cm^2 and in Figure 6.4,

both tests PBMT0201.805 and PBMT0223.805 had q_T" of 7.7 W/cm^2 . These four experiments show the lowest superheat temperature distributions and the smallest superheated thermal boundary layers at the onset of boiling, and the subsequent boiling spread associated with these was of the "slow growth," category F type. On the other hand, the remainder of the tests in Figures 6.3 and 6.4 have large heater surface superheats and large superheated thermal boundary layers, and are representative of the rapid unstable type of boiling spread, category D.

Figures 6.5 and 6.6 show the calculated liquid superheat temperature distributions and the measured heater surface temperatures at the onset of boiling for the microgravity pool boiling tests with the highest nominal subcooling of 11.1 °C, for surfaces Q-5 and Q-6, respectively. PBMT0919.820 of Figure 6.5 with a q_T" of 7.9 W/cm^2 and of Figure 6.6 with a q_T" of 7.8 W/cm^2 show the lowest superheat temperature distributions and the smallest superheated thermal boundary layers present in these two figures, and correspondingly had the "slow growth," category F boiling spread discussed earlier in Section 5.1.1.6. The remainder of the tests in Figure 6.5 demonstrate category D boiling spread. In Figures 6.1 through 6.6 for a given subcooling, δ^* associated with boiling propagation categories D and E are always larger than the δ^* corresponding to category F.

6.2 Computed Superheat Temperature Distributions at Boiling Inception: Imposed T_w

Figures 6.8 through 6.10 present the computed liquid superheat temperature distributions and the measured heater surface superheat temperatures at the onset of boiling for tests in the laboratory pool boiling vessel in the inverted position (a/g = -1) only, in order to minimize convection effects and thus permit comparisons later with the constant heat flux microgravity tests. Taking the Laplace transform of equation

2.19 with a known imposed constant surface temperature up to the moment of boiling inception, the transient liquid temperature distribution can be computed according to:

$$\frac{T(x,t)-T_w}{T_i-T_w} = \mathrm{erf}\left[\frac{x}{2\sqrt{\alpha t}}\right] \tag{6.2}$$

The tests conducted used three nominal subcooling levels, obtained by setting the system pressure to the appropriate level above the saturation pressure corresponding to the initial liquid temperature. The tests were all conducted with surface Q-14, and the specific conditions of the tests are given in the figures. The type of boiling spread observed in all of these experiments was always the single bubble pancake type, category C, previously described in Section 5.1.1.6. $q''_{T\ max}$ of these figures is the initial step in heat flux which is imposed for 400 microseconds until the heater surface temperature is at the desired level, at which point q''_T decreases.

Figure 6.8 presents calculated superheat temperature distributions for imposed heater surface superheat temperatures of 4, 4, and 5 °C. The R113 was initially near saturation conditions with a T_s of 48.9 °C, corresponding to the liquid pressure of these tests. A ΔT_{ws} of 4 °C was the minimum level for which incipient boiling would occur. This minimum surface superheat for incipient boiling was repeatable within 1 °C for the experiments shown here and in Figures 6.9 and 6.10. The δ^* was 0.11 mm for experiment T107, and was the largest δ^* of the tests in Figure 6.8. For all of the tests presented in Figure 6.8, the initial boiling always occurred at the same location, as observed in the high speed video pictures.

Figure 6.9 presents calculated temperature distributions for imposed step increases in heater surface superheat temperatures of 3, 4, 6, and 9 °C. The test liquid was initially subcooled 2.3 °C at a nominal initial temperature of 49.1 °C. 3 °C was

the minimum heater surface superheat temperature at which incipient boiling just occurred. A δ^* of 0.021 mm for test T106 was the largest superheated thermal boundary layer thickness for the experiments in Figure 6.9. The initial boiling always occurred at the same location, but was at a different location from that observed in the tests of Figure 6.8.

Figure 6.10 presents the calculated temperature distributions for imposed step increases in heater surface temperatures of 1, 5, 9, and 13 °C. The test liquid was initially subcooled by 11.0 °C at a nominal initial temperature of 49.2 °C. 1 °C was the minimum measured heater surface superheat temperature at which incipient boiling would just occur. δ^* was largest for test T114 with a value of 0.012 mm. The initial boiling was always from the same location, but was different from the initial boiling locations observed in the tests of Figures 6.8 and 6.9.

The minimum heater surface superheat temperature required for incipient boiling near saturation conditions was 4 °C, while the minimum heater surface superheat temperatures required for incipient boiling at the nominal subcoolings of 2.3 and 11.0 °C decreased to approximately 3 and 1 °C, respectively. The time delays from the onset of heating to boiling inception were much shorter than those observed for the imposed constant heat flux tests, being on the order of three to four milliseconds. It might be expected that with increasingly greater imposed steps in surface temperature that t^* would be correspondingly smaller. This was not explicitly observed here because of the relatively large uncertainty in t^* due to the camera framing rate. In the future, improved methods would be in order for more precise determination of t^*. The superheated thermal penetration depth associated with the minimum surface superheat for inception, δ^*_{min}, decreased with increasing subcooling in the tests involving surface Q-14: near saturation conditions, δ^*_{min} was 0.027 mm; at a subcooling of 2.3 °C, δ^*_{min} was 0.016 mm; and at a subcooling of 11.0 °C, δ^*_{min} was 0.002 mm. Although the superheated thermal boundary layer of 0.002 mm is

quite thin, it still contains a large number of molecules, on the order of 7 x 10^{18} for a heater surface area of 7.25 cm^2.

6.3 Comparisons of Computed Temperature Distributions: Imposed q_T" and T_w

Figures 6.11 through 6.15 present the computed liquid temperature distributions at boiling inception for both the imposed constant step increase in surface temperature and the imposed step increase in heat flux, contrasting the relative magnitudes of the superheated thermal boundary layer thicknesses which persist following heating by these two methods. The delay times from the onset of heating to the appearance of the first bubble are also shown. The measurements were conducted in both the laboratory pool boiling vessel with the heater surface in the inverted position (a/g = -1) and in microgravity.

Figure 6.11 presents a comparison of the computed one dimensional superheat temperature distributions at boiling inception for both imposed step increase in surface temperature and imposed constant heat flux, for surface Q-14 with the bulk liquid initially saturated. The imposed surface superheat temperature levels shown in Figure 6.11 are 4 and 11 °C. These two superheat levels were selected as representative of the other superheat levels conducted in the imposed surface temperature tests near saturation conditions. Since these tests were performed in earth gravity and the buoyancy force was present, the high level heat flux for the constant heat flux tests of 7.8 W/cm^2 was chosen in order that boiling inception would take place before the onset of natural convection. In Figure 6.11, the δ^* associated with incipient boiling for the imposed constant heat flux test, T207, was 0.82 mm while the largest of the δ^* corresponding to the constant imposed surface temperature tests, T110, was only 0.03 mm.

Figure 6.12 similarly shows the calculated one dimensional liquid superheat temperature distributions for imposed heater surface temperatures and imposed heat fluxes for surface Q-14 with an initial subcooling of 2.3 °C. Measured heater surface temperatures at the onset of boiling are also shown. Imposed heater surface superheat temperatures of 3 and 9 °C were considered representative of the other tests with the same initial conditions. The heat flux of 7.8 W/cm^2 with an incipient boiling delay time of 1.012 seconds, was used in order to minimize the effects of buoyancy on the computed temperature distribution. As can be noted in Figure 6.12, the δ^* of 0.52 mm for T205, an imposed constant heat flux test, was considerably greater than the δ^* of experiments T103 and T106, which were on the order of 0.02 mm.

Figure 6.13 presents a similar comparison of the one dimensional superheat temperature distributions at the time of boiling inception with a nominal subcooling of 11.0 °C, for surface Q-14 also. The representative imposed heater surface superheat temperatures of 1 and 13 °C with the corresponding liquid superheat distributions were plotted along with a test at the same initial conditions with an imposed heat flux of 7.8 W/cm^2. The boiling inception delay time for the constant heat flux test was 1.518 seconds. Similar to Figures 6.11 and 6.12, the δ^* for the imposed heat flux experiment again was greater than the δ^* corresponding to the imposed heater surface temperature experiment. The δ^* for T206 was 0.40 mm and the δ^* for T114 was 0.01 mm.

Liquid superheat temperature distributions computed at boiling incipience but using a thin film heating surface different from surface Q-14 show a considerably larger difference between the superheated thermal boundary layer for the constant heat flux tests than for the imposed increase in surface temperature tests. Figures 6.14 and 6.15 show comparisons of the liquid superheat distributions with both the imposed heater surface temperature tests and constant heat flux tests for another surface, designated as Q-6. Tests with the imposed heat fluxes were conducted under

microgravity conditions in the drop tower, and no question exists as to the absence of natural convection during the heating process, while tests with a step in surface temperature were conducted at earth gravity in the inverted position, as described previously. Figure 6.14 is for experiments near saturation conditions with two imposed heat flux levels, both conducted in microgravity conditions, of 6.3 and 7.6 W/cm^2. ΔT_{ws} is given as zero for test T51 in Figure 6.14, but ΔT_{ws} cannot be zero as nucleation would not occur. This apparent contradiction of nucleation occurring at a superheat of 0 °C results from the heater surface temperature uncertainty, which is $\pm$ 1 °C. ΔT_{ws} must actually be greater than 0 °C, but the actual value is less than the uncertainty associated with the heater surface temperature measurement. The heat flux of 7.6 W/cm^2 has the smaller t* and resulting smaller superheated thermal boundary layer of the two imposed heat flux tests, but the superheated thermal boundary layer thickness, 0.15 mm, of the 7.6 W/cm^2 test is still greater than the calculated superheated thermal boundary layer thicknesses of 0.008 mm and 0.059 mm for tests T51 and T52, respectively. Figure 6.15 is for tests similar to those of Figure 6.14 using Q-6, but with a nominal subcooling of 2.8 °C. The computed liquid superheat temperature distribution with two different heat flux levels, 4.9 and 7.7 W/cm^2, are shown with the imposed increase in heater surface temperature tests. The constant heat flux tests were performed in microgravity, and the imposed surface temperature tests were performed with the heating surface inverted. Of the two imposed heat flux tests, the test with the higher heat flux of 7.7 W/cm^2 resulted in a lower heater surface superheat at the onset of boiling, and consequently a smaller superheated thermal boundary layer. However, the superheated thermal boundary layer thickness of 0.2 mm resulting from the 7.7 W/cm^2 imposed constant heat flux test is still considerably larger than the superheated thermal boundary layer thickness of 0.027 mm resulting from an imposed surface temperature.

In the tests using surface Q-14, δ^*_{min} decreased with increasing subcooling, but for the tests with an imposed surface temperature involving surface Q-6, δ^*_{min} increased with increasing subcooling. δ^*_{min} for T50 with a subcooling of 2.61 °C was 0.027 mm while δ^*_{min} for T51 near saturation conditions was 0.008 mm as presented in Figures 6.14 and 6.15. Table 6.1 lists computed δ^* values in microns for imposed heat fluxes and imposed surface temperatures for surface Q-14 with similar initial conditions.

6.4 Estimation of Change in Internal Energy

It is conjectured that the type of boiling spread observed is related directly to the amount of thermal energy within the superheated thermal boundary layer. Superheated thermal boundary layers with more energy can be expected to exhibit more violent boiling propagation than those with less energy. With constant properties evaluated at an appropriate mean temperature, estimates of the increase in internal energy of the superheated thermal boundary layer up to the instant of incipient boiling can be made.

The change in internal energy of the superheated thermal boundary layer per heater surface area up to the point of boiling inception, ΔU^*, can be estimated by:

$$\Delta U^* = \rho\, c \int_0^{\delta^*(t)} (T(x)-T_S)\, dx \qquad (6.3)$$

where $\delta^*(t)$ denotes the superheated thermal boundary layer thickness. The integration of equation 6.3 from $x = 0$ to $x = \delta^*(t)$ for the change in internal energy of the superheated thermal boundary layer and from $x = 0$ to $x = \delta(t)$ for the change in

internal energy of the thermal boundary layer were performed using Simpson's Rule, using the appropriate analytical expressions for T(x) and values of $\delta^*(t)$ and $\delta(t)$ corresponding to the measured onset of boiling. The values of the superheated penetration depth, internal energy change of the superheated boundary layer, total internal energy change, the ratio of the change in internal energy of the superheated thermal boundary layer to that of the total thermal boundary layer, and the type of subsequent boiling spread observed are presented in Table 6.2 for the microgravity tests where a constant heat flux was imposed.

The experiments in which the increase in internal energy of the superheated thermal boundary layer was 19.150 kJ/m^2 or more at the moment of boiling inception are those in which the boiling propagation was either the rapid unstable type, category D, or the rapid violent type, category E. The rapid violent type of boiling propagation occurred only for tests in which the liquid was initially near saturation conditions. The tests with an increase in internal energy of the superheated thermal boundary layer of 6.815 kJ/m^2 or less are characterized by the slow marangoni type of spreading, category F. Experiment PBMT1101.600, which was the most violent of all tests, had the largest increase in internal energy of the superheated thermal boundary layer, 46.68 kJ/m^2, and also the largest ratio of increase in internal energy of the superheated thermal boundary layer to the increase in energy of the thermal boundary layer, 0.9977. Two other microgravity experiments with category E type of boiling propagation, PBMT1025.800, and PBMT1102.800, had a change in internal energy in δ^* of 33.22 kJ/m^2 and 31.28 kJ/m^2 , respectively, and a ratio of the increase in internal energy of δ to δ^* of 0.9974 and 0.9969, respectively. From the estimated change in internal energy, it is observed that the energy content for the most explosive type of boiling spread is the largest, 46.68 kJ/m^2. The most rapid vapor bubble growth occurred in the microgravity experiment with a heater surface temperature of 120 °C. This experiment, PBMT1101.600, had one of the lowest temperature gradients at the

heater surface, but had the largest superheated thermal boundary layer energy content of all the microgravity tests. The boiling spread that occurred with relatively small increase in internal energy in the superheated thermal boundary layers were characterized by category F spreading, while the boiling spread that occurred with relatively large increases in internal energy in the superheated thermal boundary layer were of the rapid unstable type, or on occasion for very large increases in internal energy in the superheated thermal boundary layer, the explosive type.

As can also be noted from a detailed examination of Table 6.2, the largest ratios of increase in internal energy of the superheated thermal boundary layer to the increase in energy of the thermal boundary occur with initially saturated liquid, as can be anticipated. The last two digits of the filenames in Table 6.2 provide the nominal liquid subcoolings in degrees Fahrenheit.

In the case of the imposed surface temperature tests, incipient boiling began before the superheated thermal boundary layer thickness reached the values corresponding to the imposed heat flux tests. The more non-equilibrium conditions of a steeper temperature gradient and a smaller time scale associated with the imposed heater surface temperature tests may have made the liquid-vapor interface of the nuclei in the surface cavities more unstable than under the conditions of an imposed heater surface heat flux. In Table 6.1, the boiling delay time and the liquid temperature gradient at the surface both for 400 microseconds and the onset of boiling are presented. It is noted that at a time of 400 microseconds that the surface temperature gradient tends to be larger than that associated with the imposed heat flux tests. Particularly striking is the contrast in magnitude of the boiling delay times between the imposed heat flux tests and the imposed surface temperature tests. The surface temperature at incipient boiling was always greater for an imposed heat flux than for an imposed surface temperature for similar initial conditions and the same surface. Furthermore, from examination of the area under the temperature distribution curves,

Figures 6.11 through 6.15, the tests associated with an imposed heater surface temperature have a smaller increase in the internal energy of δ^* as compared to the imposed heat flux tests, and thus category F boiling propagation is expected for the tests involving the imposed heater surface temperatures.

The integration involved in the estimation of the internal energy with equation 6.3 was found to be more convenient with an approximate polynomial representation of the liquid temperature distribution. If the temperature distribution is approximated with a quadratic polynomial, the thermal boundary layer thickness is found by the integral method as described in Arpaci (1966) to be:

$$\delta(t) = \sqrt{6at} \tag{6.4}$$

and with the x coordinate axis shown in Figure 2.2a the liquid temperature distribution from the integral method is:

$$\Delta T_i = T(x) - T_i = \frac{q''_l}{2k_l} \frac{(x - \sqrt{6at})^2}{\sqrt{6at}} \tag{6.5}$$

The integration of the approximate solution, equation 6.5, is more convenient than that of the analytic solution, equation 6.1, with an error of approximately 2%. However, the integration of the exact expression, equation 6.1, was used in Table 6.2.

6.5 Bubble Shape at Onset of Rapid Unstable Spreading in Microgravity

From Figures 5.23 through 5.25, the photos for the microgravity tests in which the imposed heat flux resulted in the rapid unstable and violent boiling spreading, categories D and E respectively, the bubble was initially smooth and symmetrical (This smooth and symmetrical bubble is not pictured here.), but later in time, Figures 24a and 24b for example, the bubble ruptures at the liquid-vapor interface and then rapid spreading occurs. The correlation of the bubble shape at the moment of this rupture in dimensionless form with the dimensionless heat flux is examined here.

For the physical situation in microgravity with no fluid motion, it is reasonably assumed that one dimensional conduction describes the heat transfer from the heated surface. For this situation the differential form of the energy equation is:

$$\frac{\partial^2 T}{\partial x^2} = \frac{\partial T}{\partial t}\frac{1}{\alpha} \tag{6.6}$$

with the boundary condition:

$$q'' = -k\left(\frac{\partial T}{\partial x}\right)_{x=0} \tag{6.7}$$

From equation 6.6, in terms of the physical dimensions of the situation:

$$\frac{T}{\delta^2} \sim \frac{T}{\tau} \quad \text{or} \quad \delta \sim \tau^{\frac{1}{2}} \tag{6.8}$$

where δ is the diffusion length scale defined in terms of some characteristic temperature difference. τ is the characteristic time scale. Figure 6.16 shows a small

bubble with D, the largest diameter parallel to the heater surface, and with H, the x coordinate dimension. The projected area of the bubble over the heating surface is much smaller than the total area of the heating surface, and the effect of the bubble presence, resulting in local cooling due to the phase change, on the remainder of the superheated thermal boundary layer is assumed to be negligible.

From consideration of the energy equation 6.6 and equations 6.7 and 6.8 it may be deduced that:

$$D = f_1(T, q'', \delta, k, H) \tag{6.9}$$

where T is a characteristic temperature, q" is the heat flux, and k is the liquid thermal conductivity. From the application of the Buckingham Pi theorem, three dimensionless groups are found:

$$\frac{D}{H} = f_2\left[\frac{\delta}{H}, \frac{q''H}{kT}\right] \tag{6.10}$$

H appears on both sides of equation 6.10, and it is desirable to have the dependent variables on one side of the dimensionless relationship only. The two dimensionless groups on the RHS of equation 6.10 are multiplied resulting in two dimensionless groups:

$$\frac{D}{H} = f_3\left[\frac{q''\delta}{kT}\right] \tag{6.11}$$

T is a characteristic temperature which may be a temperature difference. With T_w-T_s as the characteristic temperature in this situation, δ is taken as δ^*, the superheated thermal boundary layer at the time just prior to rupturing, and:

$$\frac{D}{H} = f_4\left(\frac{q''\delta^*}{k(T_w-T_s)}\right) \tag{6.12}$$

Measurements of D, H, and (T_w - T_s) were obtained at the onset of boiling for the experiments conducted in microgravity, and combined with the corresponding values of δ^* in equation 6.12. The dimensionless shape of the bubble about to rupture was correlated with the heat flux imposed at the heater surface, which was made dimensionless in equation 6.12, and these quantities are plotted in Figure 6.17. The boiling spread became more violent as the dimensionless heat flux increased, which corresponds to the tests to the right of the dashed line. The lower limit of this relationship is characterized by the slow, category F boiling spread.

6.6 Explosive Boiling Spread in Microgravity

Following the appearance of a single bubble on the heating surface at a low heat flux level near saturation conditions, the explosive type of boiling spread, category E, was observed for the first time in the present microgravity experiments as described in Section 5.1.1.6, Figures 5.25a through 5.25g and briefly referred to in section 6.5 in the discussion of the bubble shape and corresponding dimensionless heat flux. The rapidly growing vapor-liquid interface was covered with small scale disturbances which remained small at initial times, but these protuberances grew in size with time, as seen in Figures 5.25a through 5.25g. The rapidly growing vapor

mass with the interface disturbances pushed into the subcooled liquid located above the visible thermal boundary layer. Boiling inception was accompanied with a momentary spike in the measured pressure as indicated in Figure 5.10.

In classical bubble growth theories, the bubble is assumed to grow from a smooth spherical vapor bubble in a uniformly superheated liquid, and heat transfer effects are considered in the liquid but thermodynamic equilibrium is assumed for the vapor. These theories describe three consecutive stages of bubble growth: very early surface tension controlled growth followed by inertia controlled growth which is, in turn, followed by a heat diffusion dominated stage. An example of such theories are presented in Prosperetti and Plesset (1978). Figure 6.18 shows two limiting conditions for vapor bubble growth, along with the measured growth rate of the vapor mass in microgravity for experiment PBMT1101.600. The Rayleigh solution for bubble growth which is applicable to boiling, cavitation, and underwater explosions is shown as the upper limit on the growth rate. The Rayleigh solution applies to a spherical bubble growing in an infinite fluid, and assumes that the sphere expands radially outward producing a purely irrotational radial flow through the action of pressure forces alone. Panton (1984) gives the Rayleigh solution using the velocity potential and continuity equation in spherical coordinates with the Bernoulli equation. The boundary conditions specified that the fluid was stationary at infinity and that it followed the sphere motion at the sphere surface, with the resulting differential equation for the interface motion:

$$\frac{P(R)-P_{\infty}}{\rho} = R\,\frac{d^2R}{dt^2} + \frac{3}{2}\left[\frac{dR}{dt}\right]^2 \qquad (6.13)$$

where R is the bubble surface radius and ρ is taken as a constant. If P(R), the saturation pressure corresponding to the heater surface temperature at the time of the appearance of the first bubble, and P_∞ are assumed constant as a first approximation, then R(t) and R'(t) are readily determined from equation 6.13. The step in pressure from P_∞ to the saturation pressure corresponding to the heater surface temperature is considered to provide a higher than expected growth rate. The solution for R(t) appears in Figure 6.18. The other analytical solution is for heat diffusion controlled growth of the vapor bubble, and provides the lower limit. During early stages of bubble growth the pressure forces are expected to control growth and at later times heat diffusion is expected to control growth. For the present case, neither of these solutions is closely followed. The effective radius used in the measurements of Figure 6.18 is defined in Figure 6.19. Limitations in the measurements of the growth rates at the early time periods exist due to the relatively slow framing rate of the camera, 400 fps, which are indicated by the data points in Figure 6.18.

The type of boiling spread shown in Figures 5.25a through 5.25g is explosive and has not been previously observed for the conditions of no liquid motion during heating provided by microgravity. These photographs suggest that extremely large evaporation rates occur during early stages of the bubble growth which drive an instability at the bubble interface. A wrinkling of the liquid-vapor interface occurs which persists for some time after the vapor mass has covered the entire heating surface, Figures 5.25a through 5.25e. The pattern of protuberances covers the entire liquid-vapor interface, and the regularity of the pattern is striking. It is speculated that the presence of the small scale protuberances greatly increases the area of the liquid-vapor interface, which significantly increases the mass flux to the growing vapor bubble, which in turn drives the instability. It is also speculated that the wrinkles somehow arise from very rapid evaporation at the interface.

Similar small scale interface disturbances and large growth rates have been observed by Shepherd and Sturtevant (1981) and McCann et al (1988). In the experimental investigation of Shepherd and Sturtevant, a droplet of butane immersed in (immiscible) ethylene glycol in a bubble column apparatus at the homogeneous nucleation temperature was observed to vaporize explosively. At the periphery of the bubble, wrinkles were observed similar to those shown in Figures 5.25a through 5.25e and were believed to be driven by rapid instability. The wrinkles were speculated, but not proven, to be the result of the so-called Landau mechanism of instability, which is described in Landau (1944). Shepherd and Sturtevant used experimental pressure measurements to estimate the evaporation rate associated with the observed instability, and they found that the evaporation rate corresponding to this instability was two orders of magnitude greater than that predicted by conventional bubble-growth theories. Shepherd and Sturtevant believed that the large mass flux across the distorted liquid-vapor interface generated vorticity responsible for the Landau instability in the vapor by the flow transition at the interface. Vapor bubble growth in slightly superheated liquids has been investigated extensively, and this wrinkling of the interface was not seen earlier. The liquid superheat temperatures prior to the occurance of homogeneous nucleation, in the work of Shepherd and Sturtevant, were atypically large for butane, about 105 °C.

The present experiments are different from those of Shepherd and Sturtevant in that the liquid in the present study was heated from a solid boundary in the presence of a comparatively large temperature gradient, and the heater surface temperature in the present study was below the homogeneous nucleation temperature for the given liquid pressure, in test PBMT1101.600 ($T_w / T_{hom} \cong 0.9$). The heater surface temperature at incipient boiling for test PBMT1101.600 was 120 °C, which corresponded to a heater surface superheat of nearly 75 °C. This heater surface superheat temperature at boiling inception for the present test conditions is large when compared to other observed

values of the heater surface superheat temperature at incipient boiling for R113 on glass in earth gravity, as described in You et al (1990) .

6.7 Empirical Heterogeneous Nucleation Factor

As discussed previously in Chapter 2, the form of the homogeneous nucleation rate used here was given by Fisher (1948):

$$J=\frac{nkT}{h}\exp\left(\frac{-\Delta G^*}{kT}\right) \tag{6.14}$$

In the presence of a solid heating surface, ΔG^* can be expected to be considerably lower than that for homogeneous nucleation. This lowering of the thermal activation energy has been incorporated into the description of heterogeneous nucleation in terms of a dimensionless parameter defined as:

$$F=\frac{\Delta G_{het}}{\Delta G^*} \tag{6.15}$$

F is a positive number varying between zero and unity: zero implies no nucleation while unity corresponds to homogeneous nucleation. Kottowski (1973), Cole (1974), and Blander and Katz (1975) defined F in terms of a specific cavity geometry. In most situations, however, the actual cavity geometry and surface topography are seldom known, since typical boiling surface cavities are extremely small (on the order of 10^{-7} to 10^{-9} m).

Since the cavity geometry is difficult to determine at present, Gerum et al (1979) and Ngheim et al (1981) attempted to define F empirically, as discussed previously in Chapter 2. Gerum calculated F values based on measured heater surface

temperatures during quasi-steady heating, and included boiling crisis data in his work. Ngheim et al also defined F empirically in terms of the measured heater surface temperature during transient heating at the instant of the appearance of the first bubble. Since the heterogeneous nucleation appeared to take place in the fluid immediately adjacent to the heater surface, the fluid temperature was taken to be the same as the heater surface temperature. The validity of using the measured heater surface temperature and measured system pressure to determine F is re-examined here. Since the present study is primarily concerned with transient incipient boiling, the work of Ngheim et al (1981) is discussed first, followed by a discussion applicable to both the work of Ngheim et al (1981) and Gerum et al (1979).

In the work of Ngheim et al (1981), the dimensionless heterogeneous nucleation factor, F, was calculated based on the measured heating surface temperature at the instant of nucleation, and was plotted against the dimensionless temperature difference:

$$\theta = \frac{T_w - T_s}{T_{hom} - T_s} \tag{6.16}$$

for various transient boiling nucleation data.

F may be written from equations 2.4, 2.5, and 2.16 as:

$$F = \left[\ln \left(\frac{nkT_w t^*}{h} \right) \right] \frac{3kT_w (P_v - P_l)^2}{16\pi\sigma^3} \tag{6.17}$$

t*, as defined earlier, is the time delay from the onset of heating of the liquid to the appearance of the first vapor bubble. In the development of equation 6.17, J was taken to be 1/t* as a reasonable first approximation. P_v was taken approximately as the saturation pressure with a flat interface, corresponding to the heater surface temperature at nucleation. σ was evaluated at the heater surface temperature at nucleation.

t* may be neglected as a parameter in equation 6.17 since it appears in the logarithmic term. This can be demonstrated by expanding the logarithmic term as:

$$\ln\left(\frac{nkT_w t^*}{h}\right) = \ln\left(\frac{nkT_w}{h}\right) + \ln t^* \qquad (6.18)$$

The first term of the RHS of equation 6.18 is the natural log of a quantity with a typical magnitude of about 10^{30} seconds, but t* of the second term of the RHS of equation 6.18 is much less than 10^{30} seconds for most boiling situations. (As a matter of reference, 10^8 seconds is about 100 years.)

To quantify this explicitly, consider R113 near saturation conditions initially at a temperature of 310 K, and heated to a temperature of 320 K at the surface. With the appropriate properties substituted into equation 6.17, F becomes:

$$F = 7 \times 10^{-8} (93 + \ln t^*) \qquad (6.19)$$

t* may be varied by as much as 10^5 seconds with a resulting change of only 12% in F. Similar behavior also occurs with liquid nitrogen and water. Hence, F, assumed to be a measure of the liquid-heater surface character, is a strong function of the heater surface temperature at nucleation, but a weak function of the delay time to nucleation,

and the nucleation delay time cannot necessarily be used as a parameter to characterize the heater surface. Thus t* may be neglected when:

$$\frac{\ln t^*}{\ln \frac{nkT_w}{h}} << 1 \qquad (6.20)$$

The condition of equation 6.20 is expected to hold for typical engineering boiling applications for reasons given in connection with equation 6.18.

Both the work of Ngheim et al (1981) and of Gerum et al (1979) rely on the concept that F, which results from the measured heater surface temperature and the liquid pressure, are representative of the heater surface-fluid character. Because of the exponential nature of J in equation 6.14, a narrow range of F may be calculated for a large range in J (over several orders of magnitude). To demonstrate the consequences of this behavior, J was set equal to 1 sec^{-1} cm^{-3} (a reasonable value for the present experimental study) and curves for F were calculated for R113 at three different liquid pressure levels of 1, 2, and 3 atm. Figure 6.20 presents F, as defined in equation 6.17, as a function of θ, defined in equation 6.16, for R113 for these three pressures. T_{hom} for each of the three pressure levels and the corresponding curves which show calculated data points are also given in the figure. A distinctly different curve results for each of the pressure levels, which implies that the relationship for F is property dependent, and not universal. The F curves, by definition, approach unity as θ approaches unity and approach zero as θ approaches zero. F may indeed be a function of the solid surface and liquid-surface character and is not described by nucleation delay times, but perhaps from heater superheat temperature at nucleation, or some related function, together with equation 6.17.

In the work of Ngheim et al (1981) and Gerum et al (1979) and similar works, it was thought that there might be a general relationship between F and the dimensionless heater surface temperature, which was independent of the fluid type because F data calculated from measured heater surface temperatures for water and R113 heated with the same heater surface fell approximately on a single curve. In light of the present discussion, it is fortuitous that the calculated F values fell on a single curve. Considerable work remains for the more precise description of the nucleation characteristics of solid surfaces.

6.8 Conclusions

The main points of the present study are now summarized:

1. Known temperature distributions in the heated liquid at the moment of boiling incipience, obtained in microgravity or for short times with the heater surface inverted in standard earth gravity, were shown to characterize the subsequent boiling propagation across the heated surface. Large superheated thermal boundary layers formed in the conditions of microgravity and low heat flux levels on a "smooth" surface are associated with a particularly explosive type of boiling spread previously unobserved, which is believed to be the result of an interfacial instability driven by a large mass flux across the wrinkled liquid-vapor interface.

2. Buoyancy was shown to greatly affect the phase change dynamics associated with incipient boiling. Buoyancy, which produced fluid motion, affected the liquid temperature distribution during heating and the subsequent boiling propagation. Certain types of boiling spread, such as the explosive type of spreading, were observed only in microgravity, and not in earth gravity for either the horizontal up or the horizontal down heater surface orientations. Buoyancy induces convective motion

which reduces the energy of the superheated thermal boundary layer that would otherwise be available for boiling propagation. The buoyancy force carried vapor bubbles away from the heater surface when the heater surface was in the horizontal up orientation in earth gravity, but held vapor bubbles at the heater surface for the horizontal down orientation.

3. The method of heating the liquid determines the temperature distribution in the liquid, which affects the resulting phase change dynamics significantly. The tests conducted with an imposed heat flux resulted in larger superheated thermal boundary layers than did the tests conducted with imposed step changes in surface temperature. As a result, the boiling spread after boiling incipience was markedly different. The temperature gradient in the fluid at the heater surface was greater with the imposed step change in surface temperature than in the fluid with the imposed heat flux, but the phase change dynamics with the imposed heat flux were more violent. In addition, the onset of boiling with the imposed step change in surface temperature occurred at significantly shorter delay times and lower heater surface temperatures than those for imposed heat fluxes.

6.9 Recommendations for Future Study

Because of the physical limitations of the drop tower, the microgravity tests in the present work were of short duration (about 5 seconds). For these tests, boiling propagation categories D and E at the low heat flux levels, on the order of 5 W/cm^2, were particularly striking. It would be desirable to perform microgravity incipient boiling tests at lower heat flux levels, on the order of 0.5 to 2 W/cm^2, for longer times than was possible with the drop tower experiments. As a result of the knowledge gained from the present experiments, low level heat flux experiments are being planned for a future space shuttle flight.

Figures 6.1 - 6.20 follow.

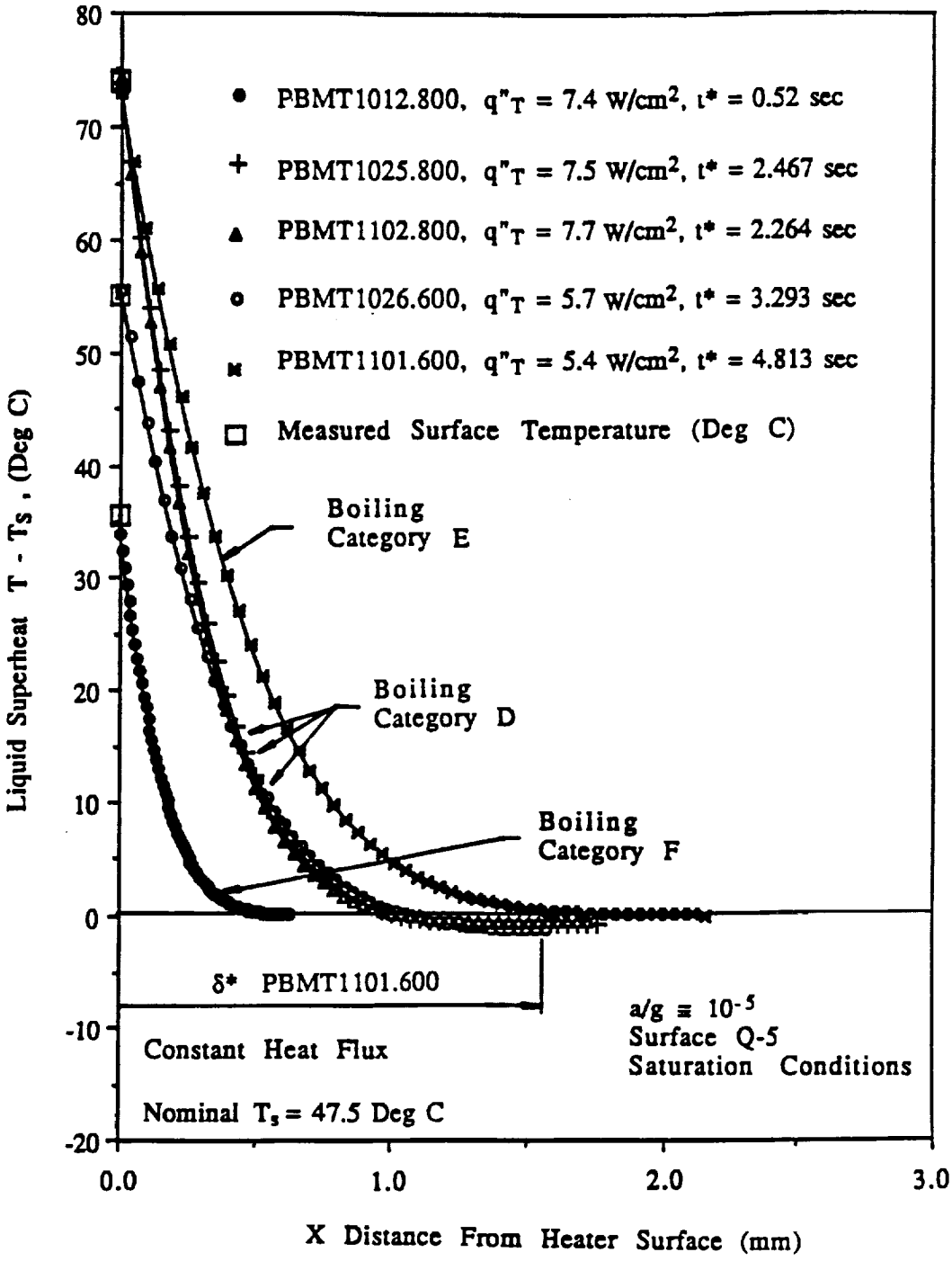

Figure 6.1 Computed liquid superheat in microgravity from imposed heat flux at boiling inception, saturation conditions (surface Q-5)

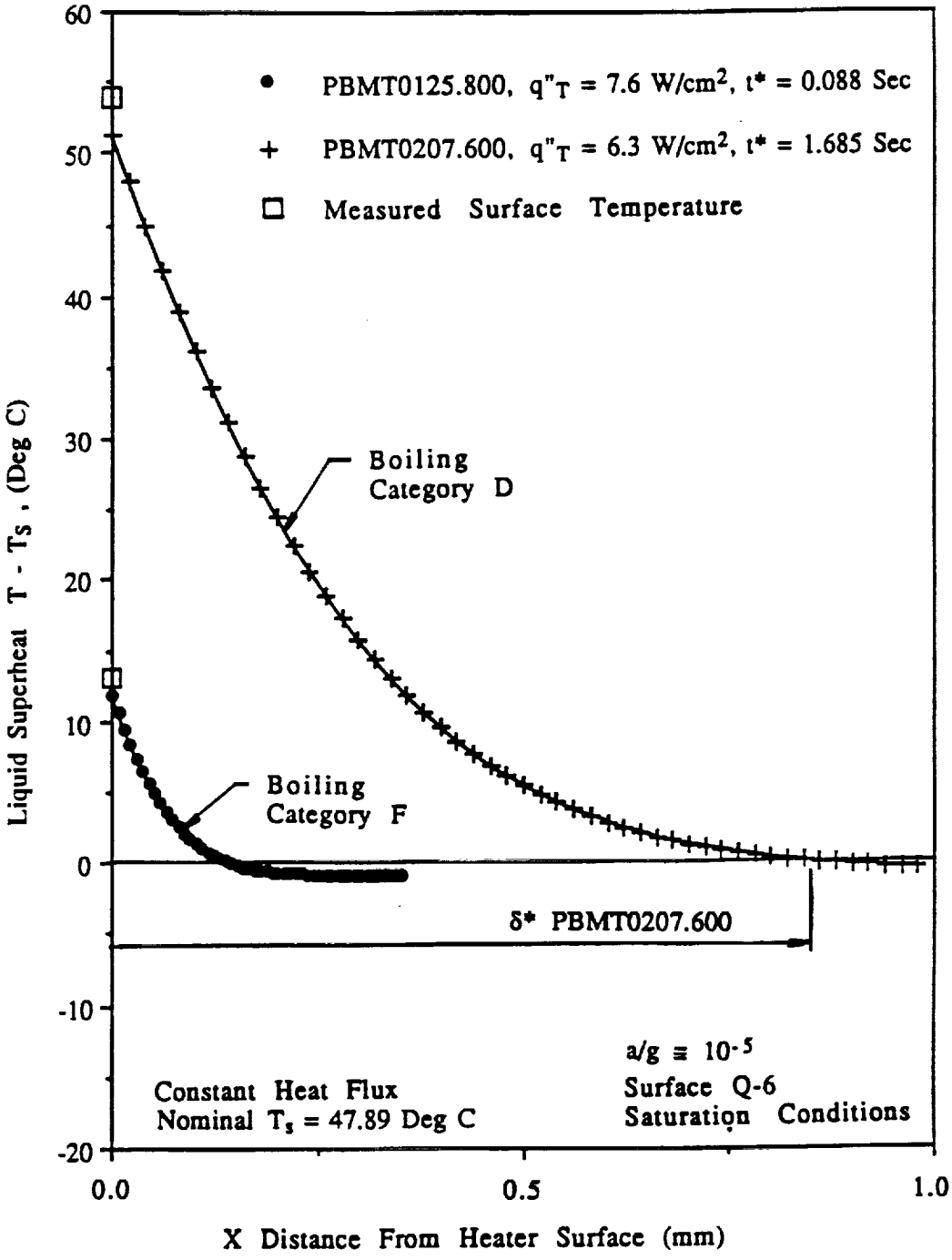

Figure 6.2 Computed liquid superheat in microgravity from imposed heat flux at boiling inception, saturation conditions (surface Q-6)

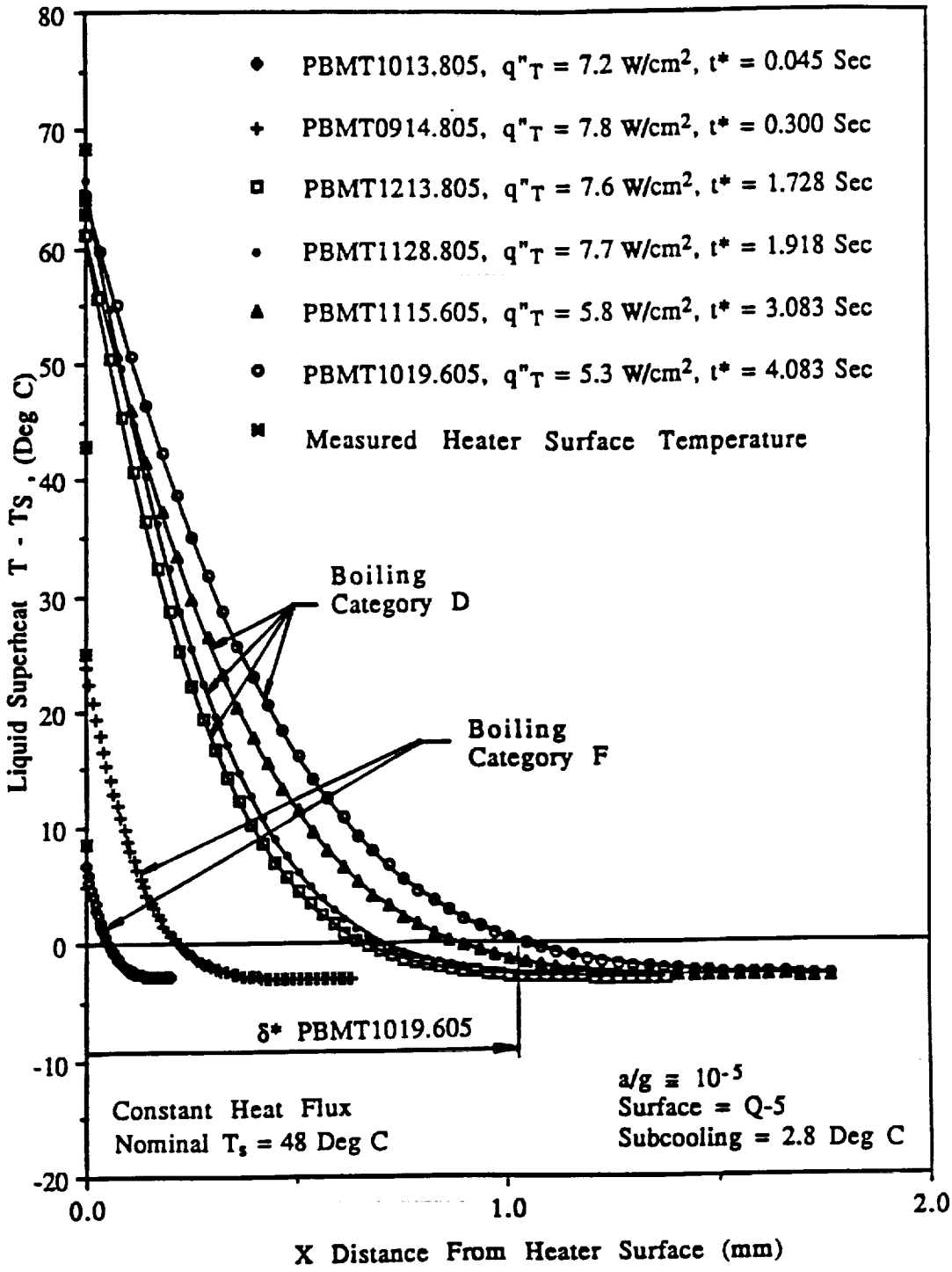

Figure 6.3 Computed liquid superheat in microgravity from imposed heat flux at boiling inception, 2.8 °C subcooling (surface Q-5)

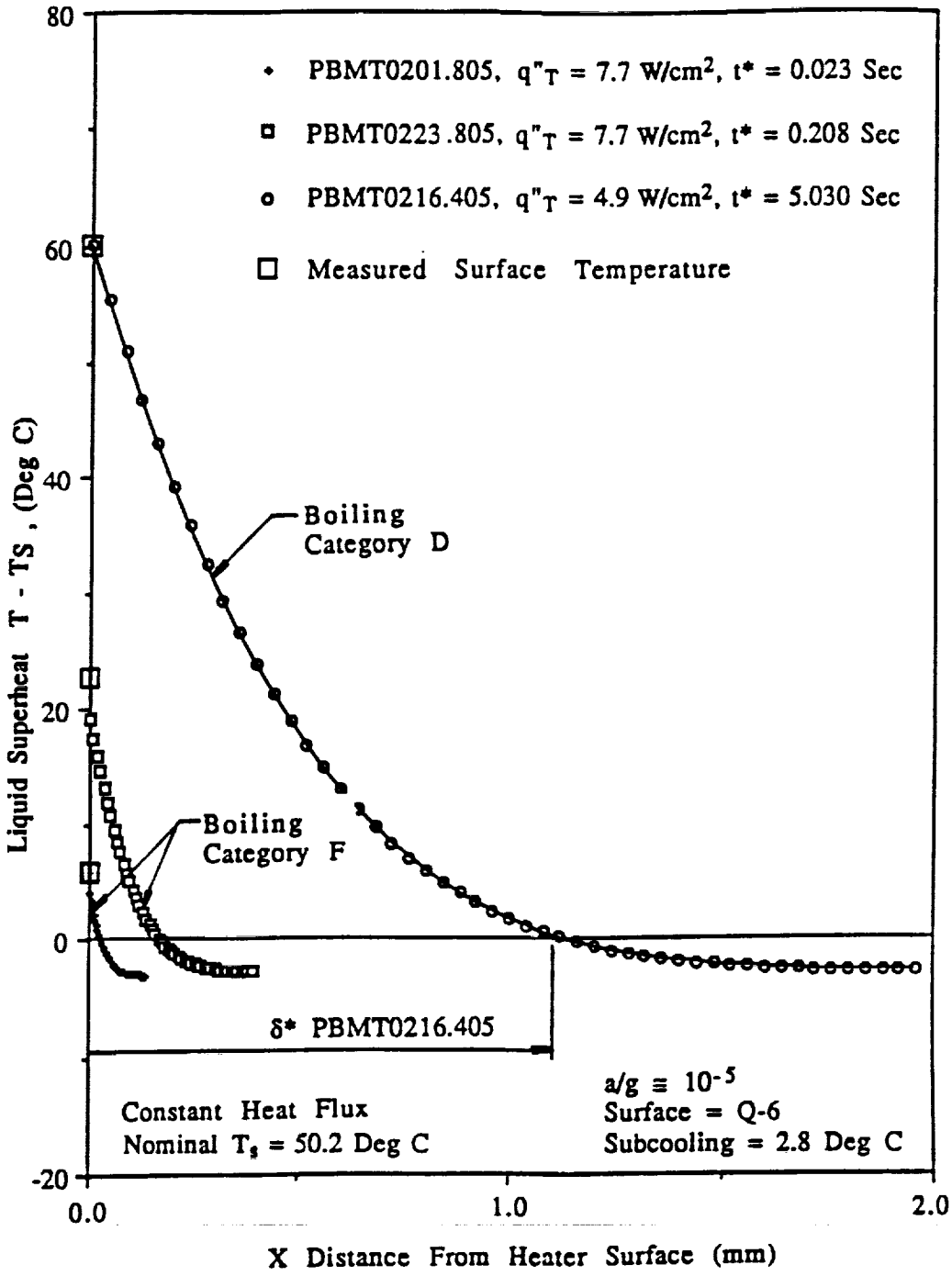

Figure 6.4 Computed liquid superheat in microgravity from imposed heat flux at boiling inception, 2.8 °C subcooling (surface Q-6)

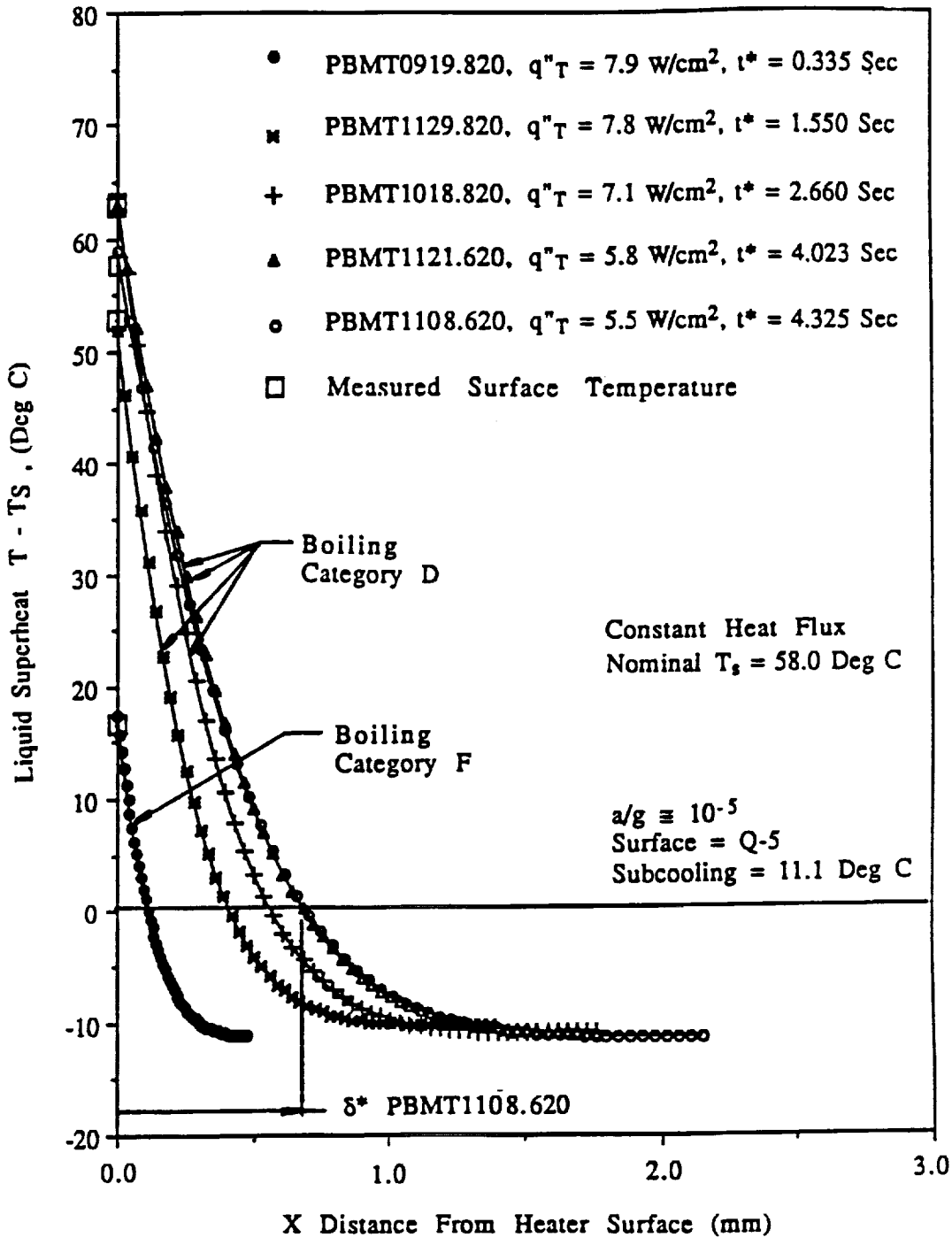

Figure 6.5 Computed liquid superheat in microgravity from imposed heat flux at boiling inception, 11.1 °C subcooling (surface Q-5)

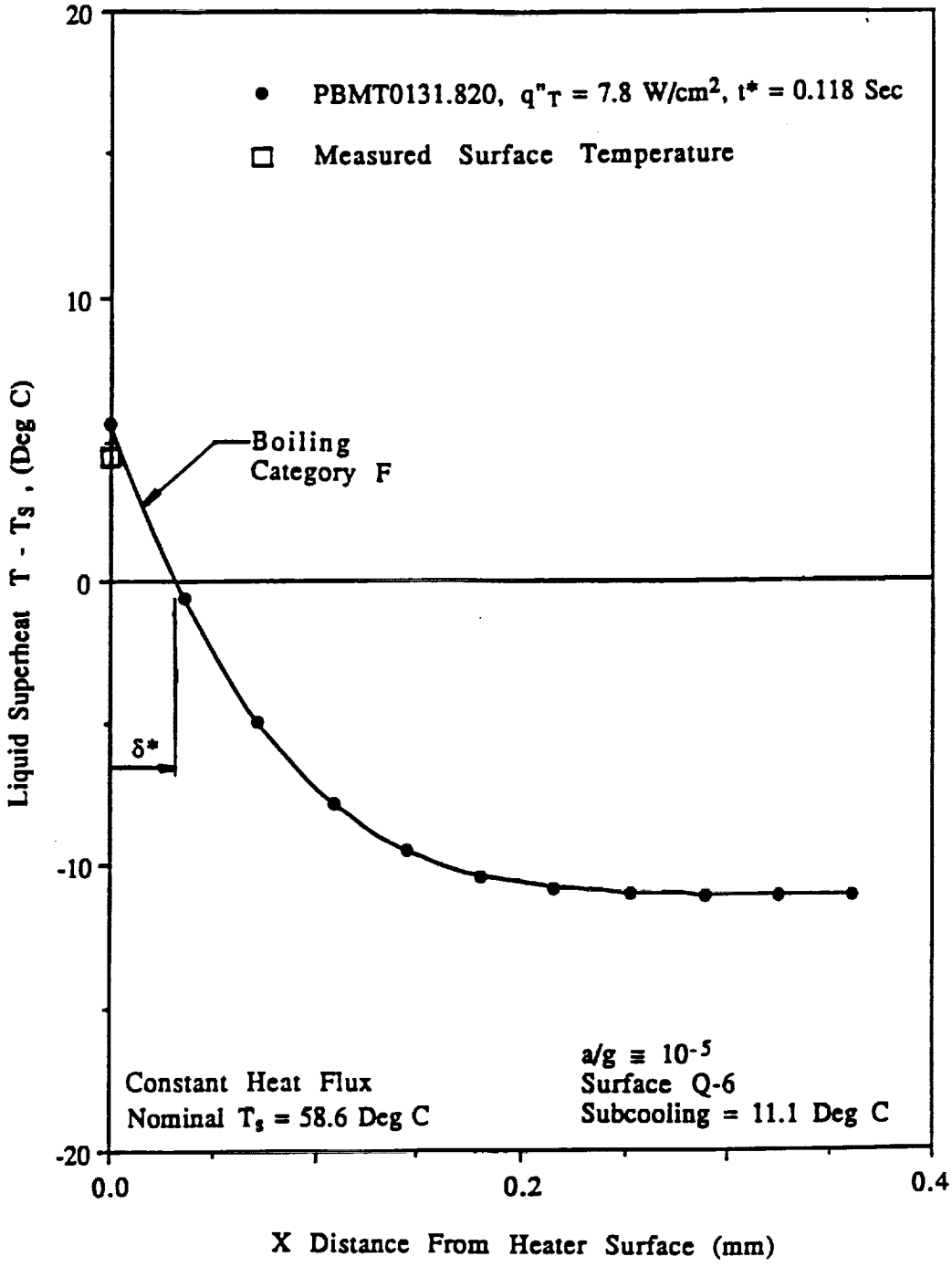

Figure 6.6 Computed liquid superheat in microgravity from imposed heat flux at boiling inception, 11.1 °C subcooling (surface Q-6)

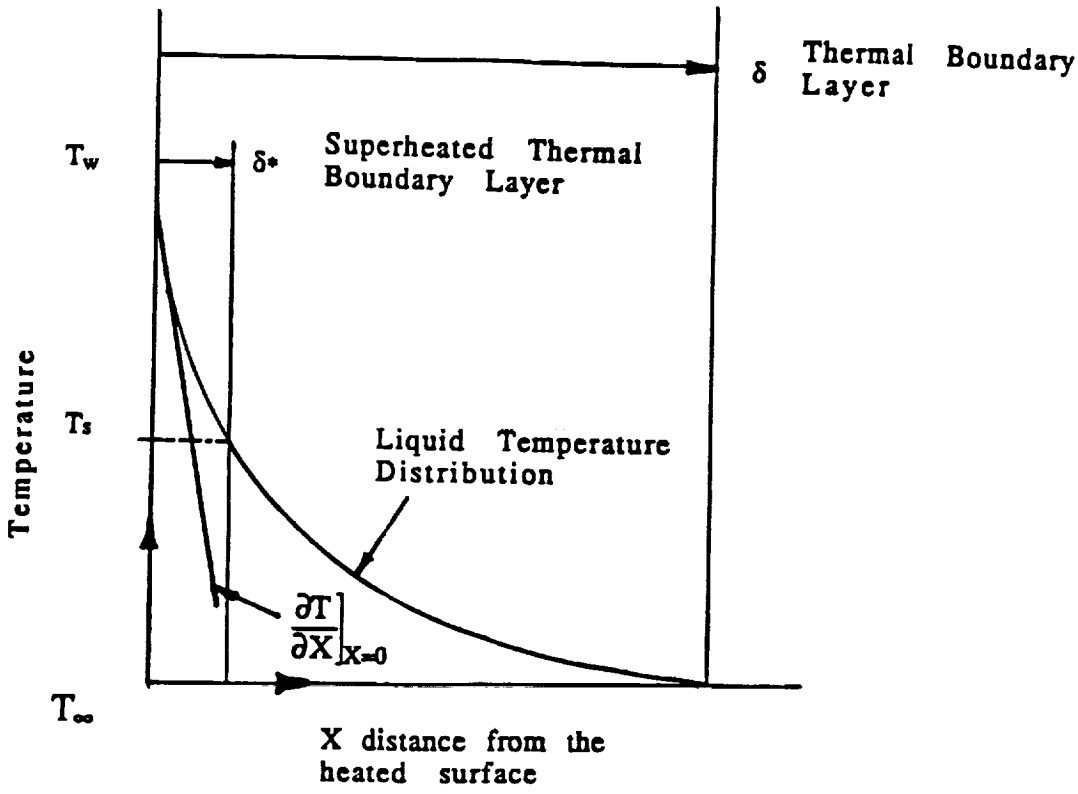

Figure 6.7 The concepts of superheated thermal boundary layer and thermal boundary layer

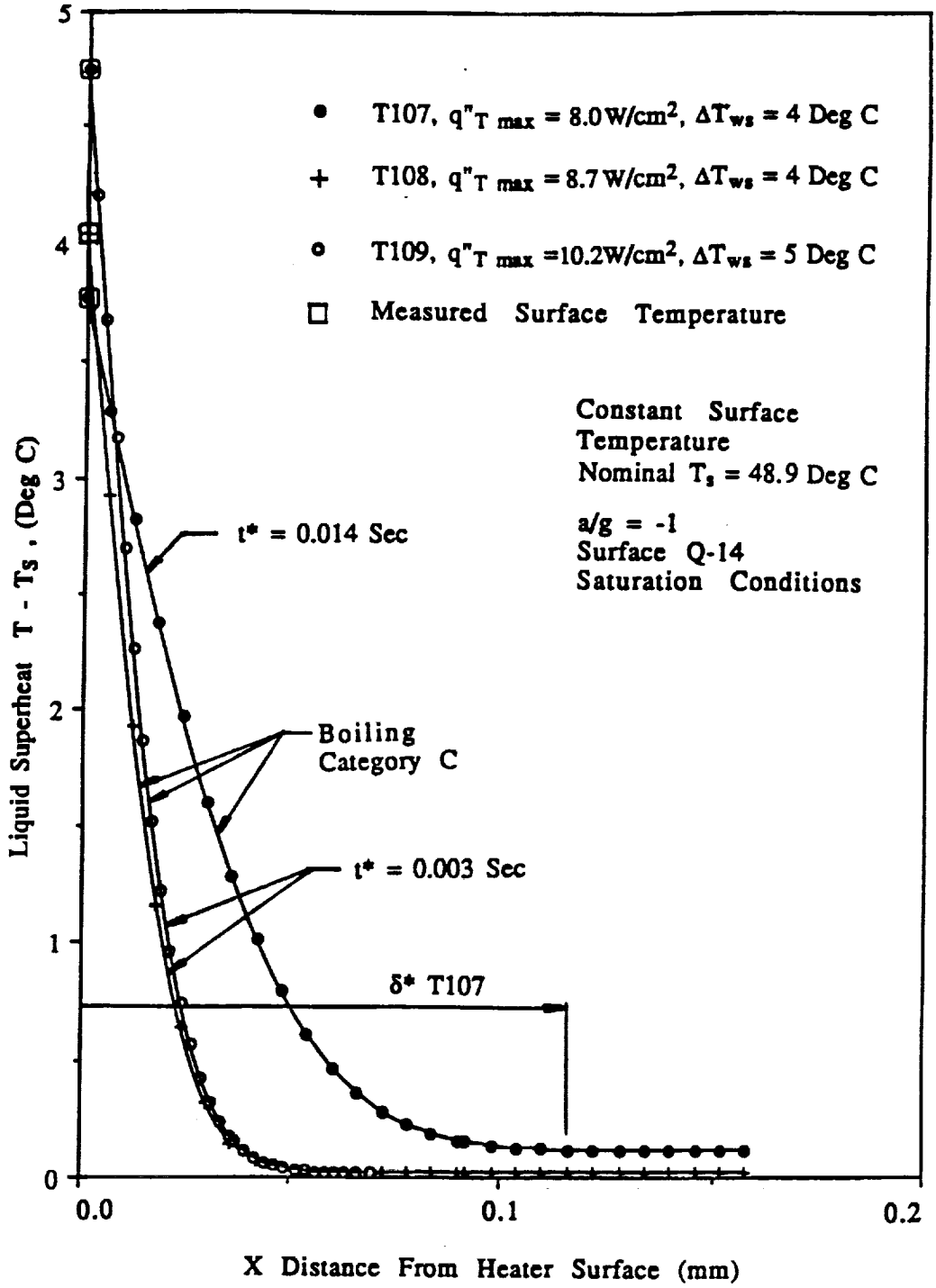

Figure 6.8 Computed liquid superheat from imposed surface temperature at boiling inception, saturation conditions (surface Q-14)

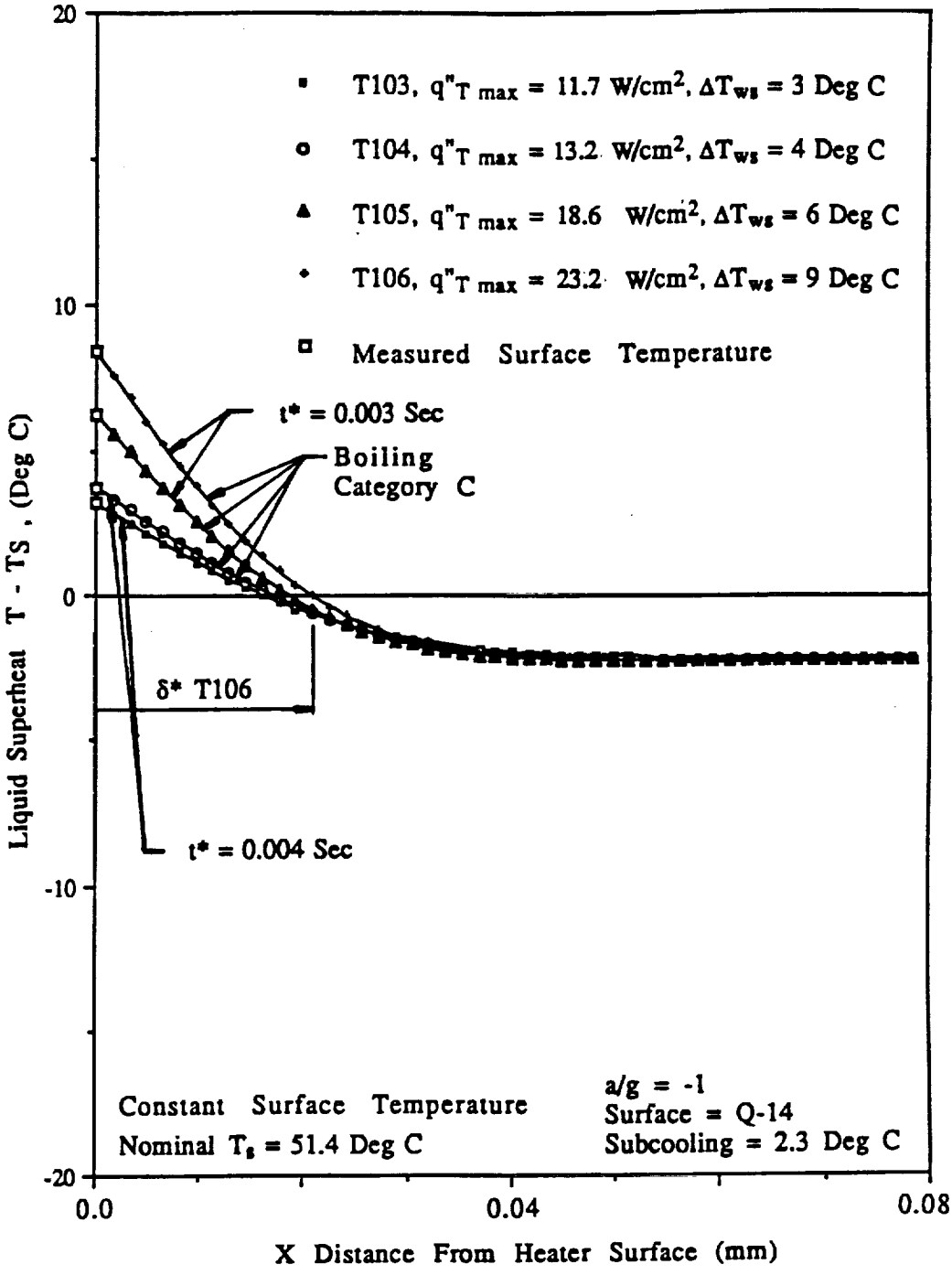

Figure 6.9 Computed liquid superheat from imposed surface temperature at boiling inception, 2.3 °C subcooling (surface Q-14)

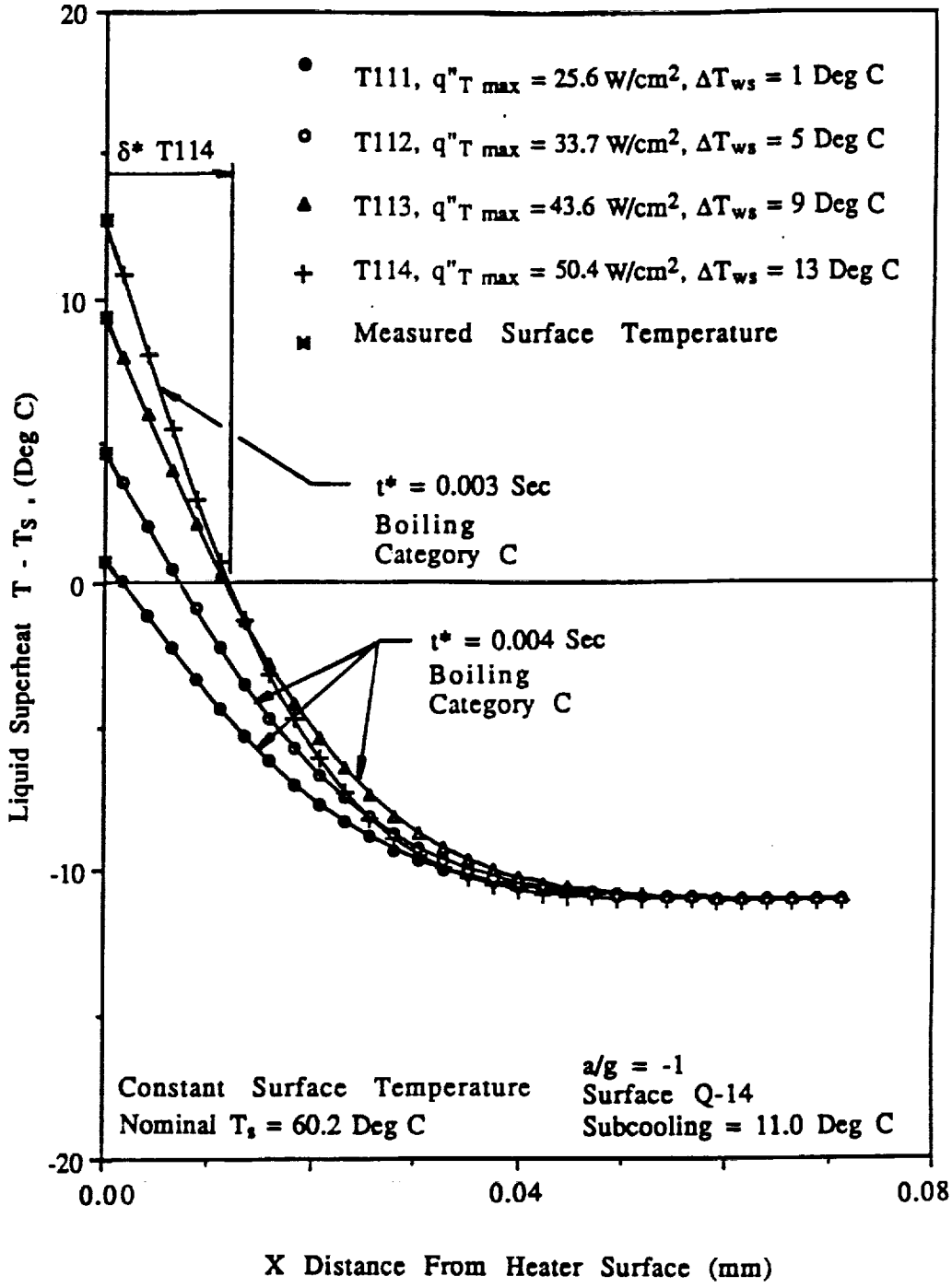

Figure 6.10 Computed liquid superheat from imposed surface temperature at boiling inception, 11.0 °C subcooling (surface Q-14)

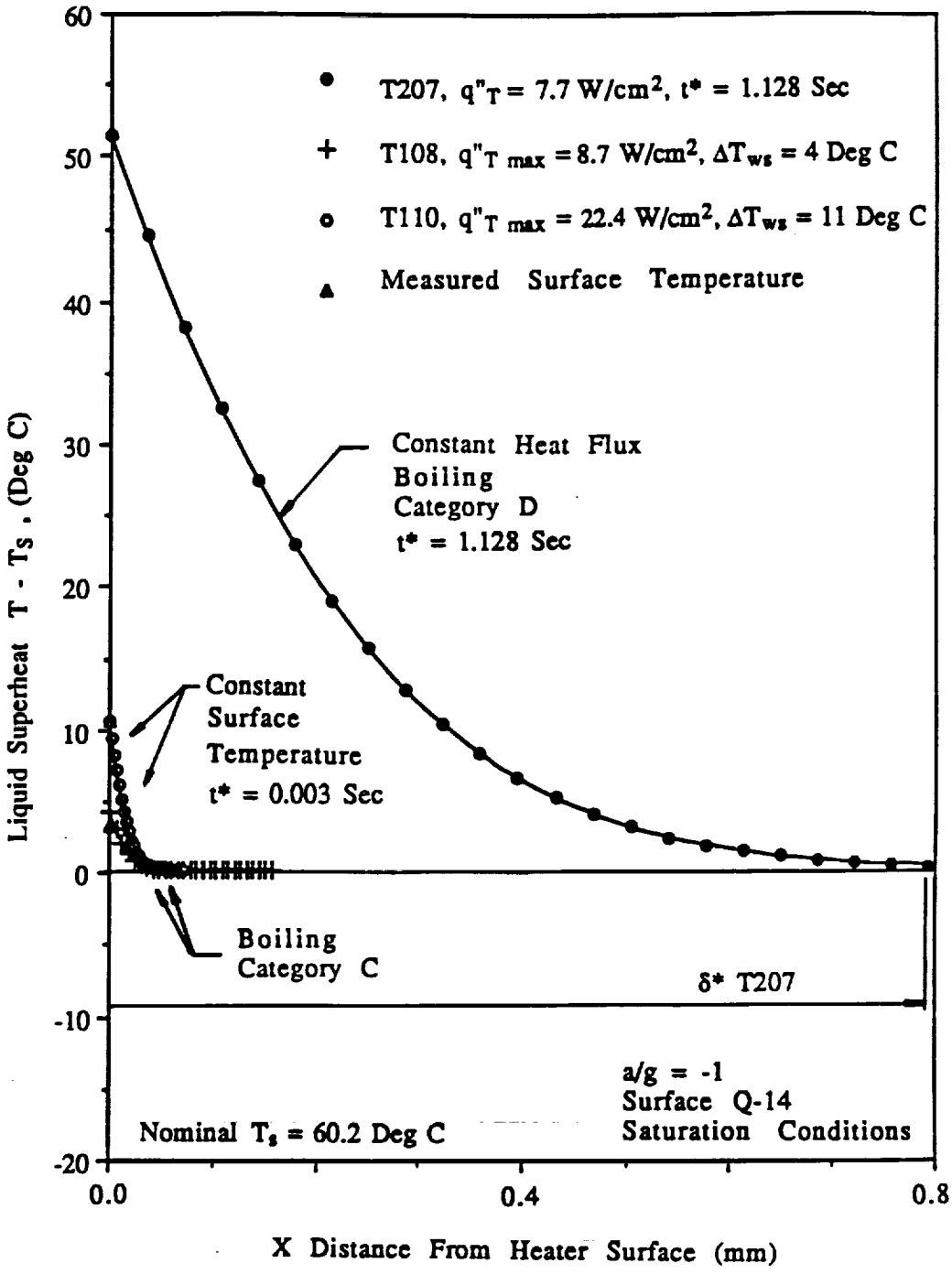

Figure 6.11 Comparison of computed imposed constant heat flux and constant surface temperature liquid temperature distributions, saturation conditions (surface Q-14)

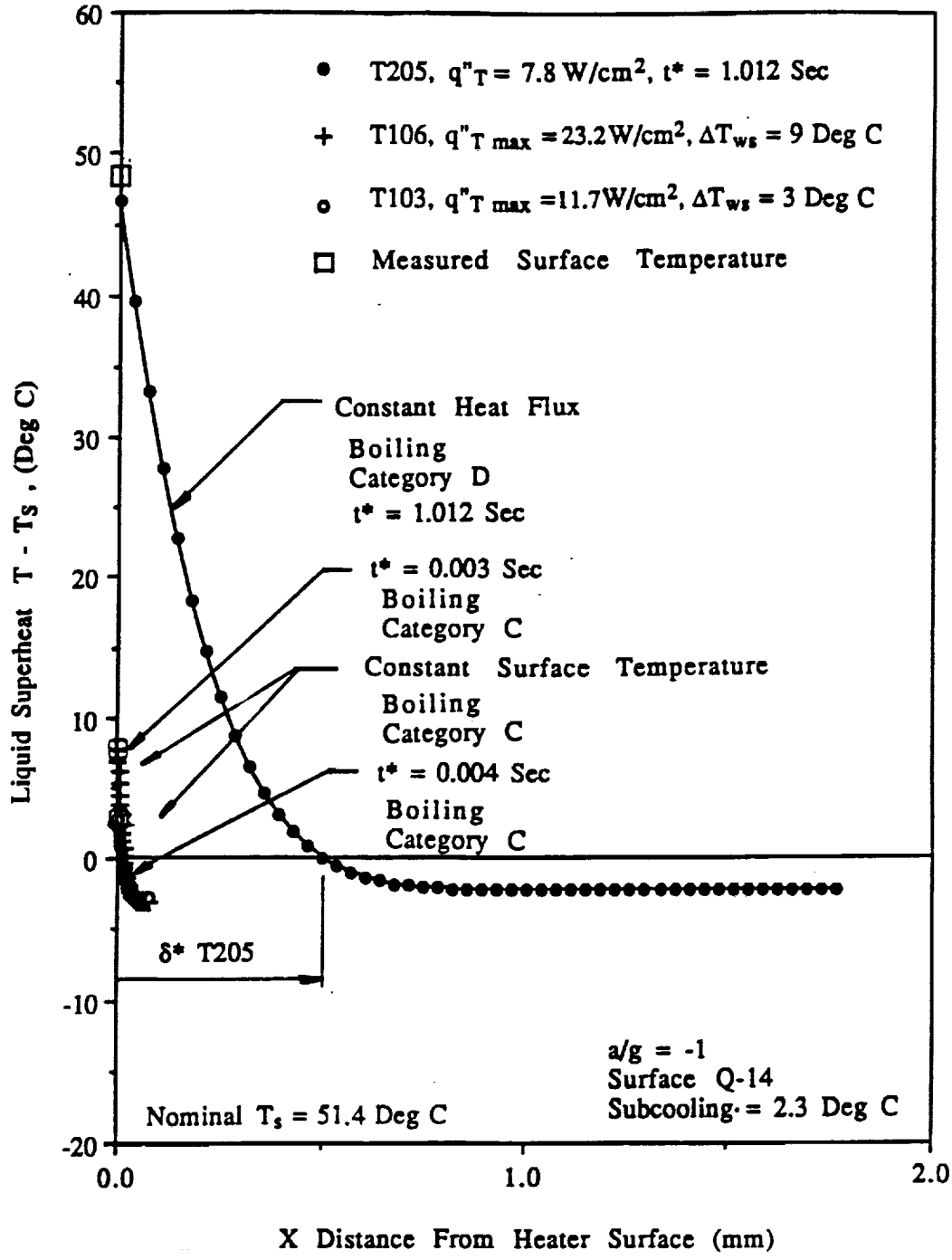

Figure 6.12 Comparison of computed imposed constant heat flux and constant surface temperature liquid temperature distributions, 2.3 °C subcooling (surface Q-14)

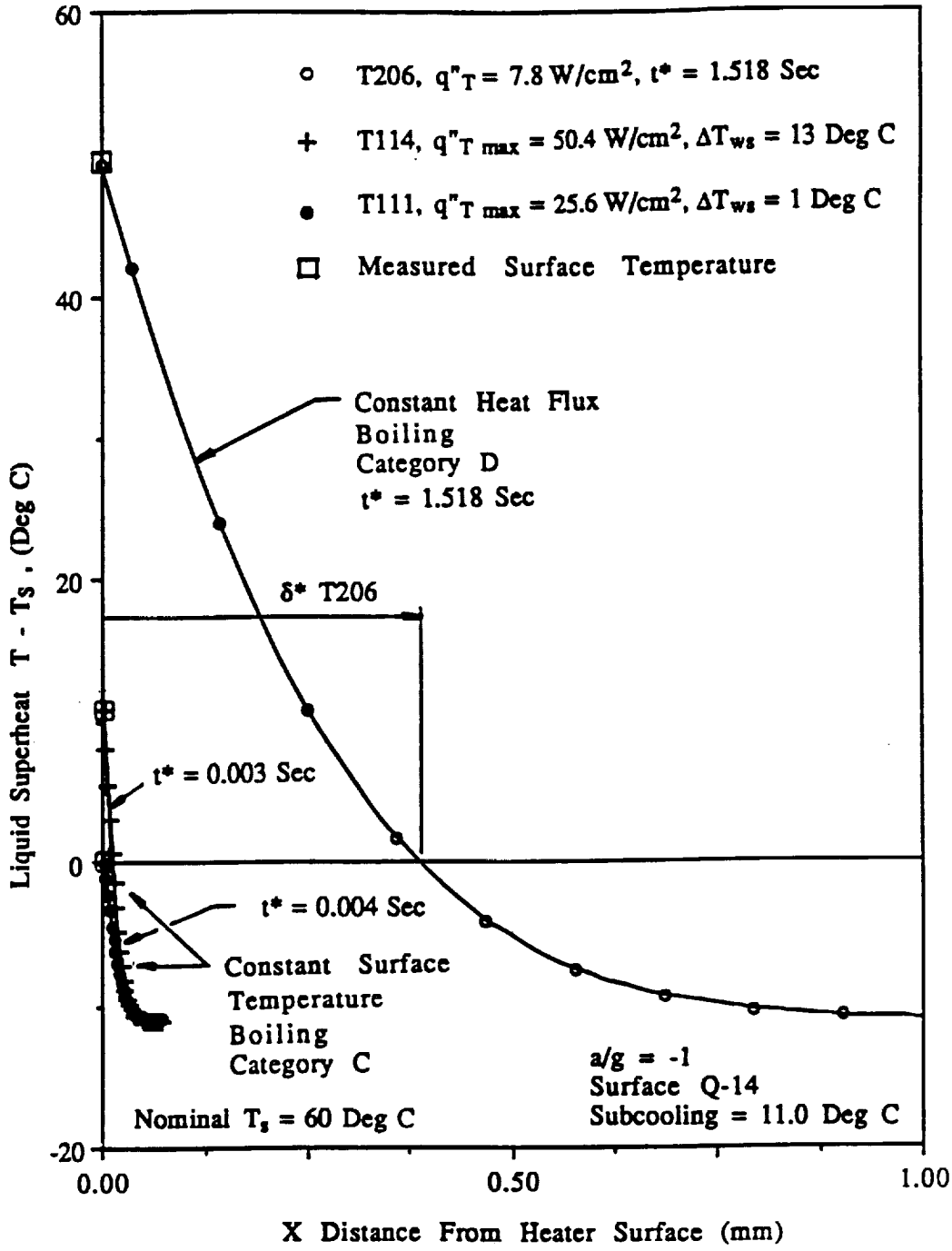

Figure 6.13 Comparison of computed imposed constant heat flux and constant surface temperature liquid temperature distributions, 11.0 °C subcooling (surface Q-14)

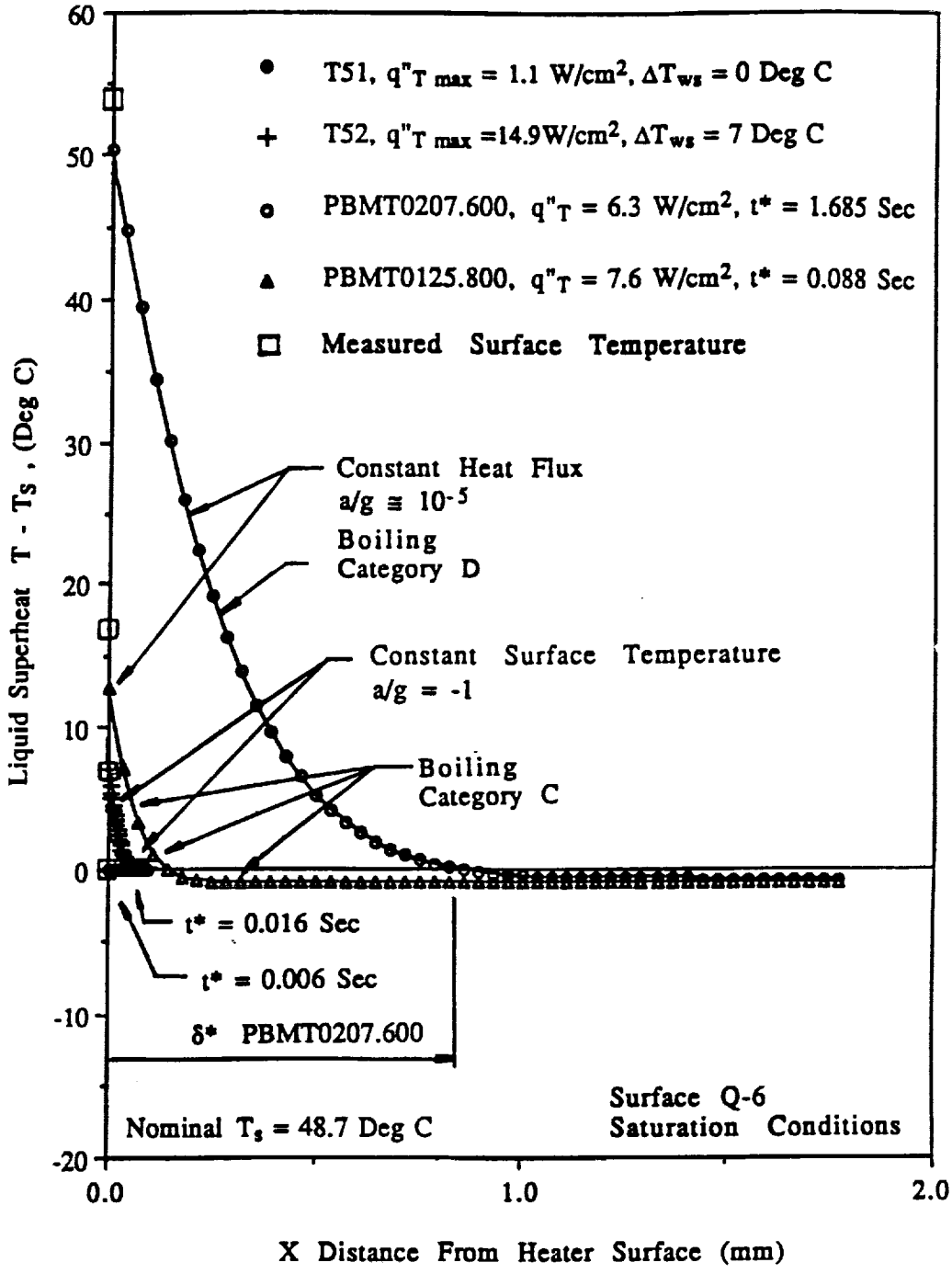

Figure 6.14 Comparison of computed imposed constant heat flux and constant surface temperature liquid temperature distributions, saturation conditions (surface Q-6)

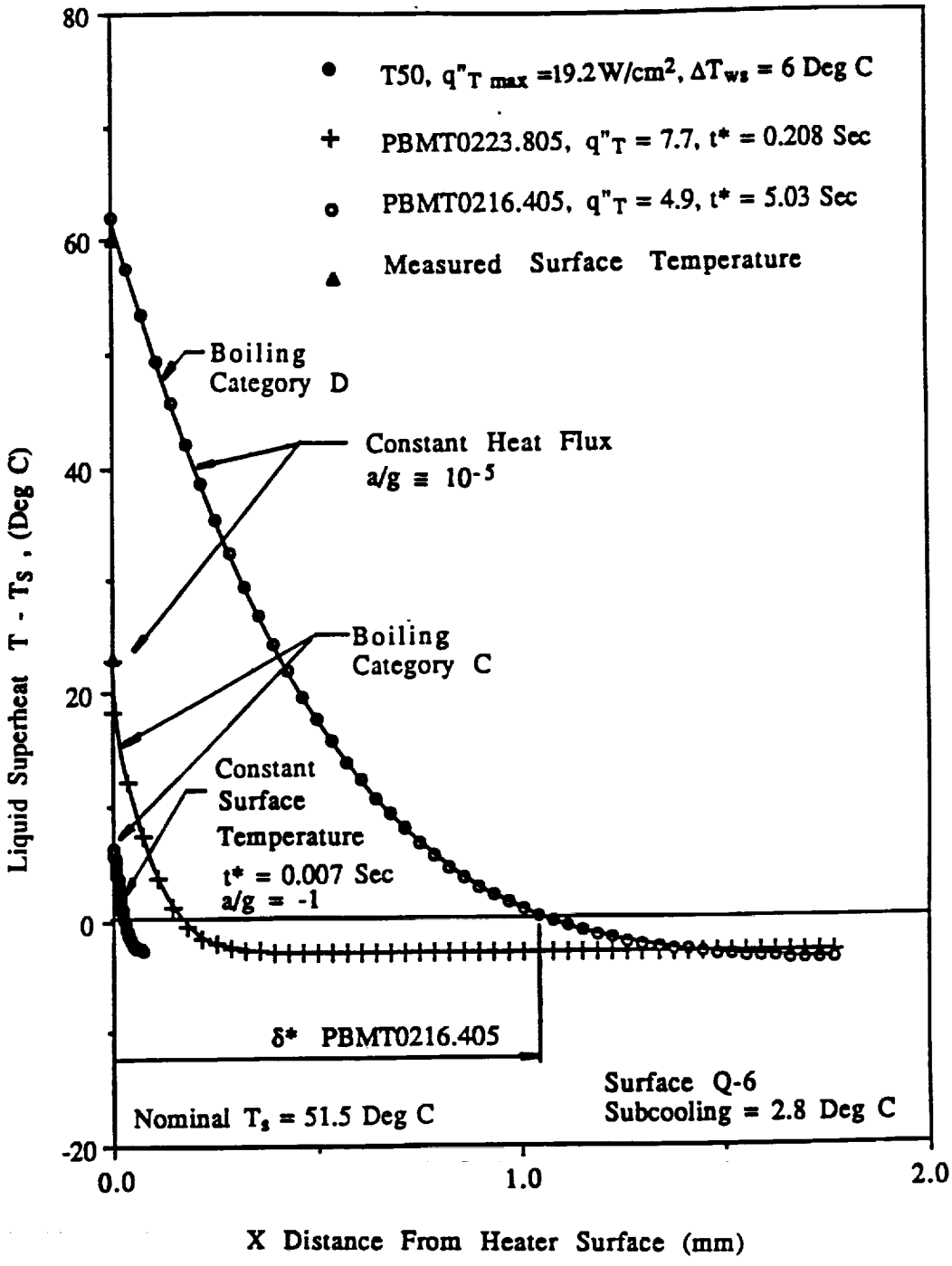

Figure 6.15 Comparison of computed imposed constant heat flux and constant surface temperature liquid temperature distributions, 2.8 °C subcooling (surface Q-6)

Table 6.1 Comparison of surface temperature gradients between imposed heat flux and imposed surface temperature tests for surface Q-14

Test	Heating Mode	Subcooling (°C)	T_w^* (°C)	t^* (Sec)	δ^* (μm)	$\frac{dT}{dx}_{x=0}$ (400μSec) (°C/μm)	$\frac{dT^*}{dx}_{x=0}$ (°C/μm)
T201	q"	Saturated	86	2.016	1440	0.11	0.11
T207	q"	Saturated	102	1.128	1090	0.21	0.21
T107	ΔT_w	Saturated	53	0.014	110	0.19	0.08
T108	ΔT_w	Saturated	53	0.003	51	0.21	0.19
T109	ΔT_w	Saturated	54	0.003	51	0.26	0.22
T110	ΔT_w	Saturated	60	0.003	56	0.56	0.49
T205	q"	2.2	100	1.012	518	0.21	0.21
T103	ΔT_w	2.2	55	0.004	16	0.30	0.22
T104	ΔT_w	2.3	55	0.004	17	0.33	0.25
T105	ΔT_w	2.3	58	0.003	18	0.47	0.41
T106	ΔT_w	2.3	60	0.003	21	0.60	0.51
T206	q"	11.2	110	1.518	399	0.21	0.21
T111	ΔT_w	11.0	61	0.004	7	0.65	0.49
T112	ΔT_w	11.0	65	0.004	2	0.86	0.65
T113	ΔT_w	11.0	70	0.004	12	1.12	0.85
T114	ΔT_w	11.0	73	0.003	12	1.30	1.13

Table 6.2 Boiling propagation and estimates of change in internal energy for δ^*

Filename	δ^* (mm)	$\rho c\int_0^{\delta^*} \Theta\, dx$ (kJ/m^2)	$\rho c\int_0^{\delta} \Theta\, dx$ (kJ/m^2)	$\dfrac{\rho c\int_0^{\delta^*} \Theta\, dx}{\rho c\int_0^{\delta} \Theta\, dx}$	Category
PBMT0914.805	0.220	3.912	4.212	0.929	F
PBMT0919.820	0.116	3.301	4.764	0.693	F
PBMT1012.800	0.411	6.814	6.926	0.984	F
PBMT1013.805	0.053	0.454	0.583	0.778	F
PBMT1018.820	0.577	30.80	33.39	0.922	D
PBMT1019.605	1.059	38.09	38.95	0.978	D
PBMT1025.800	1.161	33.22	33.30	0.997	E
PBMT1026.600	1.102	33.44	33.79	0.990	D
PBMT1101.600	1.624	46.68	46.78	0.998	E
PBMT1102.800	1.074	31.28	31.38	0.997	E
PBMT1108.600	0.722	38.54	42.82	0.900	D
PBMT1115.605	0.902	31.39	32.19	0.975	D
PBMT1121.620	0.707	38.03	42.00	0.905	D
PBMT1128.805	0.717	25.97	26.58	0.977	D
PBMT1129.820	0.404	19.15	21.76	0.880	D
PBMT1213.805	0.679	23.09	23.64	0.977	D
PBMT0125.800	0.148	1.165	1.204	0.968	F
PBMT0131.820	0.033	0.689	1.657	0.416	F

(See Section 6.4 for definition of terms)

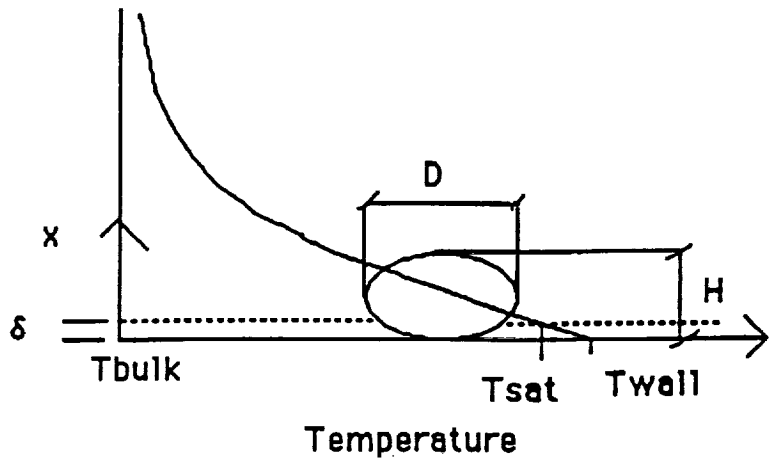

Figure 6.16 Small bubble neglecting the liquid temperature distribution immediately prior to boiling propagation

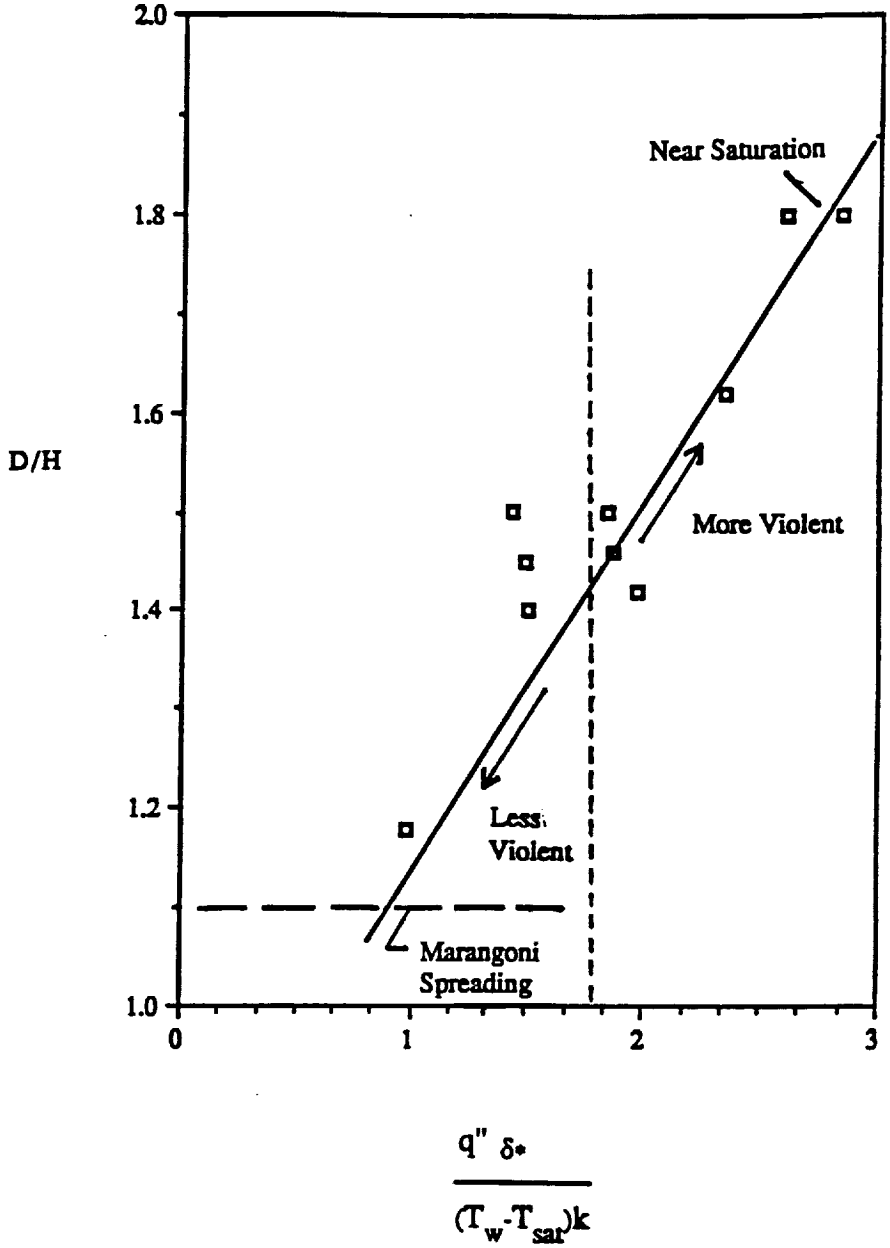

Figure 6.17 Bubble shape at onset of categories D and E in microgravity

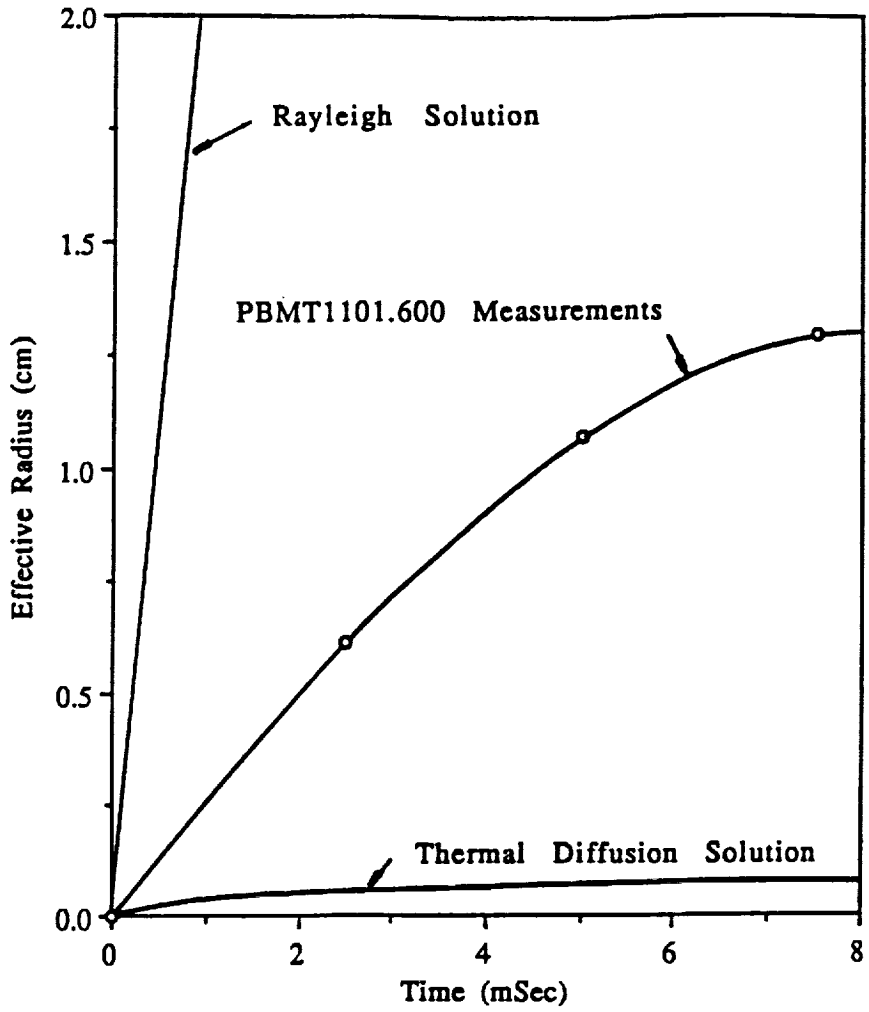

Figure 6.18 Comparison of measured bubble growth from test PBMT1101.600 with the Rayleigh solution and thermal diffusion solution

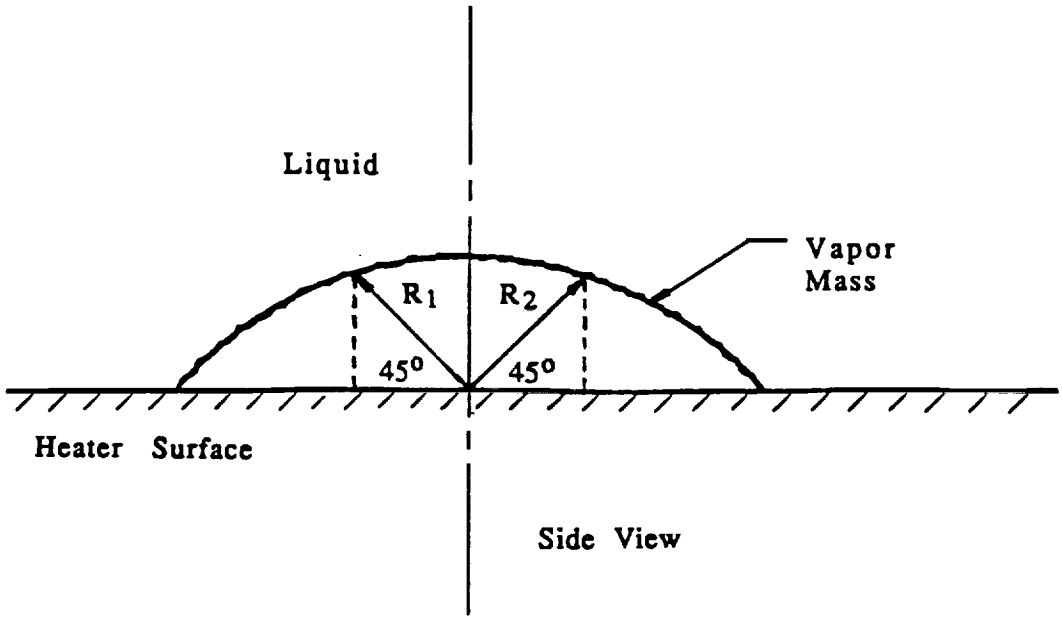

Effective Radius of Figure 6.18 $= \frac{R_1+R_2}{2}$

Figure 6.19 Definition of effective bubble radius

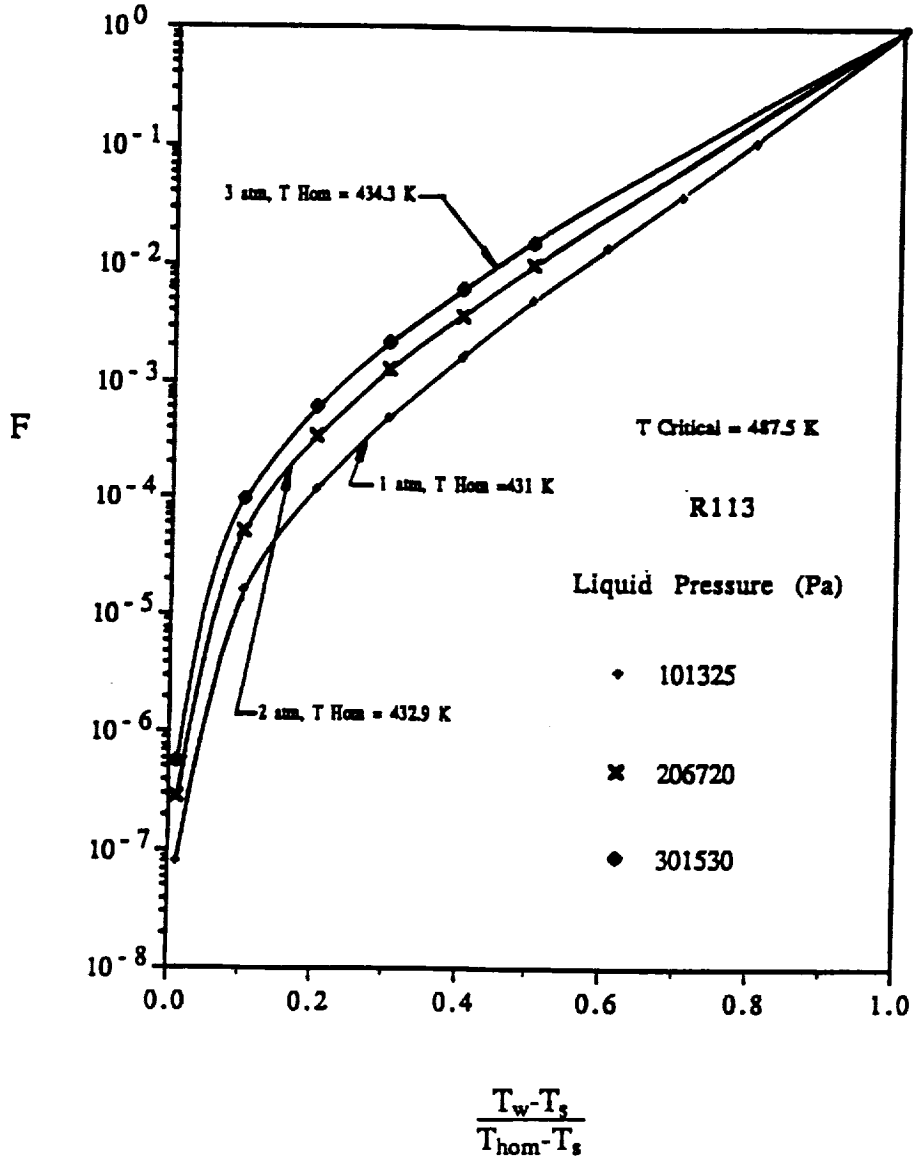

Figure 6.20 Empirical heterogeneous nucleation factor for three different pressures

APPENDICES

A. DATA TABULATION

A.1 Constant Heat Flux: Pool Boiling

Run No.	Filename	P (kPa)	T_∞ (°C)	ΔT_{sub} (°C)	q" (W/cm^2)	a/g	t* (sec)	t_{spr} (sec)	T_w* (°C)	T_{spr} (°C)	Comments	Surface No.
40	PAUT0410.805	116.94	49.07	2.86	7.517 ± 2%	1	0.109	2.624	62	115		Q-5
41	PAUT0410.805	116.94	49.12	2.81	7.492 ± 2%	1	2.703	2.703	115	115		Q-5
42	PAUT0410.820	152.02	49.15	11.17	7.405 ± 2%	1	2.686	2.686	115	115		Q-5
43	PAUT0410.820	152.04	49.12	11.2	7.356 ± 2%	1	3.342	3.342	118	118		Q-5
44	PAUT0410.405	116.89	49.38	2.53	3.907 ± 2%	1	19.69	19.685	116	116		Q-5
45	PAUT0410.405	116.91	49.41	2.51	3.892 ± 2%	1	35.02	35.019	111	111		Q-5
46	PAUT0410.805	116.98	49.47	2.47	7.300 ± 2%	1	2.35	2.35	111	111		Q-5
47	PAUT0411.420	158.55	49.28	12.42	3.844 ± 2%	1	52.08	52.08	113	113		Q-5
48	PAUT0411.420	152.01	49.48	10.84	3.844 ± 2%	1	47.4	47.402	112	112		Q-5
52	PAUT0417.400	110.5	49.54	0.64	3.704 ± 2%	1	60	60	113	113		Q-5
53	PAUT0417.400	110.5	49.62	0.58	3.686 ± 2%	1	18.5	18.5	105	105		Q-5
54	PAUT0417.200	110.1	49.43	0.91	1.840 ± 1%	1					NN	Q-5
55	PAUT0421.200	109.6	49.4	0.48	1.947±1%	1					NN	Q-5
56	PAUT0421.700	110.2	49.42	0.65	7.418 ± 2%	1	0.043	1.215	59	101		Q-5
57	PAUT0421.705	117.1	49.16	2.81	7.46 ± 2%	1	0.05	1.951	60	108		Q-5
58	PAUT0421.400	109.8	49.31	0.61	3.841±3%	1	34.58	34.584	108	108		Q-5
59	PAUT0422.700	110.2	49.37	0.67	7.452 ± 2%	1	0.048	1.755	60	105		Q-5
60	PADT0422.205	117.1	49.66	2.3	1.932 ± 1%	-1	28.27	28.268	103	103		Q-5
61	PADT0423.205	117.1	49.66	2.26	1.91 ± 1%	-1	45.51	45.512	105	105		Q-5
62	PADT0423.405	117.6	49.71	2.34	3.836±3%	-1	11.62	11.624	123	123		Q-5
63	PADT0424.405	116.9	49.71	2.2	3.872±2%	-1	7.906	7.906	114	114		Q-5
66	PADT0424.720	152.5	49.36	11	7.023 ± 2%	-1	0.397	1.22	83	104		Q-5
67	PADT0424.720	152.5	49.39	11	7.284 ± 2%	-1	0.392	1.17	82	103		Q-5
68	PADT0424.420	152.2	49.4	10.93	3.961±2%	-1	6.064	6.064	110	110		Q-5
69	PADT0424.420	152.2	49.42	10.93	3.945 ± 2%	-1	7.266	7.266	113	113		Q-5

A. DATA TABULATION

A.1 Constant Heat Flux: Pool Boiling

Run No.	Filename	P (kPa)	T_∞ (°C)	ΔT_{sub} (°C)	q" (W/cm^2)	a/g	t* (sec)	t_{spr} (sec)	T_w* (°C)	T_{spr} (°C)	Comments	Surface No.
40	PAUT0410.805	116.94	49.07	2.86	7.517 ± 2%	1	0.109	2.624	62	115		Q-5
41	PAUT0410.805	116.94	49.12	2.81	7.492 ± 2%	1	2.703	2.703	115	115		Q-5
42	PAUT0410.820	152.02	49.15	11.17	7.405 ± 2%	1	2.686	2.686	115	115		Q-5
43	PAUT0410.820	152.04	49.12	11.2	7.356 ± 2%	1	3.342	3.342	118	118		Q-5
44	PAUT0410.405	116.89	49.38	2.53	3.907 ± 2%	1	19.69	19.685	116	116		Q-5
45	PAUT0410.405	116.91	49.41	2.51	3.892 ± 2%	1	35.02	35.019	111	111		Q-5
46	PAUT0410.805	116.98	49.47	2.47	7.300 ± 2%	1	2.35	2.35	111	111		Q-5
47	PAUT0411.420	158.55	49.28	12.42	3.844 ± 2%	1	52.08	52.08	113	113		Q-5
48	PAUT0411.420	152.01	49.48	10.84	3.844 ± 2%	1	47.4	47.402	112	112		Q-5
52	PAUT0417.400	110.5	49.54	0.64	3.704 ± 2%	1	60	60	113	113		Q-5
53	PAUT0417.400	110.5	49.62	0.58	3.686 ± 2%	1	18.5	18.5	105	105		Q-5
54	PAUT0417.200	110.1	49.43	0.91	1.840 ± 1%	1					NN	Q-5
55	PAUT0421.200	109.6	49.4	0.48	1.947±1%	1					NN	Q-5
56	PAUT0421.700	110.2	49.42	0.65	7.418 ± 2%	1	0.043	1.215	59	101		Q-5
57	PAUT0421.705	117.1	49.16	2.81	7.46 ± 2%	1	0.05	1.951	60	108		Q-5
58	PAUT0421.400	109.8	49.31	0.61	3.841±3%	1	34.58	34.584	108	108		Q-5
59	PAUT0422.700	110.2	49.37	0.67	7.452 ± 2%	1	0.048	1.755	60	105		Q-5
60	PADT0422.205	117.1	49.66	2.3	1.932 ± 1%	-1	28.27	28.268	103	103		Q-5
61	PADT0423.205	117.1	49.66	2.26	1.91 ± 1%	-1	45.51	45.512	105	105		Q-5
62	PADT0423.405	117.6	49.71	2.34	3.836±3%	-1	11.62	11.624	123	123		Q-5
63	PADT0424.405	116.9	49.71	2.2	3.872±2%	-1	7.906	7.906	114	114		Q-5
66	PADT0424.720	152.5	49.36	11	7.023 ± 2%	-1	0.397	1.22	83	104		Q-5
67	PADT0424.720	152.5	49.39	11	7.284 ± 2%	-1	0.392	1.17	82	103		Q-5
68	PADT0424.420	152.2	49.4	10.93	3.961±2%	-1	6.064	6.064	110	110		Q-5
69	PADT0424.420	152.2	49.42	10.93	3.945 ± 2%	-1	7.266	7.266	113	113		Q-5

Run No.	Filename	P (kPa)	T_∞ (°C)	ΔT_{sub} (°C)	q" (W/cm^2)	a/g	t^* (sec)	t_{spr} (sec)	T_w* (°C)	T_{spr} (°C)	Comments	Surface No.
70	PADT0424.220	152.2	49.45	10.88	1.98 ± 1%	-1	53.83	53.828	114	114		Q-5
72	PADT0425.200	106.4	48.95	0.05	1.957 ± 1%	-1	66.5	66.5			DL	Q-5
73	PADT0425.400	106.1	48.93	0	3.91 ± 2%	-1	7.154	7.154	111	111		Q-5
74	PADT0425.600	106.1	49.1	0	5.734 ± 2%	-1	3.528	3.528	115	115		Q-5
75	PADT0426.605	117.3	49.05	2.99	5.694 ± 2%	-1	4.48	4.48	125	125		Q-5
76	PADT0426.520	152.5	49.03	10.57	5.283 ± 2%	-1	3.714	3.714	112	112		Q-5
77	PADT0429.700	105.1	48.65	0	7.379±2%	-1	0.011	0.011	55	55		Q-5
78	PAUT0429.220	152.2	49.62	10.69	1.880±1%	1					NN	Q-5
79	PAUT0429.605	117.1	49.47	2.47	5.690±2%	1	6.894	6.894	115	115		Q-5
80	PAUT0429.600	110.6	49.43	0.72	5.703±1.5%	1	8.186	8.186	106	106		Q-5
81	PAUT0429.620	152.2	49.44	10.9	5.511 ± 2%	1	13.59	13.586	118	118		Q-5
102	PADT0523.205	117.1	48.8	3.16	1.98±2%	-1	15.94	15.94	94	94		Q-2
103	PADT0523.205	117.3	48.77	3.22	1.98±2%	-1	19.74	19.742	99	99		Q-2
104	PADT0523.220	152.6	48.74	11.68	1.98±2%	-1	23	23.004	101	101		Q-2
105	PADT0523.200	107.1	48.77	0.42	2.02±3%	-1	16.18	16.176	96	96		Q-2
106	PADT0523.405	117.8	48.82	3.28	4.091 + 2%	-1	7.096	7.096	115	115		Q-2
107	PADT0523.420	151.7	48.9	11.33	4.110 ± 2%	-1	6.196	6.196	113	113		Q-2
108	PADT0523.400	107	48.84	0.35	4.085 ± 2%	-1	5.156	5.156	109	109		Q-2
109	PADT0523.820	152.2	48.92	11.42	8.06±5%	-1	0.083	0.083	65	65		Q-2
110	PADT0524.805	117	49.24	3.04	8*	-1	0.006	0.006			VO	Q-2
111	PADT0524.800	105.7	49.24	0	8*	-1	0.007	0.007			VO	Q-2
112	PADT0524.620	152.5	49.11	11.27	5.950 ± 2%	-1	1.622	1.622	101	101		Q-2
113	PADT0524.605	117.1	49.11	2.83	5.910 ± 2%	-1	1.684	1.684	103	103		Q-2
114	PADT0524.405	117.1	49.12	2.83	4.050 ± 2%	-1	5.624	5.624	109	109		Q-2
115	PAUT0525.805	117	49.4	2.83	8*	1	0.015	0.638			VO	Q-2
116	PAUT0525.420	152.2	49.39	10.97	4.15±3%	1	5.992	12.588	100	107		Q-2
117	PAUT0525.405	117.1	49.15	2.79	3.873±2%	1	9.492	9.492	102	102		Q-2
118	PAUT0525.400	110.8	49.16	1.04	3.998 ± 2%	1	12.25	12.248	105	105		Q-2
119	PAUT0525.820	152	49.05	11.73	8*	1	0.104	1.034			VO	Q-2

Run No.	Filename	P (kPa)	T_∞ (°C)	ΔT_{sub} (°C)	q" (W/cm^2)	a/g	t* (sec)	tspr (sec)	T_w* (°C)	T_{spr} (°C)	Comments	Surface No.
120	PAUT0525.800	110.6	49	1.17	7.990 ± 2%	1	0.014	0.436	55	98		Q-2
121	PAUT0525.220	152	48.98	11.29	2.020 ± 2%	1					NN	Q-2
122	PAUT0525.205	117.8	48.86	3.23	2.02±2%	1					NN	Q-2
123	PAUT0526.200	110.4	49.21	0.89	1.967 ± 2%	1					NN	Q-2
124	PAUT0526.620	152.5	49.2	11.18	5.950 ± 2%	1	1.844	2.079	108	101		Q-2
125	PAUT0526.605	117.1	49.2	2.72	6.161±3%	1	0.03	1.787	56	99		Q-2
126	PAUT0526.820	152.7	49.2	11.25	8.320 ± 2%	1	0.103	0.791	68	99		Q-2
127	PAUT0526.805	116.9	49.2	2.69	8.433±1%	1	0.025	0.611	58	99		Q-2
128	PAUT0601.405	117	48.71	3.58	3.896±2%	1	0.032	6.998	53	107		Q-1
129	PAUT0601.420	152.2	48.62	12.2	3.846 ± 2%	1	0.873	15.991	81	118		Q-1
130	PAUT0601.400	111.6	48.51	2.28	3.880 ± 2%	1	0.022	5.106	52	104		Q-1
131	PAUT0601.420	152.3	47.7	13.13	3.853±2.5%	1	0.957	11.773	83	113		Q-1
132	PAUT0601.205	117.8	48.55	3.95	1.989 ± 2%	1					NN	Q-1
133	PAUT0601.220	151.3	48.71	11.92	1.981 ± 2%	1					NN	Q-1
134	PAUT0601.200	110.8	48.8	1.75	1.991 ± 2%	1					NN	Q-1
135	PAUT0601.820	152.2	48.7	12.12	7.695 ± 2%	1	0.084	0.489	63	95		Q-1
136	PAUT0602.805	117.5	48.6	3.82	7.705 ± 2%	1	0.04	0.308	58	87		Q-1
137	PAUT0602.800	111.1	49.07	1.57	8*	1	0.01	0.353			VO	Q-1
138	PAUT0603.620	152.3	48.99	11.85	5.846±2%	1	0.12	0.755	62	90		Q-1
139	PADT0604.205	117	48.91	3.37	1.990 ± 2%	-1	11.61	11.608	99	99		Q-1
140	PADT0604.200	106.9	48.85	0.68	1.967 ± 2%	-1	16.98	16.98	105	105		Q-1
141	PADT0604.220	152.3	48.89	11.94	2.055±2.5%	-1	11.52	11.518	98	98		Q-1
142	PADT0604.405	117.2	48.95	3.05	3.832±3%	-1	0.023	2.055	53	95		Q-1
143	PADT0604.420	152.4	49	11.4	3.888±3%	-1	2.462	2.462	98	98		Q-1
144	PADT0604.400	107.3	48.84	0.69	3.900±2%	-1	0.013	0.013	52	52		Q-1
145	PADT0604.820	152.4	49.02	11.83	7.630 ± 2%	-1	0.017	0.119	56	66		Q-1
146	PADT0605.805	117.1	48.97	3.34	7.542±3.5%	-1	0.012	0.174	54	70		Q-1
147	PADT0605.800	106.4	48.86	0.41	7.603±2.5%	-1	0.013	0.122	54	66		Q-1
148	PADT0605.620	152.3	48.97	11.87	5.747 ± 2%	-1	0.114	0.516	61	75		Q-1

Run No.	Filename	P (kPa)	T_∞ (°C)	ΔT_{sub} (°C)	q'' (W/cm^2)	a/g	t^* (sec)	t_{spr} (sec)	T_w* (°C)	T_{spr} (°C)	Comments	Surface No.
149	PADT0605.420	152.3	48.95	11.44	3.853 ± 2%	-1	1.554	1.554	89	89		Q-1
150	PAUT0605.420	152.4	48.88	11.98	3.872±2%	1	8.722	8.722	100	100		Q-1
151	PAUT0605.800	110.7	48.91	1.61	7.665±2%	1	0.01	0.412	54	78		Q-1
152	PAUT0612.405	117.3	48.75	3.27	3.74±5%	1	40.73	40.733	105	105		Q-6
153	PAUT0612.420	151.3	48.71	11.43	3.87±3%	1	60.23	60.229	109	109		Q-6
154	PAUT0612.400	110	48.74	1.26	3.78±2%	1	28.1	28.099	101	101		Q-6
155	PAUT0612.820	152.6	48.73	11.71	7.68±2%	1	0.062	0.93	61	93		Q-6
156	PAUT0612.805	116.7	48.77	3.07	7.58±2%	1	0.046	0.52	61	83		Q-6
157	PAUT0612.800	110.1	48.76	1.29	7.57±2%	1	0.015	0.535	55	83		Q-6
158	PAUT0612.620	152.9	48.74	11.75	5.67±3%	1	9.092	9.092	113	113		Q-6
159	PAUT0612.605	116.6	48.69	3.31	5.660 ± 2%	1	8.378	8.378	111	111		Q-6
160	PADT0612.420	152.6	49.16	11.26	3.57±3%	-1	10.21	10.208	109	109		Q-6
161	PADT0613.405	127.4	49.2	2.81	3.94±3%	-1	7.978	7.978	109	109		Q-6
162	PADT0613.400	108.8	49.19	0.47	3.93±3%	-1	7.811	7.811	108	108		Q-6
163	PADT0613.220	150.2	49.18	10.71	1.92±2%	-1	39.81	39.812	101	101		Q-6
164	PADT0613.205	119.8	49.15	3.5	1.92±2%	-1	55.61	55.606	106	106		Q-6
165	PADT0613.200	106.1	49.15	0	1.93±2%	-1	36.36	36.364	101	101		Q-6
166	PADT0613.820	152.9	49.14	11.35	7.66±2%	-1	0.071	0.071	62	62		Q-6
167	PADT0613.805	117.4	49.15	2.86	7.63±2%	-1	0.011	0.011	54	54		Q-6
168	PADT0613.800	108.4	49.15	0.41	7.59±2%	-1	0.011	0.011	54	54		Q-6
169	PADT0613.620	152.9	49.14	11.35	5.73±2%	-1	3.282	3.282	110	110		Q-6
170	PADT0613.605	117.5	49.13	2.9	5.76±3%	-1	4.11	4.11	104	104		Q-6

Run No.	Filename	P (kPa)	T_∞ (°C)	ΔT_{sub} (°C)	q" (W/cm^2)	a/g	t* (sec)	tspr (sec)	T_w* (°C)	T_{spr} (°C)	Comments	Surface No.
M-17-2G	PBUT0914.805	121.28	50.28	2.67	8.2	1	0.063	1.065	65	105		Q-5
M-17-2	PBMT0914.805	99.77	44.06	3.00	7.8	0	0.3	0.78	72	90		Q-5
M-17-3G	PBUT0919.820	169.75	52.39	11.44	7.6	1	0.233	0.295	84	85		Q-5
M-17-3	PBMT0919.820	131	44.11	11.28	7.9	0	0.335	0.41	72	88		Q-5
M-17-5G	PBUT1005.400	132.24	55.83	-0.11	4	1					DM	Q-5
M-17-5	PBMT1005.400	97.01	45.17	1.06	3.8	0	5.128				NET	Q-5
M-17-6G	PBUT1012.800	133.07	55.61	0.28	7.6	1	0.028	0.965	60	106	PCF	Q-5
M-17-6	PBMT1012.800	98.11	45.56	1.00	7.4	0	0.52	0.675	82	86		Q-5
M-17-7G	PBUT1013.805	142.72	55.33	2.78	7.5	1	0.068	0.753	71	101		Q-5
M-17-7	PBMT1013.805	111.56	47.56	2.83	7.2	0	0.045	0.165	60	70		Q-5
M-17-8G	PBUT1018.820	182.99	55.28	11.06	7.1	1	1.01	2.128	102	110		Q-5
M-17-8	PBMT1018.820	142.03	46.94	11.00	7.1	0	2.66	2.66	121	121		Q-5
M-17-9G	PBUT1019.605	138.72	54.22	3.00	5.4	1	4.76	4.76	114	114		Q-5
M-17-9	PBMT1019.605	108.25	46.67	2.78	5.3	0	4.083	4.083	114	114		Q-5
M-17-10G	PBUT1025.804	149.62	57.44	2.22	7.5	1	1.748	1.748	118	118		Q-5
M-17-10	PBMT1025.800	102.8	47.44	0.39	7.5	0	2.467	2.467	122	122		Q-5
M-17-11G	PBUT1026.603	143.2	56.56	1.67	5.7	1	3.65	3.65	117	117		Q-5
M-17-11	PBMT1026.600	103.28	46.72	1.33	5.7	0	3.293	3.293	103	103		Q-5
M-17-12G	PBUT1101.600	136.24	55.83	0.78	5.1	1					NN	Q-5
M-17-12	PBMT1101.600	100.53	46.83	0.39	5.4	0	4.813	4.813	121	121		Q-5
M-17-13G	PBUT1102.800	144.03	57.61	0.78	7.8	1	0.933	0.953	110	111		Q-5
M-17-13	PBMT1102.800	103.01	47.5	0.50	7.7	0	2.264	2.264	122	122		Q-5
M-17-14G	PBUT1108.610	161.34	56.56	5.56	5.5	1					NN	Q-5
M-17-14	PBMT1108.620	143.34	47	11.39	5.5	0	4.325	4.325	116	116		Q-5
M-17-15G	PBUT1109.400	143.69	57.39	0.94	4	1					NN	Q-5
M-17-15	PBMT1109.400	101.22	46.94	0.50	4	0					NN	Q-5
M-17-16G	PBUT1115.605	143.62	55.44	2.89	6	1					NN	Q-5
M-17-16	PBMT1115.605	110.11	47.11	2.89	5.8	0	3.083	3.083	113	113		Q-5
M-17-17G	PBUT1121.620	191.19	56.61	11.22	5.7	1					NPC	Q-5

Run No.	Filename	P (kPa)	T_∞ (°C)	ΔT_{sub} (°C)	q'' (W/cm^2)	a/g	t^* (sec)	t_{spr} (sec)	T_w^* (°C)	T_{spr} (°C)	Comments	Surface No.
M-17-17	PBMT1121.620	144.45	47.39	11.11	5.8	0	4.023	4.023	122	122		Q-5
M-17-18G	PBUT1128.805	155.48	57.83	3.06	7.8	1	1.68	1.68	120	120		Q-5
M-17-18	PBMT1128.805	110.11	47.11	2.89	7.7	0	1.918	1.918	119	119		Q-5
M-17-19G	PBUT1129.805	153.75	57.61	2.94	8.1	1	1.182	1.182	115	115		Q-5
M-17-19	PBMT1129.820	143.62	47.06	11.28	7.8	0	1.55	1.55	111	111		Q-5
M-17-20G	PBUT1205.805	166.3	60.39	2.72	7.3	1	1.181	1.201	112	113		Q-5
M-17-21G	PBUT1213.805	162.3	54.33	3.00	7.9	1	1.313	1.313	117	117		Q-6
M-17-21	PBMT1213.805	109.9	47.19	2.83	7.6	0	1728	1.728	114	114		Q-6
M-18-1G	PBUT0125.805	145.27	55.72	2.94	7.7	1					CLL	Q-6
M-18-1	PBMT0125.800	103.97	47.5	0.78	7.6	0	0.088	0.305	62	76		Q-6
M-18-2G	PBUT0131.820	208.36	59.72	11.11	7.6	1	0.385	0.603	93	99		Q-6
M-18-2	PBMT0131.820	145	47.5	11.11	7.8	0	0.118	0.473	63	81		Q-6
M-18-3G	PBUT0201.805	151.34	56.94	3.06	7.9	1	0.6	0.6	98	98		Q-6
M-18-3	PBMT0201.805	111.01	47.22	3.00	7.7	0	0.023	0.223	57	68		Q-6
M-18-4G	PBUT0207.605	154.1	57.67	2.94	6	1	1.795	1.795	106	106		Q-6
M-18-4	PBMT0207.600	102.8	47.33	0.56	6.3	0	1.685	1.685	102	102		Q-6
M-18-5G	PBUT0216.405	153.96	57.78	2.78	4.5	1					NN	Q-6
M-18-5	PBMT0216.405	107.7	46.5	2.83	4.9	0	5.03	5.03	110	110	NAH	Q-6
M-18-6	PBMT0223.805	111.01	47.44	2.78	7.7	0	0.208	0.32	73	73		Q-6

Comments: NAH = Nucleated After Heater Off; NPC = No Pressure Control; VO = Video Only

DM = Diode Malfunction; NET = Not Enough Time; NN = No Nucleation

CLL = Camera Lights too Late; PCF = Pressure Control Failed; DL = Data Lost

The uncertainty associated with the tabulated heat flux values are 3% of the given value.

A.2 Constant Heat Flux and Constant Surface Temperature: Pool Boiling

Constant Heat Flux

File-name	a/g	Surface No.	t^* (sec)	T_w^* (°C)	q'' (W/cm^2)	T_s (°C)	P (kPa)	ΔT_{sub} (°C)	T_∞ (°C)
T200	-1	Q-14	5.064	106	4.2 ± 0.95%	51.37	114.94	2.44	48.93
T201	-1	Q-14	2.016	86	4.19 ± 1.19%	48.91	106.072	-0.2	49.11
T202	-1	Q-14	2.796	94	4.15 ± 1.93%	60.37	152.04	11.19	49.18
T203	-1	Q-14	28.728	103	2.01 ± 1.99%	60.32	151.84	11.13	49.19
T204	-1	Q-14	16.236	91	1.99 ± 2.01%	51.46	115.26	2.31	49.15
T205	-1	Q-14	1.012	100	7.80 ± 1.54%	51.39	115.00	2.24	49.15
T206	-1	Q-14	1.518	110	7.79 ± 2.80%	60.37	152.06	11.17	49.2
T207	-1	Q-14	1.128	102	7.74 ± 2.58%	48.94	106.17	-0.2	49.14

Constant Surface Temperature

File-name	a/g	Surface No.	t* (sec)	Vmax (Volts)	T_w* (°C)	q"T max (W/cm^2)	T_s (°C)	P (kPa)	ΔT_{sub} (°C)	T_∞ (°C)
T50	-1	Q-6	0.007	30	58	19.2	51.52	115.42	2.61	48.91
T51	-1	Q-6	0.016	15.8	49	1.1	48.63	105.03	-0.28	48.81
T52	-1	Q-6	0.006	30	56	14.9	48.69	105.24	-0.22	48.81
T100	-1	Q-14	-	33.8	-		49.84	109.351	1.12	48.71
T101	-1	Q-14	-	45	-		51.79	116.476	3.04	48.74
T102	-1	Q-14	-	71.6	-		60.38	152.08	11.57	48.81
T103	-1	Q-14	0.004	43.1	55	11.7	51.43	115.14	2.18	49.24
T104	-1	Q-14	0.004	53.1	55	13.2	51.43	115.15	2.32	49.11
T105	-1	Q-14	0.003	63.1	58	18.6	51.43	115.14	2.31	49.11
T106	-1	Q-14	0.003	73.1	60	23.2	51.43	115.16	2.33	49.11
T107	-1	Q-14	0.014	32.3	53	8.0	48.93	106.16	-0.21	49.14
T108	-1	Q-14	0.003	42.3	53	8.7	48.95	106.209	-0.22	49.17
T109	-1	Q-14	0.003	52.3	54	10.2	48.95	106.209	-0.22	49.17
T110	-1	Q-14	0.003	62.3	60	22.4	48.91	106.093	-0.28	49.19
T111	-1	Q-14	0.004	77.8	61	25.6	60.2	151.295	11.00	49.2
T112	-1	Q-14	0.004	87.8	65	33.7	60.2	151.295	11.00	49.2
T113	-1	Q-14	0.004	97.8	70	43.6	60.2	151.295	11.00	49.2
T114	-1	Q-14	0.003	107.8	73	50.4	60.21	151.295	11.00	49.21

B. CALIBRATION

B.1 Gold Film Heater Surface

A massive copper fixture was used to calibrate the tempered gold film heater surfaces and is shown in Figure B.1. The thick copper insured uniform temperature conditions for calibration. The copper fixture, which was sealed with an o-ring, was immersed in a constant temperature water bath. The Colora constant temperature bath (model NB-35 640) provided the temperatures for calibrations over the temperature range 20 to 96 °C. Legs on the fixture positioned the surface about 5 cm from the bottom of the container. A calibrated chromel-constantan thermocouple positioned near the heater surface within the sealed fixture indicated the temperature of the gold film. The voltage of the thermocouple, which used a water-crushed ice reference junction, was measured with the CR7X data acquisition system. Once the surface reached a steady-state temperature as indicated by the thermocouple, the gold film resistance was ready to be determined.

Since resistance is calculated from voltage measurements, rather than being measured directly, voltage measurements across the heater surface and across a calibrated shunt were used to calculate the heater surface resistance at an arbitrary constant temperature bath level. The voltage measurement circuit for calibration of the gold surfaces is presented in Figure B.2. A six volt battery provided the d.c. current source. The variable resistor was adjusted to a nominal value of 400 Ω so as to produce a small current which would, in turn, result in a negligible amount of ohmic heating in the gold film (0.01 watts), so that the film resistance would not be affected. A National Bureau of Standards calibrated standard shunt (Leeds and Northrup Model No. 4221-B) used for the determination of the current had a resistance of 0.1000008 Ω with an uncertainty of 0.001% at the current levels corresponding to this surface

calibration, as stated by the calibration certificate. The CR7X determined the voltages across the thin film and the shunt. A typical gold film calibration is shown in Figure B.3, and the coefficient of determination, described in Montgomery (1983), for this linear fit of the resistance and temperature is unity.

B.2 Thermocouples

Sections of a chromel-constantan thermocouple spool were calibrated individually. Copper extension wires were used between the thermocouple wires and the water-crushed ice reference junction, both during calibration and during use. Each set of thermocouple wire and extension wires were numbered for identification purposes. A Colora constant temperature bath provided the variable temperature for comparison with a platinum resistance thermometer, while a hypsometer at atmospheric pressure provided the steam point. Using a Mueller Temperature Bridge (Leeds and Northrup Model 8067) with a null detector, the resistance of the platinum element was measured to an accuracy of $\pm$ 0.0001 Ω, which corresponds to an uncertainty in the temperature of the platinum resistance thermometer of $\pm$ 0.001 °C. The output of the thermocouples were measured using a Leeds and Northrup K-5 potentiometer with a built-in null detector. The sensitivity in measuring this voltage is within $\pm$ 0.1 μV.

B.3 Pressure Transducers

A Ruska Pressure Dead Weight Calibration System (2400 Series dead weight gage) was utilized in the calibration of the Heise pressure transducers used in the laboratory boiling vessels and the Setra pressure transducer for the drop vessel. The uncertainty in the pressure level provided by the Ruska system was $\pm$ 0.0017 kPa ($\pm$

0.0003 psi) for the pressure range of the present study: 96 to 172 kPa (14 to 25 psi). A schematic of the Ruska system and measurement circuitry for the pressure transducer calibration appears in Figure B.4. A representative calibration curve is shown in Figure B.5. The Ruska system was also used for calibrating a Heise Bourdon tube gage, which in turn was used for in-place periodic checks on the pressure transducer calibration. In Figure B.4, a precision pressure regulator was connected to the pressure transducer being calibrated, which was in turn connected to the dead weight system. Since the mass of the weights were known accurately along with an accurate determination of g, the pressure transducer signal measured by the multimeter or K-3 potentiometer could be correlated with the known pressure from the dead weight tester.

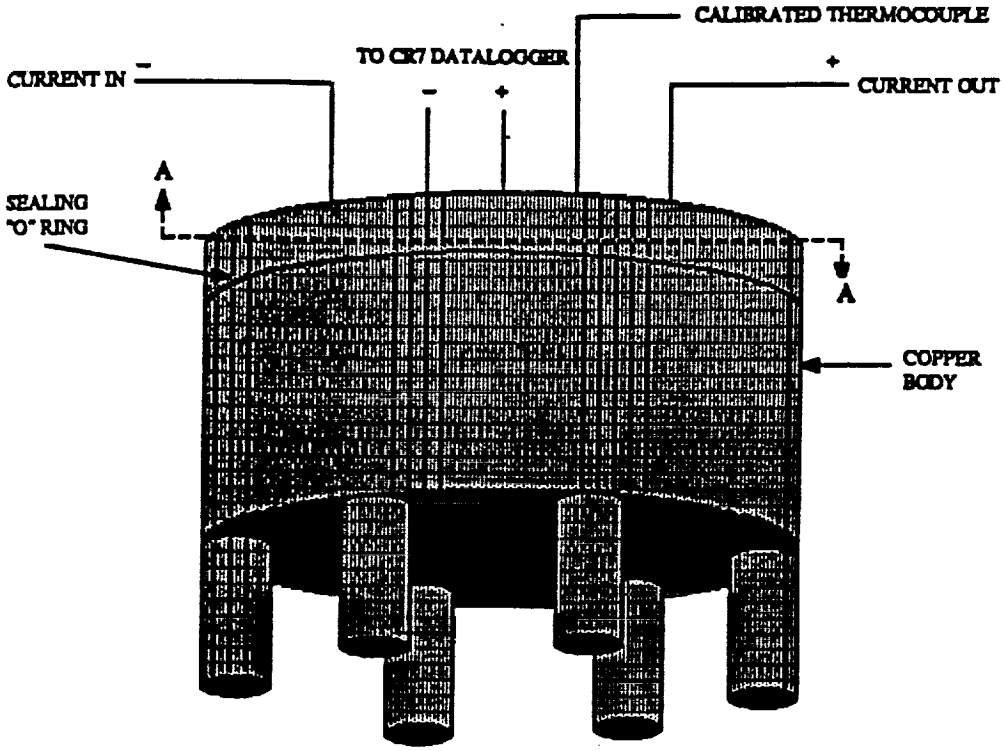

Section AA

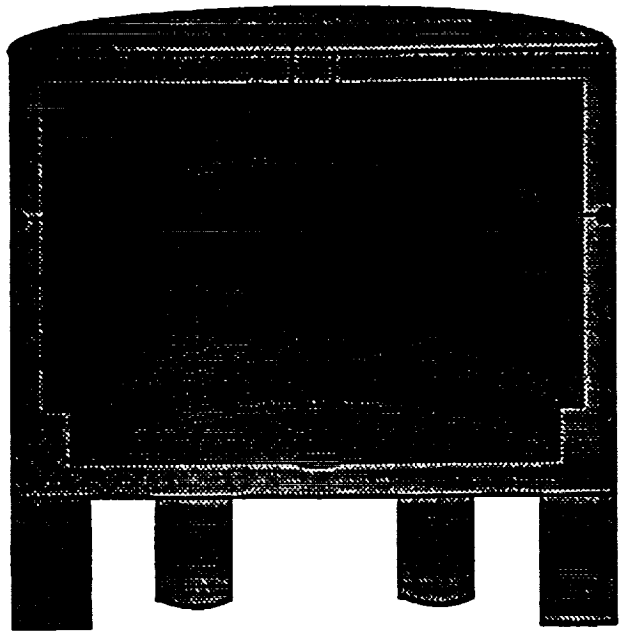

Figure B.1 The copper fixture for gold film calibration

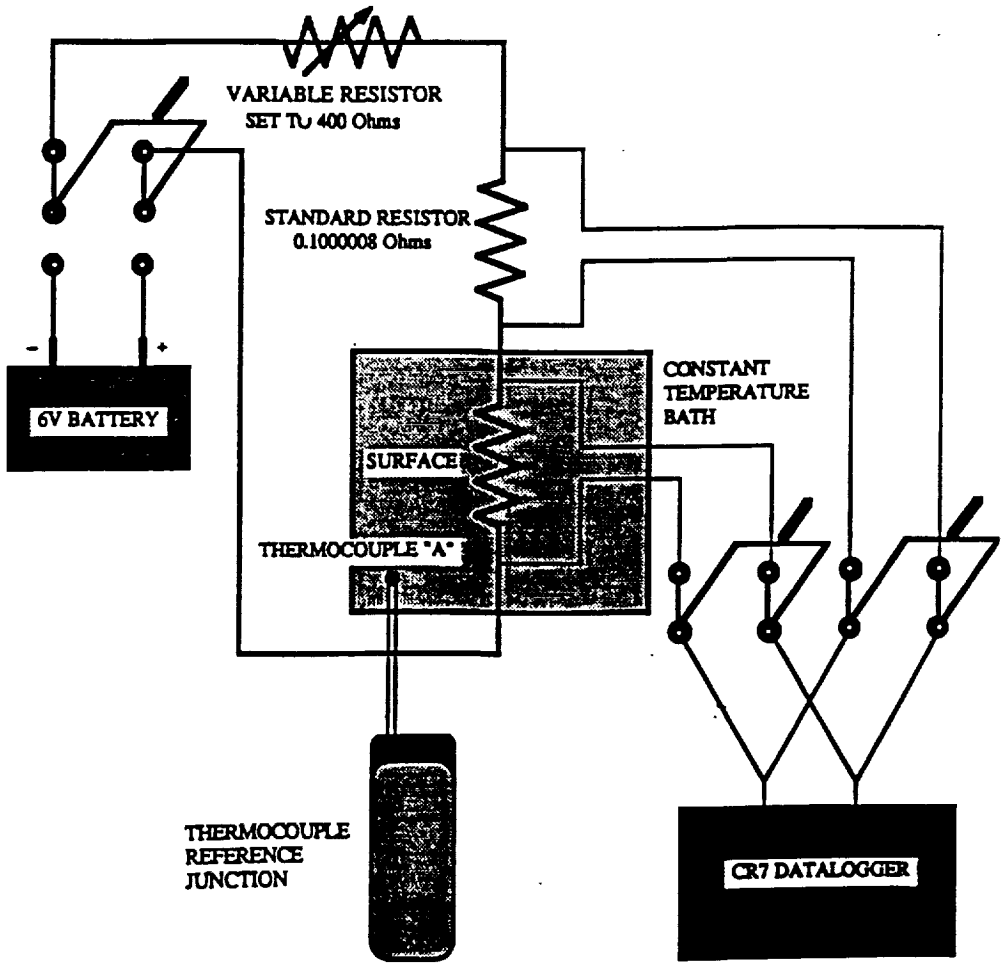

Figure B.2 The voltage measurement circuit for gold film calibration

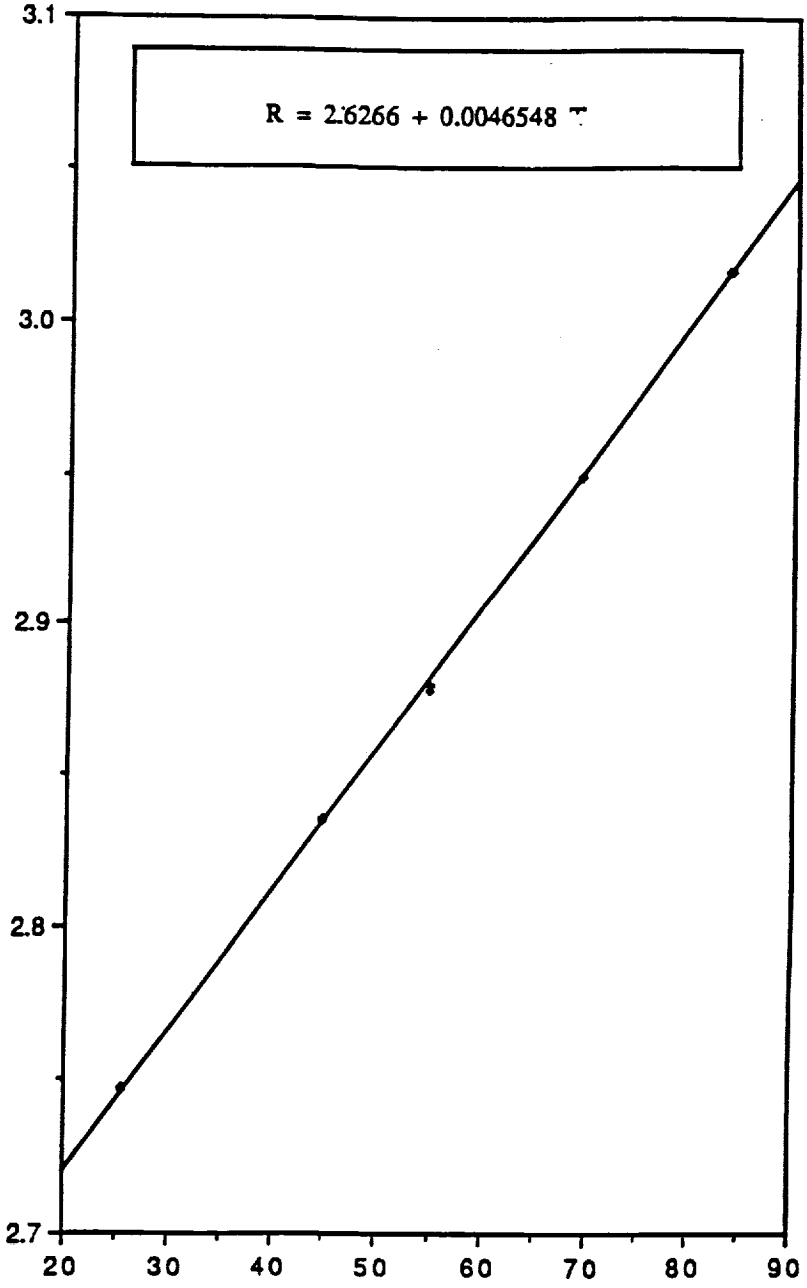

Figure B.3 Surface Q-2 gold film heater calibration

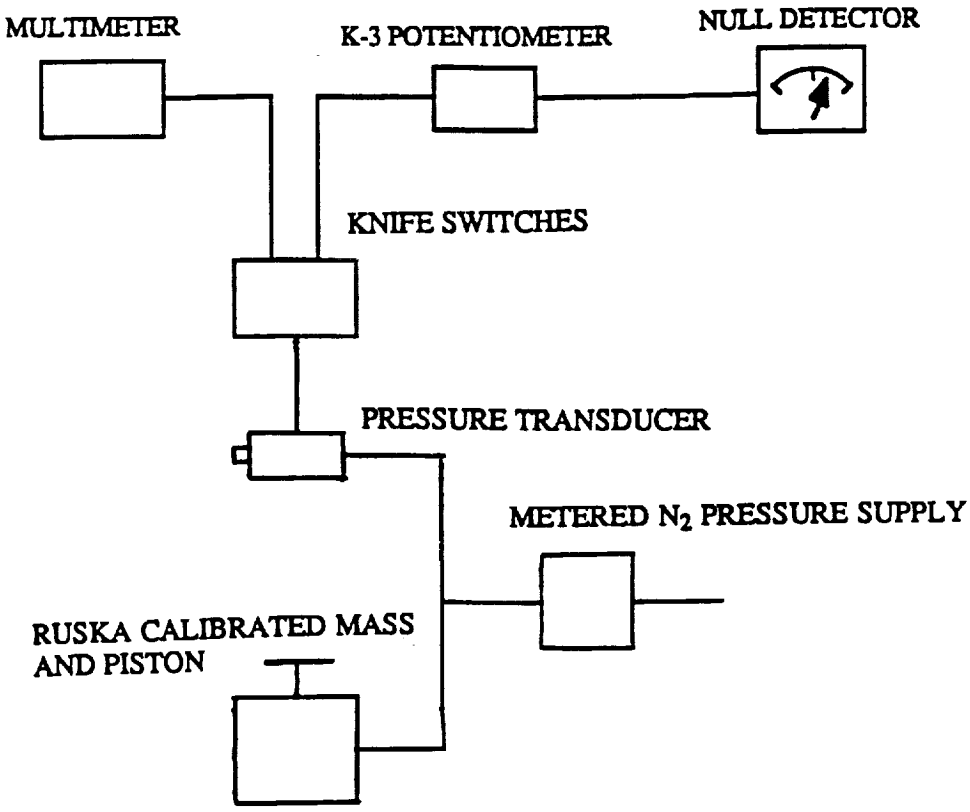

Figure B.4 Schematic for pressure transducer calibration

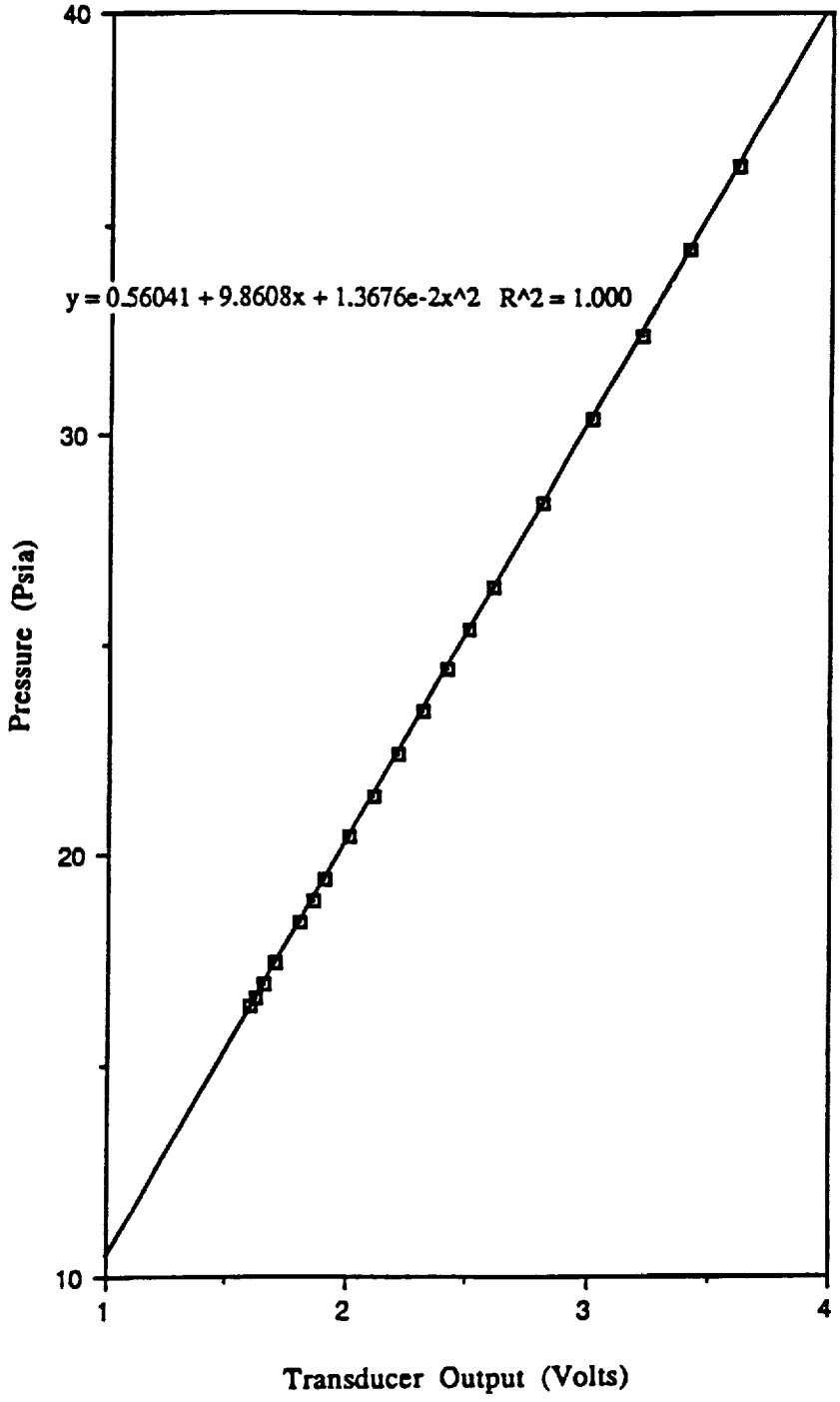

Figure B.5 Calibration for Heise pressure transducer-laboratory pool boiling vessel

C. CR7X AND CODAS DATA ACQUISITION SYSTEMS

Four tests were performed to determine the performance of the CR7X under various measuring conditions. The smallest voltages involved in this study were those of the chromel-constantan thermocouples. The accuracy desired for temperature measurement was 0.06 °C (0.1 °F) which corresponds to about 3 μV. It was found, in the first test, that an ice reference junction for thermocouples provided much more satisfactory temperature measurements than with the internal reference junction compensation of the CR7X. A set of negative and positive terminals were shorted with a copper wire to establish a condition of zero voltage in a second test. Voltage readings were taken employing both the fast and slow sampling rates of the instrument every two seconds at eight different ranges, from the 1.5 mV range to the 5 V range. It was found that two intermediate ranges, 15 mV and 50 mV, were the most desirable in terms of accuracy in temperature measurement in the 20 to 60 °C ambient temperature range.

In the third test, the accuracy of the CR7X with various input voltages for different ranges and sampling rates was verified. The accuracy at each range and speed was measured using a K-3 potentiometer (Leeds and Northrup Model 7553-5), which had a maximum sensitivity of 0.5 μV, and a null detector (Leeds and Northrup Model 9834-1), which had a maximum sensitivity of 0.1 microvolts per division, as the voltage standard. The desired maximum deviation of 3 μV was not met for all of the ranges. The ranges of 500 mV to 5000 mV in the slow sampling rate mode did not meet the 3 μV criterion for any voltage level. The 1.5 mV and the 5 mV range in the slow sampling rate mode were unable to measure voltages exceeding 5 mV. Hence, their effectiveness was diminished. For thermocouple measurements, the 15 mV and the 50 mV ranges were used at the slow sampling rate which had an uncertainty of ± 0.3 μV. The maximum uncertainty on the fast sampling rate mode was ± 0.6 μV for

the 15, 50, and 150 mV ranges at the 49 °C level, which corresponds to a maximum uncertainty in temperature of about ± 0.01 °C.

The dynamics of the CR7X were evaluated in a fourth test against a 7700 series eight channel Sanborn recorder. The Sanborn (with a Model 8803 high gain d.c. amplifier) and the CR7X were used individually and sequentially to measure the transient shunt voltage near the voltage level expected in the transient pool boiling measurements. For this test, the high gain amplifier of the Sanborn recorder had a sensitivity range of 1000 μV per division to 1 μV per division. The Sanborn pre-amp followed from 10 to 90% of a step change in 5 ms. The CR7X and Sanborn voltage measurements were in excellent agreement, as shown in Figure C.1.

Tests were performed with both the CR7X and the Codas data acquisition system in the 50 to 150 mV range, the range of the divided voltage difference across the heater surface, in order to estimate the uncertainty in the Codas system voltage measurement. In this voltage range, there were differences of about one millivolt in the voltage readings between the Codas and the CR7X with the same d.c. source. As a result, the uncertainty in the Codas voltage measurements in this voltage range were estimated to be ± 1 mV.

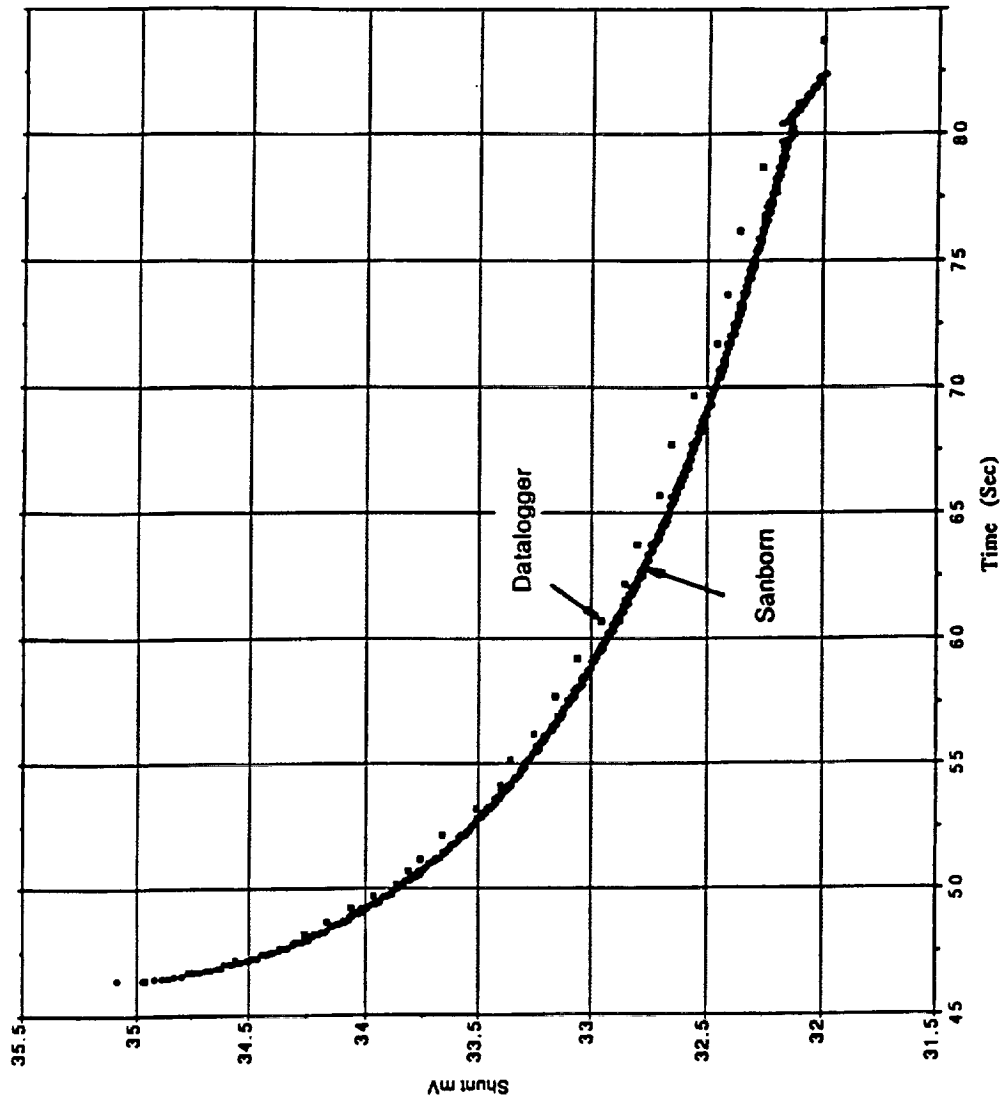

Figure C.1 Comparison of the CR7X and the Sanborn dynamic voltage measurement

D. UNCERTAINTY ANALYSIS

The uncertainties associated with the calculation of the gold film temperature, thermocouple temperature, system pressure, and total heat flux are estimated following the procedure of Kline et al (1953). According to this procedure, the uncertainty u_r in computing r is given by:

$$u_r = \left[\left(\frac{\partial r}{\partial z_1} u_{z_1}\right)^2 + \left(\frac{\partial r}{\partial z_2} u_{z_2}\right)^2 + \ldots + \left(\frac{\partial r}{\partial z_n} u_{z_n}\right)^2 \right]^{1/2} \qquad \text{(D.1)}$$

where r is a function of $z_1, z_2, \ldots, z_n$ and $u_{z_1}, u_{z_2}, \ldots, u_{z_n}$ are the uncertainties in each of these values, respectively.

D.1 Gold Film Temperature

The CR7X was used for calibration of the gold film heater surfaces and for the imposed constant heat flux tests. The uncertainty in the heater surface resistance, which ultimately results in the heater surface temperature, was less for calibration of the heater surfaces than for actual power tests. From equation D.1 the uncertainty in the gold film resistance is expressed as:

$$\frac{u_{R_w}}{R_w} = \left[\left[\frac{u_{V_w}}{V_w}\right]^2 + \left[\frac{u_{V_{sh}}}{V_{sh}}\right]^2 + \left[\frac{u_{R_{sh}}}{R_{sh}}\right]^2 \right]^{1/2} \qquad \text{(D.2)}$$

Values of the quantities in equation from a representative calibration are:

$u_{V_w} = 0.6\ \mu V$ $\qquad$ $u_{V_{sh}} = 0.6\ \mu V$

$V_w = 120\ mV$ $\qquad$ $V_{sh} = 50\ mV$

$u_{R_{sh}} = 0.001\Omega$

$R_{sh} = 3.760\ \Omega$

These values substituted into equation D.2 result in an uncertainty of 0.03%. For power runs, the above values are different and result in a greater uncertainty. Representative values for a power run are:

$u_{V_w} = 0.05\ mV$ $\qquad$ $u_{V_{sh}} = 0.6\ \mu V$

$V_w = 120\ mV$ $\qquad$ $V_{sh} = 50\ mV$

$u_{R_{sh}} = 0.000002\ \Omega$

$R_{sh} = 0.016314\ \Omega$

with a resulting uncertainty in the heater surface resistance of 0.11%.

Calibration data with the largest scatter would be expected to provide a conservative estimate of the uncertainty in the slope. From the calibration data of surface Q-2, the corresponding temperature and resistance data with the largest deviation from the fit line are 54.85 °C at 2.8801 Ω and 83.59 °C at 2.0172 Ω. An estimate for the uncertainty in the slope of the linear relationship between the surface temperature and resistance can be found by using equation D.1 together with the definition of this slope and the above values for temperatures and resistances, respectively. The uncertainty in the slope for these values is ± 0.23 °C/Ω .

The uncertainty in the surface temperature measurement can now be estimated with a known estimate of the uncertainty in the heater surface resistance and of the

slope in equation 4.1. Carrying out the indicated operations of equation D.1 on the equation for the surface heater temperature, equation 4.1, the following expression for uncertainty in the temperature measurement results:

$$u_{T_w} = \left[\left[u_{T_c} \right]^2 + \left[u_m \right]^2 + \left[u(R_w - R_c) \right]^2 \right]^{1/2} \qquad (D.3)$$

Representative values for the quantities in equation are:

$u_{T_c} = 0.05\ ^{\circ}C$ $\qquad$ $u_{R_w} = 0.003\ \Omega$

$u_m = 0.23\ ^{\circ}C/\Omega$ $\qquad$ $u_{R_c} = 0.003\ \Omega$

These values result in an estimated uncertainty in the surface temperature measurement of about $\pm$ 1 °C using the CR7X data acquisition system. The calculations were repeated in the same manner for the Codas system, and the uncertainty for representative values of the above quantities was found to be $\pm$ 6 °C.

D.2 Thermocouple Temperature

As discussed in section B.2, the thermocouple spool was calibrated against the platinum resistance thermometer which had an uncertainty in temperature of $\pm$ 0.001 °C, and a calibration equation for the spool was determined from a fourth order polynomial least square fit of the measured thermocouple voltage and the determined platinum resistance thermometer temperature. In terms of the uncertainty in the CR7X voltage measurement, which was $\pm$ 0.6 μV, the uncertainty in the temperature determination is estimated to be $\pm$ 0.01 °C.

D.3 System Pressure

There was little discrepancy, on the order of ± 0.005 psi between the Ruska pressure determination, with an uncertainty in pressure of ± 0.0003 psi and the calculated pressure resulting from the calibration equations. The uncertainty in pressure resulting from the use of these equations was then taken as ± 0.005 psi. From equation D.1:

$$\frac{u_P}{P} = \left[\frac{\partial P}{\partial V}\right] \frac{u_V}{P} \tag{D.4}$$

where P is the calculated pressure from the calibration equation and V is the pressure transducer voltage signal. For a typical run the following values were obtained:

$u_V = 1$ mV $P = 16$ psi

$\frac{\partial P}{\partial V} = 9.8608 - 2.7352 \times 10^{-2} V$ $V = 1.6$ V

The uncertainty in pressure at this level is estimated from equation to be 0.06%.

D.4 Total Heat Flux

The expression for q''_T was given earlier in equation 4.2. Using equation D.1 with equation 4.2, an expression for the uncertainty in q''_T is:

$$\frac{u_{q''_T}}{q''_T} = \left[\left(\frac{u_{V_T}}{V_T} \right)^2 + \left(\frac{u_{V_{sh}}}{V_{sh}} \right)^2 + \left(\frac{u_{R_{sh}}}{R_{sh}} \right)^2 + \left(\frac{u_A}{A} \right)^2 \right]^{1/2} \qquad \text{(D.5)}$$

In the experiments using the CR7X the following were typical values:

$u_{V_T} = 0.3\ \mu V$	$u_{R_{sh}} = 0.000002\ \Omega$
$V_T = 5\ V$	$R_{sh} = 0.016314\ \Omega$
$u_{V_{sh}} = 0.3\ \mu V$	$u_A = 0.08\ cm^2$
$V_{sh} = 0.08\ V$	$A = 7.25\ cm^2$

With equation D.5 and these values, the estimated uncertainty in the calculated q''_T is 1%.

E. ELECTRONIC CIRCUITRY

E.1 Power Supply for Step in Heat Flux and Quasi-Steady Heating

As shown in Figure E.1, the power controller receives the set point voltage from either the CR7X or a manual input command, and amplifies the signal by two. The feedback signal (FBK1) from heater card number 1, presented in Figure E.2, is then subtracted from the amplified set point voltage and extraneous noise is filtered. For a positive difference, a proportional amount of current is sent into the base of transistor number 1. For a negative or zero difference, a diode prevents current from entering the base of transistor number 1. The base current then draws an amplified amount of current from the collector which is connected to bases (B1, B2, B3, and B4) of the four transistors on heater card number 1. Thus, as the base currents to the heater card transistors are increased, more power is sent to the heater.

E.2 Power Supply for Step in Heater Surface Temperature

This power supply produces a rapidly varying, programmed schedule of power to the test heater to result in a constant temperature of the test heater. The schedule begins with the maximum power to the heater, and the power is progressively decreased.

Discrete changes in the heating power permit the use of switches. N-channel MOSFET switches are used. The heater is on a common bus which connects the sources of all of the MOSFETS. The power supply voltage is connected to a separate loading resistor for each switch, the other side of the load resistor is connected to the drain of the MOSFET. The series combination of the heater and load resistances

determines the power to the heater when the appropriate switch is on. Each gate is optically coupled to its particular switching signal.

The voltage-time schedule is divided into 24 different time intervals; as short as 20 micro-seconds for early intervals and as long as 1.3 seconds for the final interval. A micro-processor programmed in assembly times the signals to the switches.

Since the power supply starting transient requires about 50 milliseconds, an output resistor with a MOSFET permits the power supply to operate near maximum power before the actual power switching transient is imposed. Details of the electronic circuitry are presented in Figure E.3.

E.3 Pressure Controller

For large deviations from the set point pressure level, the pressure controller operates as an on/off controller by opening and closing the solenoid actuated fill/vent valves in response to large pressure deviations. More precise control is achieved through regulation of the proportional valve while a needle valve admits a constant flow rate of air into the bellows and the fill/vent valves remain closed. The proportional valve is operated within its linear range of operation so that as voltage to the proportional valve is increased or decreased, the flow rate of air exiting the bellows in direct proportion to the voltage. The electronic circuits are presented in Figures E.4 through E.6.

E.4 Drop Vessel Temperature Controller

Before a drop test, the drop vessel was brought to a uniform temperature by means of heating films attached to the external surfaces of the drop vessel. The heating films were powered by means of the drop vessel temperature controller. The

electronic circuits for the drop vessel temperature controller are presented in Figures E.7 through E.10.

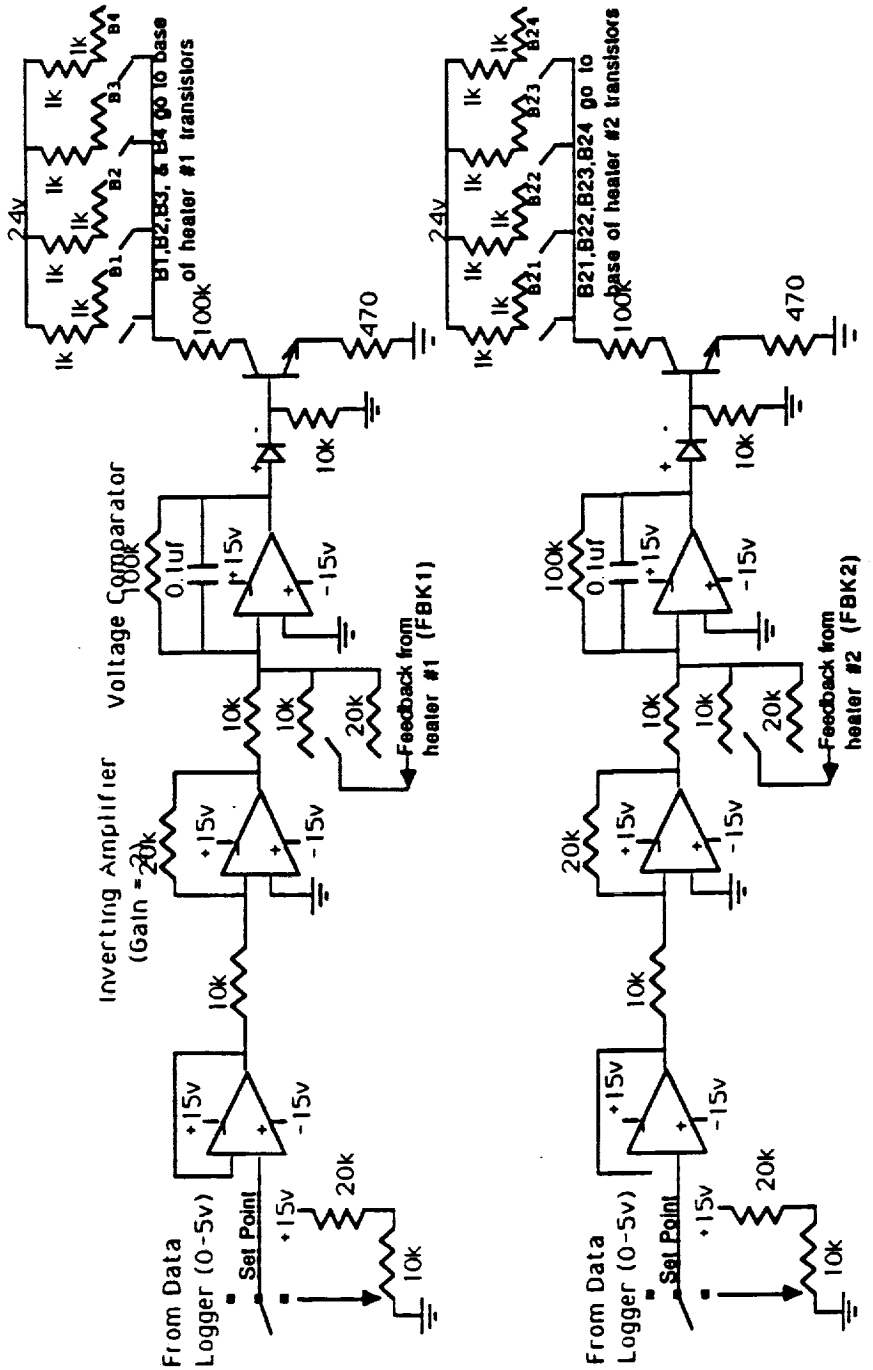

Figure E.1 Main heater controller

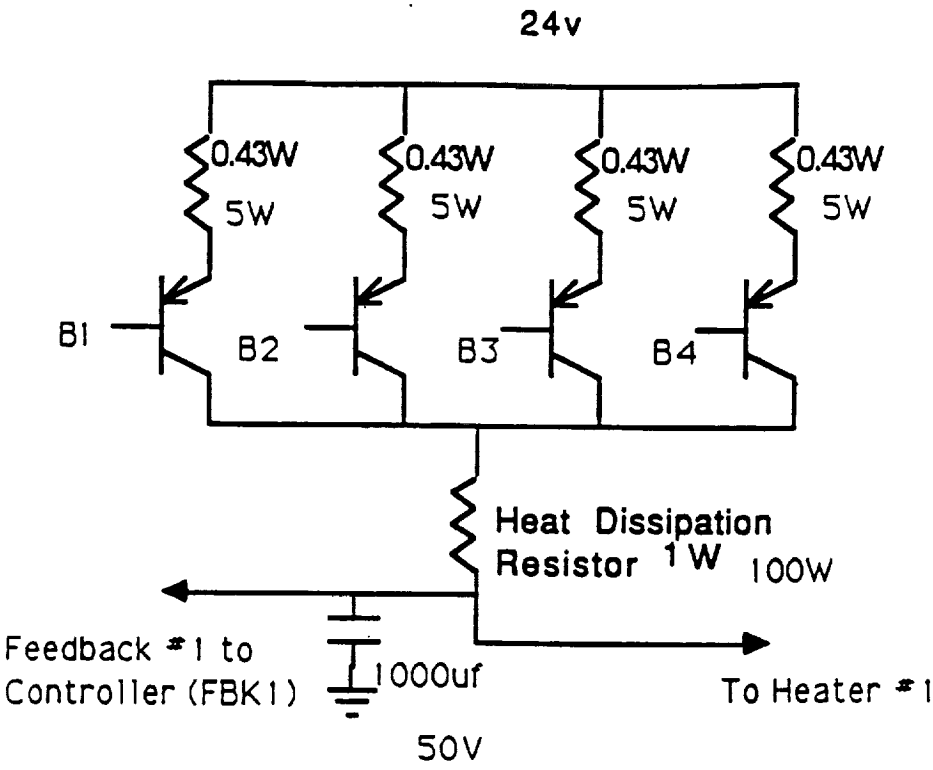

Figure E.2 Heater controller

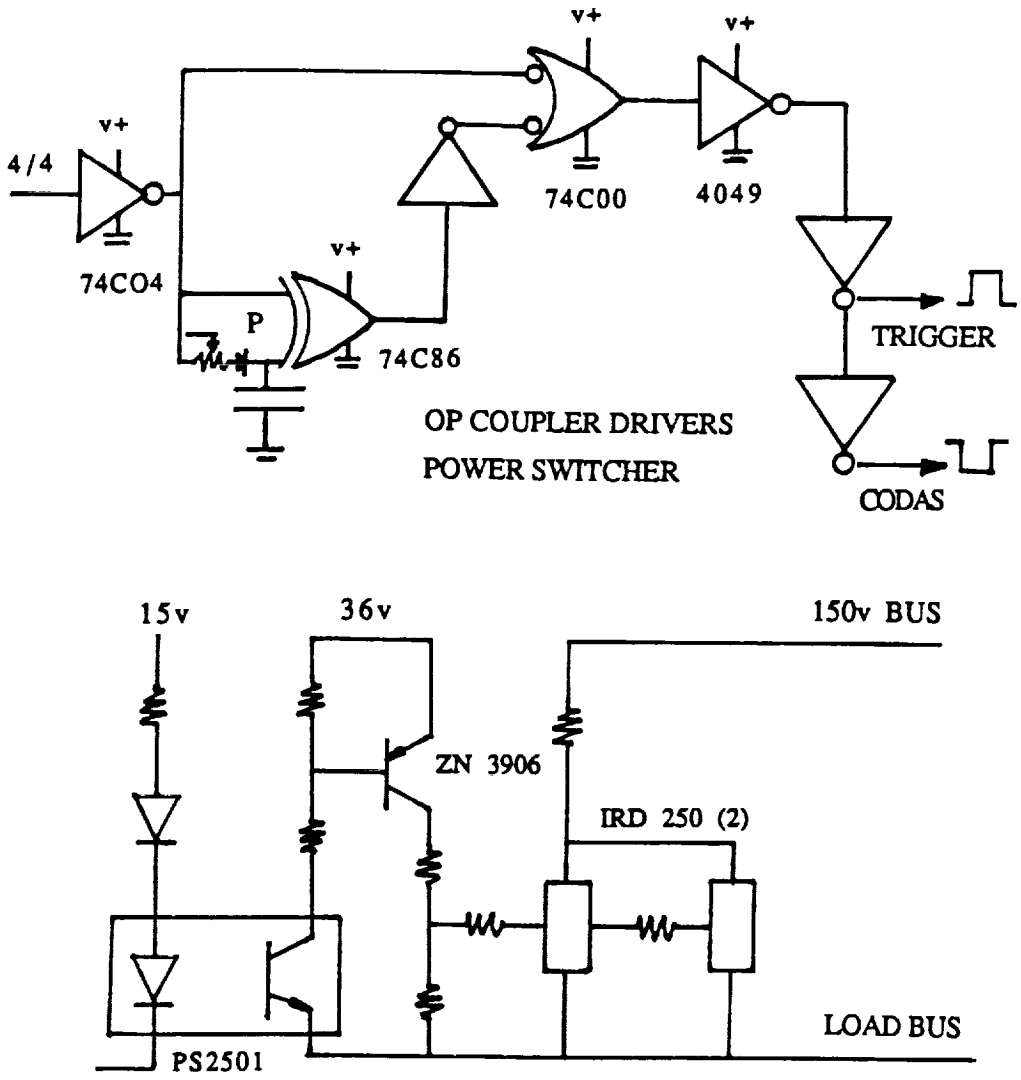

Figure E.3 Heater surface power controller for imposed step in temperature

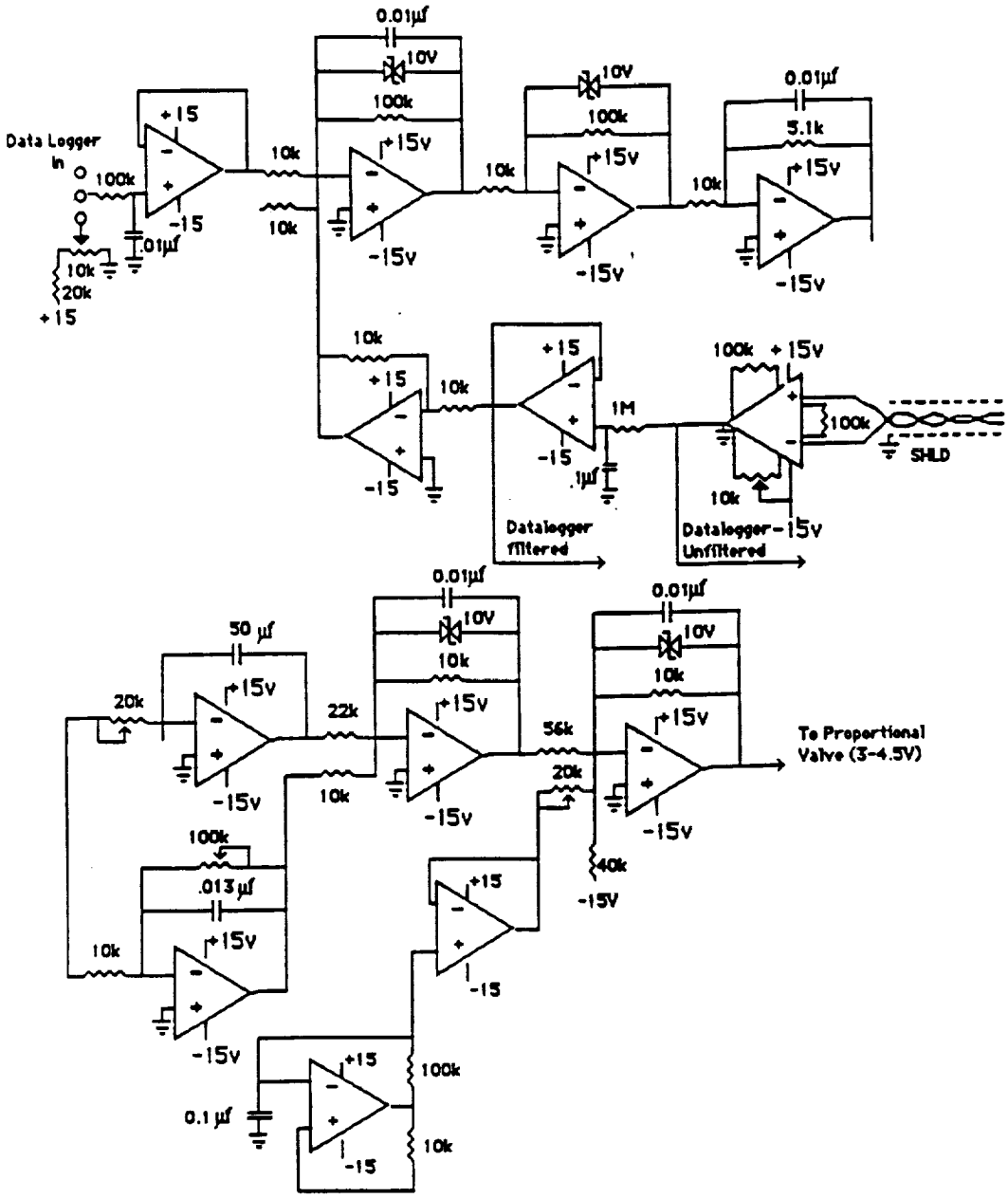

Figure E.4 Pressure controller: part one

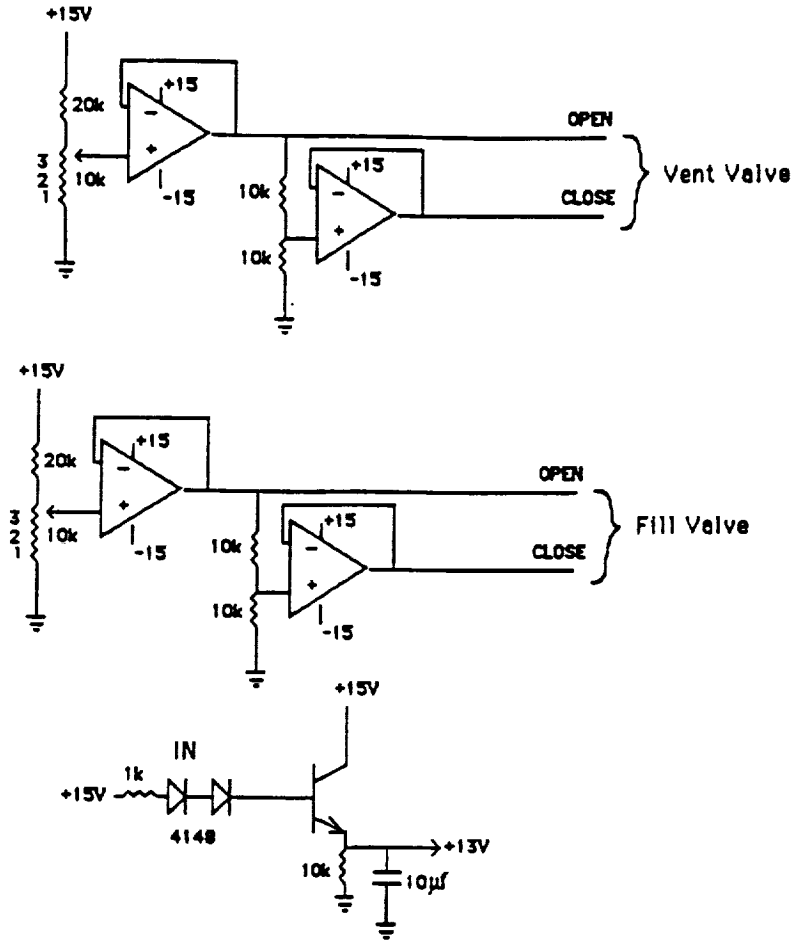

Figure E.5 Pressure controller: part two

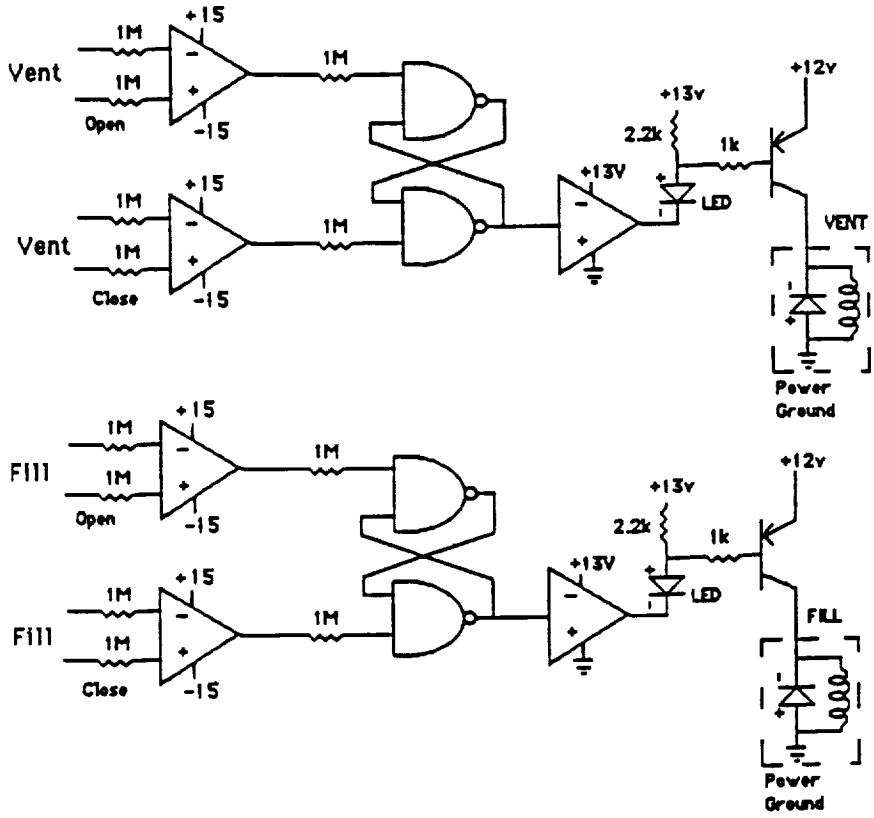

Figure E.6 Pressure controller: part three

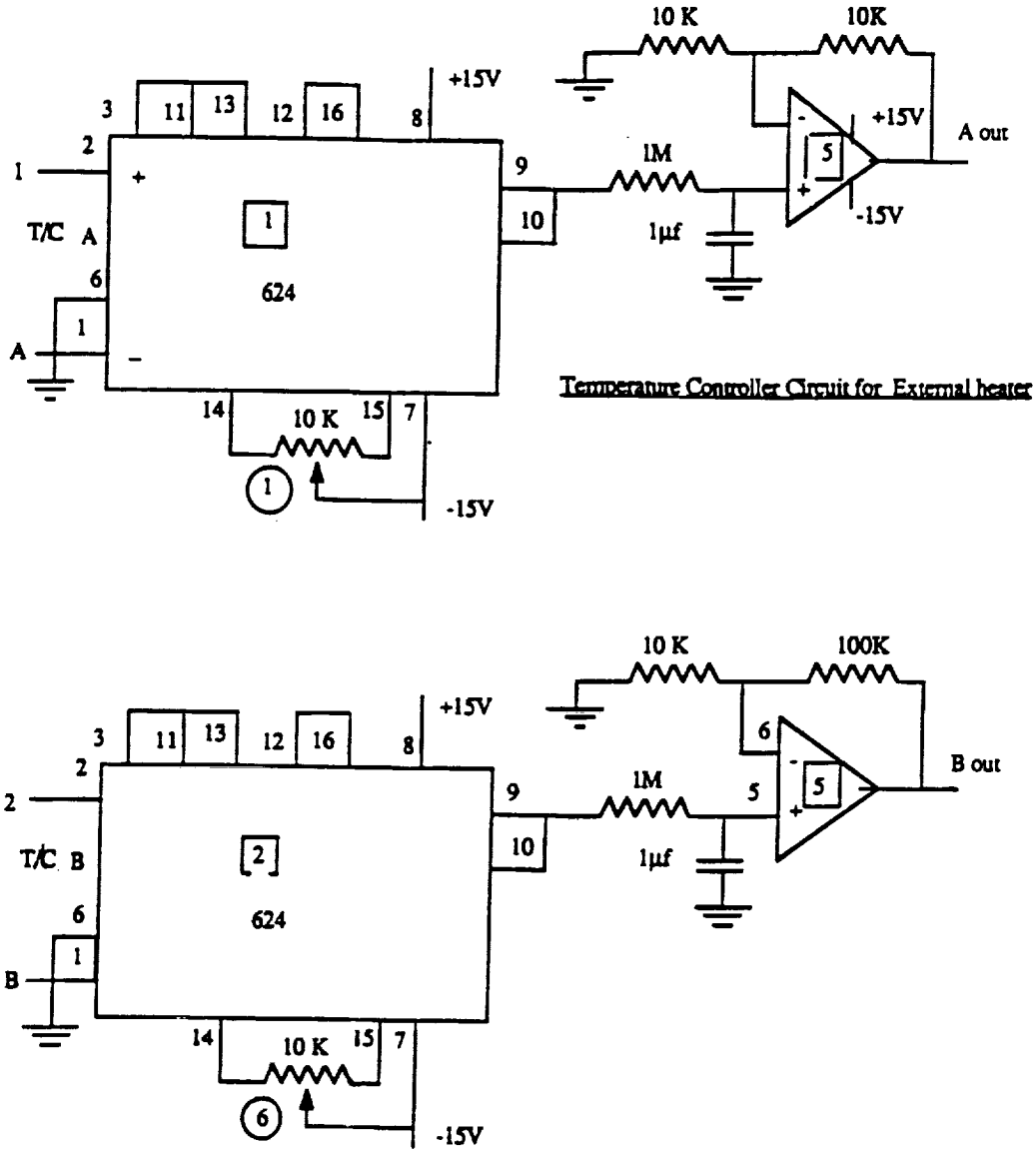

Figure E7 Drop vessel external heater power controller: part one

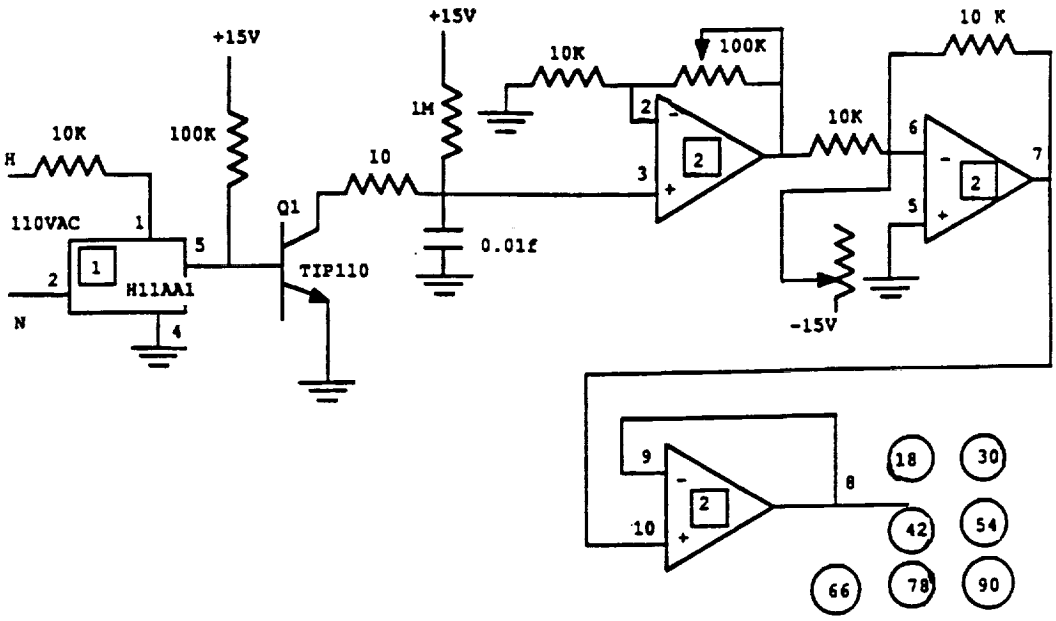

Figure E8 Drop vessel external heater power controller: part two

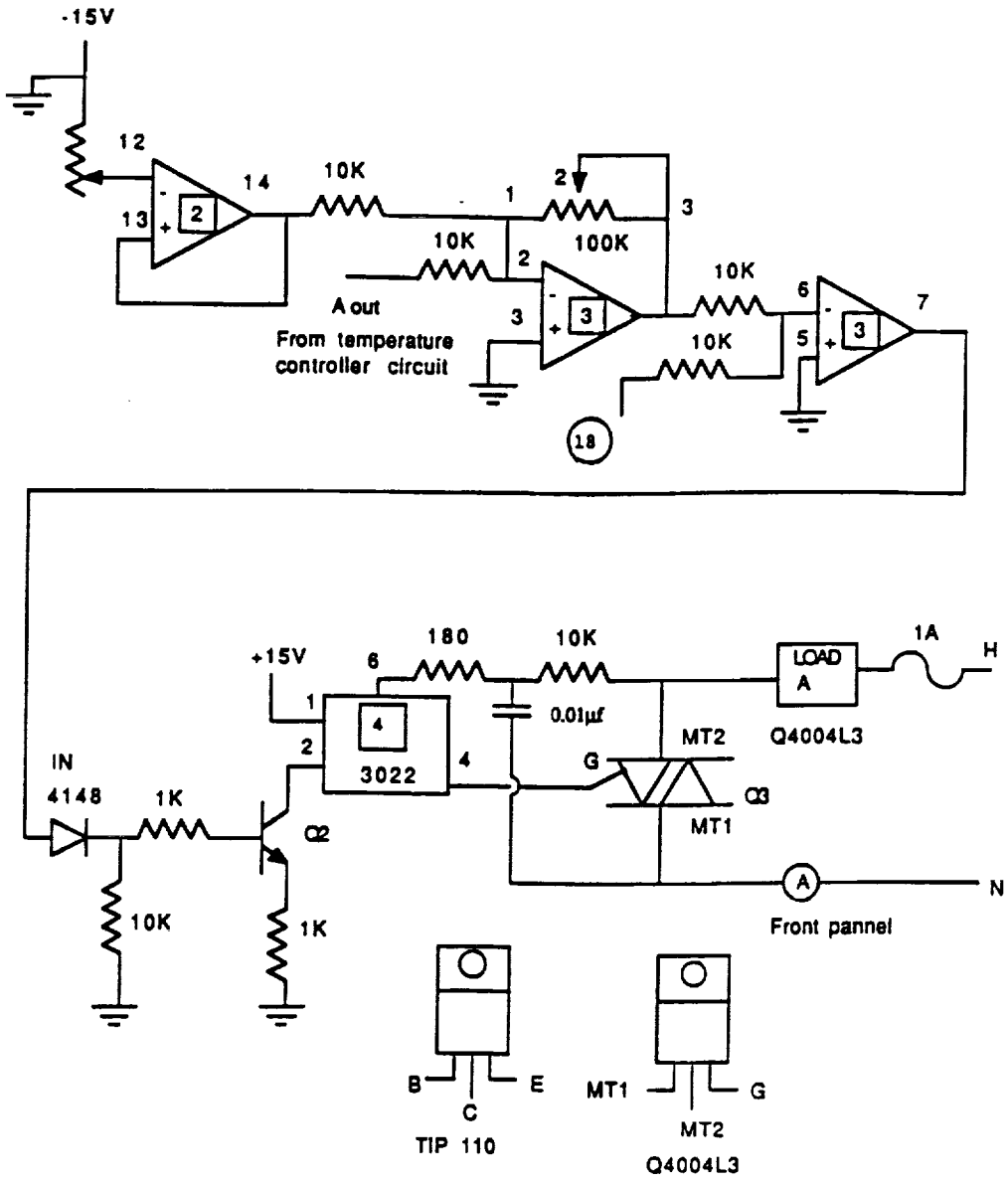

Figure E9 Drop vessel external heater power controller: part three

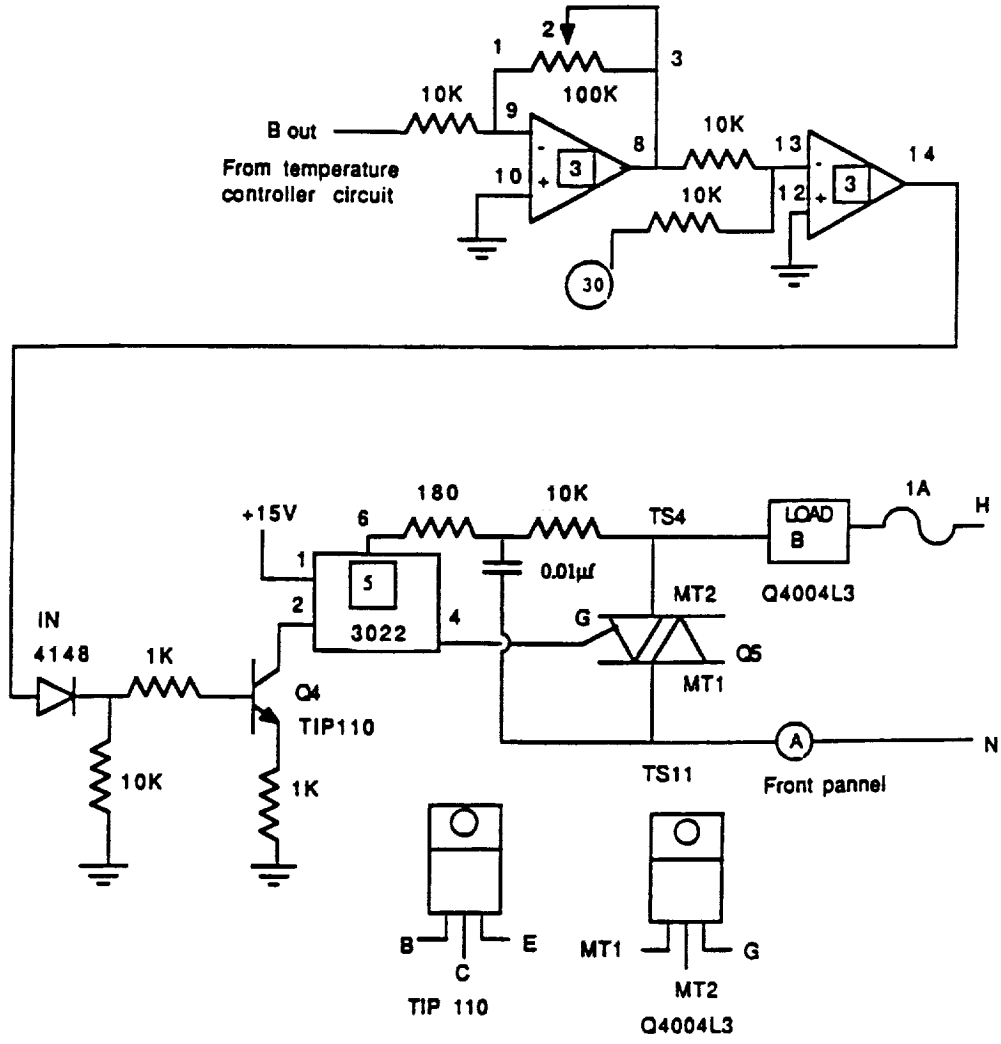

Figure E10 Drop vessel external heater power controller: part four

F. ANALYSIS OF IMPOSED STEP IN TEMPERATURE

One dimensional conduction to two semi-infinite media, in this case R113 and quartz, from the common plane heat source, which produces a step in the interface temperature at the boundary, are described analytically. The problem is considered in two domains as shown in Figure F.1. The following governing equation, initial condition, and boundary conditions are for the R113:

$$\frac{\partial \theta}{\partial t} = \alpha_l \frac{\partial^2 \theta}{\partial x^2} \tag{F.1}$$

where $\theta = T - T_w$

$$\theta(x,0) = T_\infty - T_w \tag{F.2}$$

$$\theta(0,t) = 0 \tag{F.3}$$

$$\theta(\infty,t) = T_\infty - T_w \tag{F.4}$$

The solution to F.1 and the heat flux necessary at the boundary to maintain the constant temperature are by the Laplace transform method as described in Arpaci (1966):

$$\frac{T-T_w}{T_\infty - T_w} = \text{erf}\left[\frac{x}{2\sqrt{\alpha_l t}}\right] \tag{F.5}$$

$$q''_l = -k\left[\frac{\partial \theta}{\partial x}\right]_{x=0} = k_l \frac{(T_w - T_\infty)}{\sqrt{\pi \alpha_l t}} \tag{F.6}$$

The temperature distribution in the quartz is also given by equation F.5, but with the properties for quartz substituted for the R113 properties and the origin for the quartz domain as indicated in Figure F.1. The heat flux to the quartz is given by equation F.6 with the appropriate quartz properties. The sum of the heat flux to the quartz and the heat flux to the R113 results in equation 3.1, the total power input to the heater surface divided by the surface area to impose a step increase in surface temperature:

$$q''_T = \left[\left(\sqrt{k \rho c_p} \right)_l + \left(\sqrt{k \rho c_p} \right)_{qtz} \right] \frac{T_w - T_\infty}{\sqrt{\pi t}} \tag{3.1}$$

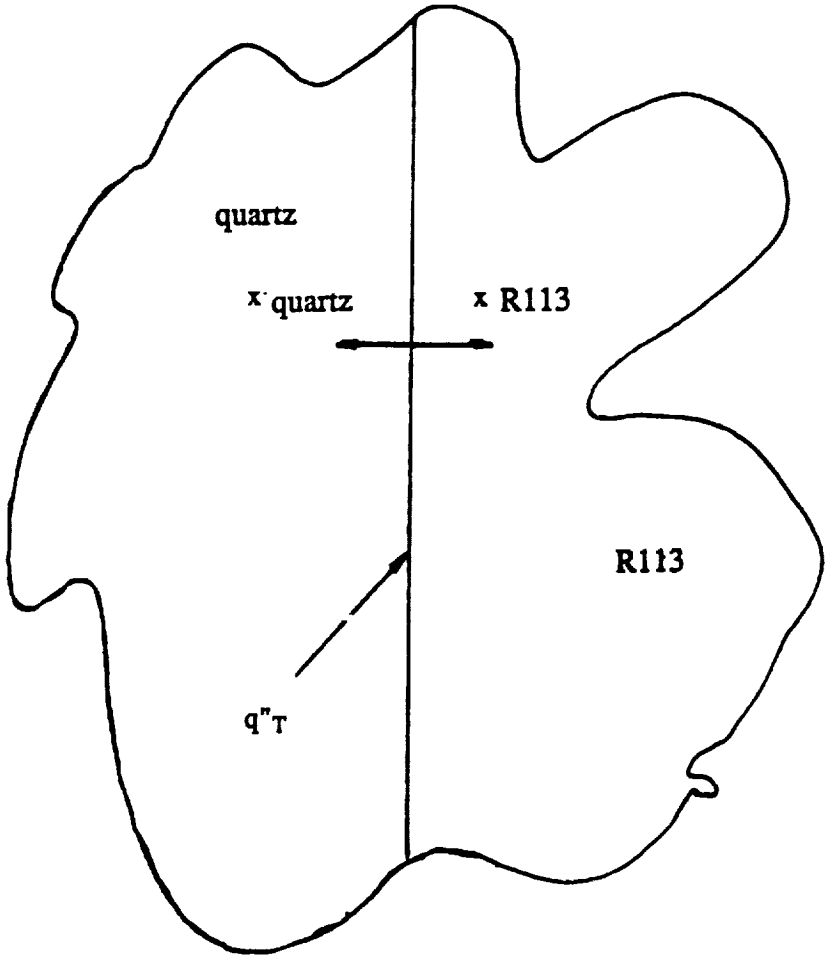

Figure F.1 One dimensional conduction to two connecting semi-infinite media with energy generation at the common plane

G. ANALYSIS OF IMPOSED STEP IN HEAT FLUX

The transient temperature distribution resulting from conduction in two connecting semi-infinite media with a uniform plane heat source q_T" at the interface may be found analytically for each of the two media. The solutions for the R113 and quartz substrate are, respectively:

$$T_l - T_\infty = \frac{2q"_T\sqrt{\alpha_{qtz}\alpha_l t}}{k_l\sqrt{\alpha_{qtz}} + k_{qtz}\sqrt{\alpha_l}}\ \text{ierfc}\left[\frac{x_l}{2\sqrt{\alpha_l t}}\right] \tag{G.1}$$

$$T_{qtz} - T_\infty = \frac{2q"_T\sqrt{\alpha_{qtz}\alpha_l t}}{k_l\sqrt{\alpha_{qtz}} + k_{qtz}\sqrt{\alpha_l}}\ \text{ierfc}\left[\frac{x_{qtz}}{2\sqrt{\alpha_{qtz} t}}\right] \tag{G.2}$$

H. THREE DIMENSIONAL CONDUCTION NUMERICAL ANALYSIS

A three dimensional numerical solution for the transient temperature distribution in the quartz and the R113 was obtained by solving the conduction equation with temperature dependent properties and power generation in the common plane. The Crank-Nicholson finite difference method, which is unconditionally stable, was used to solve the equations. The numerical grid had equivalent node spacing in all three coordinate directions, and the spacing was adjustable. Since the problem was symmetric, the temperature in one fourth of the quartz and R113 solution domain provided the three dimensional temperature distribution. Temperature solutions in several vertical planes of the quartz and R113, including the heater surface, were printed at the desired time. Boundary conditions on the bottom of the quartz surface included those of convection and an insulated boundary. The edges of the heater surface and the R113 above were assumed to be insulated.

BIBLIOGRAPHY

BIBLIOGRAPHY

Abraham, F. F., "Homogeneous Nucleation Theory", *Adv. Theor. Chem., Suppl. 1*, Academic Press, New York, NY., 1974.

Arpaci, V. S., *Conduction Heat Transfer*, Addison-Wesley, Reading, Mass., 1966.

Bankoff, S., "Entrapment of Gas in The Spreading of a Liquid Over a Rough Surface", *AIChE J.*, Vol. 4, pp. 24-26, 1958.

Becker, R., and Doring, W., "The Kinetic Treatment of Nuclear Formation in Supersaturated Vapors", *Ann. Phys.*, Vol. 24, p. 719, 1935.

Bergles, A. E., and Rohsenow, W. M., "The Determination of Forced-Convection Surface-Boiling Heat Transfer", *J. Heat Transfer*, Paper No. 63-HT-22, pp. 1-8, 1963.

Blander, M., and Katz, Joseph L., "Bubble Nucleation in Liquids", *AIChE. J.*, Vol. 21, pp. 833-848, 1975.

Boucher, E. A., "Nucleation in The Atmosphere", in *Nucleation*, Zettlemoyer, L. C., and Marcel D., Ed., p. 527, Dekker, New York, 1969.

Chowdhury, S. K. R., and Winterton, R. H. S., "Surface Effects in Pool Boiling", *Int. J. Heat Mass Transfer*, Vol. 28, pp. 1881-1889, 1985.

Clark, H. B., Strenge, P. S., and Westwater, J. W., "Active Sites for Nucleate Boiling", *Chem. Engr. Prog. Symposium Series*, Vol. 51, pp. 103-, 1959.

Coeling, K. J., and Merte, H. Jr., "Incipient and Nucleate Boiling of Liquid Hydrogen", ASME. Paper No. 68-WA/PID-4, 1968.

Cole, R., "Boiling Nucleation", *Advances in Heat Transfer*, Vol. 10, Hartnett, J. P., and Irvine, T. F. Jr.,Ed., New York, London, Academic Press, pp. 85-166, 1974.

Cooper, M.G., and Chandratilleke, "Growth of Diffusion-Controlled Vapour Bubbles at a Wall in a Known Temperature Gradient", *Int. J. Heat Mass Transfer*, Vol. 24, pp. 1475-1492, 1981.

Cornwell, K., "On Boiling Incipience Due to Contact Angle Hysteresis", *Int. J. Heat Mass Transfer*, Vol. 25, pp. 205-211, 1982.

Corty, C., and Foust, A. S., "Surface Variables in Nucleate Boiling",*Chem. Engr. Prog. Symposium Series*, Vol. 51, pp. 1-12a, 1959.

Derewnicki, K. P., "Experimental Studies of Heat Transfer and Vapour Formation in Fast Transient Boiling", *Int. J. Heat Mass Transfer*, Vol. 28, pp. 2085-2092, 1985.

E. I. DuPont de Nemours and Co., Inc., "Freon Product Information", Cat. No. B-2, E. I. DuPont de Nemours and Co., Inc.,Wilmington, De., 1969.

E.I. Dupont de Nemours and Co., Inc., Personal Communication, March 1990.

Fabic, S., "Vapor Nucleation on Surfaces Subjected to Transient Heating", Ph.D. Dissertation, U. of California, Berkeley, No.65-2978, 1964.

Faw, R.E., VanVleet, R.J., and Schmidt, D.L., "Pre-pressurization Effects on Initiation of Subcooled Pool Boiling During Pressure and Power Transients", Int. J. Heat Mass Transfer, Vol. 29, pp. 1427-1437, 1986.

Fisher, J. C., "The Fracture of Liquids", *J. Applied Physics*, Vol. 19, pp. 1062-1067, 1948.

Forest, T.W., "The Stability Of Gaseous Nuclei At Liquid-Solid Interfaces", *J. Appl. Phys.*, Vol. 53, pp. 6191-6201, 1982.

Frenkel, J., *Kinetic Theory of Liquids*, Dover Publ. Inc., New York, NY, 1955.

Gerum, E., Straub, J., and Grigull, U., "Superheating in Nucleate Boiling Calculated by the Heterogeneous Nucleation Theory", *Int. J. Heat Mass Transfer*, Vol. 22, pp. 517-524, 1979.

Gibbs, J. W., *The Collected Works of J. W. Gibbs, Vol. 1*, Longmans, Green, New York, NY, 1928.

Griffith, P., and Wallis, J. D., "The Role of Surface Conditions in Nucleate Boiling", *Chem. Engr. Prog. Symposium Series*, Vol. 56, pp. 49-63, 1960.

Hall, W. B., and Harrison, W. C., "Transient Boiling of Water at Atmospheric Pressure", *Int. Heat Transfer Conf., Institute of Mech. Eng.*, pp. 186-192, 1966.

Han, C. Y., and Griffith, P., "The Mechanism of Heat Transfer in Nucleate Pool Boiling-Part I.", *Int. J. Heat Mass Transfer*, Vol. 8, pp. 887-904, 1965.

Hino, R., and Ueda, T., "Studies on Heat Transfer and Flow Characteristics in Subcooled Flow Boiling-Part I. Boiling Characteristics", *Int. J. Multiphase Flow*, Vol. 11, pp. 269-281, 1985.

Hirth, J. P., and Pound, G. M., "Condensation and Evaporation, Nucleation and Growth Kinetics", *Prog. Materials Sci.*, Vol. 11, 1963.

Howell, J.R., and Siegel, R.," Incipience Growth and Detachment of Boiling Bubbles in Saturated Water from Artificial Nucleation Sites of Known Geometry and Size", *Int. Heat Transfer Conf. Chicago*, pp. 512-513, 1966.

Hsu, Y. Y., "On the Size Range of Active Nucleation Cavities on a Heating Surface", *J. Heat Transfer*, Vol. 84, pp. 207-216, 1962.

Ibrahim, E. A., and Judd, R. L., "An Experimental Investigation of the Effect of Subcooling on Bubble Growth and Waiting Time in Nucleate Boiling", *J. Heat Transfer*, Vol. 107, pp. 168-174, 1985.

Incropera, F. P., and DeWitt, D. P., *Fundamentals of Heat Transfer, 2nd Ed.*, John Wiley and Sons, Inc., New York, NY., 1984.

Jarvis, T. J., Donohue, M. D., and Katz, J. L., "Bubble Nucleation Mechanisms of Liquid Droplets Superheated in Other Liquids", *J. Colloid Interf. Sci.*, Vol. 50, p. 359, 1975.

Kline, S.J., and McClintock, F.A., "The Description of Uncertainties in Single Sample Experiments", *Mechanical Engineering*, Vol. 75, 1953.

Kotake, S., and Glass, I. I., "Flows With Nucleation and Condensation", *Prog. Aerospace Sc.*, Vol. 19, pp. 129-196, 1981.

Kottowski, H. M., "The Mechanism of Nucleation, Superheating and Reducing Effects on the Activation Energy of Nucleation", *Prog. in Heat and Mass Transfer*, D. E. Dweyer, Ed., Vol. 7, pp. 299-324, Permagon Press, Oxford, 1973.

Landau, L., "On the Theory of Slow Combustion", Acta Physiochimica U.R.S.S., Vol. 19, pp. 77-85, 1944.

Lee, C. H., Chang, C. J., Yin, S. T., and Huang, Y. D., "Prediction of Incipient Boiling with Forced Convective Flow at 0.1 to 20.7 MPa", *ASME 1988 Heat Transfer Conf, HTD-96*, Vol. 2, pp. 469-474.

Lorenz, J., Mikic, B., and Rohsenow, W.M., "The Effect of Surface Conditions on Boiling Characteristics", *1974 Japanese Int. Heat Transfer Conf.*, Paper No. B2.1, pp. 35-39, 1974.

Lothe, J., and Pound, G. M., "Reconsiderations of Nucleation Theory", *J. Chem. Phys.*, Vol. 36, pp. 2080-2085, 1962.

Lothe, J., and Pound, G. M., "On The Statistical Mechanics of Nucleation Theory", *J. Chem. Phys.*, Vol. 45, pp. 630-634, 1966.

Lothe, J., and Pound, G. M., "Concentration of Clusters in Nucleation and the Classical Phase Integral", *J. Chem.Phys.*, Vol. 48, pp. 1849-1852, 1968.

Lurie, H., and Johnson, H. A., "Transient Pool Boiling of Water on a Vertical Surface with a Step in Heat Generation", J. Heat Transfer, Vol. 84, pp. 217-224, 1962.

Mayer, J.E., and Harrison, S. F., "Statisical Mechanics of Condensing Systems", *J. Chem. Phys.*, Vol. 6, pp. 87-104, 1938.

McCann, H., Clarke, L.J., Masters, A.P., "An Experimental Study of Vapor Growth at the Superheat Limit Temperature", Int. J. Heat Mass Transfer, Vol. 32, pp. 1077-1093, 1989.

Merte, H. Jr., and Clark, J. A., "Pool Boiling in an Accelerating System", *J. Heat Transfer*, Vol. 83, pp. 234-242, 1961.

Merte, H. Jr., and Littles, J., "Zero Gravity Incipient Boiling Heat Transfer", *Proc. Space Transportation System Propulsion Technology Conference*, Vol. 4, pp. 1312-1348, NASA, Huntsville, Alabama, April 6 and 7, 1971.

Montgomery, D. C., *Design and Analysis of Experiments, 2nd Ed.*, John Wiley and Sons, Inc., New York, NY., 1983.

Ngheim, L. X., "Holographische Untersuchung Des Instationaren Siedens", PhD Thesis, Munich, 1980.

Nghiem, L. X., Merte, H. Jr., Winter, E. R. F., and Beer, H., "Prediction of Transient Inception of Boiling in Terms of a Heterogeneous Nucleation Theory", *J. Heat Transfer*, Vol. 103, pp. 69-73, 1981.

Oker, E., and Merte, H. Jr., "Transient Boiling Heat Transfer in Saturated Liquid Nitrogen and F113 at Standard and Zero Gravity", U. Michigan, Rept. No. 074610-52-F for NASA, 1973.

Oker, E., and Merte, H. Jr., "A Study of Transient Effects Leading up to Inception of Nucleate Boiling", *Proceedings of the 6th Int. Heat Transfer Conference, Toronto, August 1978*, pp. 139-144, 1978.

Oker, E., and Merte, H. Jr., "Semi-Transparent Gold Film as Simultaneous Surface Heater and Resistance Thermometer for Nucleate Boiling Studies", *J. Heat Transfer*, Vol. 103, pp. 65-68, 1981.

Okuyama, K., Kozawa, Y., Inoue, A., and Aoki, S., "Transient Boiling Heat Transfer Characteristics of R113 at Large Stepwise Power Generation", *Int. J. Heat Mass Transfer*, Vol. 31, pp. 2161-2174, 1988.

Panton, R.L., *Incompressible Flow*, Wiley, New York, pp. 316-318, 1984.

Prosperetti, A. and Plesset, M.S., "Vapor Bubble Growth in a Superheated Liquid", J. Fluid Mech., Vol. 85, pp. 349, 1978.

Reiss, H., "Theory of the Liquid Drop Model, Industrial and Engineering Chemistrtudies", Vol. 44, pp. 1284-1288, 1952.

Reiss, H., "The Statistical Mechanical Theory of Irreversible Condensation-Part I.", *J. Chem. Phys.*, Vol. 20, pp. 1216-1227, 1952.

Reiss, H., "Treatment of Droplike Clusters by Means of the Classical Phase Integral in Nucleation Theory", *J. Stat. Phys.*, Vol. 2, pp. 83-104, 1970.

Reiss, H., and Katz, J. L., "Resolution of the Rotational Translational Paradox in the Theory of Irreversible Condensation", *J. Chem. Phys.*, Vol. 46, pp. 2496-2499, 1967.

Rohsenow, W. M., "Nucleation in Boiling Heat Transfer", ASME Paper 70-HT-18, *ASME Symposium, Detroit, Mi., May, 1970.*, 1970

Sakurai, A., and Shiotsu, M., "Transient Pool Boiling Heat Transfer, Part 1: Incipient Boiling Superheat", *J. Heat Transfer*, Vol. 99, pp. 547-553, 1977.

Shoukri, M., and Judd, R. L., "Nucleation Site Activation in Saturated Boiling", *J. Heat Transfer*, Vol. 97, pp. 93-98, 1975.

Sigsbee, R. A., "Vapour to Condensed-Phase Heterogeneous Nucleation", in *Nucleation*, Zettlemoyer, L. C., and Marcel D., Ed., p. 151, Dekker, New York, 1969.

Simpson, H. C., and Walls, A. S., "A Study of Nucleation Phenomena in Transient Pool Boiling", *Proc. Instn. Mech. Engrs.*, Vol. 180, Pt. 3C, Vol. 135-149, 1965-66.

Sinha, D.N., "Studies Of Homogeneous Nucleation And Transient Heat Transfer In Cryogenic Liquids", PhD Dissertation, Portland State University, 1980.

Skripov, V. P., *Metastable Liquids*, Trans. by R. Kondor, Israel Program for Scientific Translations, D. Slutzkin, Ed., Wiley, 1974.

Sparrow, E.M., Goldstein, R.J., Jonsson, V.K., "Thermal Instability in a Horizontal Fluid Layer", J. Fluid Mech., Vol. 18, 1964.

Springer, G. S., "Homogeneous Nucleation", *Adv. Heat Transfer,* Vol. 14, pp. 281-346, 1978.

Straub, J., Zell, M., and Vogel, B., "Pool Boiling in a Reduced Gravity Field", Presented at the Int. Heat Transfer Conf., Jerusalem, Israel, 1990.

Sturtevant, B., and Shepherd, J.E., "Evaporative Instability at the Superheat Limit", *Appl. Sci. Res.*, Vol. 38, pp. 85-97, 1982.

Tong, W., Bar-Cohen, A., Simon, T. W., and You, S. M., "Contact Angle Effects on Boiling Incipience of Higher Wetting Liquids", *Int. J. Heat Mass Transfer,* Vol. 33, pp. 91-103, 1990.

Tsukamato, O. and Uyemura, T., "Observation of Bubble Formation Mechanism of Liquid Nitrogen Subjected to Transient Heating", *J. Adv. Cryogen. Eng.*, Vol. 25, pp. 476-482, 1980.

Ulucakli, M., "Nucleate Pool Boiling With Increased Acceleration and Subcooling", PhD Thesis, University of Michigan, Ann Arbor, 1987.

Volmer, M., *Kinetik Der Phasenbildung*, Edwards Brother, Inc., Ann Arbor, 1945.

Webb, R. L., "The Evolution of Enhanced Surface Geometries for Nucleate Boiling", *Heat Transfer Engr.*, Vol. 2, pp. 46-69, 1981.

Weinzierl, A., and Straub, J., "Nucleate Pool Boiling In Microgravity Environment", Proceedings Of The Seventh International Heat Transfer Conference, Munich, Vol. 4, pp. 21-27, 1982.

Wiebe, J.R., and Judd, R.L., "Superheat Layer Thickness Measurements In Saturated And Subcooled Nucleate Boiling", *J. Heat Transfer,* Vol. 93, pp. 455-461, 1971.

Winterton, R. H. S., "Nucleation of Boiling and Cavitation", *J. Phys. D: Appl. Phys.*, Vol. 10, pp. 2041-2056, 1977.

Winterton,R. H. S., and Blake, T. D., "Dynamic Effects in Contact Angle Hysteresis, Applied to Boiling Incipience", *Int.. Comm.. Heat Mass Transfer,* Vol. 10, pp. 525-531, 1983.

Yin, S. T., and Abdelmessih, A. H., "Prediction of Incipient Flow Boiling from a Uniformly Heated Surface", Nuclear, *Solar and Process Heat Transfer AIChE Symposium Series* , Vol. 73, pp. 236-243, 1977.

You, S.M., Simon, T.W., Bar-Cohen, A., Tong, W., "Experimental Investigation of Nucleate Boiling Incipience with a Highly-Wetting Dielectric Fluid (R-113)", Int. J. Heat Mass Transfer, Vol. 33, pp. 105-117, 1990.

Zeldovich, J., "Theory of Nucleation and Condensation", Sov. Phys.-JETP, (Eng. Trans.), Vol. 12, 1942.

Zell, M., and Straub, J., "Experimental Investigation of Boiling Phenomena Under Microgravity Conditions", Presented at the ASME/ JSME Thermal Eng. Conf., Honolulu, Hawaii, March 1987.

Zell, M., and Straub, J., "Microgravity Pool Boiling-TEXUS and Parabolic Flight Experiments", Personal Communication, 1987.

Zimmels, Y., "On The Application of Thermodynamic Potentials to The Theory of Heterogeneous Nucleation", *J. Colloid Int. Sci.*, Vol. 57, p. 446, 1976.